

NICKEL FERRITE NANOCOMPOSITE FOR THE REMOVAL OF NSAIDs, ANTIBIOTICS AND CAFFEINE

Thesis

Submitted in partial fulfilment of the requirements for the degree of

DOCTOR OF PHILOSOPHY

by

I. INDUMATHI



**DEPARTMENT OF CHEMICAL ENGINEERING
NATIONAL INSTITUTE OF TECHNOLOGY KARNATAKA,
SURATHKAL, MANGALORE - 575025**

OCTOBER 2024

NICKEL FERRITE NANOCOMPOSITE FOR THE REMOVAL OF NSAIDs, ANTIBIOTICS AND CAFFEINE

Thesis

Submitted in partial fulfilment of the requirements for the degree of

DOCTOR OF PHILOSOPHY

by

I. INDUMATHI

Reg. No.197522CH500

Under the Guidance of

Prof. Raj Mohan .B



**DEPARTMENT OF CHEMICAL ENGINEERING
NATIONAL INSTITUTE OF TECHNOLOGY KARNATAKA,
SURATHKAL MANGALORE -575025**

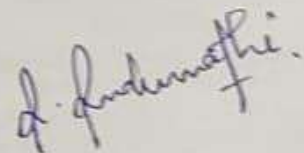
OCTOBER 2024

DECLARATION

I hereby declare that the Research Thesis entitled "**Nickel ferrite nanocomposite for the removal of NSAIDs, Antibiotics and Caffeine**" which is being submitted to the National Institute of Technology Karnataka, Surathkal in partial fulfilment of the requirements for the award of the Degree of Doctor of Philosophy in the Department of Chemical Engineering is a bonafide report of the research work carried out by me. The material contained in this Research Thesis has not been submitted to any University or Institution for the award of any degree.

Place: Surathkal, India

Date: 29th October 2024



I Indumathi

197522CH500

Department Of Chemical Engineering

CERTIFICATE

This is to certify that the Research Thesis entitled "**Nickel ferrite nanocomposite for the removal of NSAIDs, Antibiotics and Caffeine**" submitted by **Mrs. I. Indumathi** (**Register Number: 197522CH500**) as the record of the research work carried out by her, is accepted as the Research Thesis submission in partial fulfilment of the requirements for the award of Degree of Philosophy



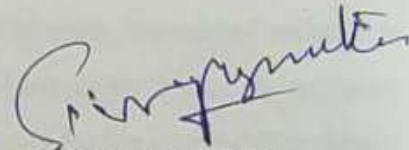
Research Guide

Dr. Raj Mohan .B

Professor

Dept. of Chemical Engineering

NITK, Surathkal



Chairman -DRPC

Dept. of Chemical Engineering

Head of the Department

विभागाध्यक्ष

Department of Chemical Engineering

रासायनिक अभियांत्रिकी विभाग

National Institute of Technology Karnataka - Surathkal

राष्ट्रीय प्रौद्योगिकी संस्थान कर्नाटक, सुरात्कल

PO Srinivasnagar, Mangalore - 575025 Karnataka

पी.ओ. श्रीनिवासनगर, मंगलूर - ५७५०२५ कर्नाटक

ACKNOWLEDGEMENTS

In the tradition of academic courtesy, the acknowledgement section is a heartfelt appreciation for those who contributed to the completion of a thesis. It serves as a platform to express gratitude to supervisors, mentors, colleagues, and family members whose support, guidance, and encouragement were indispensable throughout the research journey. I am immensely grateful to Prof. Chandrasekhar Garlapati, my M.Tech supervisor in the Department of Chemical Engineering at Puducherry Technological University (Erstwhile Pondicherry Engineering College), whose guidance and mentorship not only fueled my passion for research but also motivated me to pursue a Ph.D.

I extend my heartfelt gratitude to Prof. Raj Mohan .B, as both Principal investigator and my Ph.D. supervisor, for his unwavering support, encouragement, and guidance throughout the completion of the research work. His belief in my capabilities and relentless support were instrumental in overcoming the challenges I encountered.

I would like to express my sincere gratitude to Dr. Allwin Ebinesar, Associate Professor at Sapthagiri College of Engineering, Bangalore and Dr. Mekonnen Maschal, Assistant Professor of Environmental Sciences at Addis Ababa University for his invaluable technical guidance, which provided the initial impetus for my research endeavours.

I am deeply thankful to all the professors in the Department of Chemical Engineering for their support and for providing vital laboratory facilities, which greatly aided in the successful completion of my research.

Special recognition is extended to Dr. Jagannathan T K in the Department of Chemical Engineering and Prof. Ramesh H from the Department of Water Resources and Ocean Engineering for their continuous guidance and support during presentations as RPAC members.

I am indebted to the staff at the NITK Central Research Facility (CRF), namely Mrs. Thrithila Shetty, Mrs. Pratheeksha K P, Mrs. Suraksha S Shetty, and Mrs. Aniz Zahara, for their invaluable assistance in sample analysis.

I wish to express my sincere gratitude to Mr. Sadashiva, Mrs. Shashikala, Mr. Mahadeva, Mr. Suresh, Mr. Harish, Mrs. Vijitha Kotian, Mr. Gnaneshwar, Mrs Sandhya, Mrs Bhavya Shree and every other non-technical staff member in the department for their invaluable assistance throughout the research process.

Grateful acknowledgements go to my seniors, Dr. Pragadeesh K S, Mrs. Subraja S, Dr. Vishnu. M, Dr. Ajuy Sundar, Dr. Vrushali Vinayak Kadam, Dr. Sunaina Patil, Dr. Thara

Ratna, Dr. Manasa, Mr. Shourya and Dr. Minimol M, whose insights and support enriched my research journey.

It's an immense pride and pleasure to be a part of one of the premier institutes NITK! I thank the institute for providing a great platform to explore research and sports activities. I thank each person in the administration who has helped me during the DST project. I would like to acknowledge the Department of Science and Technology (DST) SERB for providing funding during the research work. I also wanted to express my heartfelt gratitude to my friends, Anusha Reddy, Deepti Susanna, A Selva Sudha, T Nishanthini, Harmeet Singh, Suyash Harsh, Reneeth Gabriella, Vishnu Priya, Satish, Shivaram and Sriram for their unwavering support and helpfulness throughout my research work.

Finally, I extend my deepest appreciation to my family, especially my husband, Dr. Prethiv Kumar R, for his unwavering financial and moral support, and to my in-laws, Mr. V. Ravindra Kumar and Mrs. R. Bama, Mr. R. Nivethana Kumar and my co-sister Mrs. Pooja Rayudu for their encouragement during my Ph.D. studies. I am also grateful to my father, Mr. V. Ilango, my mother, Mrs. I. Indira, my elder sister, Dr. Ilangovai Vinod, my niece Ms. Kenishka V and Ms. Shanvika V for their continuous moral, emotional, and health support during challenging times.

Lastly, I thank the Almighty God for blessing me with strength, happiness, and resilience throughout all the ups and downs of my academic journey.

INDUMATHI ILANGO

ABSTRACT

The earth's surface is made up of 97% salty seawater and the rest is freshwater, which is the only resource for drinking, domestic and industrial use. These water sources are constantly contaminated with organic and inorganic wastes, pathogens, and pharmaceutical and personal care products (PPCP) (PPCP). The release of PPCP products, particularly as nonsteroidal anti-inflammatory drugs (NSAIDs), caffeine and antibiotics is present in municipal sewage influent and effluent at low concentrations ranging from a few ng/L to mg/L. It is also transported to surface water via either a direct or indirect pathway, which is extremely harmful to aquatic habitats and has an impact on the population of naturally occurring bacteria. On the nanotechnological adsorbent basis, adsorption is now growing among wastewater remediation techniques, which can effectively remove existing PPCP in water bodies even at low concentrations. Nickel ferrite NiFe_2O_4 (NFO) has been extensively used because of its vast surface-active sites, specific surface area, exceptional magnetic and chemical characteristics and alterable shape and size with which they can be modified or functionalized. In recent years, the functionalization of NFO nanoparticles with biomolecules such as β -cyclodextrin (β -CD) and amino acid has improved the possibility of adsorption of targeted pollutants. β -cyclodextrin (β -CD) with six glucose subunits has a significant feature of forming solid inclusion complexes with a wide variety of guest molecules within the hydrophobic cavity of the host cyclodextrin. The functionalization of amino acids with at least one amino group ($-\text{NH}_2$) and one carboxyl group ($-\text{COOH}$) could improve the stability of nickel ferrite as well as its ability to absorb the targeted contaminants by providing strong chelating sites. Thus, a laboratory scale experiment was conducted to study the physical, chemical, thermal and magnetic properties of

NFO@SiO₂@β-CD, L-Leucine functionalized NFO nanocomposite (NFO@L) as an adsorbent and NFO as a catalyst was used in the activation of PMS for the degradation process. The NFO@SiO₂@β-CD was used to study the feasibility of the removal of Ketoprofen (KF) and Diclofenac (DCF). The co-precipitation approach was utilised to synthesize nickel ferrite (NFO) nanoparticles, which were then functionalized with TEOS to form NFO@SiO₂; β-cyclodextrin was then functionalized using 3-Glycidoxypropyltrimethoxysilane (GPTMS) as an interface to form NFO@SiO₂@β-CD. FTIR, XRD, FE-SEM, EDX, TGA/DTG, VSM, BET, zeta potential and particle size analysis were then used to characterise the nanocomposites. The average diameter of NFO@SiO₂@β-CD was determined to be 109.1 nm, with superparamagnetic behaviour, a mesoporous surface and a specific surface of 20.78 m²/g. The functionalized NFO@SiO₂@β-CD nanocomposite removed 94% of diclofenac in 5 min and 80% of ketoprofen in 360 min with the adsorption capacities of 8.46 and 0.54 mg/g, respectively. The obtained experimental datum for both the pollutants was fitted in kinetic and isotherm models, with the pseudo-second-order kinetic model and Freundlich adsorption isotherm showing the best fit with the highest regression of $R^2 = 0.99$. The nanocomposite was regenerated using 0.1 M NaOH and recycled for about four consecutive cycles in which the reduction in the removal efficiency of ketoprofen and diclofenac was observed to be 51.36% and 64%, respectively.

The removal of ciprofloxacin (CIP) and lomefloxacin hydrochloride (LFH) in the aqueous phase was investigated using a hydrothermally synthesized L-Leucine functionalized nickel ferrite nanocomposite (NFO@L). Various analytical techniques were used to analyze L-Leucine functionalized nickel ferrite, and the nanocomposite's average particle diameter was determined to be between 11 and 15 nm. The maximal

measured zeta potential was - 21.5 mV. Fourier transform infrared spectroscopy (FTIR), ninhydrin assay and X-ray diffraction (XRD) analysis confirmed the attachment of L-Leucine onto nickel ferrite. The nanocomposite's surface-to-volume ratio was calculated to be 92.916 m²/g. The S-shaped curve from the vibrating sample magnetometer analysis reflected the superparamagnetic behaviour of the nanocomposite with a saturation magnetization of 0.665 emu/g. Various parametric experiments were conducted, in which 93.549% ciprofloxacin was removed in 120 min at 303 K, pH 8 and with a NFO@L dosage of 100 mg in 100 mL whereas 75.192% lomefloxacin hydrochloride was removed in 140 min at 333 K, pH 9 and with a NFO@L dosage of 70 mg in 100 mL. The plot of experimental datum in kinetic and isotherm studies fitted well with the Pseudo second order kinetic model and Langmuir isotherm. The ICP – OES analysis revealed that the leaching of iron ions was within the permissible limits in the final analyte. The recycle and regeneration studies showed good stability with a small reduction after four cycle runs.

A laboratory batch study on the degradation of Lomefloxacin hydrochloride (LFH), Caffeine (CAF) and LC (CAF and LFH mixed solution) was carried out by stimulating potassium peroxy monosulfate (PMS) using NFO. The NFO nanoparticles were synthesized through a co-precipitation method and characterized using FTIR, XRD, FESEM/EDX, TGA/DTA/DTG, BET, AFM, VSM, Zeta potential, and particle size distribution from FESEM (using ImageJ software). The NFO nanoparticles' specific surface area was estimated to be 112.02 m²/g, and the magnetic properties of the NFO nanoparticles were investigated using VSM analysis. The parametric study included the study on the effect of bare NFO, PMS without catalyst, pH, catalyst dosage, PMS variation with optimized catalyst, initial concentration of LFH and CAF, and reaction

time, with nearly 98.61 % LFH was degraded in 220 min, 100 % CAF was degraded in 80 min, 78.07 % LC was degraded in 40 min. The degraded compounds m/z of LFH, CAF and LC were identified using LC-MS. The regeneration and recycling of NFO nanoparticles were investigated to determine the stability of the NFO nanoparticles in the degradation of LFH and CAF in which the degradation efficiency decreased to 90.68 % and 64.1 % respectively upon the third wash with distilled water. As a result, the NiFe₂O₄/PMS system showed improved degradation even after two recycle runs. Based on these findings, the results suggested that the NFO@SiO₂@β-CD nanocomposite, Leucine functionalized nickel ferrite nanocomposite and Nickel ferrite (NFO) could be a potent adsorbent and catalyst to target specific low-concentrated pharmaceutical pollutants, making it an efficient and economical system even for multi-pharmaceutical pollutants.

Keywords: Adsorption, Adsorption kinetics, Adsorption isotherm, Biomolecule functionalization, Degradation, Pharmaceutical pollutants, Regeneration and Recycling

TABLE OF CONTENTS

TITLE	PAGE-NO
ABSTRACT	i
TABLE OF CONTENTS	v
LIST OF FIGURES	xi
LIST OF TABLES	xvii
ABBREVIATIONS AND ACRONYMS	xix
NOMENCLATURE	xxi
GREEK SYMBOLS	xxi
1. INTRODUCTION	1
(a) Nonsteroidal anti-inflammatory drugs (NSAIDs)	2
(b) Fluoroquinolones	3
(c) Caffeine	4
1.1 Conventional treatment operations	4
1.1.1 Adsorption for the removal of Pharmaceutical and personal care products (PPCPs)	5
1.1.2 Nanosorbent	5
1.1.2.1 Nickel ferrite nanoparticles (NFO)	6
1.1.2.2 Silanization of NFO surface	8
1.1.2.3 Biomolecule functionalization	8
1.1.2.4 Amino acid functionalization (L-Leucine)	8
1.2 Nano-catalyst (NFO)	9
1.2.1 Advanced oxidation process for the degradation of (PPCPs)	9
1.3 Co-precipitation method	9
1.4 Hydrothermal method	10
1.5 Present work	10
2. REVIEW OF LITERATURE	11
2.1 Origin of the research of PPCPs in the environment	11
2.1.1 Emerging pollutants	11
2.2 Conventional method for the removal of PPCPs	12
2.3 Nano-ferrite and nano-ferrite composite in the removal of PPCPs	13
2.4 Synthesis methods for the Nickel ferrite nanoparticles	14

2.5 SCOPE AND OBJECTIVES	38
2.5.1 Scope	38
2.5.2 Objectives	38
2.6 RESEARCH GAP	39
3. MATERIALS AND METHODS	40
3.1 Choice of precursor salts	40
3.1.1 Materials and methods	40
3.2 Synthesis of adsorbent	43
3.2.1 Synthesis of NFO nanoparticles	43
3.2.2 Optimization of NiFe ₂ O ₄ @SiO ₂ nanoparticles	43
3.2.2.1 Reaction involved in the Stober method	44
3.2.3 Synthesis of NFO@SiO ₂ @GPTMS@β-cyclodextrin	45
3.2.4 Synthesis of Nickel ferrite@L-Leucine (NFO@L)	46
3.3 Characterization studies of the NFO nanocomposites	47
3.3.1 Ninhydrin test for NFO@L nanocomposite	48
3.4. Stock solution and UV -Visible scan for pharmaceutical pollutants	48
3.4.1 Preparation of stock solution & UV-visible scan for KF and DCF	49
3.4.2 Preparation of working solution preparation & UV-visible scan for CIP and LFH	49
3.4.3 Preparation of stock solution & calibration curve of CAF	50
3.4.4 Calibration plot for KF and DCF	51
3.4.5 Calibration plot for CIP and LFH	51
3.4.6 Calibration plot for CAF	52
3.5 Batch experimental investigation of the nanoparticles/nanocomposite for the removal of the pharmaceutical pollutants	52
3.6 Degradation experiment for the removal of CAF and LFH	53
3.6.1 Quantification of β-CD in the final analyte of KF and DCF using spectrophotometric titration	54
3.7 Adsorption kinetics	55
3.8 Adsorption isotherm	55
3.8.1 Langmuir isotherm	56
3.8.2 Freundlich isotherm	56

3.8.3 Temkin and Dubinin – Radushkevich isotherms	57
3.8.3.1 Temkin isotherm	57
3.8.3.2 Dubinin – Radushkevich isotherm	57
3.9 Regeneration and recycle studies of NFO nanocomposites	58
4. RESULTS AND DISCUSSION	59
4.1 Characterization of NFO nanoparticles	59
4.1.1 Fourier transform infrared spectroscopy (FTIR) of NFO nanoparticles	59
4.1.2 Field Emission – Scanning electron microscope (FE-SEM)/ Energy Dispersive X-ray Diffraction (EDX) of NFO nanoparticles	60
4.1.3 X-ray Diffraction analysis (XRD) of NFO nanoparticles	61
4.1.4 Brunauer-Emmett-Teller (BET)/Barrett-Joyner Halenda (BJH) model analysis of NFO nanoparticles	62
4.1.5 Thermogravimetric analysis (TGA) of NFO nanoparticles	63
4.1.6 Particle size distribution and electrokinetic potential of NFO nanoparticles	64
4.1.7. Vibrating sample magnetometer (VSM) analysis of NFO nanoparticles	64
4.2 Characterization results of NFO@SiO ₂	65
4.2.1 Effect of varied mass of NFO in the synthesis of NFO@SiO ₂ – FESEM image	65
4.2.2 Effect of varied concentrations of TEOS in the synthesis of NFO@SiO ₂ – FESEM image	66
4.2.3 Brunauer Emmett Teller (BET) specific surface area analysis and Barrett-Joyner Halenda (BJH) model of NFO@SiO ₂ nanocomposite	67
4.3 Characterization results of NFO@SiO ₂ @β-CD nanocomposite	68
4.3.1 Effect of β-CD mass variation on the NFO@SiO ₂ upon the removal of KF and DCF	67
4.3.2 Effect of varied β-CD mass onto NFO@SiO ₂ FE-SEM/EDX of optimized NFO@SiO ₂ @β-CD nanocomposite	69
4.3.3 Optimized NFO@SiO ₂ @β-CD - FTIR analysis	70
4.3.4 Particle size distribution/electrokinetic potential and point of zero charge of NFO@SiO ₂ @β-CD nanocomposite	71
4.3.5 Comparative study of XRD pattern of β-CD and functionalized NFO@SiO ₂ and NFO@SiO ₂ @β-CD nanocomposite	72

4.3.6 Brunauer Emmett Teller (BET) specific surface area analysis and Barrett-Joyner Halenda (BJH) model of NFO@SiO ₂ @β-CD	74
4.3.7 Thermogravimetric analysis (TGA) of NFO@SiO ₂ @β-CD nanocomposite	74
4.3.8 VSM analysis of NFO@SiO ₂ @β-CD nanocomposite	75
4.4 Optimization of parameters for the removal of KF and DCF using NFO@SiO ₂ @β-CD nanocomposite	76
4.4.1 Effect of KF and DCF aqueous solutions' pH	76
4.4.2 Effect of NFO@SiO ₂ @β-CD dosage on the removal of KF and DCF	78
4.4.3 Effect of initial concentration of KF and DCF aqueous solutions	80
4.4.4 Effect of reaction time on the removal of KF and DCF in the aqueous solutions	81
4.4.5 FTIR image of adsorption of KF and DCF	82
4.4.6 Quantification of β-CD in the final analyte of KF and DCF	83
4.5 Adsorption kinetics and isotherm modelling	83
4.5.1 Adsorption Kinetics	84
4.5.2 Adsorption Isotherms	85
4.5.2.1 Langmuir isotherm for the removal of DCF and KF	85
4.5.2.2 Freundlich isotherm for the removal of DCF and KF	86
4.5.3 NFO@SiO ₂ @β-CD nanocomposite regeneration and recycling studies	87
4.6 Adsorbent: Nickel ferrite@L-Leucine (NFO@L)	88
4.6.1 FTIR of NFO@L-Leucine	88
4.6.2 Effect of varied L-Leucine molar ratio onto NFO, reaction time and the temperature on the crystallographic structure of NFO@L nanocomposite using XRD analysis	89
4.6.3 FE-SEM/EDX of NFO@L nanocomposite	91
4.6.4 Atomic Force Microscope (AFM) and Particle size distribution from AFM and FE-SEM	93
4.6.5 TGA/DTG analysis of NFO@L nanocomposite (TGA/DTG)	94
4.6.6 VSM of NFO@L nanocomposite	95
4.6.7 Electrokinetic potential analysis of NFO@L nanocomposite	96
4.6.8 Brunauer Emmett Teller (BET) specific surface area analysis and Barrett-Joyner Halenda (BJH) model of NFO@L nanocomposite	97

4.6.9 Ninhydrin test for NFO@L nanocomposite	98
4.6.10 Effect of varied molar ratio of L-Leucine on the NFO upon the removal of LFH and CIP	98
4.6.11 Effect of pH on the removal of LFH and CIP using NFO@L	99
4.6.12 Effect of NFO@L dosage on the removal of LFH and CIP	100
4.6.13 Effect of initial concentration on the removal of LFH and CIP using NFO@L	102
4.6.14 Effect of time on the removal of CIP and LFH using NFO@L	103
4.6.14 Effect of temperature on the removal of CIP and LFH using NFO@L	104
4.6.15 Adsorption Kinetics	105
4.6.16 Adsorption Isotherm model for the removal of LFH and CIP	106
4.6.16.1 Langmuir and Freundlich Isotherm for the removal of LFH and CIP	106
4.6.16.2 Temkin isotherm for CIP and LFH removal using NFO@L	107
4.6.16.3 Dubinin – Radushkevich isotherm for the removal of LFH and CIP	108
4.6.18 Thermodynamics studies for the removal of CIP and LFH	110
4.6.19 Regeneration and recycle studies of NFO@L nanocomposite	111
4.6.20 FTIR image after adsorption of CIP and LFH	114
4.7 Adsorbent: Nickel ferrite (NFO) as a nanocatalyst/PMS	115
4.7.1 Effect of Bare NFO on the degradation of CAF and LFH	115
4.7.2 Effect of PMS with no catalyst on the degradation of CAF and LFH	116
4.7.3 Effect of pH on the degradation of CAF and LFH using NFO	117
4.7.4 Effect of NFO dosage on the degradation of CAF and LFH	118
4.7.5 Effect of variation of PMS in the optimized dosage on the degradation of LFH and CAF	118
4.7.6 Effect of initial concentration of CAF and LFH on the degradation efficiency	119
4.7.7 Effect of reaction time on the degradation of CAF and LFH	121
4.7.8 Effect of PMS, NFO dosage and reaction time on the LFH and CAF mixed solution (LC)	122
4.7.9 Mechanism involved in the degradation of CAF and LFH	123
4.7.10 Degradation kinetic studies of CAF and LFH	124

4.7.11 Regeneration and recycle studies of NFO nanoparticles	126
4.7.12 Degradation of LFH and CAF on the different water sources	127
4.7.13 Inductively coupled plasma -Optical emission spectroscopy (ICP-OES)	128
4.7.14 Identification of degraded products using Liquid chromatography-mass spectrometry (LC-MS)	128
4.7.15 LC-MS results of LC (Lomefloxacin Hydrochloride and Caffeine) mixed solution	131
4.7.16 FTIR analysis of NFO/PMS system after degradation of CAF and LFH	131
4.7.17 FTIR of NFO/PMS/LFH and NFO/PMS/CAF after each parametric batch studies	132
4.7.18 Chemical oxygen demand analysis (COD)	134
5. CONCLUSION	135
5.1 Summary	136
(a) NFO@SiO ₂ @β-CD nanocomposite for the removal of KF and DCF	136
(b) L-Leucine functionalized nickel ferrite (NFO@L) nanocomposite for the removal of CIP and LFH	137
(c) Nickel ferrite (NFO) as a nanocatalyst in the degradation of CAF and LFH	139
5.2 Future scope of the study	140
LIST OF PUBLICATIONS AND CONFERENCES	140
REFERENCES	142
BIODATA	170

LIST OF FIGURES

FIGURE NO	TITLE	PAGE NO
	Fig. 2.1 Papers having M-ferrite (M = Co, Cu, Ni, Mn, Zn) in the topic published in Web of Science Core Collection between 1975–June 2021 (Thomas Dippong et al. 2021)	13
	Fig. 3.1 (a) Schematic representation of procedural attachment of TEOS onto NFO using the Stober method	44
	Fig. 3.1 (b) Schematic representation of attachment of NFO@SiO ₂	44
	Fig. 3.2 (a) Schematic representation of procedural linkage of 3 – GPTMS and β-CD to NFO@SiO ₂	45
	Fig. 3.2 (b) Schematic representation of NFO@SiO ₂ @GPTMS@β – cyclodextrin	46
	Fig. 3.2 (c) Procedural Schematic representation of attachment of L-Leucine to NFO	46
	Fig. 3.3 Ninhydrin test of L-Leucine functionalized onto NFO	48
	Fig. 3.4 (a) KF and (b) DCF at different concentrations and their respective absorbance	49
	Fig. 3.5 UV-Visible absorbance of (a) CIP and (b) LFH solution for different Concentrations	50
	Fig. 3.5 (c) UV-visible absorbance of CAF for different concentrations	50
	Fig.3.6 (a) Calibration plot of KF and DCF	51
	Fig.3.6 (b) Calibration plot of CIP and LFH aqueous solutions	51
	Fig.3.6 (c) Calibration plot of CAF and LFH	52
	Fig.4.1 FTIR spectrum of NFO nanoparticles	60
	Fig.4.2 (a) FE-SEM image of NFO nanoparticles	60
	Fig.4.2 (b) Elemental analysis of NFO nanoparticles	60
	Fig.4.3 XRD of NFO nanoparticles	61
	Fig.4.4 Adsorption-Desorption Hysteresis loop and linear graph of relative pressure (P/P ₀) versus Volume occupied at STP (cc/g) of NFO nanoparticles from BET Test	63
	Fig.4.5 TGA of the uncalcined NFO nanoparticles	63
	Fig.4.6 (a) Particle size distribution of NFO nanoparticles using FESEM	64

Fig.4.6 (b) Zeta potential of NFO nanoparticles	64
Fig.4.7 VSM analysis of NFO nanoparticles	65
Fig.4.8 (a), (b) and (c) The FE-SEM image of varied NFO mass in the synthesis of NFO@ SiO ₂	66
Fig.4.9 The FE-SEM image of varied TEOS concentrations in the synthesis of NFO@SiO ₂	65
Fig.4.10 Adsorption-Desorption Hysteresis loop of NFO@SiO ₂ using BET/BJH method	67
Fig.4.11 Effect of β -CD mass variation on the NFO@SiO ₂ upon the removal of KF and DCF	68
Fig.4.12 (a) FESEM images of a varied β -CD mass onto NFO@SiO ₂ and (b) EDX of the optimized NFO@SiO ₂ @ β -CD nanocomposite	69
Fig.4.13 FTIR spectrum of optimized NFO@SiO ₂ @ β -CD nanocomposite	70
Fig.4.14 (a) Particle size distribution of NFO@SiO ₂ @ β -CD	70
Fig. 4.14 (b) Zeta potential of NFO and NFO@SiO ₂ @ β -CD	71
Fig. 4.14 (c) Point of zero charge NFO@SiO ₂ @ β -CD nanocomposite	72
Fig. 4.15 X-ray Diffraction analysis of NFO, NFO@SiO ₂ , β -CD, NFO@SiO ₂ @ β -CD Nanocomposite	73
Fig. 4.16 Adsorption-Desorption Hysteresis loop and linear graph of relative pressure (P/P ₀)	74
Fig. 4.17 TGA analysis of NFO@SiO ₂ @ β -CD	75
Fig. 4.18 VSM analysis of NFO and NFO@SiO ₂ @ β -CD	76
Fig. 4.19 Effect of pH on the adsorption capacity and removal efficiency of KF and DCF	77
Fig. 4.20 Effect of varying nanocomposite dosage on the adsorption capacity and the removal efficiency of KF and DCF	78
Fig. 4.21 Schematic representation of Host - guest inclusion of (a) DCF and (b) KF to β -cyclodextrin (Li et al. 2019; Shi et al. 2014)	79
Fig. 4.22 Effect of varying initial concentration on the adsorption capacity and the removal efficiency of KF and DCF	80
Fig. 4.23 Effect of varying time on the adsorption capacity and removal efficiency of KF and DCF	81

Fig. 4.24 Fourier transform infrared spectra of NFO and NFO@SiO ₂ @β-CD before and after the adsorption process	83
Fig. 4.25 (a) Pseudo-first-order kinetic model and (b) Pseudo-second-order kinetic model for the removal of KF and DCF	84
Fig. 4.26 Langmuir isotherm plot for the removal of (a) DCF and (b) KF	85
Fig. 4.27 Freundlich isotherm plot for the removal of (a) DCF and (b) KF	86
Fig. 4.28 Reusability of NFO@SiO ₂ @β-CD on the removal of KF and DCF	87
Fig. 4.29 FTIR analysis of varied L-Leucine molar ratio onto NFO	88
Fig. 4.30 X-ray Diffraction analysis of NFO@L nanocomposite at (a) different molar ratios of l-leucine onto NFO@L	90
Fig. 4.30 (c) XRD of NFO@L nanocomposite at two temperatures	90
Fig. 4.31 FE-SEM image of varied L-Leucine molar ratio onto NFO@L	92
Fig. 4.32 EDX of varied L-Leucine molar ratio onto NFO@L nanocomposite	93
Fig. 4.33 Atomic Force Microscope (AFM) 3 and 2 Dimensions of the	94
Fig. 4.34 Particle size distribution obtained from (a) AFM and (b) FESEM NFO@L Nanocomposite	94
Fig. 4.35 TGA/ DTG of the NFO@L nanocomposite	95
Fig. 4.36 VSM analysis of NFO@L nanocomposite	96
Fig. 4.37 Zeta potential of NFO@L nanocomposite	96
Fig. 4.38 N ₂ Adsorption-desorption Hysteresis loop of NFO@L nanocomposite and a BET plot of NFO@L between $1/[W((W(Po/P)-1)]$ and relative pressure (P/P _o)	97
Fig. 4.39 Effect of varied L-Leucine molar ratio on the NFO for the removal of LFH and CIP	98
Fig. 4.40 The adsorption capacity of NFO@L and its removal efficiency in the removal of LFH and CIP at different pH	99
Fig. 4.41 The adsorption capacity of NFO@L and its efficiency in the removal of LFH and CIP upon varying the catalyst dosage	101
Fig. 4.42 The adsorption capacity of NFO@L and its efficiency in the removal of LFH and CIP at different initial concentrations	102
Fig. 4.43 The adsorption capacity of NFO@L and its efficiency in the removal of LFH and CIP upon varying the time	103

Fig. 4.44 The adsorption capacity of NFO@L and its efficiency in the removal of LFH and CIP upon varying the temperature	104
Fig. 4.45 A plot of (a) Pseudo-first-order kinetic model and (b) Pseudo second-order kinetic model of CIP and LFH on NFO@L	105
Fig. 4.46 (a) Langmuir Linear isotherm of CIP and LFH on NFO@L and (b) Freundlich isotherm of CIP and LFH on NFO@L	106
Fig. 4.47 Temkin isotherm plot of $\ln C_e$ versus q_e for CIP and LFH	108
Fig. 4.48 Dubinin – Radushkevich isotherm plot of ϵ^2 versus $\ln q_e$ for the removal of (a) LFH and (b) CIP	108
Fig. 4.49 van't Hoff plot for the removal of LFH and CIP	111
Fig. 4.50 Regeneration of the NFO@L using three different solvents	112
Fig. 4.51 Removal efficiency of LFH and CIP upon regenerated NFO@L after four runs	112
Fig. 4.52 A stacked FTIR of NFO@L nanocomposite and the composite after adsorption of CIP and LFH onto nanocomposite	114
Fig. 4.53(a) Effect of pH on the removal of LFH and CAF using Bare NFO	115
Fig. 4.53 (b) Effect of catalyst dosage on the removal of LFH and CAF using Bare NFO	115
Fig. 4.54 Effect of PMS alone on the degradation of CAF and LFH	116
Fig. 4.55 Effect of pH on the degradation of CAF and LFH using NFO	117
Fig. 4.56 Effect of varied NFO dosage on the degradation of CAF and LFH	118
Fig. 4.57 Effect of varied PMS with the optimized dosage on the degradation of LFH and CAF	119
Fig. 4.58 Effect of initial concentration on the degradation of CAF and LFH	120
Fig. 4.59 Effect of reaction time on the degradation of CAF and LFH	121
Fig. 4.60 (a) Calibration graph of LFH and CAF mixed solution (LC)	122
Fig. 4.60 (b) Variation of PMS Concentration in the LFH and CAF mixed solution (LC) at pH 3	122
Fig. 4.60 (c) Variation of NFO dosage at optimized PMS in the LFH and CAF mixed solution (LC)	123
Fig. 4.60 (d) Variation of reaction time at optimized NFO dosage in the LFH and CAF mixed solution (LC)	123

Fig. 4.61 (a) Zero-order reaction (b) Pseudo first-order kinetics for the removal of LFH and CAF	125
Fig. 4.61 (c) Pseudo second order kinetics for the removal of LFH and CAF	125
Fig. 4.62 (a) Regeneration of NFO nanoparticles on different solvents	127
(b) Three recycle runs of NFO nanoparticles for the degradation of CAF and LFH	
Fig. 4.63 Degradation of LFH on different water sources	128
Fig. 4.64 Mass spectrum of Initial (a) and after (b) degradation of LFH	129
Fig. 4.65 Mass spectrum of (a) Initial and (b) after degradation of CAF	130
Fig. 4.66 Degradation pathway of LFH	131
Fig. 4.67 Degradation pathway of CAF	131
Fig. 4.68 (a) MS-MS spectrum of LFH and CAF mixed solution (Initial)	132
Fig. 4.68 (b) MS-MS spectrum of LFH and CAF mixed solution (Final)	132
Fig. 4.69 FTIR of NFO/PMS system after degradation of CAF and LFH	133
Fig. 4.70 FTIR of NFO/PMS/LFH and NFO/PMS/CAF after each parametric batch studies	134

LIST OF TABLES

TABLE NO	TITLE	PAGE NO
Table 1.1	Properties of Nickel ferrite nanoparticles in comparison with the other ferrite nanoparticles (Jadhav et al. 2020; Kaur et al. 2016; Tatarchuk et al. 2020)	6
Table 2.1a	Advantages and Disadvantages of synthesis of nanoparticles and nanocomposites	15
Table 2.1b	Overview of synthesis of Nickel ferrite using different methods	18
Table 2.2	Overview of synthesis of NFO using the Co-precipitation method	21
Table 2.3	Overview of Nickel ferrite and other metal oxide nanocomposites in the removal of emerging pollutants and other applications	24
Table 2.4	Overview of removal of KF drug using various adsorbent	27
Table 2.5	Overview of removal of DCF drug using various adsorbent	29
Table 2.6	Overview of removal of CIP using various adsorbent	31
Table 2.7	Overview of removal of LFH using various adsorbent	33
Table 2.8	Overview of removal of CAF using various adsorbent	36
Table 3.1	List of pollutant drugs and main chemicals used in functionalization	40
Table 4.1	XRD values of NFO nanoparticles	62
Table 4.2	XRD 2 theta values, d-spacing, and lattice parameter values of NFO@SiO ₂ and NFO@SiO ₂ @β-CD	73
Table 4.3	Kinetic datum for the removal of KF and DCF	84
Table 4.4	Adsorption isotherm parameters for KF and DCF	86
Table 4.5	Separation factor in the removal of KF and DCF	86
Table 4.6	XRD parameters of optimized NFO@L nanocomposite	91
Table 4.7	Estimated kinetic model parameters in the removal of CIP and LFH	106
Table 4.8	Separation factor of NFO@L upon LFH and CIP from the Langmuir isotherm	107

Table 4.9	List of parameters from the Langmuir, Freundlich, Dubinin–Radushkevich, Temkin isotherm	109
Table 4.10	Thermodynamic parameters for adsorption of LFH and CIP onto NFO@L	111
Table 4.11	A comparison of commercially used adsorbent in the removal of LFH and CIP	112
Table 4.12	Kinetic parameters in the removal of LFH and CAF	126

ABBREVIATIONS AND ACRONYMS

ATR	- Attenuated Total Reflectance
AFM	- Atomic Force Microscope
BET	- Brunauer-Emmett-Teller
BJH	- Barette Joyner Halenda
β – CD	- Beta cyclodextrin
CAF	- Caffeine
CIP	- Ciprofloxacin
Conc	- Concentration
CT	- Combustion Temperature
DCF	- Diclofenac
DTA	- Derivative thermogravimetric analysis
DTG	- Derivative thermalgravimetric analysis
EDX	- Energy Dispersive X-ray Diffraction
EPs	- Emerging pollutants
FTIR	- Fourier Transform Infrared Spectroscopy
FE-SEM	- Field Emission - Scanning Electron Microscope
GPTMS	- (3-Glycidioxypropyl) trimethoxy silane
HPBCD	- Hydroxypropyl β -Cyclodextrin
ICP-OES	- Inductively Coupled Plasma-Optical Emission spectroscopy
KF	- Ketoprofen
LFH	- Lomefloxacin Hydrochloride
L	- L-Leucine
NFO	- Nickel Ferrite
NFO@L	- Nickel ferrite@L-Leucine
NSAIDs	- Non-Steroidal Anti-Inflammatory Drugs
PPCP	- Pharmaceutical and personal care products (PPCP)
NFO	- Nickel Ferrite
RPM	- Revolutions per minute
TEM	- Transmission Electron Microscope
TEOS	- Tetraethyl Orthosilicate

TGA - Thermogravimetric Analysis
VSM - Vibrating Sample Magnetometer
XRD - X-ray Diffraction Analysis

NOMENCLATURE

a	- Lattice parameter
A_T	-Equilibrium binding constant (L/g)
B	- Heat of adsorption (constant) J/mol
C_o	- Initial Concentration of drugs (mg/L)
C_f	- Final Concentration of drugs (mg/L)
d_{hkl}	- Interplanar spacing
E	-Mean free energy (kJ/mol)
H_c	- Coercivity
hkl	- Miller indices
K	- Kelvin (unit of Temperature)
K	- Scherrer constant in XRD
M_s	- Saturation magnetization
M	- Molar concentration
m	- Mass of adsorbent (g)
mL	- Milliliter
$q_{e, cal}$	- Equilibrium adsorption capacity (mg/L)
q_{max}	- Maximum adsorption capacity (mg/L)
q_t	- Equilibrium adsorption capacity at time t (mg/L)
R_L	- Separation factor
s	- Seconds
T	- Tesla
t	- Time (seconds)
V	- Volume of the solution (L)

GREEK SYMBOLS

b_T	-Temkin isotherm constant
β	- Full width at half maximum (FWHM) in XRD
β	- Binding energy (j^2/mol^2) in Temkin isotherm
ε	- Adsorption potential (kJ/mol)
λ	- X-ray wavelength

CHAPTER 1

INTRODUCTION

Water pollution/contamination is a major environmental issue that has piqued the interest of scientists and research communities all over the world. The rapid development in both population and industrialization has led to the shortage of water resources and has created an ever-increasing demand for water (Pavithra et al. 2017). According to the National Commission on Integrated Water Resources Development (NCIWRD), water demand would exceed 843 billion cubic metres in 2025 and 1180 billion cubic metres in 2050, encompassing agriculture, drinking water, industry, energy, and other requirements. According to projections, the world's population will increase from 7 billion to 9 billion by 2050. India accounts for 17.7 % of the total global population. Every year, more than 2.2 million people worldwide die as a result of a lack of safe drinking water and contaminated water (Ahammad et al. 2022; Manna and Sen 2022; Pavithra et al. 2017). Therefore, the discharge of unregulated micropollutants into water resources as a result of anthropogenic activities has pushed us to protect existing water sources and recycle wastewater in productive ways (Chandrashekar Kollarahithlu and Balakrishnan 2021).

The “emerging hazardous micropollutants” include pharmaceuticals such as non-steroidal anti-inflammatory drugs, antibiotics, antidepressants, anticonvulsants, anti-microbial and beta blockers, another class is synthetic and endocrine-disrupting chemicals (Ahammad et al. 2022; Tran et al. 2018). The word emerging refers to either new pollutants discovered in aquatic media and organisms or new properties and the effects of compounds already present in the environment (Taheran et al. 2018). These pollutant concentrations in the environment are now identified as hazardous to ecosystems and have garnered considerable attention. (Fent et al. 2006; Jjemba 2006; Kolpin et al. 2002). One such class of emerging pollutants is pharmaceuticals which have received a lot of attention in recent decades, especially since the early 2000s. In 1993, the global production of Pharmaceuticals and personal care products (PPCPs) exceeded 1×10^6 tonnes and the annual production of PPCPs could exceed 2×10^7 tonnes (Wang and Wang 2016). From 2000-2015, the usage of antibiotics has scaled up by 65 % and it might climb up three times more than that in 2015 and increase of 6.8 % is seen between 2011 to 2019 (He et al. 2022b).

India, with a population of 1.44 billion people, is one of the top five countries in pharmaceutical product production, with a high generation of domestic sewage, of which only 31% is treated (Balakrishna et al. 2017; Subedi et al. 2017). Furthermore, due to the high demand for PPCPs in preventing or curing disease and sustaining economic development such as aquaculture and livestock farming, PPCPs production is still increasing. As a result, environmental pollution caused by the pervasive use of PPCPs is becoming predominant (Wang and Wang 2016). PPCPs have been consumed and discharged in water bodies at low concentrations from a few ng/L to µg/L in surface water and from µg/L to mg/L in groundwater (Wang and Wang 2016). These drugs enter the ecosystem via either a direct or indirect pathway through various channels such as discarded medicine, patient body waste from medical centres, and pharmaceutical industries which is extremely harmful to aquatic habitats and has an impact on the population of naturally occurring bacteria (Ramos-Payan et al. 2016). The emerging pollutants in the aquatic environment, if left unnoticed and consumed become life-threatening because, some of them can disrupt the enzymatic, hormonal and genetic systems of humans (Falconer et al. 2006). Furthermore, the drugs in aquatic environments can cause a significant decrease in the renal and necrotic shift in vertebrates, perturbation, and an increase in toxicity (Rodriguez-Narvaez et al. 2017).

(a) Nonsteroidal anti-inflammatory drugs (NSAIDs)

A class of pharmaceuticals known as nonsteroidal anti-inflammatory drugs (NSAIDs) have been widely used in humans and animals to treat pain, fever, and swelling (Laine 2001; Wang et al. 2017). Among the NSAIDs, Ketoprofen (KF) and Diclofenac (DCF) are the most recurrently noted pharmaceutical drugs in the hydrous environment globally. Typically, KF is used to treat strains, sprains, bone disorders, inflammation, gout, muscles, and joint pain (Méndez-Arriaga et al. 2008; Wang et al. 2017; ALOthman et al. 2021). DCF is also used to relieve pain and inflammation, musculoskeletal injuries, prevent intraoperative myositis during cataract extraction, treat inflammation after laser eye surgery and reduce allergic conjunctivitis (Silveira et al. 2020). KF and DCF are both used to treat arthritis (ALothman et al. 2021; Silveira et al. 2020). The accumulation of DCF in pharmaceutical remnants can have an irreversible impact on aquatic habitats, causing cytological transmutation in fish livers, kidneys, and gills (ALothman et al. 2020; Schwaiger et al. 2004; Silveira et al. 2020). (Lindqvist et al. 2005) found 1.2 mg/L of KF

in wastewater influent in Finland. The influent and effluent wastewater samples of the Mediterranean catchment (France) in the amount range of approximately 0.38–3.15 mg/L of KF (ALothman et al. 2021). The accumulation of DCF in marine aquatic 2.96/29.62/296.15/ 2961.49 mg/L in the marine organism *Catactyx laticeps* (fish) at an exposure time of 30 min and 31.25/62.5/125/250/500/1000 mg/L in the marine organism *Perna pernas* (mussel). Similarly, KF and DCF have been found in various water resources across the world from ng/L to mg/L. In India, particularly in the southwest monsoon region, an influent concentration of approximately 721.37 µg/L of DCF and 2747.29 µg/L of KF was observed at the Kavor Municipal wastewater treatment plant (Patel et al. 2019; Thalla and Vannarath 2020).

(b) Fluoroquinolones

Fluoroquinolones have been extensively used in the treatment of humans and veterinary for antimicrobial resistance (Van Doorslaer et al. 2014). In India, the release of large amount of antibiotics from the pharmaceutical and hospitals effluent treatment plant is of ciprofloxacin (185µg/L), norfloxacin (703µg/L) and lomefloxacin (159µg/L). The release of the antibiotics into the hydrous environment can cause bioaccumulation, resist bacteria and biodegradation in the environment (Li et al. 2022; Zhang et al. 2020a). Ciprofloxacin (CIP) is a second-generation fluoroquinolone, used to treat bacterial infections, respiratory infections, diarrhoea, typhoid fever, urinary tract, abdominal infections, bone and joint infections, skin and genitals infections (Falyouna et al. 2022; He et al. 2022a; Mahjoore et al. 2022) whence Lomefloxacin Hydrochloride (LFH), a third-generation di-fluoroquinolone antibiotic is a very good antibacterial agent towards both gram-positive and gram-negative bacteria (Zhang et al. 2020a). It has the potential to treat dangerous vision infections, urinary tract infections, otitis media, bronchitis, and hematosepsis (Ma et al., 2020; You et al., 2021; Zhang et al., 2019). The concentration of CIP in the pharmaceutical industrial effluent in Croatia is 17.48 mg/L (Gor and Dave 2020) and it has also been reported that the approximate ranges of CIP in the effluent are between 28 to 31 mg/L and the concentration of LFH is also as high as CIP (Bhagat et al. 2020; Phonsiri et al. 2019).

(c) Caffeine

The presence of 71% of Caffeine (CAF) in coffee, has been widely used in the food and beverage industries especially with soft drinks at 16% and tea at 12 %. It is used as a cognitive enhancer due to its psychoactive properties; it is also used as a legal drug throughout the world (Ndabankulu et al. 2019; Qi et al. 2014). In India, the average consumption of CAF in the adolescent category is 96.5 mg/day. The CAF concentration in the river water ranges from 0.007 to 49.60 $\mu\text{g/L}$, in the groundwater system is from 0.02 to 23.97 $\mu\text{g/L}$, and in the lake water system from 0.019 to 37.48 $\mu\text{g/L}$ (Korekar et al. 2020). The concentration of CAF in the influent of sewage treatment plant ranges from 1.5 to 300 mg/L and in the effluent is 0.3 to 106 mg/L (Jogannatha et al. 2017). The presence of 30 $\mu\text{g/L}$ CAF in the water sources affects the natural biotransformation of fish specifically at a concentration of 150 mg/L, there observed a malfunction in the zebrafish on its locomotion (Quesada et al. 2019; Ramirez-Ubillus et al. 2022). The bioavailability, longer half-life of these pollutants in the environment and also considering the perilous consequences, there is an urgent need for cost-effective and reliable water purification technologies. However, pharmaceutical compounds are difficult to degrade or remove via traditional wastewater treatment and microbial degradation. There is also a need for an economically viable alternate method to efficiently degrade the pollutants.

1.1 Conventional treatment operations

Adsorption, chemical reduction, chemical oxidation, hydrolysis, reverse osmosis, ozonation, biological processes, ion exchange, membrane filtration, precipitation, flotation, electrolysis, photocatalysis and advanced oxidation processes are few conventional treatment operations and processes that have been developed to extract the pharmaceutical compounds from contaminated water of these, the most conventional physicochemical wastewater treatment methods are ineffective in removing pharmaceutical pollutants (Gao et al. 2021; Li and Yang 2018; Streit et al. 2021). The importance of adsorption and AOPs among wastewater remediation techniques is growing, as is concern that the presence of rising PPCP contaminants may be harmful (Kadam et al. 2021; Tan and Hameed 2017; Uddandarao et al. 2019).

1.1.1 Adsorption for the removal of Pharmaceutical and personal care products (PPCPs)

Adsorption is widely regarded as one of the most simple, practical, and cost-effective processes for removing pharmaceutical pollutants from wastewater. It is a surface phenomenon that occurs when adsorbate molecules from gas or liquid media accumulate on the adsorbent surface (Balakrishnan et al. 2020; Manirethan et al. 2018, 2020). Adsorption techniques can be coupled with wastewater treatment plants to achieve industrial-scale removal. The most commonly used adsorbents are biological, activated carbons, biochar, mineral oxides, polymer resins, and many other solids that have been tested to remove emerging pollutants from aqueous solutions (Patel et al., 2019). Among them, activated carbon is used in the treatment of many organic pollutants. The release of hazardous compounds through conventional adsorption techniques using activated carbon has created a need to develop an adsorbent on a nanotechnological basis which can effectively remove existing PPCPs in water bodies even at low concentrations. Over the last two decades, the adsorption of pharmaceutical pollutants on nano adsorbents has grown in favour of a low-cost and viable wastewater treatment technique. The other alternate process have huge disadvantages in comparison with the adsorption process in membrane process there is clogging and fouling of the membrane. The biological removal treatment is a slow process, requirement of nutrient and it is a environmental sensitive to the microbial activity and operation of ion exchange involves limited capacity and requires quick regeneration (Bhuyan and Ahmaruzzaman 2023; Reddy and Yun 2016; Sigonya et al. 2023; Tan and Hameed 2017).

1.1.2 Nanosorbent

In recent years, there has been a surge of interest in nanostructured materials research (both synthetic and natural) for the removal of emerging PPCP's pollutants. On comparing transition metal ions, single metal oxide catalyst activators, and mixed metal oxide catalysts, spinel ferrite has received little attention. Nanosized ferrite particles have been employed in the areas of nanomedicine, lithium-ion batteries, protein fixation, bioengineering and environmental treatment; owing to their outstanding characteristics, it has also proven to be an effective adsorbent and catalyst in the removal of hazardous pollutants (Xu et al. 2021; Zhang et al. 2020b). Despite their rapid sorption kinetics, iron

oxide nanoparticles can undergo phase changes to other oxides under different environmental conditions and show poor stability at low pH levels. Recently metal oxide nano-ferrites such as $MgFe_2O_4$, $NiFe_2O_4$, $CaFe_2O_4$, $BaFe_2O_4$, $ZnFe_2O_4$, $MnFe_2O_4$, $CuFe_2O_4$, and $CoFe_2O_4$ have been utilized in the removal/degradation of dyes, and pesticides and pharmaceutical pollutants (Kollarahithlu and Balakrishnan 2021; El-saied and El-Fawal 2021). Among these $NiFe_2O_4$ nanoparticles exhibit good magnetic, chemical and thermal stability (Kollarahithlu and Balakrishnan 2019; Sun et al. 2022b).

1.1.2.1 Nickel ferrite nanoparticles (NFO)

$NiFe_2O_4$ is a soft magnetic material with a mixed inverse spinel structure that has Fe^{3+} ions at tetrahedral sites and Fe^{3+} and Ni^{2+} at octahedral sites; because of its simplicity, low cost, low synthesis temperature, high saturation magnetization, high biocompatibility and small particle size, the co-precipitation method is widely used (Aliahmad et al. 2013; Kollarahithlu and Balakrishnan 2021; Cherpin et al. 2021; Springer et al. 2016; Wei et al. 2020). Despite the above-mentioned properties of NFO, its high surface energy leads to agglomeration, affecting its magnetic property and adsorption capacity. Further, the leaching of nickel and ferrite ions under highly acidic conditions and undergoing oxidation were some of their limitations. To address these drawbacks and employ in the removal of specific pollutants of interest, these nanoparticles' properties are modulated either by functionalizing or through coating via certain advanced technologies that could significantly improve the stability, bio-commutability and overall life longevity. Researchers are currently exploring functionalization with organic or inorganic components such as surfactants, polysaccharides, biopolymers, organic acids, carbon, and amino acids (Soares et al. 2019; Zhang et al. 2020b).

Table 1.1 Properties of Nickel ferrite nanoparticles in comparison with the other ferrite nanoparticles (Jadhav et al. 2020; Kaur et al. 2016; Tatarchuk et al. 2020)

Properties	Magnetic	Chemical	Biocompatibility	Electrical
$NiFe_2O_4$	Exhibits high saturation magnetization 40 to 60 emu/g	Good chemical stability under various environmental conditions, less prone to oxidation	Biocompatible and non-toxic when properly synthesized and surface-modified	Higher electrical conductivity compared to cobalt and

				manganese ferrite
CoFe₂O₄	Exhibits lower saturation magnetization 30 to 40 emu/g	Lower stability, more susceptible to oxidation	Biocompatibility can vary; surface modification may be required to improve biocompatibility	Moderate electrical conductivity, suitable for applications requiring magnetic and conductive properties
MnFe₂O₄	Exhibits lowest saturation magnetization 20 to 30 emu/g	Chemically stable, more prone to oxidation compared to nickel ferrite	Biocompatibility can vary; surface modifications are often necessary to reduce toxicity	Lower electrical conductivity compared to nickel and cobalt ferrite nanoparticles
CaFe₂O₄	Exhibits lowest saturation magnetization 20 to 30 emu/g	Stable, but may have lower stability under acidic conditions	Biocompatibility can vary; surface modifications may be required	Moderate electrical conductivity
BaFe₂O₄	High coercivity and high saturation magnetization 50 to 60 emu/g	Good chemical stability, resistant to oxidation and corrosion	Less biocompatible due to potential toxicity concerns	Moderate to high electrical conductivity, useful in magnetic and conductive applications
ZnFe₂O₄	Exhibits lower saturation magnetization 30 to 40 emu/g	Moderate chemical stability may oxidize under certain conditions	Biocompatibility can vary; surface modifications are often necessary	Moderate electrical conductivity
MgFe₂O₄	Similar magnetization as ZnFe ₂ O ₄ 30 to 40 emu/g	Stable under normal conditions, but less resistant to oxidation compared to nickel and barium ferrites	Biocompatibility can vary; surface modifications may be needed to reduce the toxicity	Lower electrical conductivity compared to barium and nickel ferrite nanoparticles

Table 1.1 depicts that the Nickel ferrite nanoparticle's properties have shown superior properties compared to all other ferrite materials.

1.1.2.2 Silanization of NFO surface

Chemical instability and magnetic losses of nickel ferrite nanoparticles were observed under strong acidic pH and strong oxidizing conditions. To overcome these, the functionalization of NFO with polymers/organic molecules or inorganic substances such as inert silica is one viable option (El-Nahhal et al. 2016; Kollarahithlu and Balakrishnan 2019; Nagao et al. 2004). The high binding strength in the magnetic oxide core, ease of attachment, resistance to organic solvents, availability and functionalization have led to a high preference for silica functionalization on the nanoparticles (Diallo et al. 2021). The inclusion of surface silanol groups provides stability and inertness and also enables the grafting of specific ligands to the NFO surface. Grafting ligands are usually carried out by surface silanization with silane coupling agents such as epoxy, amine, thiol, carboxylic acid, or isocyanate moieties (Isasi et al. 2019; Ogden et al. 2008). These grafted nanoparticles are employed in adsorption procedures to improve the sorption capacities of silica-coated magnetite nanoparticles (Pape 2017).

1.1.2.3 Biomolecule functionalization

In recent years, the functionalization of NFO nanoparticles with biomolecules such as β -cyclodextrin (β -CD) and amino acid has improved the possibility of adsorption of targeted pollutants (Conde et al. 2014; Enache et al. 2017a; Kollarahithlu and Balakrishnan 2019). β -CD with six glucose subunits has a significant feature of forming solid inclusion complexes with a wide variety of guest molecules within the hydrophobic cavity of the host cyclodextrin (Lv et al. 2014).

1.1.2.4 Amino acid functionalization (L-Leucine)

Amino acids are used as capping agents on bare magnetite, whose surface is normally covered by both H_2O molecules and OH^- ions, they are partly chemisorbed but mainly physisorbed onto the Fe_3O_4 particles. For most effective applications in separation areas (for ions or biomolecules), the amino acid-coated magnetite nanoparticles should be prepared in a chemisorbed approach (Enache et al. 2017b). This amino acid functionalization has been investigated for the removal of antibiotics since it produces no

or fewer secondary pollutants within the standards during adsorption. L-Leucine alone was experimented for the removal of CIP and LFH. The choice of L-Leucine is owing to its structural stability, pH stability, the hydrophobic side chain can involve in hydrophobic interactions with the nonpolar pollutants and involves in targeting specific contaminants (You et al. 2021a; Zhang et al. 2020b).

1.2 Nano-catalyst (NFO)

A variety of components, including semiconductors, carbon-based materials, transition metals, ultrasonication, and radiation, have been used to test the production of sulfate radicals using potassium peroxymonosulfate (PMS) (Balakrishnan et al. 2021). However, the nickel ferrites are regarded as promising nano adsorbents and nano-catalysts due to their unique properties such as large specific surface area, porosity, small pore size, high thermal activities, good electrical and mechanical properties and good catalytic activity, and firm spinel structure, which aids in better activation of PMS and ease of recovery using external magnets when compared to iron oxide catalysts and recuperation via chemical regenerant or intense heating.

1.2.1 Advanced oxidation process for the degradation of (PPCPs)

The advanced oxidation process (AOP) is one of the most environmental friendly new technologies since it mineralizes hazardous pollutants rather than converting them from one phase to another (Carvalho et al. 2014). The radical oxidant has various advantages, that includes being highly reactive, having a short half-life, being non-toxic and non-corrosive, and adequately oxidising wastewater, organic pollutant streams and toxic effluents from the hospital, pharmaceutical and municipal wastes (Miklos et al. 2018). The post-treatment of such waste effluents using AOPs results in products that are more amenable to bioremediation, less hazardous and have a lower pollutant load (Pandis et al. 2022).

1.3 Co-precipitation method

Among the several nanoparticle synthesis processes, the coprecipitation approach is a practical way to produce magnetic nanoparticles (Baruwati and Manorama 2008). The coprecipitation method uses no hazardous intermediates or solvents, does not require precursor complexes, and operates at temperatures less than 100 °C (Maaz et al. 2009).

Because of its capacity to be scaled up, reproducibility, and environmentally benign reaction conditions, this technique has been acknowledged for its industrial usefulness.

1.4 Hydrothermal method

Many researchers have been drawn to the hydrothermal technique because of its unique advantages, including simple equipment, low cost, and gentle preparation conditions. It is a solution-reaction technique (Gan et al. 2020). Depending on the vapour pressure of the major component in the reaction mixture, either low-pressure or high-temperature conditions can be utilized to control the morphology of the materials to be synthesized with minimal material loss (Guo et al. 2021).

1.5 Present work

The high saturation magnetization and biocompatibility of nickel ferrite nanoparticles make it stand out to be unique in the choice among the ferrite nanoparticles. The co-precipitation method was used to prepare NFO, which was then used as a catalyst in the activation of PMS for the degradation of LFH and CAF. The experiments were carried out with bare NFO as an adsorbent for the removal of 10 mg/L concentrations of all the pharmaceutical compounds, the removal efficiency of bare NFO was ineffective against the pharmaceutical pollutants, and hence a novel low-cost adsorbent for removing the pharmaceutical pollutants in the hydrous environment was worked on to remove these compounds. A few limited publications for the experimental investigation on the sorptive removal of pharmaceutical pollutants using NFO and its composites were proposed in the literature. Thus, a laboratory scale experiment was conducted to study the physical, chemical, thermal and magnetic properties of NFO@SiO₂@β-CD and L-Leucine functionalized NFO nanocomposite (NFO@L). The NFO@SiO₂@β-CD was used to study the feasibility for the removal of KF and DCF meanwhile the NFO@L nanocomposite was experimented with, for the removal of CIP and LFH. So far, research on the combination of NFO@SiO₂@β-CD and L-Leucine functionalized NFO nanocomposite for the removal of NSAIDs and antibiotics has not yet been studied however the combination of CoFe₂O₄@L has worked on the application of drug delivery.

CHAPTER 2

REVIEW OF LITERATURE

2.1 Origin of the research of PPCPs in the environment

(Hignite and Azarnoff 1977) published a paper describing the presence of clofibric acid, a hypolipidemic drug, and salicylic acid at low concentrations in sewage treatment plant effluents and the discharge of the effluent in the Missouri River (Philip et al. 2018). Later, in Germany in 1990, the presence of pesticide residues containing phenoxyalkanoic acid herbicides in drinking water and groundwater was noted to be clofibric acid. A study in Ganga river in India has reported the presence of ciprofloxacin, azithromycin and ofloxacin with a concentration ranging from 100 to 1000 ng/L. In urban areas of Delhi reported to the release of parabens and triclosan in wastewater treatment plant with the concentrations ranging from 10 to 500 ng/L. This origin has drawn significant attention to the scientific community and chemists to research the release of PPCPs into the environment; since then, data related to the various classes of PPCPs prevailing in the environment has come to light over the years (Buchberger 2011).

2.1.1 Emerging pollutants

The occurrence of emerging pollutants (EPs) is continuously reported worldwide. More than 1000 substances, gathered in 16 classes (algal toxins, antifoaming and complexing agents, antioxidants, detergents, disinfection by-products, plasticizers, flame retardants, fragrances, gasoline additives, perfluoroalkylated substances, personal care products, pharmaceuticals, pesticides, anti-corrosives) are classified as new emerging pollutants addressing their environmental and health effects (Pruss et al. 2002; WHO 2000). Due to different factors, EPs are found in surface water; they undergo transport phenomena in natural waters and soil by runoff, erosion, or leaching (Fàbrega et al., 2014). These pollutant's concentrations can vary from the wastewater discharge point to the water abstraction point because of biotransformation, volatilization, photolysis, sorption, dispersion, or different water sources combination, which can attenuate initial concentrations or transform pollutants (Basheer 2018). PPCPs can be toxic to the fish, invertebrates and algae disrupting their growth, reproduction and can enter into the endocrine system leading to the hormonal changes, bioaccumulation might alter the food

chain, could alter the ecosystem dynamics, development of antibiotic resistance and can contaminate the ground and drinking water.

2.2 Conventional method for the removal of PPCPs

The conventional method for the removal of PPCP's are membrane bioreactor which can remove about 46-99 % of ketoprofen and fluoroquinolones (Adeoye et al. 2024). The removal of ciprofloxacin using reverse osmosis as a single process is about 98.7 % (Ghazal et al. 2022). A mixture of 30 pharmaceuticals along with pesticides using granular activated carbon adsorption is only 30 to 50 % dissolved organic carbon (Kennedy et al. 2014). Nanofiltration and ozonisation can remove and degrade pharmaceuticals from 15 to 100 % (Maryam et al. 2020; Talib and Randhir 2016). UV photolysis and photocatalytic membrane reactor can remove pharmaceuticals upto 30 to 70 % and 56 to 100 % (Pal et al. 2010; Plakas et al. 2019). The combined processes such as sono photolysis and activated sludge process, anaerobic and aerobic digestion, dioxychlorination, coagulation/flocculation, settling, sand filtration, ultrafiltration, ultraviolet disinfection, reverse osmosis and remineralization, chlorine, coagulation/flocculation, filtration, ozonation, granular activated carbon, final chlorination, ultrafiltration and nanofiltration, coagulation/flocculation, sedimentation, filtration, chloramine, ozonation, GAC filtration, UV pre-disinfection, filtration, nanofiltration/reverse osmosis, remineralisation and chlorine disinfection all of these combinations have shown the highest removal efficiency of pharmaceuticals, drugs of abuse, herbicides and pesticides greater than 92 % (Boleda et al. 2009; Huerta-Fontela et al. 2008; Klavarioti et al. 2009; Radjenović et al. 2008). From all the above-mentioned techniques, in laboratory scale single process, adsorption and advanced oxidation process are found to be superior in removing the emerging hazardous PPCPs.

Adsorption involves the interaction forces between the adsorbate and the adsorbent surface causing the adsorbate molecules to bind to the adsorbent's surface (Quesada et al. 2019). Pollutants' interaction with the adsorbent is determined by its inherent surface properties and functional groups on their surface. The specific nature of the interaction depends on the two species involved which follow four steps: solute transport in a bulk fluid phase, film diffusion, pore diffusion, and adsorption to the solid involves physisorption, in which the adsorbate attaches to the adsorbent via weak van der Waals force, - interaction, electrostatic attraction, or chemisorption, which involves covalent bonding. Adsorption is

more effective in removing contaminants at lower concentrations, its versatility, simplicity, cost effectiveness, minimal chemical usage and reduces operational cost by using regeneration (Quesada et al. 2019). Meanwhile, AOP using oxidizing agents has shown promising results from the literature review. AOP is highly effective for wide range of pollutants which could breakdown the pollutants into simpler compounds or degrade it fully by reducing their toxicity. AOP's has a high ability to degrade refractory pharmaceutical pollutants by stimulating peroxymonosulfate (PMS, HSO_5^-), peroxydisulfate (PDS, $\text{S}_2\text{O}_8^{2-}$), and Fenton reactions (Duo et al., 2022; Liu et al., 2012; Zhang et al., 2020); among them, PMS is capable of producing $\bullet\text{SO}_4^-$, $\bullet\text{O}_2^-$, $^1\text{O}_2$ and $\bullet\text{OH}$ of which sulfate radicals with high redox potential ($\text{SO}_4^{\bullet-}$, 2.5–3.1 V) with a half-life of ($t_{1/2} = 30\text{--}40 \mu\text{s}$) and hydroxyl radicals (OH^{\bullet} , 1.8–2.7 V) with a lesser half-life of ($t_{1/2} = <1\mu\text{s}$) at pH 7 in both homogeneous and heterogenous activations (Guo et al. 2020a; He et al. 2022b; Jia et al. 2021; Ma et al. 2020). The electrophilic nature of sulfate radical, which could selectively attack organic molecules, preferably with electron-donating groups such as alkoxy (-OR), hydroxyl (-OH), amino (-NH₂), and electrons present on aromatic molecules has drawn a lot of attention to the degradation of pollutants. Furthermore, PMS is a non-toxic strong oxidant as well as a chlorine-free disinfectant, making it a superior replacement for chlorine (Guo et al., 2020a).

2.3 Nano-ferrite and nano-ferrite composite in the removal of PPCPs

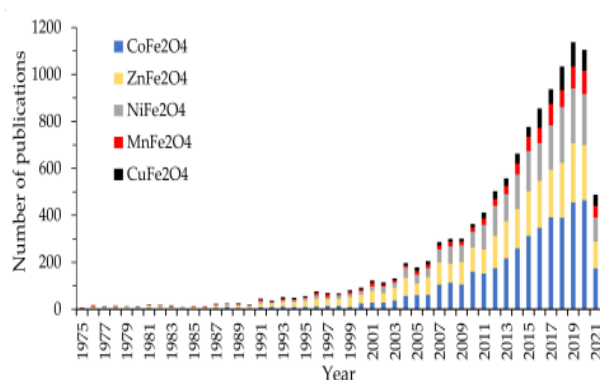


Fig. 2.1 Papers having M-ferrite (M = Co, Cu, Ni, Mn, Zn) in the topic published in Web of Science Core Collection between 1975–June 2021(Thomas Dippong et al. 2021)

The recognition of this fact has resulted in the pursuit of magnetic photocatalysts as well. In large water treatment plants, where the volume of water remedied is huge, centrifugal

separation is not feasible. Fe₃O₄-based systems are the most widely studied magnetic nanoparticles at the moment (Jacob et al., 2013). Among the studied ferrite, Co-ferrite was the topic of 4276 papers, followed by Zn-ferrite (3073), Ni-ferrite (2432), Mn-ferrite (895), and Cu-ferrite (880) as per the data collection in the year between 1975 – June 2021. For every ferrite, the number of papers started to grow exponentially in the last 20 years were shown in Fig. 2.1, with the highest increasing rate being observed for the Co, Zn, Ni-ferrite (Thomas Dippong et al. 2021).

The growing attention to these ferrites may be ascribed to the advancement of new equipment that allowed the ferrites characterization and the surge of the demand for materials with special properties for a wide range of applications (Jacob et al., 2013). Literature studies results reveal that nano ferrites and their composites show a high tendency to remove different types of organic and inorganic pollutants from wastewater. Recently, biopolymer-coated nanoparticles have gained wide attraction for surface modification of nano ferrite owing to their peculiar properties such as high adsorption capacity, selectivity, biocompatibility, and cost-effectiveness. Crini 2005 reviewed developments in the synthesis of polysaccharides-based materials used as adsorbents in wastewater treatment using biopolymers and their composites as adsorbents in water purification (Kumar et al. 2020).

2.4 Synthesis methods for the Nickel ferrite nanoparticles

From time to time, researchers kept on modifying the synthesis process for nickel ferrite (NFO) nanoparticles and succeeded in improving their properties. In 1966, Saito and Takei prepared NFO using the hydrothermal method. Two techniques of synthesizing nickel ferrite through a co-precipitation and hydrothermal approach were implemented: the co-precipitation of hydroxide made from a solution of constituent of two hydroxides-ferric hydroxide, and nickel hydroxide-suspended in water at pH 11. The intricate collection of routes that lead to nanoparticle synthesis, produces particles with a wide size distribution. In general, the magnetic nanoparticles formed during the coprecipitation process crystallize in a near-instantaneous manner at room temperature (Ahn et al. 2012). The size and composition of nanoparticles can be greatly controlled by optimizing the pH concentration and temperature. The co-precipitation method can easily be scaled up to larger production of nanoparticles with significant changes in the process. The rapid production,

environmental friendly, uniform mixing of precursor helps in the homogeneity of the formation of nanoparticles. Another one is hydrothermal synthesis method has major advantages over other methods.

In hydrothermal synthesis, the compositions of nanomaterials/nanocomposite to be generated may be precisely regulated. Nanomaterials can be resized and shaped using hydrothermal synthesis. Nanoparticle shape is principally determined by reaction time, temperature, and solution concentration (Majid et al. 2021). As a result, the nanoparticle's physical and chemical properties could be altered. The choice of nanoparticles based on their shape has been used in many applications (Gan et al. 2020). In 1967, Poplawsky et al. adopted the arc image furnace technique for the preparation of Ni ferrites and reported the chemical, structural, and electron probe as well as metallographic analyses (Narang and Pubby 2021). An overview of the advantages and disadvantages of synthesis of nanoparticles and nanocomposite is mentioned in Table 2.1a and the synthesis of nickel ferrite using different methods has been presented in Table 2.1 b.

Table 2.1a Advantages and Disadvantages of synthesis of nanoparticles and nanocomposites

S.No	Synthesis methods	Advantages	Disadvantages
1	Sol-Gel	<p>Controlled Composition: Precise control over the stoichiometry and homogeneity.</p> <p>Conducted at low temperature compared to other methods.</p> <p>Versatile: Can be used to produce various metal oxides and composites.</p>	<p>Time consuming: Time consuming process due to multiple steps.</p> <p>Complexity: Requires careful control of pH and temperature.</p>
2	Chemical Vapor Deposition	<p>High Purity: Produces high purity nanoparticles due to the gaseous nature of reactants</p>	<p>Equipment Cost: Requires expensive and complex equipment.</p>

		Uniform coating: Excellent for creating uniform coatings on substrates	Limited Scale-Up: Not always suitable for large scale production.
3	Hydrothermal and Solvothermal method	High Quality: Produces high-quality nanoparticles with controlled size and morphology. Versatility: Can be used for wide range of materials.	High Pressure : Requires specialized equipment to handle high pressure. Long reaction times: Can take a significant amount of time.
4	Co-precipitation method	Simplicity: Easy to perform and requires less sophisticated equipment. Scalability: Suitable for large-scale production	Inhomogeneity: Might lead to inhomogeneous particle sizes. Post-Synthesis Treatment: often requires additional processing (e.g., washing, drying).
5	Physical methods (Milling and sputtering)	Direct Approach: Can produce nanoparticles directly from bulk materials. Minimal Chemical Waste: Often generates fewer chemical byproducts.	Particle Agglomeration: High energy processes can lead to agglomeration. Limited Control: Less control over size and shape compared to chemical methods.
6	Biological method (Green Synthesis)	Eco-friendly: Uses biological materials, reducing environmental impact. Simplicity: Generally simpler and safer compared to chemical methods.	Variability: Results can be less consistent due to biological variability. Slower Production: Typically slower than conventional chemical synthesis.

7 Electrochemical methods	Fine control: Allows for fine control over particle size and morphology. High Purity: Typically produces high-purity nanoparticles.	Complexity: Requires specialized setups and knowledge of electrochemistry. Limited Materials: May be limited to certain types of metal oxides.
---------------------------	--	---

Table 2.1 b Overview of synthesis of Nickel ferrite using different methods

S.No	Method	Precursor	Particle size	Remarks/ Application	Reference
1	Auto-combustion method	Fe(NO ₃) ₃ ·9H ₂ O, Ni(NO ₃) ₂ ·6H ₂ O	Average particle size from XRD - 49 nm From TEM- 47 nm	Pure spinel crystal structure was observed. Studies on electrochemical properties of metal ferrites	(Khairy et al. 2020)
2	Solution Combustion Method	Fe(NO ₃) ₃ ·9H ₂ O, Ni(NO ₃) ₂ ·6H ₂ O (C ₆ H ₈ O ₇)	CT-550°C for 4 hrs Average particle size - 22 nm	Single cubic spinel nanocrystalline structure. Structural and magnetic properties of nickel ferrite	(Bharati et al. 2020)
3	Sono-chemical synthesis	FeCl ₃ ·6H ₂ O NiCl ₂ ·6H ₂ O	Average particle size - 9 to 17 nm The band gap of the Nanoparticles - 2.26 Ev	Formation of inverse spinel with face-centred cubic structure. Photocatalytic and electrochemical applications	(Amulya et al. 2020)
4	Greener synthesis using rosemary leaves	FeCl ₃ ·6H ₂ O NiCl ₂ ·6H ₂ O	Particles are Amorphous from the XRD results.	Spinel nickel ferrite nanowhiskers with rod-like structures.	(Alijani et al. 2020)

			Agglomeration with irregular morphology could be visible from TEM results.	Biomedical application	
5	Molten salt method	(NiCO ₃ ·2Ni(OH) ₂ ·4H ₂ O) NaCl KCl K ₂ SO ₄ Na ₂ SO ₄	Using NaCl-KCl grains size of 250 - 400 nm Using the KCl-K ₂ SO ₄ particle size was 100 - 200 nm Using Na ₂ SO ₄ -K ₂ SO ₄ the particle size was 400 nm	Cubic spinel structured NiFe ₂ O ₄ . Removal of heavy metal ions and fluoroquinolones	(Liu et al. 2019a)
6	Sol-gel and combustion methods with different Chelating agents like PVA, citric acid and urea	Ni(NO ₃) ₂ ·6H ₂ O Fe(NO ₃) ₃ ·6H ₂ O	The crystallite size was in the range of 6 - 14 nm Average particle diameters for the three samples were in the range of 10-25 nm	Cubic spinel ferrite. Studies of structural and magnetic properties	(Vara Prasad et al. 2018)
7	Single-step chemical combustion method using citric acid	Ni(NO ₃) ₂ ·6H ₂ O Fe(NO ₃) ₃ ·9H ₂ O	The temperature varied from 600 to 800°C crystallite size increased from 17 ± 1 nm to 35 ± 1 nm	The single-phase formation of nickel ferrite was confirmed. Preparation of nickel ferrite at low temperature regime	(Shanmugavel et al. 2015)
8	Auto combustion method	Ni(NO ₃) ₂ ·6H ₂ O, Fe(NO ₃) ₃ ·9H ₂ O	Temperature maintained at 700 °C The average grain size obtained from TEM was 60 nm	A single-phase cubic single structure was confirmed. Studies	(Shanmugavel et al. 2014)

			Crystalline size from XRD was found to be in the range of 45-55 nm	on structural and magnetic properties	
9	Microwave-assisted combustion method	Ni(NO ₃) ₂ ·6H ₂ O Fe(NO ₃) ₃ ·9H ₂ O	The particle size was 20 nm	Cubic spinel phases and no secondary phase. Mössbauer and magnetization studies of nickel ferrite nanoparticles	(Mahmoud et al. 2013)
10	Citrate precursor gel formation	Ni(NO ₃) ₂ Fe(NO ₃) ₃	Mean crystallite size from XRD ranges between 26.2 -28.5 nm Single-phase particles form clusters with particle size in the range of 21-82.5 nm TEM showed a particle size of 55.4 nm	Cubic spinel phase. Studies on crystallization and magnetic behavior of nickel ferrite	(Nguyet et al. 2011)
11	Simple solvothermal method (Ethylene glycol as solvent) (NaAc as electrostatic stabilization)	NiCl ₂ ·6H ₂ O FeCl ₃ ·6H ₂ O	Temperature - 180°C for about 6-48 hrs The average size of nickel ferrite nanoparticles increased as the reaction time was prolonged for the following time 6 hrs -90 nm; 12 hrs-120 nm; 48 hrs-180 nm	Cubic nickel ferrite with a polycrystalline nature. Synthesis and magnetic properties of nickel ferrite nanoparticles	(Wang et al. 2009)
12	Hydrothermal method	Ni(NO ₃) ₂ ·6H ₂ O Fe(NO ₃) ₃ ·9H ₂ O	Nanorods at temperature 150°C Nanosphere above 150°C Particle size was between 10-70 nm	Nanorods, nanospheres, and nano cubes are formed. Synthesis	(Xiangfeng et al. 2007)

and analysis of gas sensing properties

An overview of the synthesis of nickel ferrite using the co-precipitation method is presented in Table 2.2. Table 2.3 provides an overview of NFO and other metal oxide composite and their applications.

Table 2.2 Overview of synthesis of NFO using the Co-precipitation method

S. No	Precursor	Characteristics	Remarks	Reference
1	(Ni (NO ₃) ₂ ·6H ₂ O) (Fe (NO ₃) ₃ ·9H ₂ O)	Calcination temperature - 900°C for 3 hrs, pH - 12 The average crystallite size from XRD – 43.28 nm, BET test specific surface area – 186 m ² /g	Non spherical geometry. Studies on synthesis and properties.	(Kizilduman et al.2024)
2	(Ni (NO ₃) ₂ ·6H ₂ O) FeCl ₃	Calcination temperature - 350 to 500°C for 3 hrs The average crystallite size from XRD - 30.2 nm	High purity, single phase, crystalline, spherical shape of particles. Removal of heavy metals.	(Khoso et al. 2021)
3	FeSO ₄ ·7H ₂ O NiSO ₄ ·7H ₂ O	Calcination temperature - 800 °C for 5 hrs The average diameter of the particle is 78.4 nm Diamond-shaped particles with an average size of 70-80 nm	Cubic spinel structure, ferromagnetic structure with low coercivity and large saturation magnetization. Stability and cytotoxicity studies	(Egizbek et al. 2020)
4	FeCl ₃ NiCl ₂	Average crystallite size - 18 nm The average size of the nanoparticles using TEM was about 28 nm	Single phase cubic spinel structure, spherical and some elongated particles, increased value of coercivity. Synthesis and	(Sagadevan et al. 2018a)

			Characterization of nickel ferrite nanoparticles	
5	(Ni (NO ₃) ₂ .6H ₂ O (Fe (NO ₃) ₂ .6H ₂ O	Calcined at 600°C for 4 hrs The average particle size of 69 nm	Formation of inverse spinel phase of nickel ferrite, with some fractions of iron oxide phases, superparamagnetic. Synthesis of nickel ferrite nanoparticles.	(Ansari 2017)
6	Ni(NO ₃) ₂ .6H ₂ O, Fe (NO ₃) ₂ .9H ₂ O	400 °C, 600 °C, 800 °C -Average particle size 16, 23 and 31 nm	Inverse spinel cubic crystalline. Synthesis and characterization.	(Sivagurunathan and Gibin 2016)
7	Nickel acetate, ferrous sulfate heptahydrate, Ferric nitrate nonahydrate	1. First set of precursors 20 - 30 nm, 2. Second set of precursors 80 - 150 nm 3. Third set of precursors 25 - 35 nm	Inverse single phase spinel cubic, spherical, superparamagnetic. Studies on synthesis and magnetic properties at low temperature.	(Tejabhram et al. 2014)
8	Nickel nitrate, ferric nitrate	Average crystallite size varies in the range of 8-20 nm with varying sintering temperatures from 250 to 550°C	Single-phase cubic mixed spinel crystal, magnetic properties increase with increase in sintering temperature. Structural and properties of nickel ferrite nanoparticles	(Joshi et al. 2014)
9	FeCl ₃ and NiCl ₂	The size of particles 500 and 1000°C obtained 7 and 82 nm	Particle size increases with an increase in temperature, superparamagnetic nature depends on the magnetocrystalline anisotropy. Synthesis and	(Aliahmad et al. 2013)

			properties of nickel ferrite nanoparticles
10	<p>FeCl₂, NiCl₂, NaOH</p> <p>Four different precursors ratio (Fe: Ni) are varied at 40:60, 60:40 and 80:20</p>	<p>40: 60 -32.96 nm,</p> <p>60:40 - 54.85 nm</p> <p>80:20 - 82.12 nm</p>	<p>Magnetic saturation decreases with decreasing Fe content, inverse spinel structure. Synthesis and characterization of nickel ferrite nanoparticles.</p> <p>(Ong et al. 2012)</p>
11	<p>Fe(NO₃)₃·9H₂O</p> <p>Ni(NO₃)₂·6H₂O</p>	<p>Co-precipitation - 600°C</p> <p>Co-precipitation (8-20 nm) and superparamagnetic nature.</p>	<p>Irregular shape, very small particle size and wide size distribution, superparamagnetic with small saturation magnetization. Structural and characterization studies of nickel ferrite nanoparticles.</p> <p>(Jacob et al. 2011a)</p>
12	<p>Iron chloride, nickel chloride and sodium hydroxide were used as the precipitating agent while oleic acid</p>	<p>Annealed at 600 °C</p> <p>24 ± 4 nm size of nickel ferrite nanoparticles</p>	<p>In single-phase nickel ferrite nanoparticles, superparamagnetic blocking temperature increases with an increase in increase particle size. Structural and characterization studies of nickel ferrite nanoparticles.</p> <p>(Maaz et al. 2009)</p>

Table 2.3 Overview of Nickel ferrite and other metal oxide nanocomposites in the removal of emerging pollutants and other applications

S. No	Metal Oxide & Metal oxide nanocomposite	Synthesis methods	Applications	Reference
1	NiFe ₂ O ₄ @Chitosan	Co-precipitation method	Removal of Ciprofloxacin, erythromycin, ampicillin	(Mohammed et al. 2024)
2	L-Lysine coated magnetic core-shell nanoparticles	Co-precipitation method	Removal of acetylsalicylic acid	(Maciel et al. 2023)
3	NiFe ₂ O ₄ nanoparticles	Bioconjugate synthesis The leaves extract of Juglans regia	Removal of ciprofloxacin and Congo red	(Taj et al. 2021)
4	NiFe ₂ O ₄ /BiPO ₄ nanocomposites	Hydrothermal technique	Tetracycline (TC) and Rhodamine B (RhB) removal	(Koutavarapu et al. 2021)
5	UV-enhanced nano-nickel ferrite-activated Peroxymonosulfate	Hydrothermal synthesis	Degradation of chlortetracycline hydrochloride	(Zhang et al. 2021)
6	Glutathione functionalized NiFe ₂ O ₄ /GO	Hummer's method of ultrasonication	Removal of heavy metals	(Khorshidi et al. 2020)
7	NiFe ₂ O ₄ nanoparticles incorporated into G. ghatti-cl-P(AAm) nanocomposites hydrogel	Free radical solution polymerization	Adsorption of ciprofloxacin	(Gor and Dave 2020)

8	Core-Shell Fe ₃ O ₄ @MIL-100(Fe) Magnetic Nanoparticle	Chemical method	Removal of Meloxicam and Naproxen	(Liu et al. 2019b)
9	Dopamine cobalt ferrite nanoparticles Glutathione cobalt ferrite nanoparticles Melamine	Sonication	Removal of ciprofloxacin and norfloxacin	(Malik et al. 2019)
10	Cysteine-modified silane-coated magnetic nanomaterial	Co-precipitation method Stober method	Adsorption of ibuprofen	(Kollarahithlu and Balakrishnan 2019)
11	CoFe ₂ O ₄ activated peroxymonosulfate (PMS) process	Co-precipitation method	Degradation of atrazine	(Li et al. 2018)
12	Nickel ferrite nanoparticles	Co-precipitation method	Removal of polar pharmaceutical	(Springer et al. 2018)
13	Nickel ferrite nanoparticles	Co-precipitation	Removal of azo dye	(Ayazi et al. 2018)
14	β-Cyclodextrin coated iron oxide nanoparticles	Co-precipitation method	Biomedical applications	(Shelat et al. 2018)
15	Beta-cyclodextrin capped Graphene-magnetite (G-Fe ₃ O ₄ -β-CD) nanocomposite	Synthesized by ethylenediamine conjugation	Removal of Bisphenol-A (BPA)	(Ragavan and Rastogi 2017)

16	Magnetic cobalt ferrite composite	chemical ultrasonication-assisted co-precipitation technique	photocatalytic oxidation of carbamazepine	(He et al. 2017)
17	Cysteine-functionalized silica-coated magnetite nanoparticles Fe ₃ O ₄ @SiO ₂ @ICPTES-cysteine	Four-step functionalization process	Removal of Pb (II)	(Enache et al. 2017b)
18	Magnetic targeted nanoparticles double-coated with β-cyclodextrin (β-CD) and chitosan (CS)	Co-precipitation methods	Drug delivery	(Chen et al. 2017)
19	NiFe ₂ O ₄ @SiO ₂ -decorated reduced graphene oxide nanosheets	Hydrothermal method Stober method One-step hydrothermal method	Synthesis, characterization and electromagnetic properties	(Wang et al. 2016)
20	β-cyclodextrin functionalized Fe ₃ O ₄ magnetic nanoparticles	Co-precipitation method Layer-by-layer chemical method	Removal of methylene blue	(Zhou et al. 2016)
21	β-Cyclodextrin modified with magnetic nanoparticles	Non-covalently bonded by Host-guest inclusion	β-Naphthol removal from wastewater (tanning agents, antioxidants, and antiseptics)	(Song et al. 2016)
22	Magnetic nickel ferrite nanoparticles	Co-precipitation	Removal of dipyrone	(Springer et al. 2016)
23	Magnetic CuO@Fe ₃ O ₄ nanocomposite	Impregnation method	Degradation of 2,4-dichlorophenol	(Sun et al. 2015)

24	Rhodamine–adamantane/ β -cyclodextrin-modified $\text{Fe}_3\text{O}_4@ \text{SiO}_2$	Host–guest interaction Multi-step process (Stober method)	Chemosensor	(Zhang et al. 2015)
25	Nickel Ferrite- SiO_2 /Ag Core/Shell Nanocomposites	Chemical method (Sol-gel technique)	New composite synthesis	(Blanco-Esqueda et al. 2015)
26	Fe_3O_4 nanoparticles bearing aminated β -cyclodextrin	Chemical Co-precipitation method	Removal of naproxen and carbamazepine and one EDC, Bisphenol A	(Ghosh et al. 2013)

Tables 2.4 and 2.5 provide an overview of the removal of KF and DCF using various adsorbents. Tables 2.6, 2.7 and 2.8 present the overview of the removal of CIP, LFH and CAF using various adsorbents.

Table 2.4 Overview of removal of KF drug using various adsorbent

S. No	Adsorbent	Parameters, mechanism, kinetics and isotherm	Remarks	Reference
1	Al/Ni layered double hydroxide onto polyaniline-wrapped sisal fibres	Adsorption capacity 38.68 mg/g, pH -5, dosage – 100 mg, conc -100 mg/L, contact time – 90 min, 53 % removal efficiency,	chemisorption, fitted with Temkin isotherm, pseudo second order kinetics	(Negarestani et al. 2024)
2	Silver nanoparticle-modified luffa	Adsorption capacity – 56.88 mg/g, pH -5, Contact time – 60 min, conc -100 mg/L, 97 % removal efficiency adsorbent dosage -25 mg,	Fitted with Temkin isotherm, Pseudo second order kinetics	(Tavassoli et al. 2024)

3	Acid-treated physalis peruviana biomass	Adsorption capacity 172 mg/g, pH - 2 at 298 K, volume of solution - 50 mL, time - 240 mins, agitation rate - 150 rpm, dosage - 0.8 g/L,	endothermic multilayer adsorption	(Dhaouadi et al. 2022)
4	Activated carbon prepared from winery wastes (ACWC)	pH-3 0.5 mol/L of HCl solution, volume of solution- 20 mL, ACWC amount - 20 mg, agitation rate - 140 rpm, shaking time - 300 min,	Physisorption	(Sellaoui et al. 2021)
5	MnFe ₂ O ₄ /Bi ₂ MoO ₆ /PPy	pH - 6, dosage - 0.6 g/L, T - 313 K, conc -5 to 40 mg/L, adsorption capacity - 22.21 mg/g,	Fitted with Langmuir, pseudo second order kinetics	(Wang et al. 2021)
6	ZnAl/biochar	pH - 5, dosage - 0.1 g/L, T - 298 K, conc -25 to 125 mg/L, adsorption capacity -1081.35 mg/g,	O-H, C-H complex formation, anion exchange, fitted with Langmuir, pseudo second order kinetics	(Li et al. 2021)
7	Copper nanoparticles	pH - 5, dosage -1g/L, T-298 K, initial conc - 50 mg/L, 89 % removal efficiency	Fitted with pseudo first order kinetics, Langmuir and exothermic reactions	(ALothman et al. 2021)
8	MnFe ₂ O ₄ /Bi ₂ MoO ₆ /PPy	pH - 6, dosage -0.6 g/L, T-313 K, conc -5 to 40 mg/L, adsorption capacity - 22.21 mg/g,	Fitted with Langmuir and pseudo second order kinetics	(Wang et al. 2021)
9	NiFe ₂ O ₄ /activated carbon	pH - 2, dosage -0.5 g/L, T-328K, Conc – 10 to 100 mg/L, adsorption capacity -97.95 mg/g,	Physical interactions, fitted with pseudo second order kinetics, Sips isotherm	(Fröhlich et al. 2019)
10	Synthesized ionic liquids modified CNTs	pH -7, dosage - 0.67 g/L, T- 298 K, initial conc - 5 to 50 mg/L, 5 mins,	π - π interactions, fitted with pseudo second order kinetics and Freundlich isotherm	(Lawal et al. 2018)

Table 2.5 Overview of removal of DCF drug using various adsorbent

S. No	Adsorbent	Optimized conditions	Remarks	Reference
1	Multiwalled carbon nanotubes functionalized with iron nanoparticles	Adsorption capacity – 0.539 – 0.559 mmol/g, volume of solution – 10 mL, conc – 0.02 – 1 mmol/L, stirring speed -200 rpm, adsorbent dosage – 0.015 g equilibrium time – 6 hr	Fitted with Langmuir isotherm model	(Dutra et al. 2024)
2	Polyaniline-coated magnetic nanoparticles	pH – 4, adsorbent dosage – 25 mg, contact time -10 min, adsorption capacity – 23.06 mg/g removal efficiency – 90 %, stirring speed – 200 rpm	Fitted with a pseudo second order kinetic model, Langmuir Freundlich dual-site model	(da Cunha et al. 2023)
3	Magnetic gelatin-activated biochar from agricultural biomass	pH - 6.50 adsorbent dosage - 2000 mg/L shaking time - 600 min, adsorption capacity - 349.90 mg/g, T - 298 K	Fitted with a pseudo second order kinetic model, Temkin isotherm model, electrostatic interactions, hydrogen bonds interactions and π - π interactions	(Thi Minh Tam et al. 2022)
4	Carbon-encapsulated iron nanoparticles	Adsorbent dosage - 0.05 - 4000 mg/L shaking time - 30 min, adsorption capacity - 74.38 mg/g	Fitted with pseudo second order kinetics, lower concentration - monolayer adsorption, higher concentration - multilayer adsorption	(Munoz et al. 2021)
5	Trimethylamine functionalized clay	pH – 3, adsorbent dosage - 1000 mg/L shaking time - 90 min, adsorption capacity - 387.25 mg/g, adsorption dosage - 1.5 g/L	Fitted with Langmuir, pseudo second order kinetics	(Shayesteh et al. 2020)
6	Amino hydroxyapatite/chitosan hybrids reticulated	pH - 3, adsorbent dosage - 2000 mg/L, shaking time - 15 min, adsorption capacity - 125 mg/g,	Fitted with Pseudo first order kinetics, Pseudo second order kinetics, Langmuir isotherm	(Pereira et al. 2020)

			hydrogen bonding, electrostatic interactions, van der Waals force	
7	Pyridine-functionalized mesoporous SBA-15 organosilica	pH - 5.50 adsorbent dosage - 333.33 mg/L shaking time - 180 min, adsorption capacity -274-632 mg/g, Langmuir -Freundlich isotherm model, removal efficiency - 75-87%,	electrostatic interactions and hydrogen bonds	(Barczak 2018)
8	Commercial granular activated carbon	pH - 4, adsorbent dosage - 500 mg/L, shaking time - 60, adsorption capacity - 36.23 mg/g,	Fitted with Freundlich isotherm, endothermic	(de Franco et al. 2018)
9	Magnetic poly (St-AMPS) nanoparticles	pH - 5.50, adsorbent dosage - 12,500 mg/L, shaking time - NIL, adsorption capacity - 150.60 mg/g, Langmuir isotherm - 150.062 mg/g, physisorption, removal efficiency - 91.3%,	Fitted with pseudo second order kinetics	(Hayasi and Saadatjoo 2018)
10	Magnetic amine - functionalized chitosan	pH - 4.50, adsorbent dosage - 600 mg/L, shaking time - 60, adsorption capacity - 469.48 mg/g,	Fitted with Langmuir isotherm, pseudo second order kinetics, electrostatic interactions, hydrogen bonding	(Liang et al. 2019)
11	Metal -Loaded Carbonated Mesoporous Calcium Silicates	pH - 6, adsorbent dosage -1000 mg/L, shaking time - NIL, adsorption capacity - 23.70-11.80 mg/g, pristine MCS sample - 10 mg/L - 98 %, 20 mg/L - 77%, Ce-MCS - 5mg/L- 69 % removal efficiency	pore filling, hydrogen bonds interactions and π - π interactions fitted with Langmuir isotherm	(Tomul et al. 2019)

Table 2.6 Overview of removal of CIP using various adsorbent

S. No	Adsorbent	Optimized conditions	Remarks	Reference
1	Nanofibrous membranes modified by zwitterionic polyelectrolyte brushes	Adsorption capacity -245.6 mg/g, pH – 7, equilibration time – 15 hr, stirring speed – 120 rpm/min, Conc – 30 to 150 mg/L, temperature – 298 – 328 K,	Fitted with pseudo second order kinetics Hydrogen bonding, electrostatic and $\pi - \pi$ interactions	(Wang et al. 2024)
2	Pumice – Bentonite composites	Adsorption capacity – 54 mg/g, pH - 2, contact time – 240 min, conc – 30 mg/L, temperature – 298 K – 318 K,	spontaneous, endothermic, fitted with Langmuir and DR isotherm, pseudo second order kinetics, $\pi - \pi$ interactions, chemical complexation and surface interactions	(Husain et al. 2024)
3	Magnetic ML101-Fe metal-organic framework/NiFe ₂ O ₄	pH -8, adsorbent dosage - 20 mg for 100 mg/L in 50 mL at the optimum time - 20 mins, adsorption capacity - 796.23 mg/g, removal efficiency -100 %.	Fitted with Pseudo second order kinetic model, Langmuir isotherm model, hydrogen bonding, electrostatic and $\pi - \pi$ interactions, pore filling, endothermic,	(Bazgir et al. 2022)
4	Porphyrin-Zr-MOFs	pH -7, (300 nm) adsorbent dosage - 0.5 g/L, CIP initial concentration - 10 mg/L, shaking time -180 min, adsorption capacity - 207.16 mg/g, removal efficiency -84 %	Fitted with Pseudo second order kinetic model, homogeneous monolayer chemisorption, Langmuir isotherm, hydrogen bonding, $\pi - \pi$ interactions, electrostatic interactions, exothermic	(Zong et al. 2021)
5	Metal-organic framework HKUST-1	pH -7, adsorbent dosage - 0.5 g/L at the optimum time - 360 mins, initial concentration - 10-60 mg/L, adsorption capacity - 67.5 mg/g,	Fitted with Pseudo second order kinetic model, Temkin isotherm model, hydrogen bonding, $n - \pi$ and $\pi - \pi$ interactions, endothermic.	(Tran et al. 2020)

	Cu/Cu ₂ O/CuO@ C porous Composite			
6	ZIF -67-SO ₄	pH - 6.82, adsorbent dosage - 0.8324 g/L, optimum time - 39.95 min, adsorption capacity - 2537.5 mg/g, removal efficiency - 99 %,	Fitted with a Pseudo second order kinetic model, the Langmuir isotherm model.	(Dehghan et al. 2019)
7	Chitosan -grafted SiO ₂ /Fe ₃ O ₄	pH - 12 adsorbent dosage - 1 mg, shaking time - 60 min, adsorption capacity - 100.74 mg/g	Fitted with a Pseudo second order kinetic model, Langmuir isotherm, intraparticle diffusion as the rate-limiting step	(Danalıoğlu et al. 2018)
8	Polyelectrolytes into alumina nanoparticles	pH -7, adsorbent dosage - 5 mg/mL, shaking time - 90 min, adsorption capacity - 37.8 mg/g, removal efficiency - 99 %, pH -6, adsorbent dosage - 5 mg/mL, NaCl - 10 Mm, shaking time - 90 min, adsorption capacity - 100.74 mg/g, removal efficiency - 95 %,	Fitted with the pseudo-second-order kinetic model, two step isotherm model, electrostatic interactions at low salt concentration and non -electrostatic interactions at high salt concentration	(Dao et al. 2018)
9	Konjac glucomannan based zeolite imidazolate framework composite aerogels	pH -7, adsorbent dosage - 20 mg/100 mL, optimum time - less than 12 hrs, adsorption capacity - 811.03 mg/g at 1500 mg/L of CIP concentration at 303 K removal efficiency - 100 %,	Fitted with Pseudo second order kinetic model, Langmuir isotherm model, electrostatic interactions and, endothermic.	(Yuan et al. 2018)

10	Magnetic copper-based organic framework	pH -7, adsorbent dosage -2 mg/50 mL, optimum time - 30 min, adsorption capacity - 538 mg/g,	Pseudo second order kinetic model, Langmuir isotherm model, electrostatic and π - π interactions, exothermic.	(Wu et al. 2018)
11	MIL 101-(Cr)	pH - 8, adsorbent dosage - 1 mg for 15 mg/L at optimum time - 90 min, adsorbent dosage - 1 mg for 25 mg/L at optimum time -50 mins, adsorption capacity -63.28 mg/g,	Fitted with Pseudo second order kinetic model, Langmuir isotherm model, electrostatic and π - π interactions, exothermic.	(Bayazit et al. 2017)
12	Zeolite imidazolate framework derived nanoporous carbon	pH - 6, adsorbent dosage - 1 mg for 10 mg/L at the optimum time - 21 hrs, adsorption capacity - 416.7 mg/g, removal efficiency - 99.6 %.	Fitted with a Pseudo second order kinetic model, Both Langmuir and Freundlich isotherm models, hydrogen bonding, electrostatic and π - π interactions, pore filling, endothermic,	(Li et al. 2017)

Table 2.7 Overview of removal of LFH using various adsorbent

S. No	Adsorbent	Optimized conditions	Remarks	Reference
1	Red mud-based CoFe ₂ O ₄ / PMS	PMS conc – 5 mmol/L, pH – 7, conc – 100 mg/L, removal efficiency - 86.36 %, contact time – 12 min, dosage – 1.33 g/L	Ball milling can improve the catalytic activity of Red mud based CoFe ₂ O ₄ towards the removal of LFH	(Gu et al. 2024)

2	Zr-based metal-organic framework from waste plastic bottle	Adsorption capacity – 588 mg/g, pH -10, Temperature – 303 K, 313 K, 323 K	π- π interactions, hydrogen bonding	(Huang et al. 2024)
3	Au/TiO ₂	Catalyst dosage - 0.15g, pH -5, initial concentration -10 mg/L, optimum time - 60 min, removal efficiency - 90.15 % at room temperature	Au/TiO ₂ , in this the short wavelength light was converted into photogenerated carriers with TiO ₂ support and the long-wavelength light was converted into heat, this caused the localized surface plasmon resonance effect of Au, synergistically promoting the LFH degradation	(Duo et al. 2022)
4	NiFe ₂ O ₄ /CuS	PMS - 0.6g/L, catalyst dosage (1:5) - 0.8 g/L, reaction temperature - 25°C, pH - 5.86, initial concentration - 10 mg/L, optimum time - 5 min, reaction volume -50 mL, removal efficiency - 88.1%	0.632 %, 0.061 % and 0.433 % of Cu, Ni and Fe ions leached, this reflects the physical and chemical stability of the catalyst	(Zhang et al. 2022)
5	Natural Hematite/Persulfate	PS - 0.8 mmol/L, catalyst dosage - 50 mg/L, reaction temperature - 25°C, pH- 2.87 - 8.84, initial concentration - 10 mg/L, optimum time - 120 min, reaction volume -50 mL, removal efficiency - 82.2%	Natural Hematite/Persulfate showed excellent removal of antibiotics in wastewater, and metal ions dissociated showed good stability and low risk of secondary contamination during LFH degradation	(Guo et al. 2022)
6	UiO-66MoS ₂	Catalyst dosage (1:2) - 0.03 g/L, reaction temperature - 25 °C, initial concentration -20 mg/L, optimum time - 90 min, reaction volume - 100 mL, removal efficiency - 87 % at 40°C,	Pseudo-first order kinetics	(Gao et al. 2021)
7		PMS - 0.2g/L, catalyst dosage - 0.6g/L, reaction temperature - 25°C, pH - 5.52, initial	87.5 % removal efficiency was observed after five consecutive re-use.	(You et al. 2021b)

	MBC/CoFe ₂ O ₄ /PMS	concentration -10 mg/L, reaction volume - 50 mL, optimum time - 20 min, removal efficiency - 86.9%.		
8	Co-Cu-LDH	PMS - 0.15g/L, catalyst dosage - 0.04 g/L, reaction temperature - 25°C, pH - 6.67, initial concentration - 10 mg/L, optimum time -5 min, removal efficiency - 96.19%	The catalyst had excellent stability, crystallinity, and reusability after six cycle runs the removal efficiency was 83.11 %	(Guo et al. 2020b)
9	AC@CoFe-LDH	PS - 0.2g/L, catalyst dosage (1:2) - 1 g/L, reaction temperature - 25°C, pH - 5, initial concentration -5 mg/L, optimum time - 60 min, reaction volume - 100 mL, removal efficiency - 93.2 % at 40 °C and 82.2% at 20 °C	The catalyst showed good stability and reusability after three cycle runs the removal efficiency was found to be 80 %	(Ma et al. 2020)
10	Bi ₂ O ₃ /CuNiFe LDHs	PS - 0.74 mM, catalyst dosage (1:1) - 0.4 g/L, reaction temperature - 25 °C, initial concentration - 10 mg/L, pH - 6.08, optimum time - 40 min, reaction volume -100 mL, removal efficiency - 84.6 % at 40°C, Pseudo-first order kinetics.	Large pore volume and high specific surface area provided more active sites	(Zhang et al. 2020a)
11	Co ₃ O ₄ /δ-FeOOH	PMS - 0.49 mM, catalyst dosage - 0.25g/L, reaction temperature - 25°C, pH - 6.08, initial concentration -10 mg/L, reaction volume - 50 mL, optimum time - 25 min, removal efficiency -> 82%,	Fitted in first order kinetics	(Zhang et al. 2019b)

Table 2.8 Overview of removal of CAF using various adsorbent

S. No	Adsorbent	Optimized conditions	Remarks	Reference
1	Thermally modified bentonite	pH – 8 contact time – 120 min, adsorption capacity – 80.3 mg/g, stirring speed 400 rpm, removal efficiency – 96.54 %, adsorbent mass – 111.8 mg/g, Conc – 21.8 mg/L,	Fitted with pseudo second order kinetic and Elovich model	(Quintero-jaramillo et al. 2024)
2	Zeolite imidazolate frameworks based on magnetic on three-dimensional graphene	pH – 7, Volume of solution – 4 mL, conc – 5 mg/L, adsorbent dosage – 50 mg, Stirring speed – 45/20 min, Removal efficiency – 96.55%, adsorption capacity – 19.56 mg/g	Fitted with pseudo second order and Langmuir isotherm model, chemisorption	(Hua et al. 2024)
3	Graphene oxide magnetic nanocomposite	H ₂ O ₂ -5 mmol, catalyst dosage - 0.2g/L, pH - 3, initial concentration - 1000 µg/L, reaction volume - 50 mL, optimum time - 90 min, degradation efficiency - 97.32 %	Fenton degradation of CAF, after five consecutive cycles of degradation resulted in a decrease in the removal efficiency from 98 to 82 %	(Ramirez-Ubillus et al. 2022)
4	Magnetic -hematite	Catalyst dosage - 0.13 g/L, initial concentration and volume - 20 mg/L/150 mL, reaction time -60 min, removal efficiency - 98%	Density functional theory helped in finding the stable species during CAF degradation, after five recycle there observed no performance loss.	(Fernandes et al. 2021)
5	Ce -TiO ₂	Ozone - 2.5 mg/L, catalyst dosage (0.5 weight %) - 0.05 g, room temperature, pH - 6, initial concentration - 2.57×10 ⁻⁵ M, reaction volume - 300 mL, optimum time - 120 min, removal efficiency - 99.9 %	Highly mesoporous structure possessed large surface area and fitted with first order kinetics	(Ndabankulu et al. 2019)
6	ZnO supported on zeolite pellets	PMS - 0.2 mM, catalyst dosage - 200 mg/L, pH - 7.10, initial concentration - 0.05 mM,	The five successive recycle of photocatalytic oxidation of CAF using	(Sacco et al. 2018)

		optimum time - 120 min, removal efficiency - 98 %	a catalyst resulted in the same removal efficiency.	
7	Cobalt nanosheet	PMS -150 mg/L, catalyst dosage -50 mg/L, pH -9, initial concentration -50 mg/L, optimum time -20 min	CoNS could re-used with PMS for the degradation of CAF with no activity loss. It is a highly effective and stable 2D catalyst	(Lin et al. 2018)
8	Mg doped ZnO - Al ₂ O ₃	Catalyst dosage (1%) - 20 mg/L, initial concentration - 0.3 g/L, reaction volume -2 L, pH - 9.5, Irradiation time - 70 min, Degradation efficiency - 98.9%	1 % Mg-doped ZnO -Al ₂ O ₃ sample showed the highest adsorption capacity and photocatalytic activity in the degradation of CAF	(Elhalil et al. 2018)
9	ZnO -ZnAl ₂ O ₄	Catalyst dosage - 0.3g/L, pH - 9, initial concentration - 20 mg/L, optimum time - 90 min, degradation efficiency - 97.32 %	The 3M and catalyst calcined at 500 °C with a larger adsorption capacity than Degussa P-25 Titanium dioxide	(Elhalil et al. 2017)
10	Cobalt/Carbon nanocomposite -ZIF -67	Oxone - 250 mg/L, catalyst dosage - 50 mg/L, reaction temperature - 20 °C, reaction time - 120 min	Magnetic carbon-supported cobalt could be a promising heterogeneous catalyst in the degradation of CAF using PMS	(Andrew Lin and Chen 2016)
11	Cobalt MCM41/PMS	PMS - 0.2 mM, catalyst dosage - 200 mg/L, pH - 7.10, initial concentration - 0.05 mM, optimum time -120 min, degradation efficiency - 98 %	The experimental data were fitted in both pseudo first and second order kinetics	(Qi et al. 2014)

The functionalization of silane as a coupling agent, β -CD and amino acid over the adsorbent or as a catalyst in the removal of emerging hazardous PPCP is seen to grow from the literature study. This is because, in the coupling of silane, there observed a stable formation of Si-O-Si in the stober type reactions by undergoing hydrolysis of the n-silane alkoxy groups to highly reactive silanol species and condensation of the resulting silanols with surface-free OH groups to form stable Si-O-Si bonds by forming an amorphous silica shell on the NFO surface (Bruce and Sen 2005; Enache et al. 2017b; Malay et al. 2013; Soto-Cantu et al. 2012). The 3-glycidyl trimethoxy silane (3-GPTMS) acts as a linker between the stable formation of inorganic amorphous silica and β -CD which are pseudo-amphiphilic molecules outside with 21 groups of OH reacting molecules and hence the removal of pollutants upon β -CD happens irrespective of its physicochemical properties(Chen et al. 2021; Moulahcene et al. 2023).

The functionalization of amino acids with at least one amino group ($-\text{NH}_2$) and one carboxyl group ($-\text{COOH}$) could improve the stability of nickel ferrite nanoparticles as well as its ability to absorb the targeted contaminants by providing strong chelating sites. L-Leucine one among the 20 kinds of amino acid, is an aliphatic branched-chain amino acid consisting of one proton donor carbonyl group and one proton acceptor amino group that exists as zwitterions. L-Leucine coated cobalt ferrite has been used in the biomedical application specifically for drug delivery (Adhikari and Kar 2012; Zhang et al. 2020b).

2.5 SCOPE AND OBJECTIVES

2.5.1 Scope

The present research aims to synthesis nickel ferrite nanoparticles (NFO)/ nanocomposites for the removal of pharmaceutical pollutants such as ketoprofen (KF), diclofenac (DCF), ciprofloxacin (CIP), lomefloxacin hydroxide (LFH) and caffeine (CAF).

2.5.2 Objectives

The following are the objectives of the research work framed to accomplish the above aims:

1. To synthesis, the nickel ferrite nanoparticles via a suitable wet-chemical method.
2. To study and analyze the stability, physical, chemical, thermal and magnetic properties of synthesized metal oxide nanoparticles
3. To identify the suitable compound and grafting techniques for the functionalization of nanoparticles.

4. To optimize the functionalization process and characterise nanocomposites.
5. To study the effective removal efficiency of the various emerging hazardous pollutants using the nanocomposites and optimize the batch experiments by varying the operating parameters.
6. To study the regeneration capacity and recyclability of the nanocomposite.

2.6 RESEARCH GAP

The quality of our water resources is deteriorating day by day due to the continuous addition of undesirable chemicals in them. Among various water pollutants, the residues of drugs and pharmaceuticals (new emerging pollutants) in water are hazardous. Drugs and pharmaceuticals are used to cure different diseases in human beings. But also have certain side effects and if the drugs and pharmaceuticals residues entered into the human body can cause severe side effects. These pollutants also target some organisms, which are responsible to sustain our earth's ecosystem. In this way, the new emerging pollutants are disturbing our ecology (Ali and Aboul-Enen 2004; Ali and Gupta 2007; Basheer 2018b; Crane et al. 2006; Falconer et al. 2006). Therefore removing these emerging pollutants at trace levels is a rising research area that appeals to academicians, researchers, clinicians, regulatory authorities and the need of the day in environmental science (Rocha et al. 2020). There are various materials used in different pollutant removal. Firstly, the activated carbon was used to remove pollutants from water, which later on, was replaced by some cost-effective materials (Ali 2010; Ali and Gupta 2007; Larsen et al. 2004).

During the last two decades, nanotechnology has been developed with its applications in every discipline of science and technology, including water treatment. These nano-sized adsorbents have been called new-generation adsorbents (Ati et al. 2013). Nickel ferrite nanoparticles have unique characteristics such as catalytic potential, small size, high reactivity, and large surface energy with high adsorption capacity in varied experimental and natural environmental conditions. The surface modification of nickel ferrite nanosized particles can still enhance their overall properties which can serve as a novel and low-cost promising material that replaces activated carbon (Turk Sekulic et al., 2019). Hence, research in this field will provide alternate eco-friendly surface-modified adsorbents for the removal of emerging pollutants and thus will go a long way in reining the menace of potable water scarcity existing in many parts of the world (Kumar et al. 2020).

CHAPTER 3

MATERIALS AND METHODS

To synthesis Nickel Ferrite nanocomposite material, the following methodologies were adopted. The nanocomposite material thus synthesised was subjected to characterization and further checked for its potential to remove and degrade the pharmaceutical and personal care products pollutants such as KF, DCF, CIP, LFH and CAF

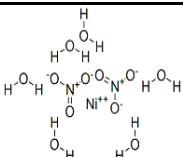
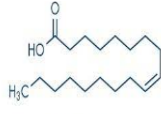
3.1 Choice of precursor salts

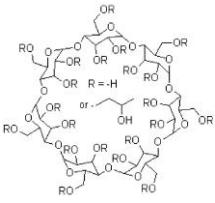
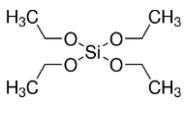
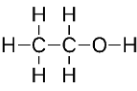
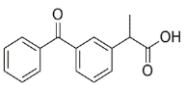
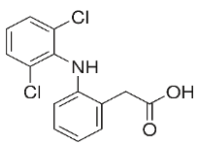
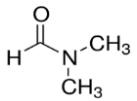
The precursor salts for the preparation of bare and functionalized nanoparticles/nanocomposite would be chosen based on solubility, i.e. (easily soluble) and purity of the salts.

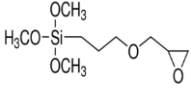
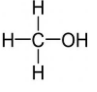
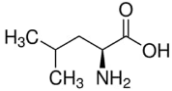
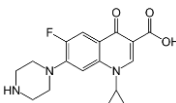
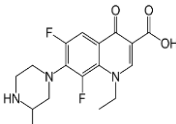
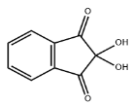
3.1.1 Materials and Methods

The pollutant drugs and the prime chemicals used in the functionalization with their chemical formula, structure and CAS Number are listed in Table 3.1.

Table 3.1 List of pollutant drugs and main chemicals used in functionalization

Compound	Structure	Molecular weight (M _w) (g/mol)	CAS Number	Purity
Nickel nitrate hexahydrate	 (Ni(NO ₃) ₂ ·6H ₂ O)	290.79	3478-00-7	98% Extra Pure
Ferric nitrate nonahydrate AR/ACS	(Fe(NO ₃) ₂ ·9H ₂ O)	404	10421-48-4	98%
Sodium Hydroxide pellets	Na–OH	39.99	1310-73-2	98%
Oleic acid		282.5	112-80-1	

Sodium hydride	Na-H	24	7646-69-7	60% Extra Pure
Ammonia solution	OH^- NH_4^+	17.031	1336-21-6	25% extra pure
Hydroxypropyl- β -Cyclodextrin (HPB CD)	 $\text{C}_{42}\text{H}_{70-n}\text{O}_{35} \cdot (\text{C}_3\text{H}_7\text{O})_n$	1400	28446-35-5	Exiplus 98%
Tetraethyl Orthosilicate (TEOS)	 $\text{SiC}_8\text{H}_{20}\text{O}_4$	208.33	78-10-4	Extra pure 98% 28-28.8% SiO_2
Ethanol (solvent)	 $\text{C}_2\text{H}_5\text{OH}$	46.07	64-17-5	99.9%
KF	 $\text{C}_{16}\text{H}_{14}\text{O}_3$	254.281	22071-15-4	> 98.0%
DCF sodium salt	 $\text{C}_{14}\text{H}_{11}\text{Cl}_2\text{NO}_2$	296.1	15307-79-6	-
N, N-Dimethylformamide anhydrous	 $\text{HCON}(\text{CH}_3)_2$	73.09	68-12-2	99.8%

3-Glycidyloxypropyl trimethoxysilane (3-GPTMS)		236.34	2530-83-8	≥ 98%,
	$C_9H_{20}O_5Si$			
Methanol		32.04	67-56-1	99 %
	CH_3OH			
L-Leucine		131.18		99%
	$C_6H_{13}NO_2$			
Ciprofloxacin		331.34	85721-33-1	>98%
	$C_{17}H_{18}FN_3O_3$			
Lomefloxacin Hydrochloride		387.81		>98%
	$C_{17}H_{19}F_2N_3O_3.HCl$			
Ninhydrin (AR/ACS)		178.14		
Indantrione Hydrate	$C_9H_6O_4$			
Caffeine	$C_8H_{10}N_4O_2$	194.19		>99%

Nickel nitrate hexahydrate ($Ni(NO_3)_2 \cdot 6H_2O$) 98% extra pure, ferric nitrate nonahydrate AR/ACS ($Fe(NO_3)_3 \cdot 9H_2O$) 98%, sodium hydroxide pellets 98% AR, sodium hydride (NaH) suspension 60% extra pure, ammonia solution 25% extra pure, oleic acid ($C_{17}H_{33}COOH$) were purchased from Loba Chemie, Mumbai, India. Hydroxypropyl- β -Cyclodextrin (HPBCD) Exiplus 98%, tetraethyl orthosilicate (TEOS) extra pure 98%, 28-28.8% SiO_2 were bought from SRL; ethanol solvent was purchased from Changshu. KF > 98.0% purchased from TCI and DCF sodium salt, N, N-Dimethylformamide anhydrous 99.8%, and (3-Glycidyloxypropyl) trimethoxysilane (3-GPTMS) ≥ 98%, methanol was purchased from Sigma Aldrich. Ninhydrin (AR/ACS) Indantrione Hydrate was purchased from Loba Chemie. Lomefloxacin

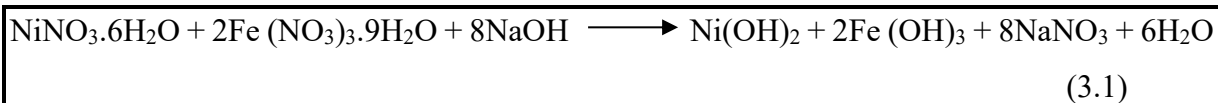
Hydrochloride > 98% purchased from TCI, ciprofloxacin \geq 98 % from Sigma Aldrich, L-leucine 99 % purchased from Otto Chemie Pvt. Ltd, ethylene glycol 99 % EMPLURA[®] was purchased from Merck Life Science Private Limited. Potassium monopersulfate triple salt/oxone/potassium peroxymonosulfate (KHSO₄, Oxone[®]), caffeine was purchased from EMPARTA[®] \geq 99 % Merck grade.

3.2 Synthesis of adsorbent

NFO, NFO@SiO₂, NFO@SiO₂@ β -CD and NFO@L nanocomposite were synthesized in a step-by-step procedure in the section from 3.2.1 to 3.2.4.

3.2.1 Synthesis of NFO nanoparticles

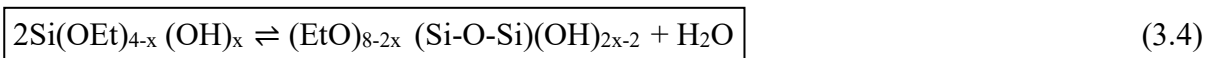
Nanosized NFO particles were synthesized by the facile co-precipitation method. The precursor materials such as nickel nitrate hexahydrate (Ni(NO₃)₂).6H₂O and ferric nitrate nonahydrate (Fe(NO₃)₃).9H₂O were weighed in a stoichiometric ratio of 1:2 and dissolved separately for few min. The clear and homogeneous solution was mixed at 200 - 250 rpm and heated to a temperature of about 80 °C. Then, 3M sodium hydroxide (NaOH) was added slowly in a dropwise manner; the temperature was then raised to 95°C, to which 4 to 5 drops of oleic acid were added and stirred for about 40 min. A black-coloured precipitate thus formed was magnetically detached by rinsing several times with distilled water and ethanol. The final product was dried overnight at 60 °C in a hot-air oven. The dried powder was grounded well and calcined at 400 °C for an hour in a furnace. Thus the nanocrystalline NFO particles were obtained (Maaz et al. 2009).



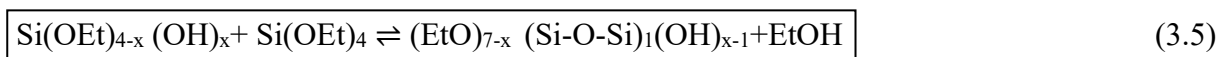
3.2.2 Optimization of NiFe₂O₄@SiO₂ nanoparticles

A reaction mixture was prepared with 0.01 g, 0.5 g, and 0.1 g of bare NFO nanoparticles in a solution containing 50 mL distilled water, 150 mL ethanol, and 10 mL ammonia were sonicated for 10 min, and 2 mL tetraethyl orthosilicate (TEOS) was added dropwise, after which it was stirred for 6 hrs. The NFO@SiO₂ were separated using an external magnet. The decanted nanoparticles were washed with ethanol and distilled water and then dried overnight at 60 °C (Isasi et al., 2019). The same procedure with the appropriate amount of NFO was varied with

The silanol monomers undertake condensation between two silanol groups from the above reactions to generate branched siloxane clusters, which are further linked to trigger the nucleation and growth of silica particles.



The silanol monomers may also react with the unhydrolyzed ethoxyl groups of TEOS via condensation between silanol and ethoxyl groups (Han et al. 2017)



3.2.3 Synthesis of NFO@SiO₂@GPTMS@β-cyclodextrin

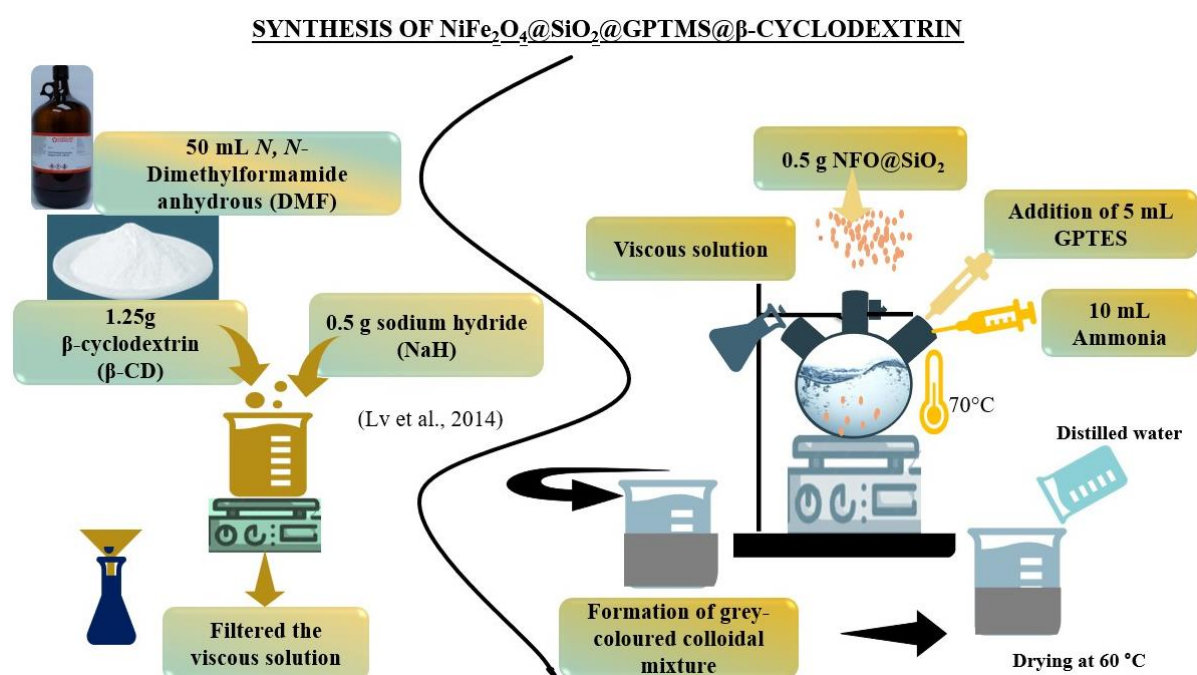


Fig. 3.2 (a) Schematic representation of procedural linkage of 3 – GPTMS and β-CD to NFO@SiO₂

A reaction mixture of 1.25 g of β - cyclodextrin (β-CD) and 0.5 g of sodium hydride (NaH) in 50 mL of N, N-Dimethylformamide anhydrous (DMF) was mixed under constant stirring until the formation of a well-mixed viscous solution, after which the mixture was filtered. 0.5 g of NFO@SiO₂ was taken in a three-necked round bottom flask to that the filtered reaction mixture, and 5 mL of 3-Glycidyloxypropyl Trimethoxysilane (3 - GPTMS) was added in a dropwise manner and heated at 70 °C. Simultaneously, 10 mL of 25 % ammonia solution was added to the reaction mixture on the other side. Once the thick grey-coloured colloidal mixture

was formed, the reaction mixture was cooled to room temperature, then it was washed and filtered several times with distilled water and dried overnight at 60 °C (Lv et al., 2014). The schematic representation of procedural attachment of 3-GPTMS and β -CD to NFO@SiO₂ and formation of NFO@SiO₂@GPTMS@ β -CD is shown in Fig. 3.2 (a) and (b).

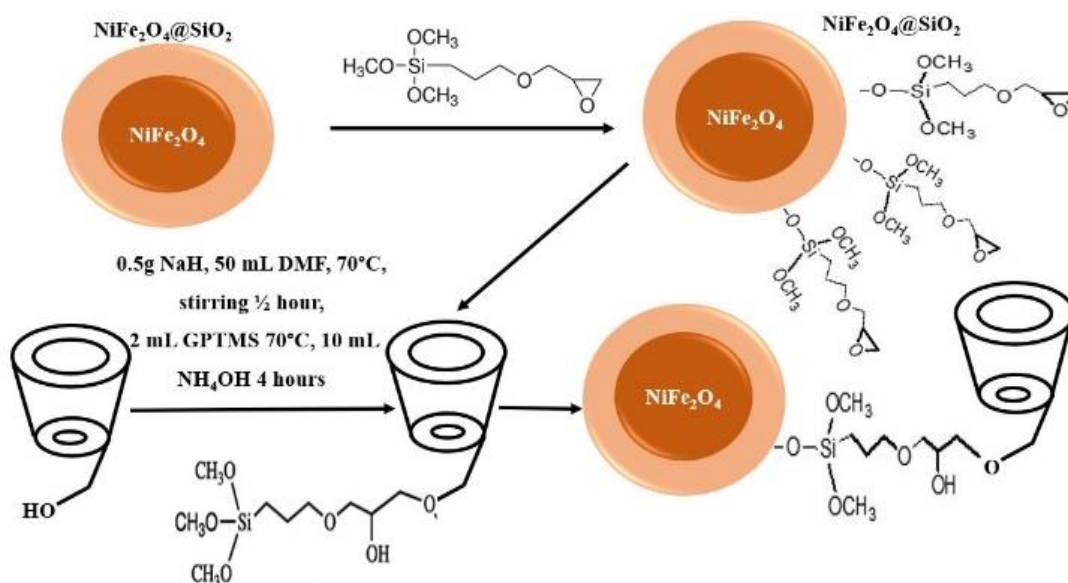


Fig. 3.2 (b) Schematic representation of NFO@SiO₂@GPTMS@ β – cyclodextrin

3.2.4 Synthesis of Nickel ferrite@L-Leucine (NFO@L)

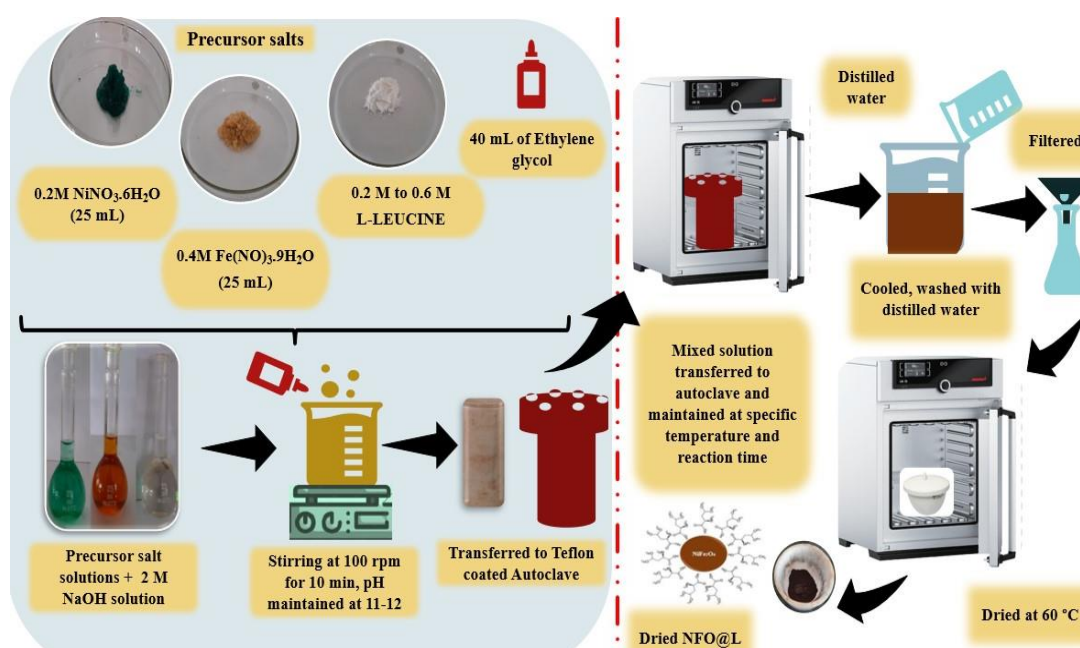


Fig 3.2 (c) Schematic representation of procedural attachment of L-Leucine onto NFO

The precursor salts with a molar concentration of 0.2 M nickel nitrate hexahydrate ($\text{Ni}(\text{NO}_3)_2 \cdot 6\text{H}_2\text{O}$), 0.4 M ferric nitrate nonahydrate ($\text{Fe}(\text{NO}_3)_3 \cdot 9\text{H}_2\text{O}$) and 0.5 M L-Leucine were mixed in a round bottom flask and kept in constant stirring at room temperature; to the obtained mixture 40 mL of ethylene glycol was added. Once the L-Leucine in the solution was dissolved completely, 2 M NaOH solution was added in a dropwise manner using a syringe and stirred for about 10 min. The mixture was then transferred to a Teflon-coated autoclave and was maintained at 423 K for about 12 hrs, after which the autoclave was allowed to cool down. The resulting mixture is filtered and washed with distilled water and further dried in an oven at 333 K overnight (Zhang et al. 2020b).

3.3 Characterization studies of the NFO nanocomposites

The properties of synthesized NFO nanoparticles and NFO nanocomposite were investigated using techniques such as Fourier transform infrared spectroscopy (FT-IR), X-ray diffraction analysis (XRD), Field emission scanning electron microscopy (FESEM) / Energy Dispersive X-ray Diffraction (EDX), Atomic force microscopy (AFM), vibrating sample magnetometer (VSM), thermal gravimetric analysis (TGA)/Derivative thermogravimetric analysis (DTG), Brunauer-Emmett-Teller (BET)/Barrett-Joyner Halenda (BJH) model, zeta potential and particle size analysis.

FT-IR spectra of NFO and NFO nanocomposite (before and after removal) were recorded using an FTIR/ATR Perkin Elmer spectrum system with a resolution of about 1 cm^{-1} in the 4000 to 450 cm^{-1} range. XRD was performed in EMPYREAN with the anode material Cu and K-Alpha wavelength of 0.154 nm in spinner mode for β -CD, NFO, $\text{NFO}@SiO_2$, $\text{NFO}@SiO_2@ \beta$ -CD, $\text{NFO}@L$. The particle morphology, shape, and size of the nanoparticles/ nanocomposite were characterized using a FESEM Zeiss GeminiSEM 300-820201722 analyzer at a magnification of 200 nm ; before imaging, the samples were gold sputtered due to the charging effect of the nanoparticles and nanocomposite, and the elements constituted in the NFO and functionalized NFO were observed and identified using EDX at 200 keV . The thermal stability, oxidative stability, and decomposition kinetics of the NFO, $\text{NFO}@SiO_2@ \beta$ -CD and $\text{NFO}@L$ were investigated using a Perkin-Elmer Pyris Diamond 6000 TGA/DTA/DTG analyzer. The magnetic properties of NFO, $\text{NFO}@SiO_2@ \beta$ -CD and $\text{NFO}@L$ were investigated using the VSM Lakeshore 7410S model at room temperature in a magnetic field of 1.5 T with an average time of 3 seconds and a field increment of 500 Oe .

The BET multi-point method was used to estimate the specific surface area, pore volume, and pore radius of the NFO nanoparticles and NFO nanocomposites using Quantachrome®

ASiQwin™- Automated Gas Sorption Data Acquisition and reduction under nitrogen gas at 77.35 K. The particle size distribution and surface charge of the NFO, NFO@SiO₂@β-CD and NFO@L were measured using an Anton Paar Lite sizer 5; the analysis was performed using the salt addition method with 50 mg of NFO and NFO nanocomposites each separately was dispersed in 50 mL of 0.1 M NaNO₃ for 24 hrs at varied pH using 0.1 M NaOH and HNO₃ at room temperature. The presence of amino acid-functionalized NFO nanoparticles was confirmed with the ninhydrin test. The leaching of nickel and iron ions from the NFO nanoparticles in the final analyte of the respective pollutant was also determined using the Inductively Coupled Plasma-Optical Emission Spectrometry (ICP-OES) Agilent Technologies MY15340006 instrument.

3.3.1 Ninhydrin test for NFO@L nanocomposite



Fig. 3.3 Ninhydrin test of L-Leucine functionalized onto NFO

Initially, NFO@L nanocomposite was dispersed in 0.2 % w/v of ninhydrin solution prepared in a phosphate buffer. The nanocomposite in ninhydrin solution was heated in a water bath at 75 °C for about 15 min as in Fig. 3.3. Further cooling of the solution, the NFO@L nanocomposite was separated using an external magnet. The resulting colour change confirms the presence of amino acid attached to the NFO nanocomposite (Arévalo-Cid et al. 2018).

3.4. Stock solution and UV -Visible scan for pharmaceutical pollutants

The stock solution and standard working solution for each of the pollutant concentrations were prepared and scanned in the UV-visible spectrophotometer and it is presented in sections 3.4.1 to 3.4.6.

3.4.1 Preparation of stock and working solution & UV-visible scan for KF and DCF

The stock solution of KF was prepared by dissolving 100 mg KF in 25 mL methanol and 75 mL distilled water in a 100 mL standard flask. Methanol was used as a solvent to dissolve the KF drug. DCF stock solution was prepared by dissolving 100 mg DCF in 100 mL of distilled water. 10 mL KF solution and 10 mL DCF solution at concentrations such as 2, 4, 6, 8, 10, 12 and 14 mg/L and 2, 4, 6, 8, 10, 12, and 14 mg/L respectively were prepared and scanned using UV-spectrophotometer at a wavelength between 200 to 800 nm which were shown in Fig. 3.4 (a) and (b).

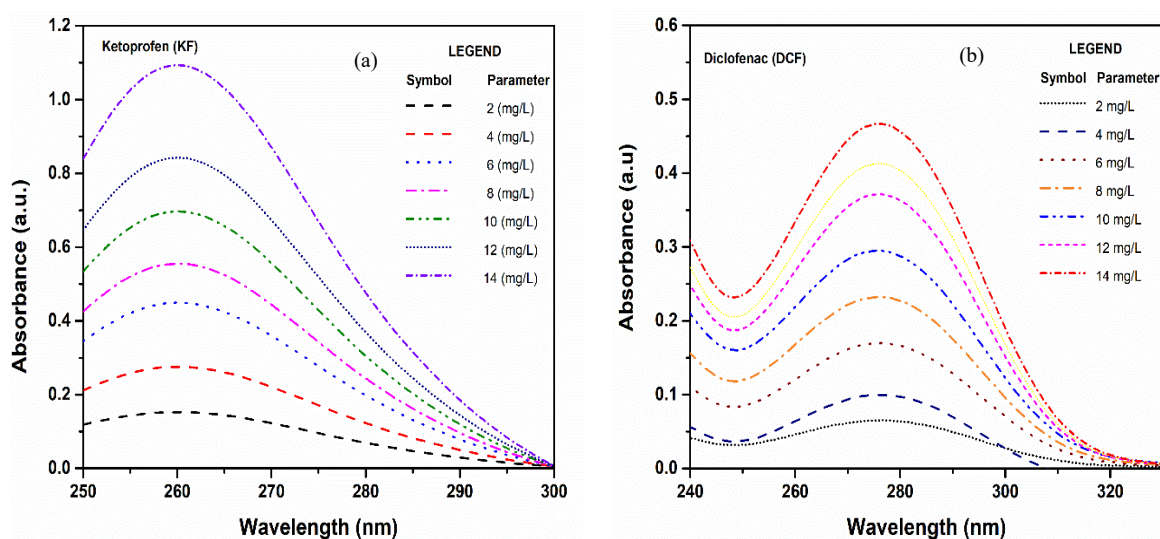


Fig. 3.4 (a) KF and (b) DCF at different concentrations and their respective absorbance

3.4.2 Preparation of working solution & UV-visible scan for CIP and LFH

10 mL of different solution concentrations such as 1, 2, 3, 4, 5, 6, 7, 8, 9, 10, 11 and 12 mg/L for CIP and 1, 2, 3, 4, 5, 6, 7, 8, 9 and 10 mg/L for LFH solution was prepared and scanned using a UV-spectrophotometer at a wavelength between 200 to 800 nm, as shown in Fig. 3.5.

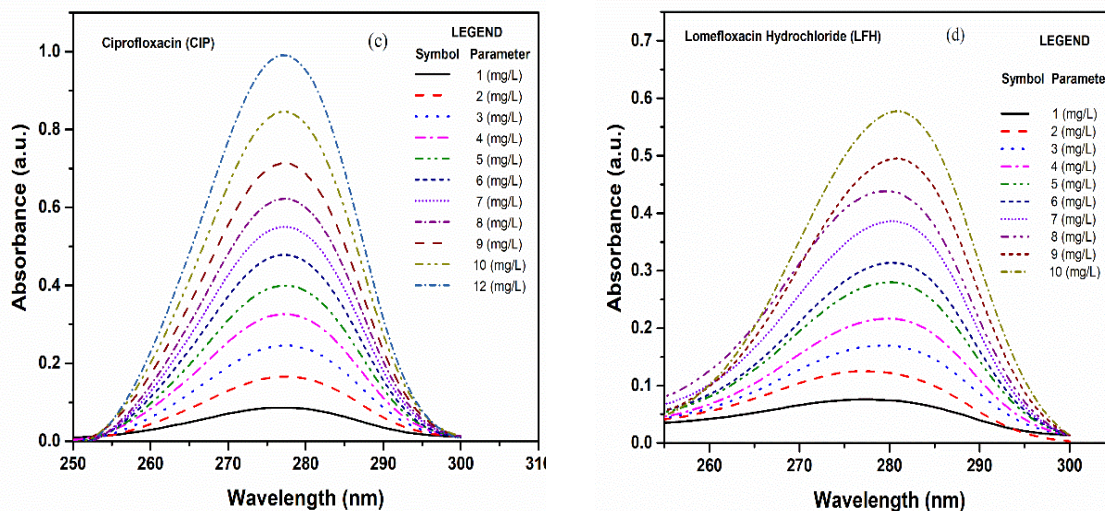


Fig. 3.5 UV-Visible absorbance of (a) CIP and (b) LFH solution for different concentrations

3.4.3 Preparation of working solution & UV-visible scan of CAF

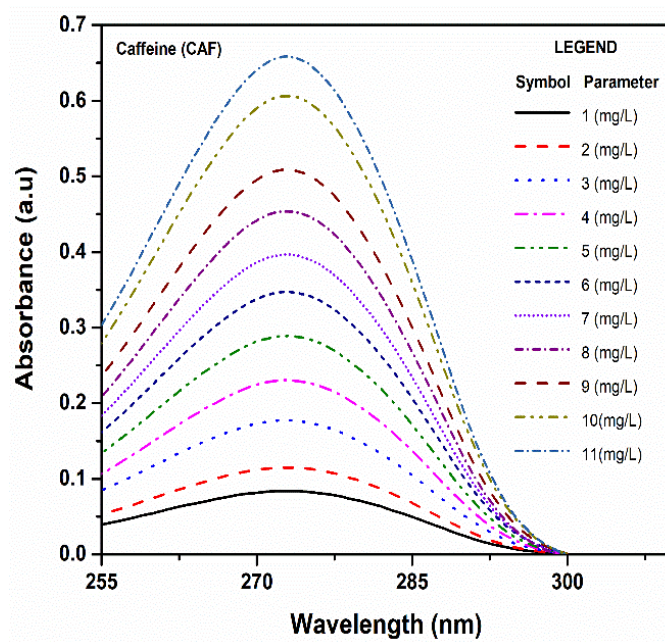


Fig. 3.5 (c) UV-Visible absorbance of CAF for different concentrations

10 mL of different solution concentrations such as 1, 2, 3, 4, 5, 6, 7, 8, 9, 10 and 11 mg/L of CAF was prepared and scanned using a UV-spectrophotometer at a wavelength between 200 to 800 nm, as shown in Fig. 3.5.

3.4.4 Calibration plot for KF and DCF

The known concentrations of KF and DCF aqueous solutions scanned at 260 and 276 nm respectively against their corresponding absorbance were plotted to obtain the calibration plots as displayed in Fig. 3.6 (a). The unknown concentrations of KF and DCF sample solutions were obtained using the calibration plots.

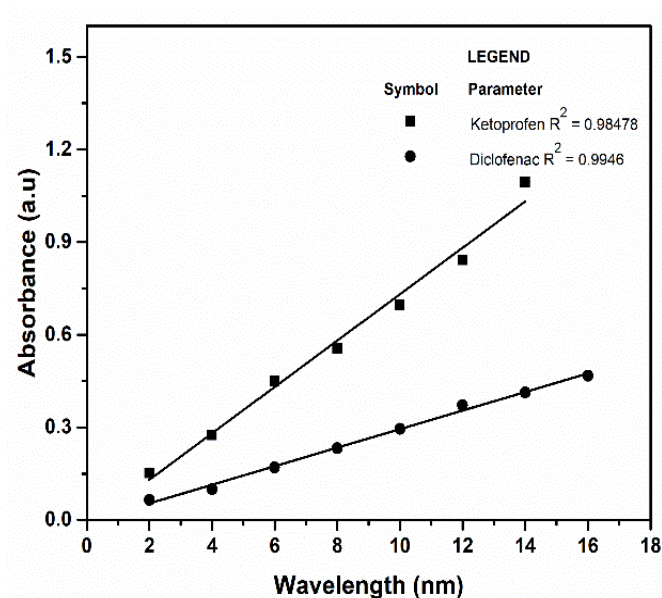


Fig. 3.6 (a) Calibration plot of KF and DCF

3.4.5 Calibration plot for CIP and LFH

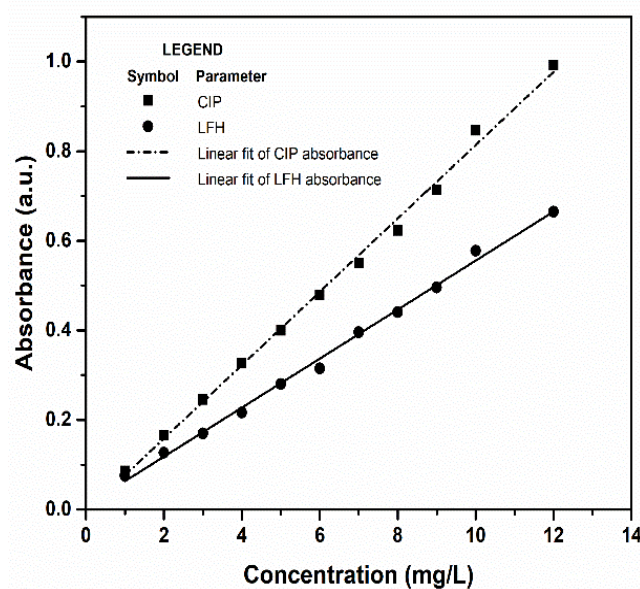


Fig. 3.6 (b) Calibration plot of CIP and LFH aqueous solutions

The absorbance of CIP and LFH was observed at the wavelength of 277 nm and 281 nm respectively. The scanned wavelengths for each of the concentrations are presented in Fig. 3.6 (b), and the unknown concentrations are obtained from the calibration plot.

3.4.6 Calibration plot for CAF and LFH

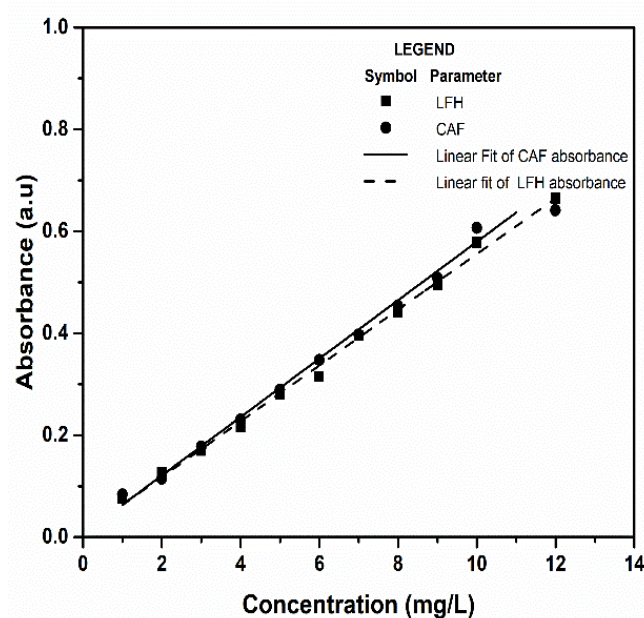


Fig. 3.6 (c) Calibration plot of CAF and LFH

Fig. 3.6 (c) depicts a calibration plot for both CAF known concentration solutions and their respective absorption spectrum. The wavelengths of the final filtered samples were analyzed in the 273 nm for CAF. The standard calibration graph was employed to compute the final concentration.

3.5 Batch experimental investigation on the removal of pharmaceutical pollutants

All experiments were carried out by changing one variable at a time in a 100 mL volume of solution each containing a 10 mg/L concentration of KF, DCF, LFH and CIP at room temperature. Initially, a 10 mg NFO@SiO₂@β-CD nanocomposite was taken in a 100 mL volume of solution each containing a 10 mg/L concentration of KF and DCF in which the pH was varied from 3 to 10. Similarly, 10 mg of NFO@L nanocomposite was taken in a 100 mL volume of solution each containing a 10 mg/L concentration of LFH and CIP in which the pH was varied from 4 to 11 using 0.1M NaOH and HCl. The contents were kept in a rotary shaker at 120 rpm for 12 hrs. Under optimal pH, the different dosage of NFO@SiO₂@β-CD nanocomposite was varied from 10 mg to 140 mg in each of the KF and DCF aqueous solutions.

In the same way, NFO@L nanocomposite dosage was varied from 10 mg to 120 mg for CIP and 10 to 80 mg for LFH. The obtained optimal pH, dosage of NFO@SiO₂@β-CD was used to vary the initial concentration of KF and DCF aqueous solutions from 10 mg/L to 60 mg/L. Likewise, with the fixed NFO@L nanocomposite dosage and pH, the initial concentration of the LFH and CIP was varied as 5, 10, 20, 30 and 40 mg/L. All the parameters other than varied reaction time were maintained at an equilibrium time of 12 hrs in a rotary shaker.

The effect of time was investigated at the optimized conditions; at the outset, the DCF final sample was withdrawn for every 5 min for the first half an hour after which both the KF and DCF final aliquots, were withdrawn for every 30 min. Similarly, the obtained optimized parameters were utilized in studying the effect of reaction time for the removal of LFH and CIP by withdrawing the sample at a regular time interval of 10 min upto 180 min for both pollutants. The effect of temperature on the removal of LFH and CIP was also studied at temperatures such as 303 K, 313 K, 323 K, 333 K and 343 K. After each adsorption experiment, the sample was withdrawn using an external magnet and a nylon syringe filter (0.22μm) and the final analytes were subjected to UV-visible spectrophotometric analysis at the drugs' maximum wavelength. Thus, the obtained absorbance was used in calculating the final concentration by constructing a calibration graph as mentioned in section 3.4. The experimental datum from the parametric study was used in kinetic and isotherm studies. The removal percent and adsorption capacity were calculated using the below equation (3.6) and (3.7). The equilibrium adsorption capacity q_e of the nanocomposite adsorbent was calculated using the below equation 3.6

$$q_e = \frac{(C_o - C_f) \times v}{m} \quad (3.6)$$

The % η removal efficiency was calculated using the equation (3.7)

$$\% \text{ Removal efficiency } \eta = \frac{(C_o - C_f)}{C_f} \times 100 \quad (3.7)$$

C_o and C_f are the initial and final concentrations of drugs (mg/L), respectively; v is the volume of the solution (L), and m is the mass of the adsorbent (g). Using equations 3.6 and 3.7, the equilibrium adsorption capacity (q_e mg/g), adsorption capacity at any time t (q_t , mg/g), and drug removal efficiency (%) were calculated. The kinetics and adsorption isotherms were studied based on the experimental results (Fröhlich et al. 2019).

3.6 Degradation experiment for the removal of CAF and LFH

All experiments were conducted at ambient conditions, with a 10 mg/L concentration of LFH and CAF in a 100 mL volume of an aqueous solution. Initially, PMS alone was varied from 0.1

to 0.6 mM without catalyst, and the molar ratio of PMS at which the maximum removal percent attained was taken for pH studies, in which pH was varied from 3 to 8 with 10 mg of NFO nano-catalyst; then, with the optimized PMS and pH, the amount of NFO nano-catalyst was varied from 10 mg to 90 mg. By varying the initial concentrations of each of the pollutants from 10 to 40 mg/L, the optimal NFO dosage that can degrade specific concentration of both pollutants at maximum extent was found. The equilibrated values were kept constant to determine the required dosage of PMS for the optimized NFO nano-catalyst to degrade these pollutants. Following that, the time required to degrade these pollutants were tested by withdrawing the sample at regular intervals of 10 min. The final aliquots were filtered, and the filtered samples were tested for UV-visible spectrophotometric analysis. Equation 3.8 was used to calculate the degradation percentage.

$$\eta = \frac{C_o - C_f}{C_o} \times 100 \quad (3.8)$$

where η is the degradation efficiency of LFH and CAF. C_o is the initial concentration of the solution in mg/L and C_f is the final concentration of the solution (mg/L).

3.6.1 Quantification of β -CD in the final analyte of KF and DCF using spectrophotometric titration

The mass of β -CD in the range of 10, 20, 30, 40, 50, 60, 70 and 80 mg was varied in a 0.02 mg/mL of phenolphthalein solution as a calibrant prepared in a carbonate buffer at pH 10.5. The aforementioned calibrant solution with β -CD was used in plotting the standard calibration graph from which the unknown concentration of β -CD in the NFO nanocomposite and the presence of β -CD in the final analyte of both pollutants were determined. A 20 mg of NFO nanocomposite to 20 mL of phenolphthalein solution was stirred for 2 hrs, after which the solution with the nanocomposite was filtered and subjected to UV-vis spectrophotometric analysis. The content of β -CD in the nanosorbent was calculated from

$$C_{\beta-CD} = \frac{V_{phenolphthalein} \times C_s}{m_{sorbent} \times M_{\beta-CD}} \quad (3.9)$$

Where $C_{\beta-CD}$ is the content of β -CD in nanocomposite sample (mmol/g), $V_{phenolphthalein}$ is the volume of phenolphthalein solution (mL), C_s is the concentration of β -CD calculated from a standard curve (mg/mL), $m_{sorbent}$ is the mass of nanocomposite (g), $M_{\beta-CD}$ is the molecular weight of the β -CD (g/mol).

3.7 Adsorption kinetics

The reaction time between adsorbent and drug molecules is vital. It enables us to comprehend more aspects such as adsorbent traits, adsorption mechanisms, the layout of the adsorption process, solid-liquid reaction rate, and steady-state time (Xiao et al. 2018). The kinetics of adsorption also helps in determining the rate law in designing a proper adsorption system. Moreover, it also outlines the adsorption rate of pollutants at the respective time at the adsorbent-adsorbate interface. From this perspective, both pseudo first order and pseudo second order kinetic models (Ho and McKay 1999) were investigated to evaluate the adsorption kinetics and the percent removal involved in the removal of pharmaceutical pollutants.

The pseudo first order kinetic model is expressed in equations (3.10) and (3.11) as follows

$$\frac{dq}{dt} = k_2(q_{e,cal} - q_t)^2 \quad (3.10)$$

$$\ln(q_e - q_t) = \ln q_e - k_1 t \quad (3.11)$$

q_e and q_t is the adsorption capacity of nanocomposite on the removal of KF and DCF at equilibrium and at time t and is expressed in (mg/L), t is the time (min), k_1 (1/ min) is the first order rate constant.

The pseudo second order kinetic model is given in equation (3.12) as follows

$$\frac{t}{q_t} = \frac{1}{k_2 q_{e,cal}^2} + \frac{t}{q_{e,cal}} \quad (3.12)$$

where k_2 (mg/ g·min) is the second order rate constant, q_t (mg/g) is the adsorption capacity at time t (min), and q_e (mg/g) is the adsorption capacity at equilibrium condition.

The pseudo first order kinetics assumes that the adsorption is limited by the rate of diffusion to the adsorbent surface. It also assumes a linear relationship between amount adsorbed at time t and time, leading to the logarithmic relationship when integrated and the model is generally valid at low concentrations.

The pseudo second order kinetic model assumes that the adsorption sites are equivalent and that the interactions between adsorbed molecules are negligible. The adsorption process is controlled by chemical reactions between the nanocomposite and the pollutant rather than by diffusion.

3.8 Adsorption isotherm

Adsorption isotherm curves are worth delineating the occurrence that governs the withhold or free-up of a substance from the aqueous phase to the adsorbent at a particular pH and temperature. Langmuir and Freundlich's adsorption models were exercised to determine the

adsorption capacity of nanosorbent to analyze the solid-liquid interactions. It is also momentous to create a more relevant interrelation of equilibrium datum to optimize the conditions for laying an outline design of an adsorption system (Wong et al. 2004).

3.8.1 Langmuir isotherm

Langmuir's model surmises the monomolecular layer in the adsorbent such that all the active sites have a limited measure of identical and energetic counterpart active sites. They also have a similar rapport for the drug molecule with invariable sorption activation energy. The linearized Langmuir isotherm was represented using equation (3.13a) (Langmuir 1916)

$$\frac{C_e}{q_e} = \frac{1}{K_L q_{\max}} + \frac{C_e}{q_{\max}} \quad (3.13a)$$

The linear Langmuir isotherm equation is given by equation (3.13b)

$$\frac{1}{q_e} = \frac{1}{K_L q_{\max} C_e} + \frac{1}{q_{\max}} \quad (3.13b)$$

One of the significant aspects of the Langmuir isotherms to forecast the viability of adsorption can be stated in the context of a constant called separation factor, R_L , and was calculated using equation (3.14)

$$R_L = \frac{1}{1 + K_L \cdot C_0} \quad (3.14)$$

where q_e (mg/g) is the amount of adsorbates adsorbed at the equilibrium concentration, C_e (mg/L) is the equilibrium concentration of adsorbate, q_{\max} (mg/g) represents the maximum single-layered adsorption capacity, and K_L (L/mg) is the Langmuir constant related to the adsorption energy and the closeness of the coupling sites (Appel 1973). If the values of the separation factor are in the range of ($0 < R_L < 1$), then the adsorption is viable, whereas if $R_L > 1$, then the adsorption is unachievable (Kebede et al., 2019).

3.8.2 Freundlich isotherm

The Freundlich model assigns that the adsorbent surface has various active sites with varied activation energy in the manifold layers. This varied activation energy works, a role in the boundary surface coverage area and the active sites. The Freundlich adsorption isotherm is interpreted using equations (3.15) and (3.16)

$$q_e = K_F C_e^{\frac{1}{n}} \quad (3.15)$$

$$\log q_e = \log K_F + \frac{1}{n} \log C_e \quad (3.16)$$

where K_F (L/mg) is the Freundlich constant and n is the heterogeneity factor. q_e corresponds to the equilibrium adsorption capacity (Foo and Hameed 2010).

3.8.3 Temkin and Dubinin - Radushkevich isotherms

Temkin isotherm was used in studying the interactions between the NFO@L nanocomposite and the fluoroquinolones illustrating that the quantity of heat of adsorption of LFH and CIP molecules decreases linearly rather than logarithmic with the surface coverage of NFO@L. Dubinin -Radushkevich isotherm accounts for the potential theory of adsorption and also includes assumptions such as adsorption occurs through micropore volume filling rather than multi-layer adsorption on the surface, it also includes the adsorption on the porous structure of the nanocomposite (Araújo et al. 2018; Hu and Zhang 2019).

3.8.3.1 Temkin isotherm

The Temkin isotherm is represented in the following equations (3.17), (3.18) and (3.19)

$$q_e = \frac{RT}{b_T} (\ln A_T \cdot C_e) \quad (3.17)$$

$$q_e = \frac{RT}{b_T} \ln A_T + \frac{RT}{b_T} \ln C_e \quad (3.18)$$

$$\text{Slope, } B = \frac{RT}{b_T} \quad \text{Intercept, } B \ln A_T$$

$$q_e = B \ln A_T + B \ln C_e \quad (3.19)$$

q_e is the equilibrium adsorption capacity (mg/g), R is the gas constant (8.314 J/mol.K), T is the temperature in Kelvin (K), B is the heat of adsorption (constant) J/mol, A_T equilibrium binding constant (L/g), b_T Temkin isotherm constant.

3.8.3.2 Dubinin -Radushkevich isotherm

The Dubinin - Radushkevich isotherm is represented in equations (3.20), (3.21) and (3.22)

$$q_e = q_{\max} \exp(-\beta_T \varepsilon^2) \quad (3.20)$$

$$\ln q_e = \ln q_{\max} (-\beta_T \varepsilon^2) \quad (3.21)$$

$$\varepsilon = RT \ln \left(1 + \frac{1}{C_e}\right) \quad (3.22)$$

q_e is the adsorption capacity (mg/g), q_{\max} is the maximum adsorption capacity (mg/g), β_T adsorption energy constant (mol^2/kJ^2) is also used in calculating the mean free energy $E = 1/\sqrt{2\beta_T}$, ε is the adsorption potential (kJ/mol), R is the universal gas constant (8.314 J/mol.K) and C_e is the equilibrium concentration (mg/L).

3.9 Regeneration and recycle studies of NFO nanocomposites

The capability of adsorbent materials after the regeneration and recycling process was studied. The choice of regeneration technique for the desorption of pharmaceutical drugs from the nanocomposite depends on the polarity and eco-friendly usage (non-toxicity) of the regenerant. Rapid chemical regeneration methods are more appealing at the field level. The desorption studies of the NFO nanocomposites for each of the pollutants were experimented on choosing the suitable solvent at first. The used NFO nanoparticles and composite were washed with different regenerants such as distilled water, methanol and ethanol, 0.1 M HCl, and 0.1 M NaOH sequentially and dried in a hot air oven overnight. After that, the dried NFO and its nanocomposite were experimented with the optimized conditions and checked for the removal percent for each of the regenerants using a UV-Vis spectrophotometer. The maximal removal efficiency obtained from the regenerant washing of NFO nanoparticles and nanocomposite was further used in the recyclable studies. At last, the desorbed pollutant could be eluted, dried and incinerated.

CHAPTER 4

RESULTS AND DISCUSSIONS

This chapter comprises the characterization, removal and degradation studies of NFO and its composite over certain emerging hazardous pollutants falling under pharmaceuticals and personal care products' such as Ketoprofen (KF), diclofenac (DCF), lomefloxacin hydrochloride (LFH), ciprofloxacin (CIP) and caffeine (CAF) have been presented and discussed in the following sections.

4.1 Characterization of NFO nanoparticles

The characterization results that constitute analytical techniques such as FTIR, XRD, FESEM/EDX, VSM, TGA/DTG, BET, electrokinetic potential and particle size analysis of the NFO nanoparticles and nanocomposite have been presented to prove its adsorbent characteristics. The prepared nanocomposite has been subjected to batch-wise adsorption in the following combinations (NFO@SiO₂@β-CD (adsorbent) to KF and DCF (pollutants)), (NFO@L (adsorbent) to CIP and LFH (pollutants)) and (NFO/PMS system (catalyst) to CAF and LFH (pollutants)) upon which the effect on various affecting parameters results have been presented and detailly discussed in the following section.

4.1.1 Fourier transform infrared spectroscopy (FTIR) of NFO nanoparticles:

FTIR was performed to identify the functional groups and their vibrational characteristics that are present in the NFO nanoparticles. FTIR spectrum of NFO nanoparticles in Fig. 4.1 illustrates the presence of Ni-O at 478 cm⁻¹ and Fe-O at 534 cm⁻¹ in the tetrahedral and octahedral modes which confirms the formation of NFO nanoparticles. The bending vibrations at 1636.20 cm⁻¹ correspond to the C-O-C (Jacob et al. 2011b; Sagadevan et al. 2018b) this might be due to the presence of oleic acid, the surfactant that was used in the synthesis. The bands with peaks observed at 1038 cm⁻¹ could be assigned to O-H bending vibration. 2151.69 cm⁻¹ and 2081.30 cm⁻¹ were due to the bending vibrations caused by the free or adsorbed water molecules (H-O-H). The symmetric vibration of O-H groups was observed at 3416.68 cm⁻¹.

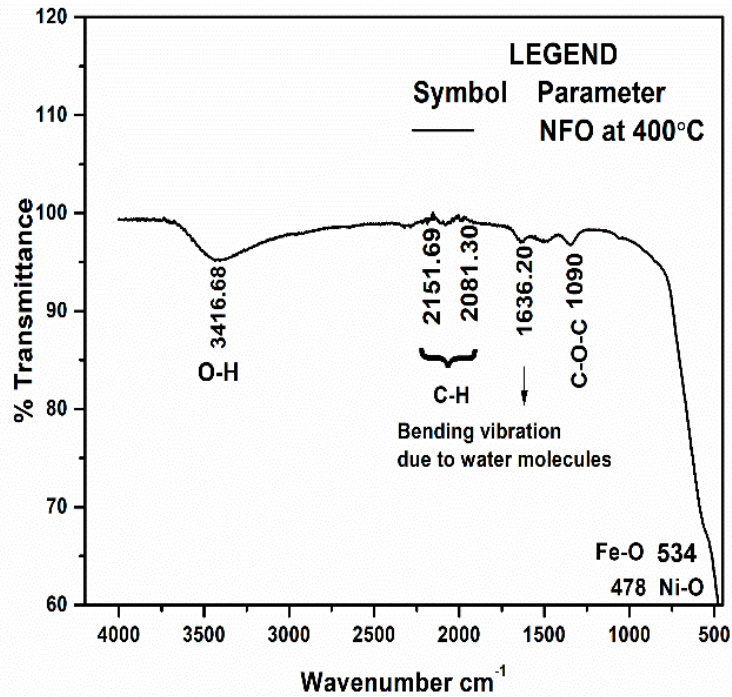


Fig. 4.1 FTIR spectrum of NFO nanoparticles

4.1.2 Field Emission -Scanning electron microscope (FE-SEM)/ Energy Dispersive X-ray Diffraction (EDX) of NFO nanoparticles

The surface morphology and the stoichiometric proportion of elements that constitute the NFO particles were analysed via the imaging of a Field Emission - Scanning Electron Microscope and Energy Dispersive X-ray Diffraction analysis.

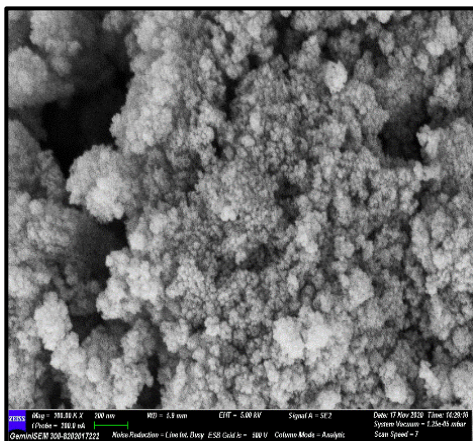


Fig. 4.2 (a) FE-SEM image of NFO nanoparticles

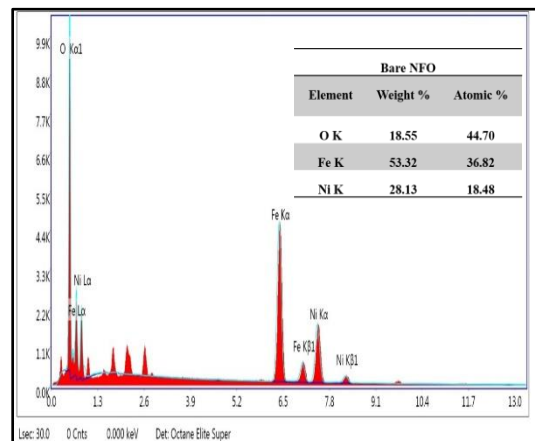


Fig. 4.2 (b) Elemental analysis of NFO nanoparticles

A highly agglomerated NFO nanoparticles imaged at a magnification of 200 nm were presented in Fig. 4.2 (a). This agglomerated form of NFO nanoparticles might be owing to the high surface energies and so the NFO nanoparticles have grown to a micron size particle. The elemental analysis of the NFO nanoparticles is presented in Fig. 4.2 (b) and the composition of elements that are present in the NFO is presented in terms of atomic weight % and weight %. The elemental composition depicts that the NFO molar ratio matches the synthesized stoichiometric ratio with a few extra peaks in the NFO EDX image reflecting the gold sputtering on the NFO nanoparticles.

4.1.3 X-ray Diffraction analysis (XRD) of NFO nanoparticles

The nature of the NFO nanoparticles was estimated using X-Ray Diffraction analysis in which the crystalline nature of NFO was revealed in Fig. 4.3 and the mean crystallite size of the NFO nanoparticles was computed using Scherrer's formula as seen in equation (4.1)

$$D = \frac{K\lambda}{\beta_T \cos\theta} \quad (4.1)$$

The lattice parameter was calculated using equation (4.2)

$$d_{hkl} = \frac{a}{\sqrt{h^2+k^2+l^2}} \quad (4.2)$$

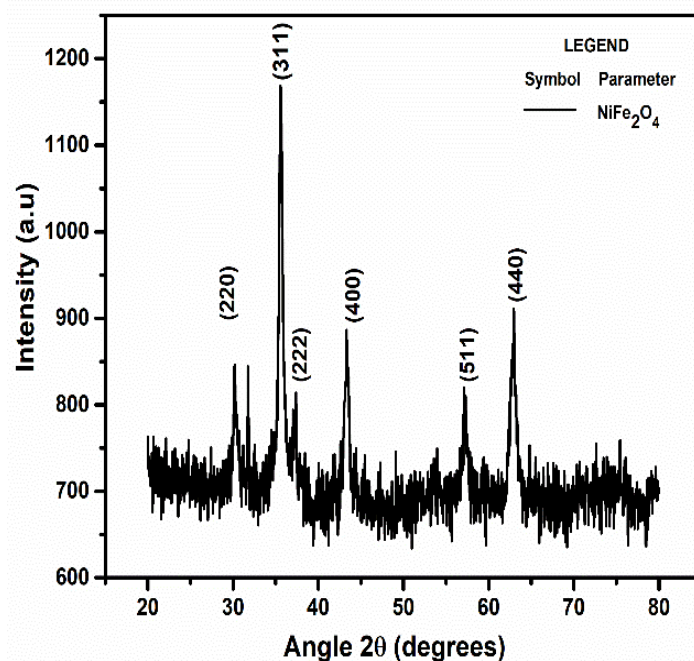


Fig. 4.3 XRD of NFO nanoparticles

where D is the mean crystallite size, K_{XRD} is known as the Scherer's constant ($K= 0.94$) λ is the Cu-K α radiation, β_T is the full width at half maximum (FWHM) in radians, hkl is the miller indices, d_{hkl} is the interplanar spacing, a is the lattice parameter (nm) and θ is the corresponding Bragg diffraction angle in radians is shown in table 4.1. NFO is crystalline with the maximal peak orientation (311) at 35.55° . The hkl of NFO such as (1 1 1), (2 2 0), (2 2 2), (3 1 1), (4 0 0), (4 2 2) and (5 1 1) were compared with standard data (JCPDS PDF card No. 074-2081)(Jacob et al. 2011b; Khoso et al. 2021; Shanmugavel et al. 2014).

Table 4.1 XRD values of NFO nanoparticles

S. No	2 θ (degrees)	d-spacing (nm)	Lattice parameter (nm)
NFO			
1	30.193	0.295	0.836
2	35.556	0.252	0.836
3	37.343	0.240	0.833
4	43.296	0.208	0.834
5	57.389	0.160	0.833
6	62.560	0.148	0.838

4.1.4 Brunauer-Emmett-Teller (BET)/Barrett-Joyner Halenda (BJH) model analysis of NFO nanoparticles:

The adsorption isotherm type, specific surface area, pore volume, and pore diameter of the NFO nanoparticles were estimated from the BET multiple-point method and BJH analysis. The adsorption-desorption hysteresis loop in Fig. 4.4 illustrates the Type IV isotherm and the micropores nature of NFO nanoparticles. The linear graph at very low relative pressure indicates a high micropore material with a uniform pore size (Thommes et al. 2015). The surface-to-volume ratio of the NFO nanoparticles is $112.02 \text{ m}^2/\text{g}$, the total pore volume is 0.148 cc/g , and the pore diameter is 1.891 nm .

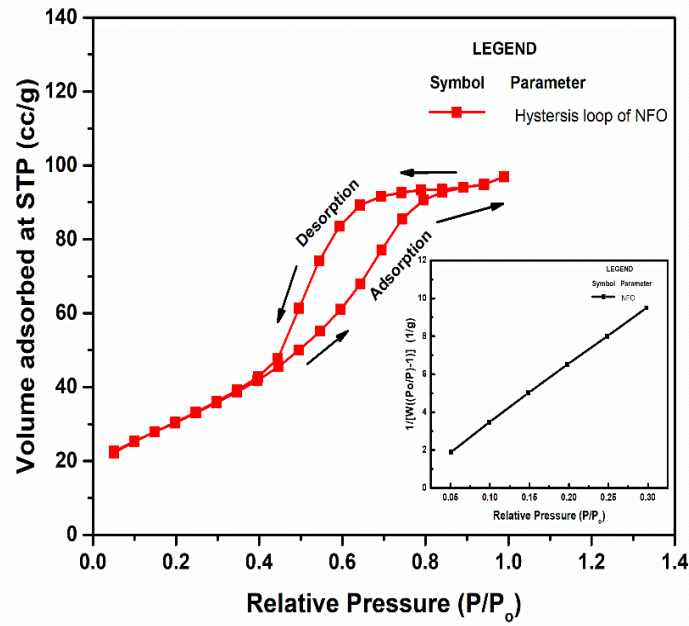


Fig. 4.4 Adsorption-Desorption Hysteresis loop and linear graph of relative pressure (P/P_0) versus Volume occupied at STP (cc/g) of NFO nanoparticles from BET Test

4.1.5 Thermogravimetric analysis (TGA) of NFO nanoparticles

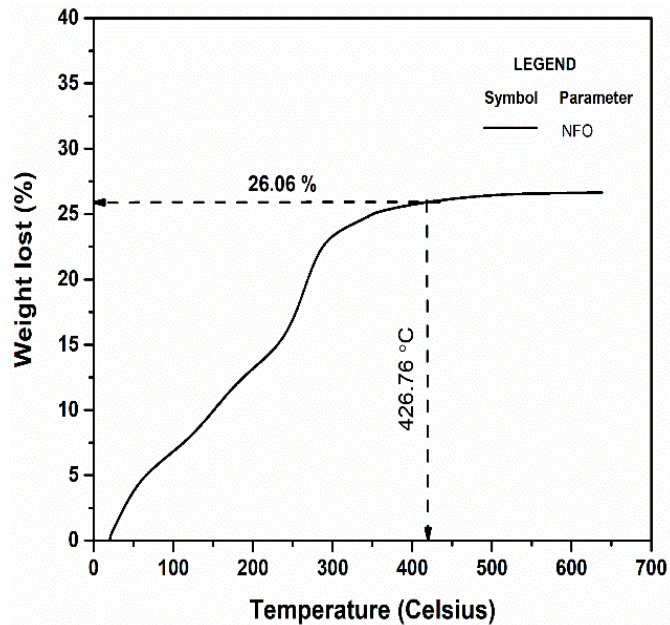


Fig. 4.5 TGA of the uncalcined NFO nanoparticles

The thermal stability of the NFO nanoparticles was studied at increasing temperatures using TGA analysis as shown in Fig. 4.5. A 17 % weight physically adsorbed moisture loss and low

boiling point volatile organic compounds gets evaporated at the initial rise in temperature with in 250°C. Above that, a 10 % mass loss of organic compounds such as carbon chains was observed between 250 °C and 350 °C. Further rise in temperature may lead to material decomposition and depolymerization. There is no notable weight loss was observed further increasing the temperature and overall, the sample lost 27% of its weight.

4.1.6 Particle size distribution and electrokinetic potential of NFO nanoparticles

The particle size distribution histogram of the NFO nanoparticles is seen in Fig. 4.6 (a) which was obtained using the FESEM image in ImageJ software, and the average particle diameter was estimated to be 43.87 nm. The surface charge of the NFO nanoparticles was studied using the electrokinetic potential analysis, performed at pH levels from 3 to 10. In all the pH ranges the negative surface charge of the NFO nanoparticles was found to be dominant with the maximum zeta potential of -26 mV at pH 11, as shown in Fig. 4.6 (b).

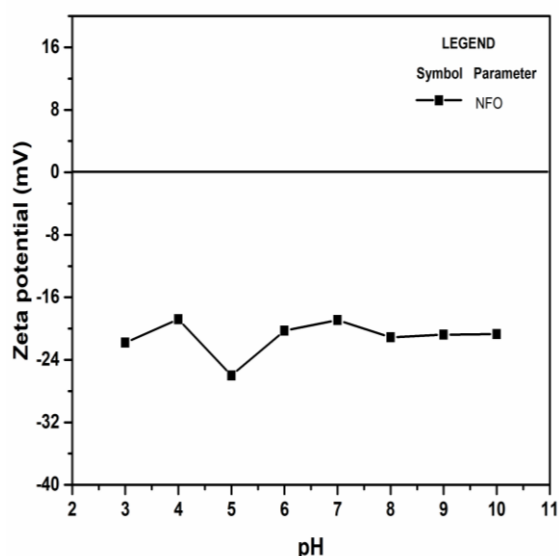
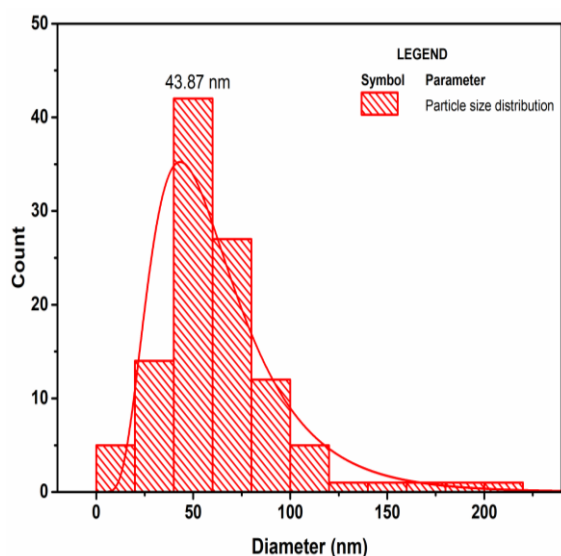


Fig. 4.6 (a) Particle size distribution of NFO nanoparticles using FESEM

Fig. 4.6 (b) Zeta potential of NFO nanoparticles

4.1.7. Vibrating sample magnetometer (VSM) analysis of NFO nanoparticle:

The magnetic traits of the NFO nanoparticles were analysed using VSM analysis. The superparamagnetic nature of the NFO nanoparticles could be seen in Fig. 4.7. The saturation magnetization (M_s) and coercivity (H_c) of the NFO nanoparticles were found to be 99.07×10^{-3}

emu and 0.495×10^{-3} emu with the retentivity value of 13.21×10^{-6} emu, indicating that the NFO nanoparticle is of soft magnet and hence magnetization and demagnetization occurs freely.

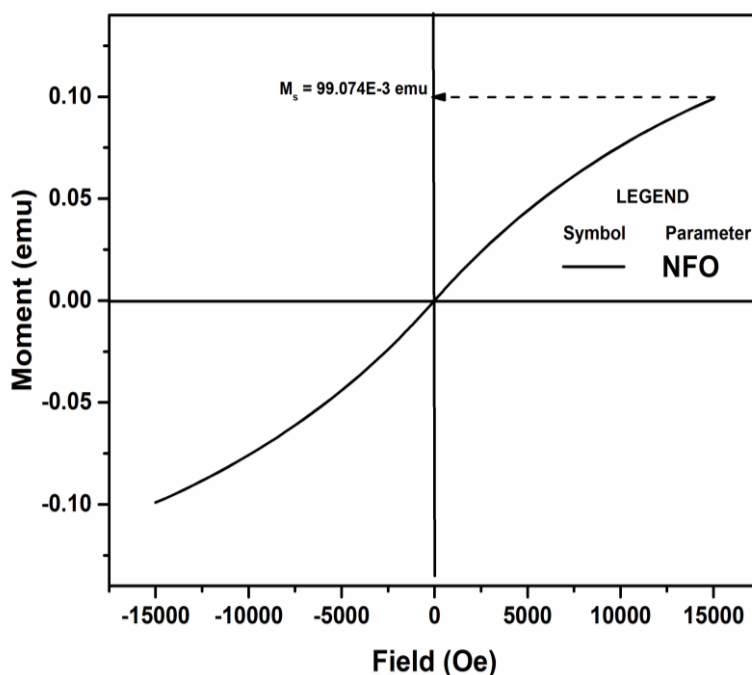


Fig. 4.7 VSM analysis of NFO nanoparticles

4.2 Characterization results of NFO@SiO₂

The characterization results of the NFO@SiO₂ nanoparticles were discussed in this section from 4.2.1 to 4.2.4.

4.2.1 Effect of varied mass of NFO in the synthesis of NFO@SiO₂ -FESEM image

The effect of the varied NFO nanoparticle mass in the synthesis of NFO@SiO₂ was studied and the optimum mass of NFO that is required for the functionalization of TEOS was estimated by visualizing the FESEM image. Fig. 4.8 (a), (b) and (c) depicts the FESEM image of a varied mass of NFO nanoparticles (0.1 g, 0.5 g, 1 g) in the synthesis of NFO@SiO₂ at a magnification of 200 nm. 0.1 g NFO nanoparticle reveals a spherical shape of different sizes with different spherical size of NFO whereas 0.5 g NFO nanoparticles depict an almost distinct uniform spherical shape of functionalized NFO@SiO₂. Further, an increase in the mass of NFO to 1 g exposed both a distinct feature of spherical shape and also a cluster of NFO@SiO₂ which implies that the functionalization of NFO nanoparticles was not achieved fully. The mass

variation has distinguished the distinct and agglomeration of nanocomposite hence an optimized mass of 0.5 g was used for further experimental investigation.

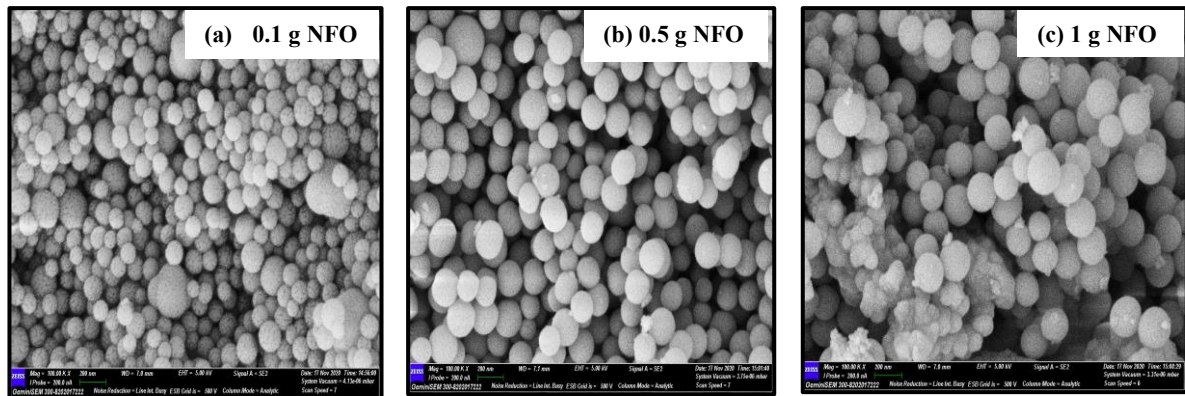


Fig. 4.8 (a), (b) and (c) The FE-SEM image of varied NFO mass in the synthesis of NFO@SiO₂

4.2.2 Effect of varied concentrations of TEOS in the synthesis of NFO@SiO₂ -FESEM image

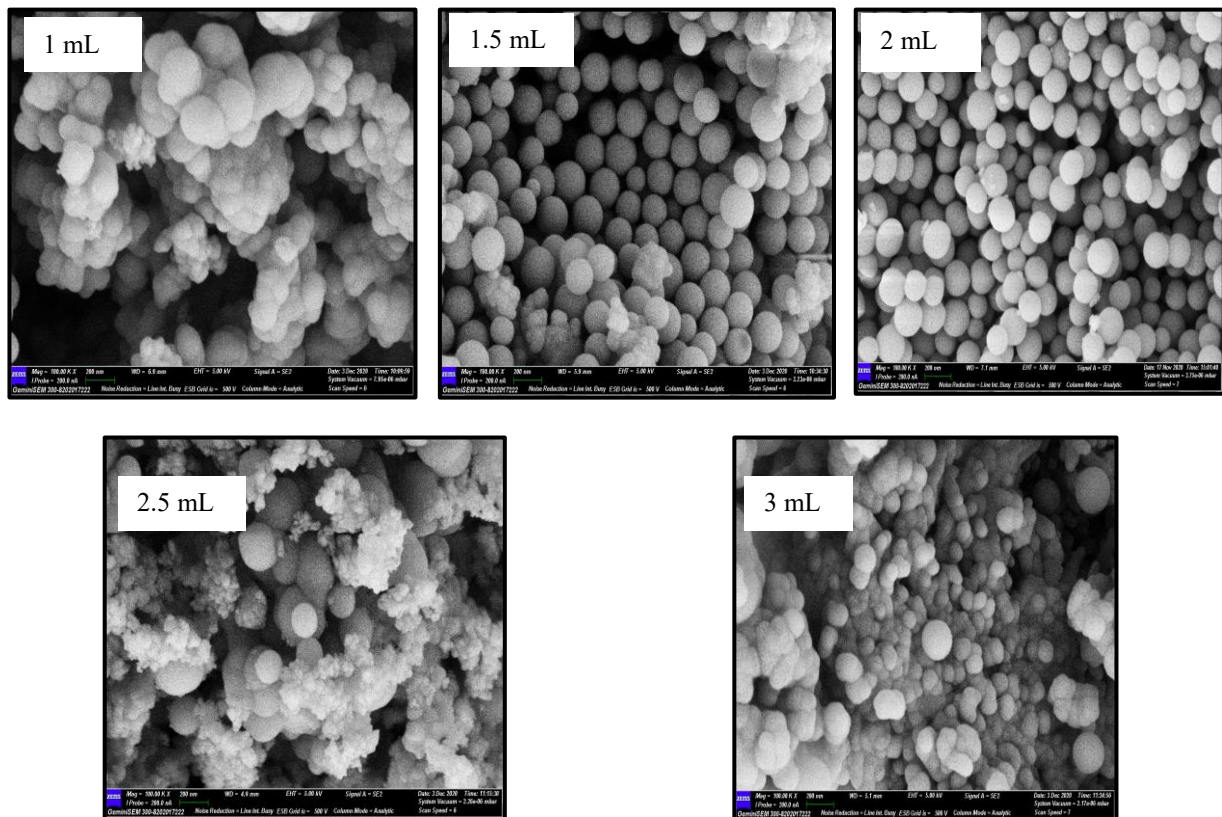


Fig. 4.9 The FE-SEM image of varied TEOS concentration in the synthesis of NFO@SiO₂

The effect of varied concentrations of TEOS in the synthesis of NFO@SiO₂ was studied in this section. The optimized mass of 0.5 g NFO nanoparticles obtained in the synthesis of NFO@SiO₂ was used in varying the TEOS concentration. Fig. 4.9 exposes the FESEM image of varied TEOS concentrations say (1 mL, 1.5 mL, 2 mL, 2.5 mL, 3 mL) in the synthesis of NFO@SiO₂ at a 200 nm magnification. The enhancement in the formation of the distinct spherical shape is seen from the 1 mL to 2 mL TEOS image on NFO, in which the 2 mL TEOS exposed a distinct uniform spherical shape. An increase in the concentration of TEOS exposed an agglomerated form of NFO@SiO₂ revealing that 2 mL of TEOS was sufficient for the synthesis of NFO@SiO₂ nanoparticles.

4.2.3 Brunauer Emmett Teller (BET) specific surface area analysis and Barrett-Joyner Halenda (BJH) model of NFO@SiO₂ nanocomposite

The optimized NFO@SiO₂ was subjected to BET and BJH analysis to study the type of isotherm and to estimate the specific surface area, pore volume and pore size of NFO@SiO₂ from the adsorption-desorption hysteresis loop. Fig. 4.10 illustrates the BET hysteresis loop which belongs to the type III isotherm. The isotherm of this type infers that the NFO@SiO₂ might be non-porous or mesoporous and there would be a weak interaction between the adsorbent - adsorbate.

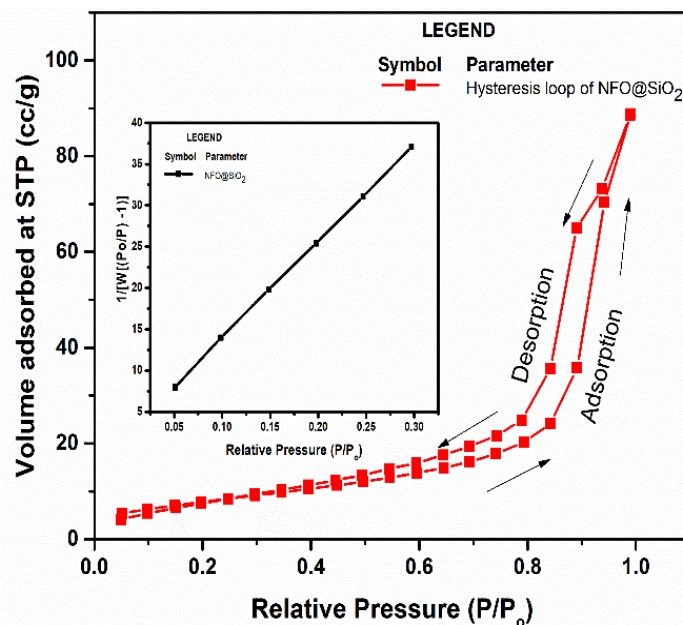


Fig. 4.10 Adsorption-Desorption Hysteresis loop of NFO@SiO₂ using BET/BJH method

The specific surface area of the NFO@SiO₂ is 29.11 m²/g and the total pore volume is 1.37e-01 cc/g at P/P₀ = 0.990 with an average pore radius of 9.44 nm. A reduction in the specific surface was observed after the functionalization of SiO₂.

4.3 Characterization results of NFO@SiO₂@β-CD nanocomposite

The characterization results of NFO@SiO₂@β-CD nanocomposite are presented and it is discussed in sections 4.3.1 to 4.3.5

4.3.1 Effect of β-CD mass variation on the NFO@SiO₂ upon the removal of KF and DCF

The effect of β-CD mass variation on the NFO@SiO₂ for the removal of KF and DCF is depicted in Fig. 4.11. In the case of both pollutants, the 8.92×10⁻⁴ M β-CD showed the maximal removal percent of 30.80 % KF and 33.03 % DCF. Beyond 8.92×10⁻⁴ M β-CD, the excess of β-CD might have caused the formation of clusters that might have resulted in a significant drop in the removal percent of both pollutants. The noticeable pattern in the KF removal at the 5.35×10⁻⁴ M and 8.92×10⁻⁴ M of β-CD and a slightly varied pattern in the removal of DCF could be a result of the improper functionalization and the twisting properties of both the pollutant, a detailed explanation is given in section 4.4.2. Thus 8.92×10⁻⁴ M β-CD functionalized NFO@SiO₂ was used as an optimum adsorbent for the removal of KF and DCF.

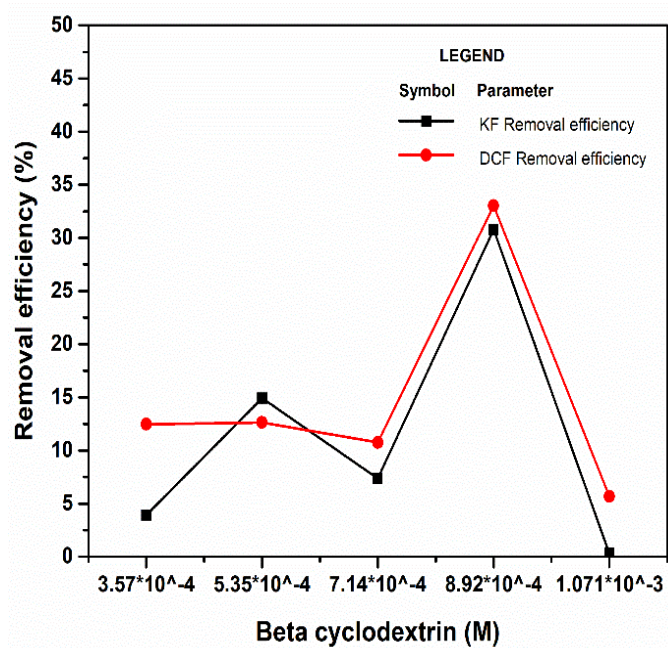


Fig. 4.11 Effect of β-CD mass variation on the NFO@SiO₂ upon the removal of KF and DCF

4.3.2 Effect of varied β -CD mass onto NFO@SiO₂ FE-SEM/EDX of optimized NFO@SiO₂@ β -CD nanocomposite

The effect of the varied β -CD mass onto NFO@SiO₂ was studied using FE-SEM imaging and the elemental composition of the optimized NFO@SiO₂@ β -CD nanocomposite was determined via EDX analysis. The FE-SEM images of varied β -CD mass onto NFO@SiO₂ in Fig. 4.12 (a) to (e) reveal the development of pores and cavities onto the rough surface of all the varied masses is visible. The elemental molar ratios of Ni/Fe/O/C/Si in the NFO@SiO₂@ β -CD nanocomposites are depicted in Fig. 4.12 (f). The atomic weight percentage and weight percentage of each element in the NFO@SiO₂@ β -CD confirm the functionalization of NFO particles with TEOS, GPTMS, and β -CD through morphological and elemental changes. Since XRD and FE-SEM/EDX didn't show any difference in the varied β -CD mass onto NFO@SiO₂.

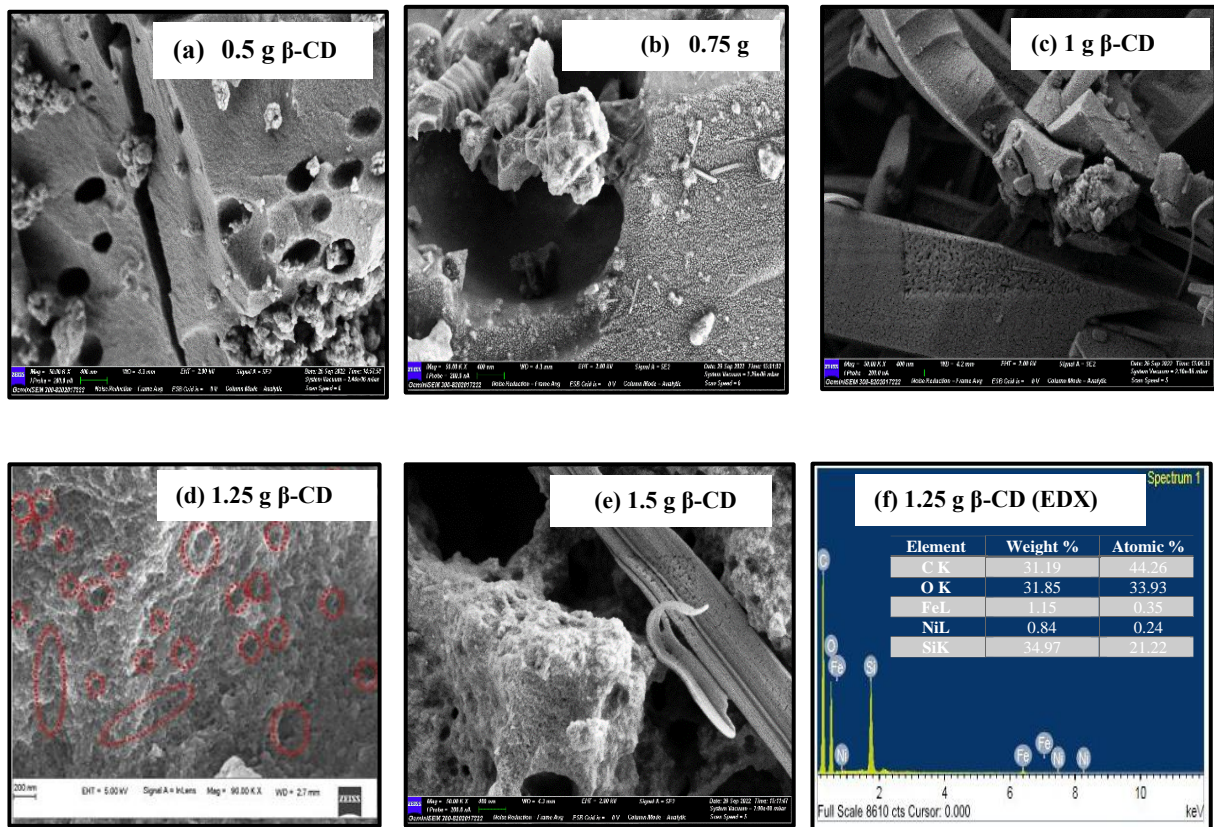


Fig. 4.12 (a) (b) (c) (d) (e) FESEM images of a varied β -CD mass onto NFO@SiO₂ and (f) EDX of the optimized NFO@SiO₂@ β -CD nanocomposite

From section 4.3.1, 1.25 g, β -CD functionalized onto NFO@SiO₂ with almost numerous uniform pores was taken as the optimized amount of β -CD functionalized NFO@SiO₂. Further analysis was concentrated on 1.25 g of β -CD functionalized NFO@SiO₂.

4.3.3 Optimized NFO@SiO₂@ β -CD - FTIR analysis

The functional group attached to the optimized β -CD mass onto NFO@SiO₂ and its vibrational characteristics were analysed using the FTIR spectrum. The characteristic peaks at 1642 cm⁻¹ and 1025 cm⁻¹ correspond to C=O, which is relative to the β -CD molecule. The peak at 2299 cm⁻¹ corresponds to H-O-H bending vibration, and the broad bending in 3384.70 and 3416.68 cm⁻¹ represents the β -CD molecule's O-H bending. The C-H propyl group is present at 2859 cm⁻¹ and 2932 cm⁻¹ and the epoxide group is present at 1203 and 1243 cm⁻¹, which justifies the attachment of GPTMS silane to the NFO@SiO₂. The presence of a peak at 1098 cm⁻¹ in the NFO@SiO₂@ β -CD FTIR trend confirms the fabrication of the Si-O group on the surface of NFO (Pham et al. 2018; Ponchel et al. 2004; Xu et al. 2022). This demonstrates the fact that the β -CD, GPTMS, and SiO₂ molecules remain intact in the NFO as seen in the Fig. 4.13.

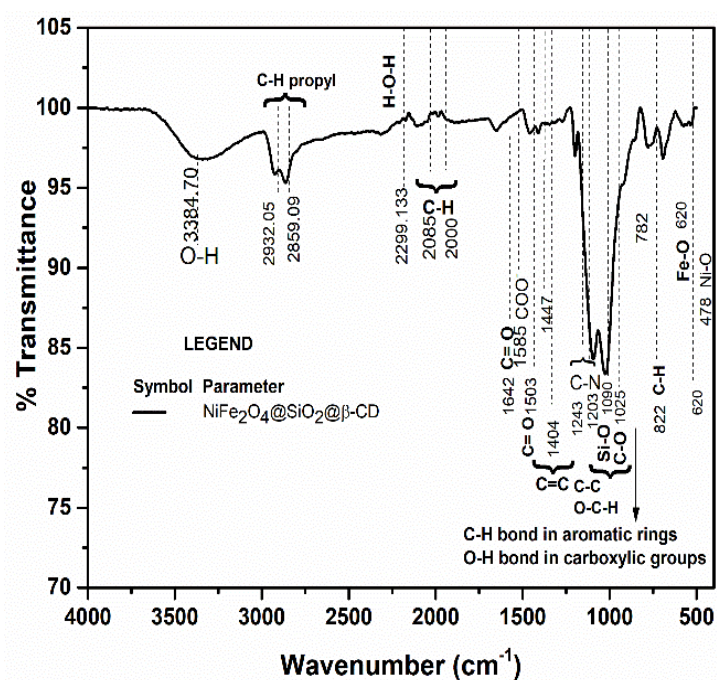


Fig. 4.13 FTIR spectrum of optimized NFO@SiO₂@ β -CD nanocomposite

4.3.4 Particle size distribution/electrokinetic potential and point of zero charge of NFO@SiO₂@β-CD nanocomposite

The optimized NFO@SiO₂@β-CD nanocomposite was subjected to particle size distribution, electrokinetic potential analysis and point of zero charge. The average diameter of NFO@SiO₂@β-CD nanocomposite was estimated to be 109.1 nm as seen in Fig. 4.14 (a). The amplitude of the zeta potential implies the extent of electrostatic repulsion amidst adjoining, likewise charged particles in a dispersion. At pH 12, the functionalized nanoparticles have a maximum zeta potential of -28.1 mV. The high negative zeta potential infers the strong electrostatic repulsion of the NFO nanoparticles which prevent agglomeration and provides high suspension and stability in the liquid medium. The metal oxide NFO nanoparticles forms hydroxyl ions and hence making it negative surface at a broad spectrum range of pH towards basic. As shown in Fig. 4.14 (b), the isoelectric point of NFO@SiO₂@β-CD is pH 3.11, where pH 3.11 is positively charged and pH > pH (3.11) is negatively charged. The reduced zeta potential value of nanocomposite at pH 3 could be attributed to the compression of the electrical double layer caused by the higher salt content of the solution in which the nanocomposite was dispersed.

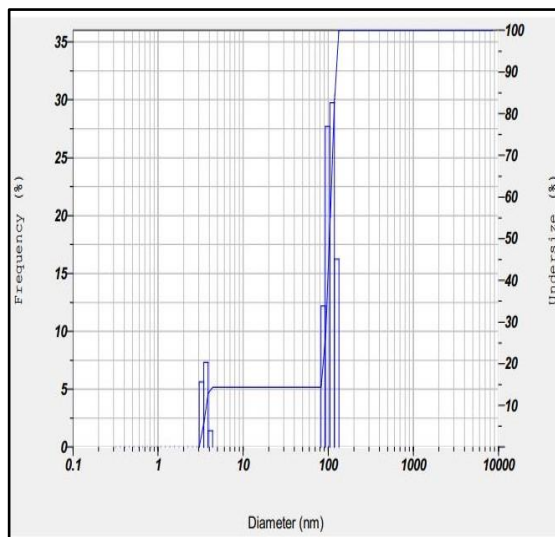


Fig. 4.14 (a) Particle size distribution of NFO@SiO₂@β-CD

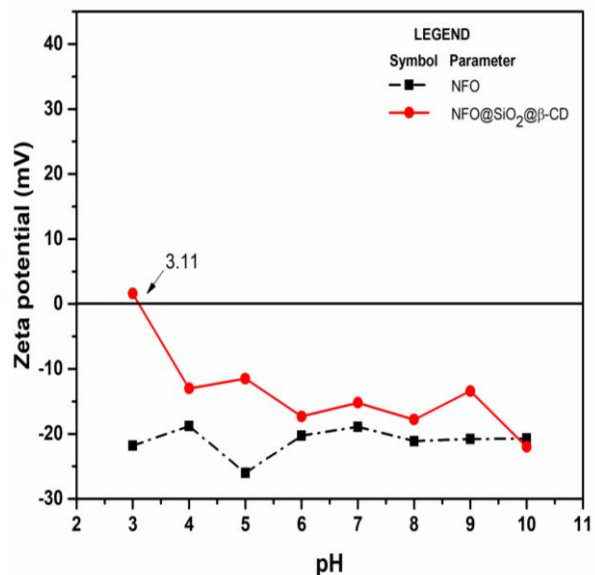


Fig. 4.14 (b) Zeta potential of NFO and NFO@SiO₂@β-CD

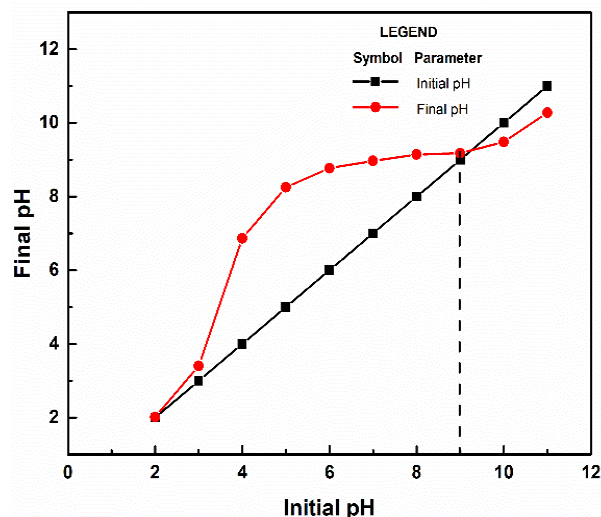


Fig. 4.14 (c) Point of zero charge NFO@SiO₂@β-CD nanocomposite

The nanocomposite tends to aggregate, therefore the sorption process was carried out in a rotary shaker at 100 rpm which would have aided the dispersion of discrete/ individual nanocomposite in suspension and supported the adsorption rate (Song et al., 2010; Winiewska et al., 2015). The point of zero charge of NFO@SiO₂@β-CD is at pH 9 as seen in Fig. 4.14 (c) and is not the same as the isoelectric point, the negative surface of the adsorbent is dominant when the pH of the drug aqueous solution > pH_{pzc} thereby raises the concentration of H⁺ ions upon protonation of functional groups and it is vice versa for pH of the drug aqueous solution < pH_{pzc}.

4.3.5 Comparative study of XRD pattern of β-CD and functionalized NFO@SiO₂ and NFO@SiO₂@β-CD nanocomposite

The optimized nature of NFO, HPBCD (hydroxypropyl beta-cyclodextrin), NFO@SiO₂ and NFO@SiO₂@β-CD were compared and the XRD pattern is illustrated in Fig. 4.15; in which the NFO, *hkl* (1 1 1), (2 2 0), (2 2 2), (3 1 1), (4 0 0), (4 2 2), and (5 1 1) were compared to standard data (JCPDS PDF card No. 074-2081), the similar orientation confirms the formation of NFO nanoparticles (Shanmugavel et al. 2014). Thus, the intensity difference between NFO and NFO@SiO₂ confirms the attachment of TEOS to NFO.

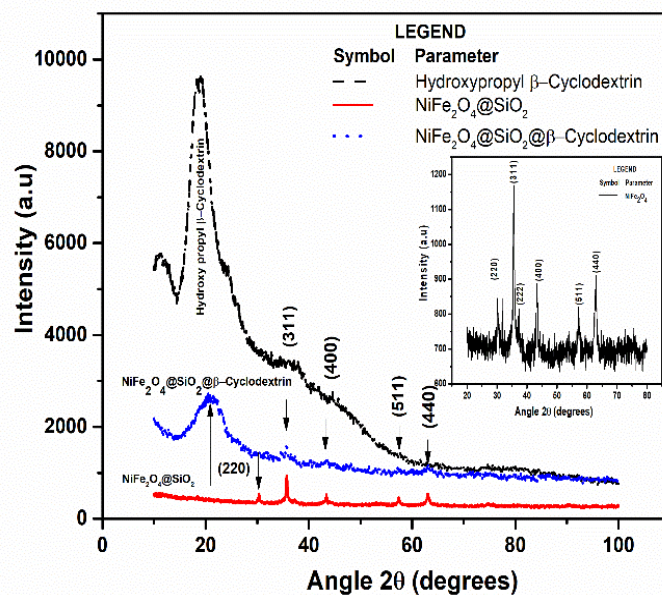


Fig. 4.15 X-ray Diffraction analysis of NFO, NFO@SiO₂, β-CD, NFO@SiO₂@β-CD nanocomposite

Table 4.2 XRD 2 theta values, d-spacing, and lattice parameter values

S. No	2θ (degrees)	d-spacing (nm)	Lattice parameter (nm)	2θ (degrees)	d-spacing (nm)	Lattice parameter (nm)
NFO@ SiO₂				NFO@SiO₂@β-CD		
1	30.371	0.293	0.831	20.665	-	-
2	35.513	0.252	0.837	30.471	0.420	0.828
3	43.237	0.208	0.835	35.839	0.293	0.830
4	57.282	0.160	0.834	43.413	0.250	0.832
5	63.150	0.147	0.831	57.482	0.208	0.835

The amorphous peak of β-cyclodextrin causes a bulge peak at an angle of 2θ, 20°, which could be seen from the difference in peaks in the hydroxypropyl beta-cyclodextrin, NFO@SiO₂ and NFO@SiO₂@β-CD confirms the functionalization of β-cyclodextrin. The lattice parameter and d-spacing are displayed in Table 4.2. The average crystallite size of the NFO@SiO₂@β-CD, NFO@SiO₂, and NFO was found to be 3.501 nm, 2.025 nm, and 1.712 nm, respectively.

4.3.6 Brunauer Emmett Teller (BET) specific surface area analysis and Barrett-Joyner Halenda (BJH) model of NFO@SiO₂@β-CD

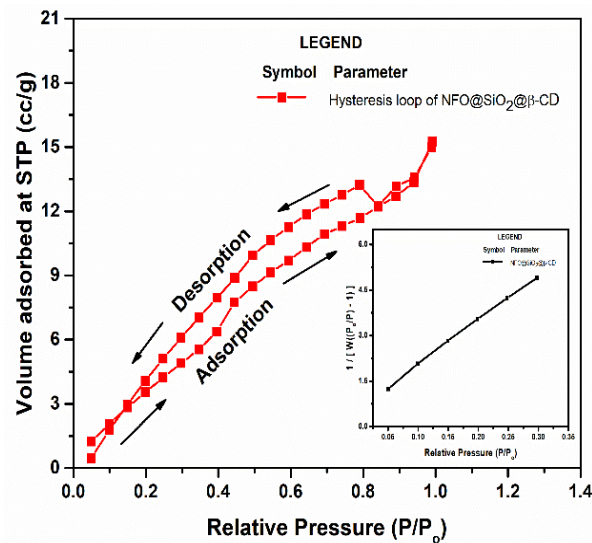


Fig. 4.16 Adsorption-Desorption Hysteresis loop and linear graph of relative pressure (P/P_0) versus volume occupied at STP (cc/g) of NFO@SiO₂@β-CD nanoparticles from BET Test

The specific surface, pore volume and pore size of the NFO@SiO₂@β-CD were estimated using BET/BJH analysis. Fig. 4.16 depicts that the BET hysteresis loop is of reversible type V adsorption isotherm and is mesoporous in nature. This V type isotherm raises when the effects of the intermolecular attraction are large and when the adsorption takes place in pores. There is a further reduction in the specific surface area is 20.78 m²/g in comparison with NFO, NFO@SiO₂ and the total pore volume is 2.360e-02 cc/g at $P/P_0 = 0.99$ with an average pore radius of 2.271 nm. The lateral interactions of adsorbed molecules are stronger than the adsorbent-adsorbate interactions. It also indicates an unrestricted multilayer formation (Thommes et al. 2015)

4.3.7 Thermogravimetric analysis (TGA) of NFO@SiO₂@β-CD nanocomposite

The thermal stability of the NFO@SiO₂@β-CD was investigated at increasing temperatures and compared with the NFO thermal stability as shown in Fig. 4.17. Initially, a 10.23 % water loss was observed at temperatures less than 250 °C. A temperature increase from 250 °C to 500 °C resulted in a significant weight reduction of 56.18 % due to the disintegration of covalent bonds, which resulted in a surge of decomposition temperature in the NFO@SiO₂@β-CD.

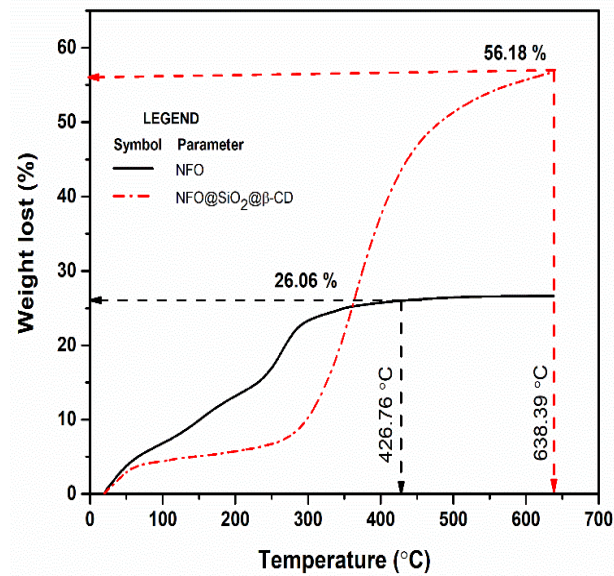


Fig. 4.17 TGA analysis of NFO@SiO₂@β-CD

Above 500 °C to 638 °C, a constant weight loss of approximately 5.705 % of the NFO@SiO₂@β-CD occurred relative to the accretive breakdown of the organic fractions (Yuan et al. 2015). Thus, the NFO@SiO₂@β-CD nanocomposite shows a more stable nature up to a lower temperature of 300 °C. The functionalized nanocomposite has high thermal stability is because of the both inorganic SiO₂ and organic groups grafted over the metal oxide that prevents sintering and oxidation at high temperatures. The higher decomposition temperatures is due to the stabilization effects of the functional groups which can prevent from thermal breakdown.

4.3.8 VSM analysis of NFO@SiO₂@β-CD nanocomposite

A comparison of magnetic properties of bare NFO and NFO@SiO₂@β-CD nanocomposite was analyzed using vibrating sample analysis and an observable reduction in the magnetic behaviour of NFO@SiO₂@β-CD could be visibly seen in Fig. 4.18. In addition, a superparamagnetic behaviour of NFO and NFO@SiO₂@β-CD could be observed at room temperature. The saturation magnetization (M_s) and coercivity (H_c) of NFO@SiO₂@β-CD nanocomposites were found to be 6.537×10^{-3} and -17.371 emu, respectively, with a retentivity value of 5.240×10^{-6} emu. The reported results revealed a shift in the graph, revealing its

decreased amplitude towards magnetic nature. However, there was observed ease of magnetization and demagnetization indicating its soft magnet properties.

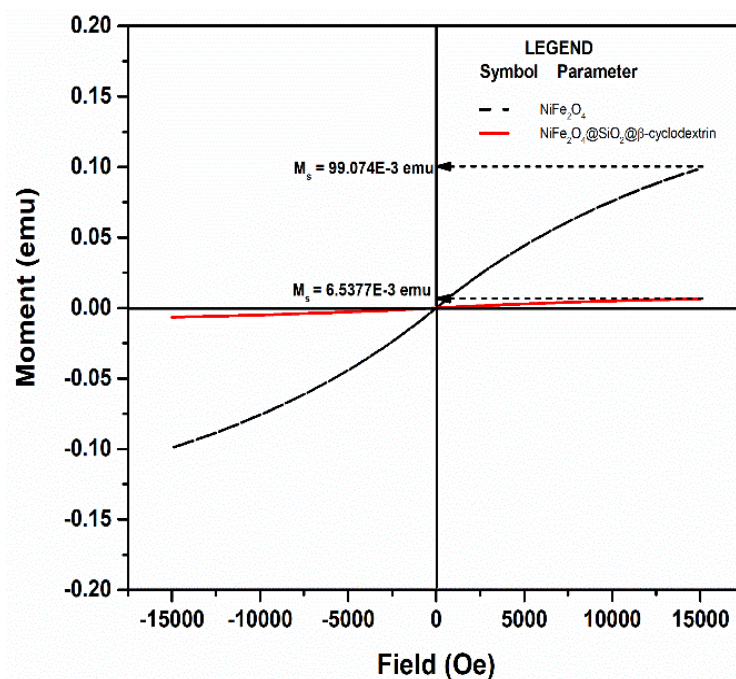


Fig. 4.18 VSM analysis of NFO and NFO@SiO₂@β-CD

4.4 Optimization of parameters for the removal of KF and DCF using NFO@SiO₂@β-CD nanocomposite

The effect of various operating parameters such as pH, nanocomposite dosage, initial concentration of the pollutants KF and DCF and the reaction time required for the maximum removal of KF and DCF aqueous solutions was experimented with and discussed in this section from 4.4.1 to 4.4.4.

4.4.1 Effect of KF and DCF aqueous solutions' pH

The effect of pH on the removal of KF and DCF using NFO@SiO₂@β-CD has been studied to identify whether varying the KF and DCF aqueous solution's pH has any significant role in the removal of KF and DCF.

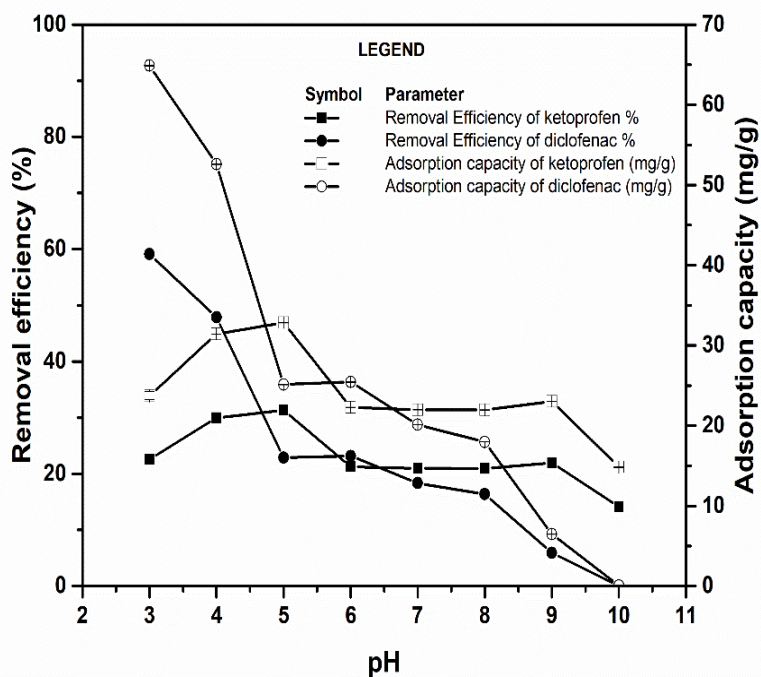


Fig. 4.19 Effect of pH on the adsorption capacity and removal efficiency of KF and DCF

Fig. 4.19 illustrates the maximal removal of 31.32 % of KF and 59.12 % of DCF at pH 5 and 3 with the adsorption capacity of 32.85 and 64.89 mg/g, respectively. The values of zeta potential at pH 3 is 1.6 mV and at pH 5 is -11.5 mV, which are within +30 and -30 mV, respectively, indicating that the nanocomposite exhibits incipient stability. Both the chosen pollutants are acidic such that the pKa value of KF and DCF is 4.45 and 4.15 respectively which, exist in an ionic state when $\text{pH} < \text{pKa}$ value; and it is in anionic form when $\text{pH} > \text{pKa}$ value (Alothman and Apblett 2009). Below this pKa value, DCF is presented as neutral DCFH; this protonated form of DCF gets attached to the OH group of $\text{NFO@SiO}_2@\beta\text{-CD}$, which enhances the removal process. From the briefed zeta potential results, the pH of DCF is slightly less than $\text{pH}_{(\text{IEP})}$ whence the protonated form of DCFH gets attached to the OH^- ions in the adsorbent surface; subsequently, the removal efficiency and the adsorption capacity have raised (Baccar et al. 2012). This phenomenon has brought an electrostatic attraction between the adsorbent surface and the analytes; whereas, in the case of KF, whose pH is close to pKa and also pH is slightly greater than the $\text{pH}_{(\text{IEP})}$. This neutrality in the KF drug and the negative surface of the adsorbent resulted in electrostatic repulsion. Hence, the hydrogen bonding and dispersive $\pi\text{-}\pi$ interactions would have been the mechanism involved between the carboxyl group in the aromatic ring of KF and the hydroxyl group in the $\beta\text{-CD}$ of $\text{NFO@SiO}_2@\beta\text{-CD}$ (Rocha et al. 2020).

A similar removal mechanism of KF at pH 5 and DCF at pH 3 was observed in the previous literature work (ALothman et al. 2021; Shayesteh et al. 2020). Further increase of pH from its optimal value, for both cases, showed an observable decrease in the removal efficiency and adsorption capacity till pH 7. At pH 8, a slight increase in both adsorption capacity and removal efficiencies from 8.65 to 9.04 % for KF, and from 12.31 to 15.19 % for DCF could be seen in Fig. 4.19, which might be due to the twisting effect caused by the chemical structure of drugs as discussed in the following section (Kozłowska et al. 2017).

4.4.2 Effect of NFO@SiO₂@β-CD dosage on the removal of KF and DCF

The effect of NFO@SiO₂@β-CD dosage in the removal of KF and DCF has been investigated in this section. Here, the amount of the NFO@SiO₂@β-CD was varied in the 10 mg/L aqueous solution of KF and DCF each at optimized pH 5 and 3, for which the removal efficiency was calculated to be 80.92 % and 80.83 %. The adsorption capacity of KF and DCF was calculated to be 0.54 and 7.3 mg/g respectively.

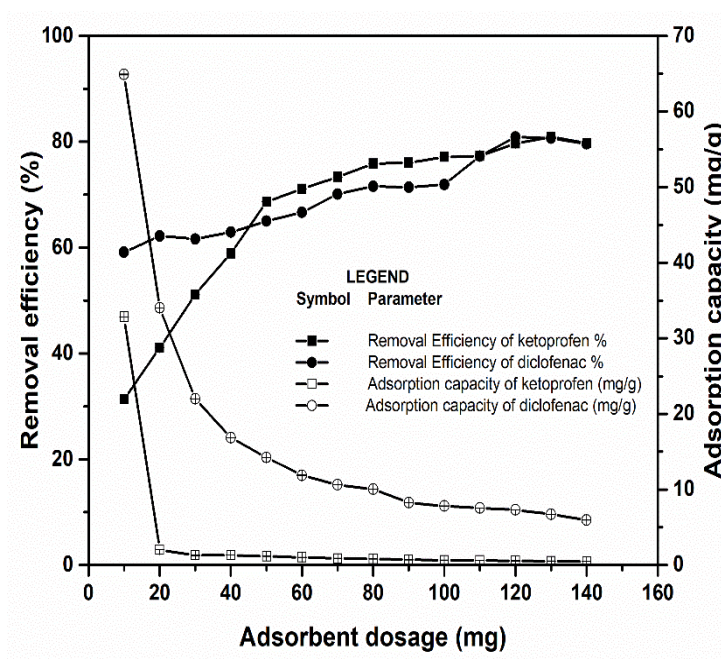


Fig. 4.20 Effect of varying nanocomposite dosage on the adsorption capacity and removal efficiency of KF and DCF

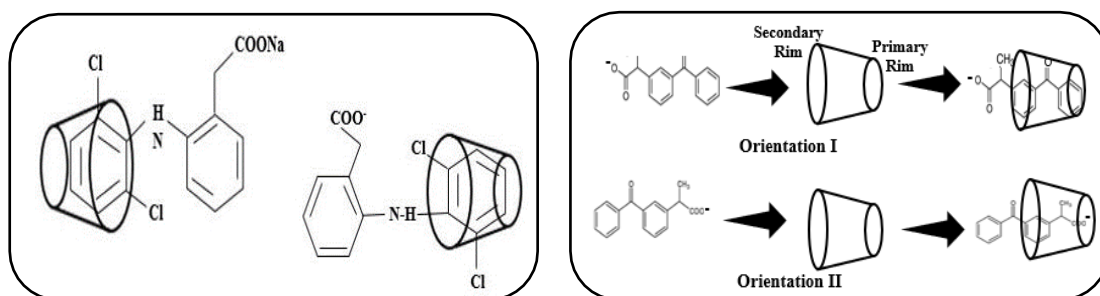


Fig. 4.21 Schematic representation of Host - guest inclusion of (a) DCF and (b) KF to β -cyclodextrin (Li et al. 2019; Shi et al. 2014)

Observing Fig. 4.20 the pollutant removal and adsorption capacity followed an increasing trend parallel to the dosage increase up to an optimum value of 130 mg and 120 mg for KF and DCF respectively. This trend might be due to a rise in the number of active sites in the NFO@SiO₂@ β -CD (Pavan et al. 2014). Beyond the aforementioned optimal measure, both the pollutants attained a steady state as a result of more interaction between the adsorbate molecules and the surface-active sites of the NFO@SiO₂@ β -CD, which has turned out in the saturation of surface-active sites upon further raising the measure of the adsorbent, detachment of adsorbate could have occurred. Similar behaviour of adsorbent upon the removal of KF and DCF was observed in the work of (Husein et al. 2019; Shayesteh et al. 2020; Wang et al. 2021).

The physicochemical properties of drug molecules may also influence the adsorption process. The chemical structure of the drug, in which both the drug molecule has two aromatic rings. DCF constitutes two aromatics with phenylacetic and chlorine functional groups, bounded by a secondary amino group that splits the carbonyl oxygen and chlorine atoms with intramolecular hydrogen bonding. The repulsion between the Cl⁻ ions and acetate group causes a twisting effect amidst the aromatic rings to an angle of about 69°. This structural spin may lead to good binding onto the adsorbent O-H groups. KF with a similar structure has no placeholder for the phenyl ring; in addition, a carbonyl group swaps a secondary amino group. Accordingly, frail repugnance between the phenyl rings lowers the twist angle; thus, a weak intramolecular hydrogen bond is formed, and a rapid shift in the movement of phenyl rings in KF, resulted in weak binding of KF to the adsorbent (Kozłowska et al. 2017). A schematic representation of the attachment of KF and DCF onto β -cyclodextrin is shown in Fig. 4.21.

4.4.3 Effect of initial concentration of KF and DCF aqueous solutions

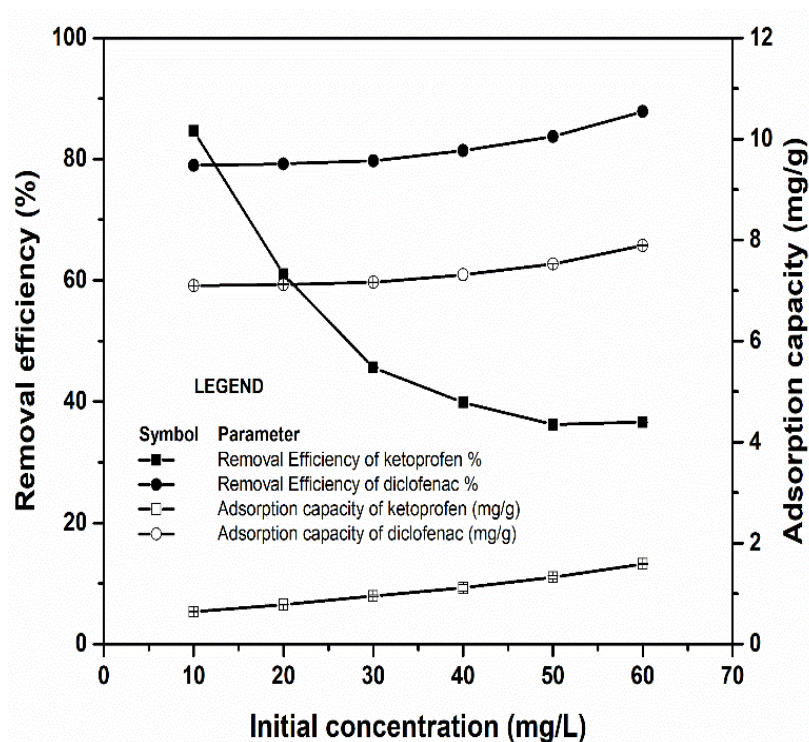


Fig. 4.22 Effect of varying initial concentration on the adsorption capacity and removal efficiency of KF and DCF

The effect of varied initial concentrations of KF and DCF aqueous solutions has been investigated to estimate the extent of optimized NFO@SiO₂@β-CD dosage that can remove the most concentrated KF and DCF in the aqueous solutions. A rise in the adsorption capacity was observed from 7.55 to 20.01 mg/g due to the increased driving force of KF molecules an increase in mass motive force at the adsorbent-adsorbate interface could be the cause of an increase in adsorption capacity with rising initial concentration (Abdul Aziz et al. 2013) At an optimal pH 5, an adsorbent mass of 130 mg, a reduction in the removal efficiency of KF from 84 % to 35 % could be observed. From 10 to 40 mg/L, the removal efficiency decreased this could be, owing to the greater availability of vacant sites and the surface area of NFO@SiO₂@β-CD to the low concentrated KF molecule (Fu et al. 2017), as shown in Fig. 4.22. Further raising the initial concentration from 40 to 60 mg/L, the removal efficiency nearly reached saturation. A similar trend of KF behaviour was noted in the polypyrrole functionalized magnetic Bi₂MoO₆ for the removal of KF (Wang et al. 2021). On the other hand, DCF's adsorption capacity and removal efficiency increased from 7.3 to 8.2 mg/g and from 81.25 to

92.24 %, respectively; likewise, the same sort of trend was observed in the work (Hayasi and Saadatjoo 2018; Larous and Meniai 2016). Regardless of the physicochemical characteristics of the adsorbent, raising the DCF initial concentration increased the adsorption capacity and removal efficiency. According to Amran and Zaini (2022), this trend could be attributed to the increased mass motive force and numerous collisions between DCF molecules and the O-H group in the exterior and interior adsorbent surface, which would have led to the formation of more host-guest complexes with the help of the mass motive force (Njoku et al. 2014).

4.4.4 Effect of reaction time on the removal of KF and DCF in the aqueous solutions

The effect of reaction time on the removal of KF and DCF in the aqueous solutions has been investigated to estimate the maximum time that is required to remove the pollutants in the aqueous phase.

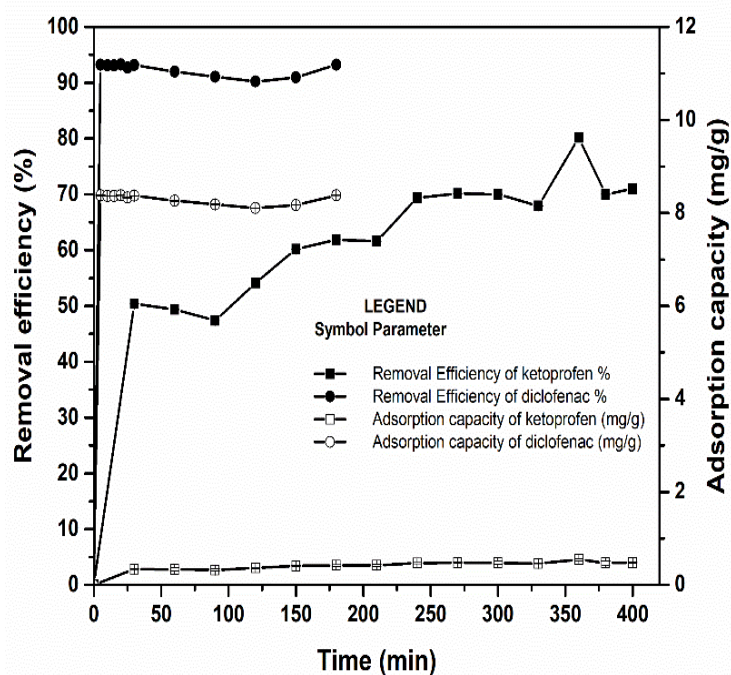


Fig. 4.23 Effect of varying time on the adsorption capacity and removal efficiency of KF and DCF

Fig. 4.23 plot depicts the removal of 94 % DCF from the aqueous solution within 5 min with the maximum adsorption capacity of 8.37 mg/g whereas, in the case of KF, the optimum removal of 80 % was obtained in 360 min with the adsorption capacity of 0.54 mg/g. In the adsorption of DCF, the equilibrium was attained after 30 min; beyond this reaction time, no

significant alteration was witnessed; this attributed to the saturation of relevant sites that hindered the adsorption process; whereas in the adsorption of KF equilibrium was attained till 330 min upon increasing the contact time for another half an hour (i.e., to 360 min) showed a drastic increase of removal percent, implies that the increase of contact time could improve the removal of KF.

The rate of drug removal was rapid, at the outset of the adsorption, as a consequence of empty active sites inside the nanocomposite and its boundary surface has paved the way for more significant adsorption of the drugs (Lotfi et al. 2019). The DCF was removed to a greater extent in a shorter period comparable to KF. Hydrophobicity ($\log K_{ow}$) is one such important property where K_{ow} is the partition coefficient and the $\log K_{ow}$ values are DCF = 4.52 and KF = 3.17. The more significant hydrophobicity of DCF compound with lower flexibility results in higher partitioning with better removal of DCF (Groisman et al. 2004).

4.4.5 FTIR image of adsorption of KF and DCF onto NFO@SiO₂@ β -CD

Fig. 4.24 depicts the functionalization of NFO, NFO@SiO₂@ β -CD before and after the adsorption process. The C-N group in 1203 and 1243 cm⁻¹ wavenumber and the N-H stretching in 3305.06 cm⁻¹ indicate the presence of an amine group in the DCF structure in the after-adsorption of DCF trend. The bending between 850-550 cm⁻¹ corresponds to C-Cl, whereas other stretching in 950-675 cm⁻¹, 1000-650 cm⁻¹ and 2000-2152 cm⁻¹ might be due to the presence of the C-H bond in the aromatic rings of the pollutants. The presence of COO, N-H bond and C=O and C=C bending could be identified in 1585, 1503, 1404 and 1447 cm⁻¹ wavenumber (Baki et al. 2014; Bratu et al. 1998; Maia et al. 2019).

The notable changes around the band 1000 cm⁻¹ were observed in both KF and DCF and the variation in the N-H groups in 3384 cm⁻¹, C-H propyl group in 2932.09, 2859.05 cm⁻¹ confirms the adsorption of KF; on the other hand, the variation in the intensity of bending vibration around 1000 cm⁻¹, 500 cm⁻¹ and between 1000 to 1500 cm⁻¹ indicates the presence of =CH, C=C, C-C-C and C-H which confirms the attachment of KF functional groups on the adsorbent as per the FTIR trend (Baratam and Harsha 2020; Floriano et al. 2018; P et al. 2022).

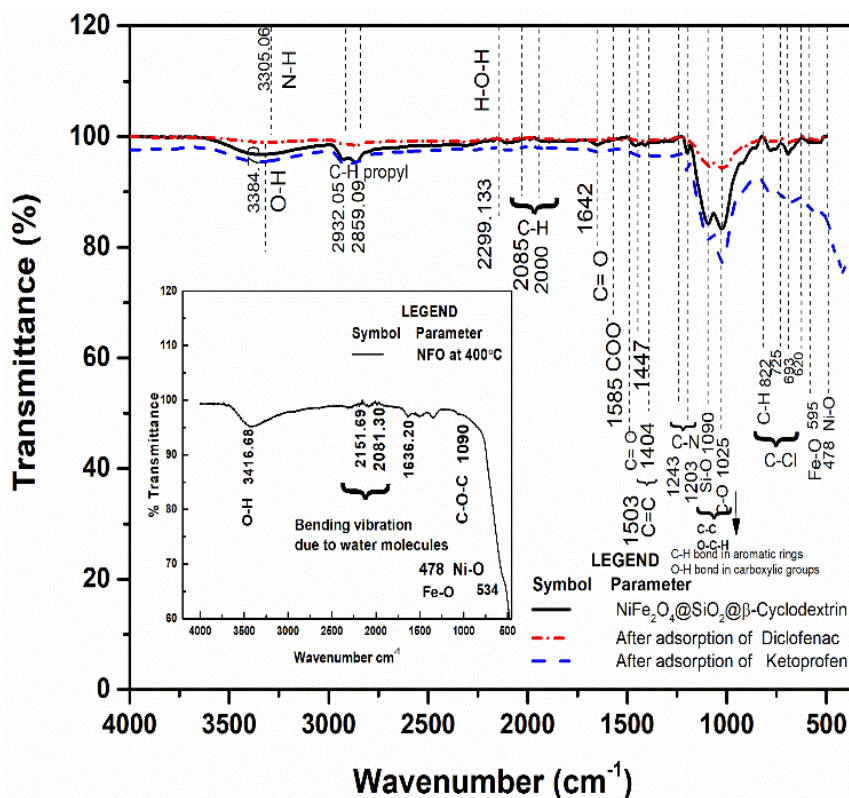


Fig. 4.24 Fourier transform infrared spectra of NFO and NFO@SiO₂@β-CD before and after the adsorption process

4.4.6 Quantification of β-CD in the final analyte of KF and DCF

The spectrophotometric analysis revealed that the content of β-CD in the final analyte of KF and DCF was estimated to be 35.22 % and 16.88 %. The physical property of β-CD, the solubility of β-CD in water, is 1.8 g/mL at ambient conditions and a small percent of methanol content in the KF stock solution preparation might have resulted in more leaching of β-CD in the KF final analyte. This solubility property of β-CD in the nanocomposite in water and solvent such as methanol resulted in the presence of β-CD in the final analyte of KF and DCF (Cho et al. 2006).

4.5 Adsorption kinetics and isotherm modelling

From the reaction time experimental datum, the kinetics and isotherm modelling were performed and studied in sections 4.5.1 to 4.5.2.

4.5.1 Adsorption Kinetics

The reaction time performed in the removal of KF and DCF was utilized in plotting the pseudo-first and second-order kinetics. Fig. 4.25 (a) and (b) shows a linear plot of $\ln(q_e - q_t)$ versus time (t) and t/q_t versus time (t) min, which were useful in calculating the kinetic data. The graphically calculated variables such as R^2 , k_2 , k_1 and $q_{e,cal}$ were presented in table 4.3. Initially, the drug molecules interact with the surface of the NFO@SiO₂@ β -CD; at this point, the reciprocal action between the drug molecules and the nanocomposite surface would have occurred. The rate of incremental adsorption was monitored as the reaction progressed. Finally, the steady state was reached, and equilibrium was visible among the drug molecules and NFO@SiO₂@ β -CD in both cases.

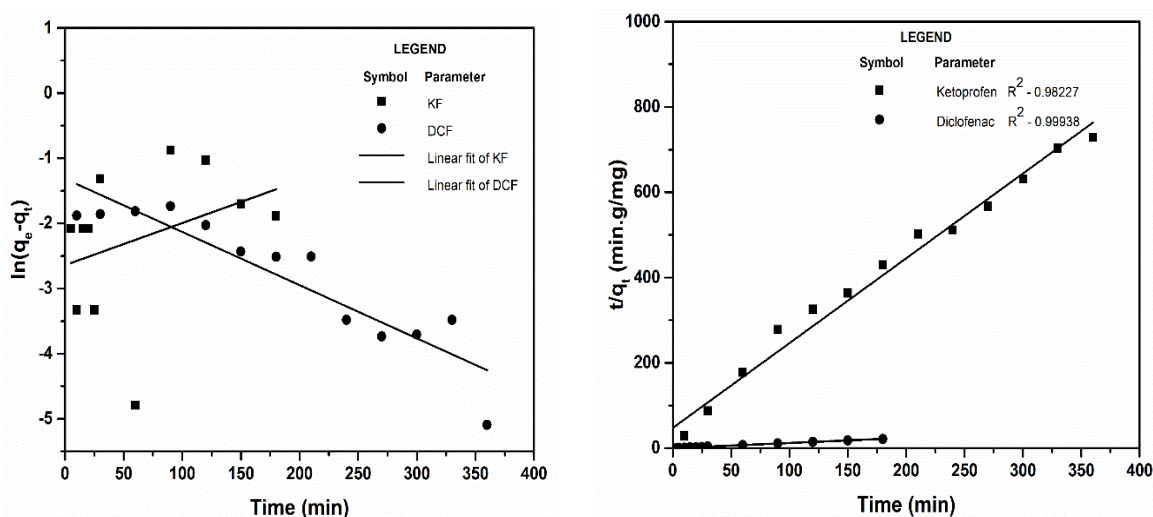


Fig. 4.25 (a) Pseudo first-order kinetic model and (b) Pseudo second order kinetic model for the removal of KF and DCF

Table 4.3 Kinetic datum for the removal of KF and DCF

Models	Pseudo-First-order kinetic model			Pseudo-second-order kinetic model		
	$q_{e,cal}$ (mg/g)	k_1 (1/min)	R^2	$q_{e,cal}$ (mg/g)	k_2 (g/mg min)	R^2
KF	0.991	-0.007	0.833	0.502	0.083	0.982
DCF	0.125	-2.44E-05	0.074	8.263	0.479	0.999

The regression coefficient of pseudo-second order was found to be the highest for both pollutants and to be the best fit, and the constant k_2 also decreased in the subsequent order: KF < DCF, similarly most of the literature in the removal of KF and DCF follows pseudo-second order kinetic model rather than pseudo first order kinetics. Based on this kinetic model, it is possible to conclude that KF and DCF adsorption might have occurred via chemisorption rather than physisorption (Suriyanon et al. 2013; Turk Sekulic et al. 2019).

4.5.2 Adsorption Isotherms

From the reaction time experimental datum, isotherm modelling was performed and studied in sections 4.5.2.1 to 4.5.2.2.

4.5.2.1 Langmuir isotherm for the removal of DCF and KF

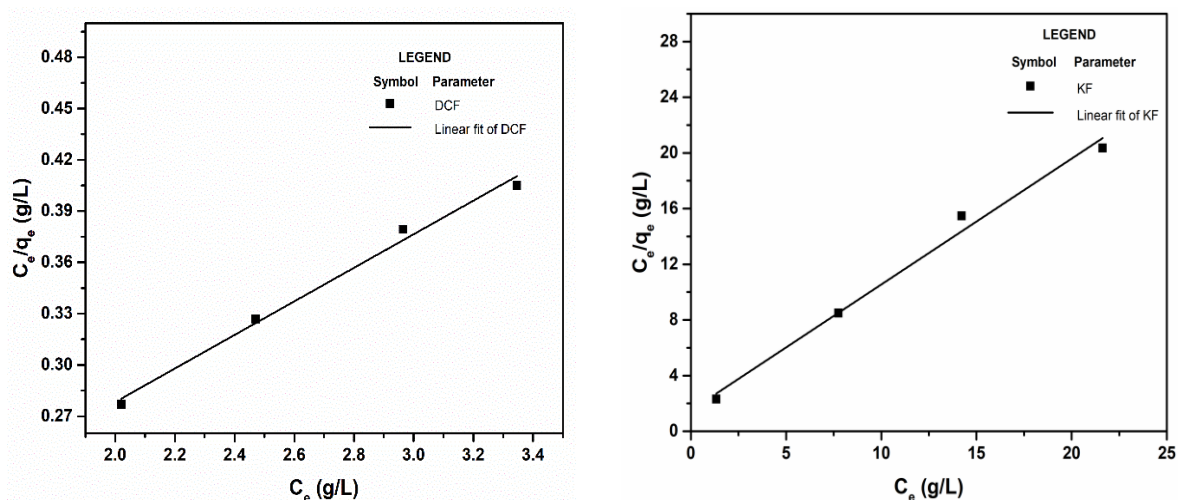


Fig. 4.26 Langmuir isotherm plot for the removal of (a) DCF and (b) KF

Fig. 4.26 (a) and (b) illustrate the interrelationship between C_e/q_e and C_e . As shown in table 4.5, the R_L values do not equal zero ($0 < R_L < 1$), indicating a viable adsorption process for drug compound removal by the NFO@SiO₂@β-CD. The Langmuir maximum adsorption capacity is found to be 0.66 mg/g for KF similarly a lower value of maximum adsorption capacity of mesoporous SBA-15 on the removal of KF and in the phosphorous-doped carbonaceous material in the removal of DCF was also noted (Bui and Choi 2009; Turk Sekulic et al. 2019).

4.5.2.2 Freundlich isotherm for the removal of DCF and KF

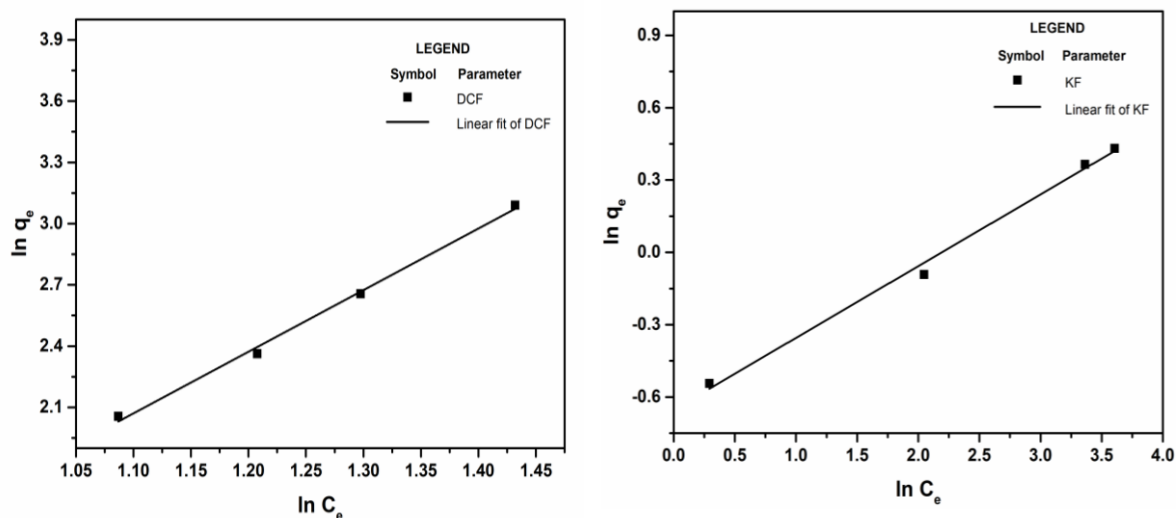


Fig. 4.27 Freundlich isotherm plot for the removal of (a) DCF and (b) KF

Table 4.4 Adsorption isotherm parameters for KF and DCF

Isotherm models	Freundlich constants			Langmuir constants		
	n	K_F (mg/g)(L/mg) ¹	R^2	q_{max} (mg/g)	K_L (L/mg)	R^2
KF	3.36	0.52	0.99	0.66	1.65	0.99
DCF	0.33	0.28	0.99	12.20	0.83	0.98

Table 4.5 Separation factor in the removal of KF and DCF

Initial Concentration (mg/L)	R_L (KF)	R_L (DCF)
10	0.056	0.106
20	0.029	0.056
30	0.019	0.038
40	0.014	0.029

Fig. 4.27 (a) and (b) demonstrate the best-fitted with both Langmuir and Freundlich isotherm model for the chosen drug molecule with $R^2 = 0.99$, similar results were observed in (Georgin et al. 2022). Tables 4.4 show the isotherm parameters q_{max} , b , and R_2 values in which the value of $1/n$ is 3.021 and 0.297 for the adsorption of DCF and KF. The value of $1/n$ less than unity

implies the heterogenous nanocomposite surface with the exponential distribution of active sites in the adsorption of KF (Tiwari et al. 2015) whereas the value of $1/n$ greater than 1 indicates cooperative adsorption of DCF upon NFO@SiO₂@β-CD nanocomposite (Foo and Hameed 2010).

4.5.3 NFO@SiO₂@β-CD nanocomposite regeneration and recycling studies

The potentiality of NFO@SiO₂@β-CD after regeneration and recycling was investigated.

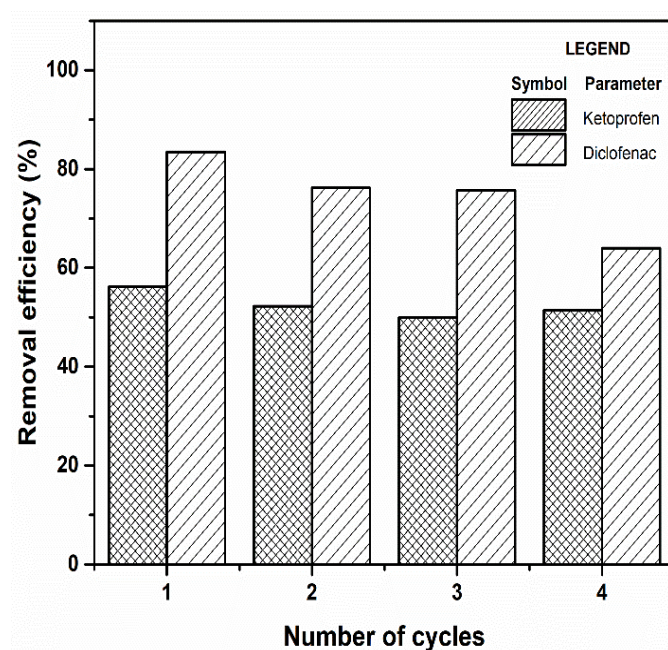


Fig. 4.28 Reusability of NFO@SiO₂@β-CD on the removal of KF and DCF

The pollutants KF and DCF were experimented with in an acidic environment (pH = 3 and 5), the used nanocomposite was washed with 1 mL of 0.1 M NaOH in a 20 mL volume of distilled water and kept in a rotary shaker for 30 min at 120 rpm followed by distilled water washing, this is to neutralize the nanocomposite; to remove the trace amount of KF and DCF present over the surface of NFO@SiO₂@β-CD followed by drying the adsorbent overnight. Thus, 0.1 M NaOH and deionized water were used to detach the drug molecule, (Lee et al. 2015).

Fig. 4.28 showed that after four cycles of using the nanocomposite, the average removal efficiencies were reduced to 51.36 % for KF and 64 % for DCF. The hydroxyl groups in the 0.1 M NaOH as regenerant can permeate easily through the available adsorbent pores more energetically, allowing the drug molecule to be easily solubilized and dislocated (Lee et al. 2015). The collapse of the functional group, the leaching of β-CD in the nanocomposite as

mentioned in section 4.4.6 and the pore structure of the NFO@SiO₂@β-CD might have resulted in the decreased removal efficiency of both pollutants (Li et al. 2020). Finally, the pollutant could be eluted, dried, and incinerated.

4.6 Adsorbent: Nickel Ferrite@L-Leucine (NFO@L)

The section from 4.6.1 to 4.6.19 focused on discussing the properties of the NFO@L-Leucine (NFO@L) as well as the impact of operational factors in the batch experiments, isotherm behaviour, kinetic modelling and the studies related to regeneration and recycling. All of these aspects were explored for their role in removing LFH and CIP.

4.6.1 FTIR of NFO@L-Leucine

FTIR was performed to identify the functional groups and their vibrational characteristics that are present in the NFO@L nanocomposite. Metal-oxide bonds, particularly in ferrite-based particles, were observed between the wavenumbers 1000 and 500 cm⁻¹, with the highest stretching caused by the tetrahedral metal oxygen-bond discovered between 600 and 550 cm⁻¹ and the lowest stretching occurred between 450 and 385 cm⁻¹ (Jacob et al. 2011a).

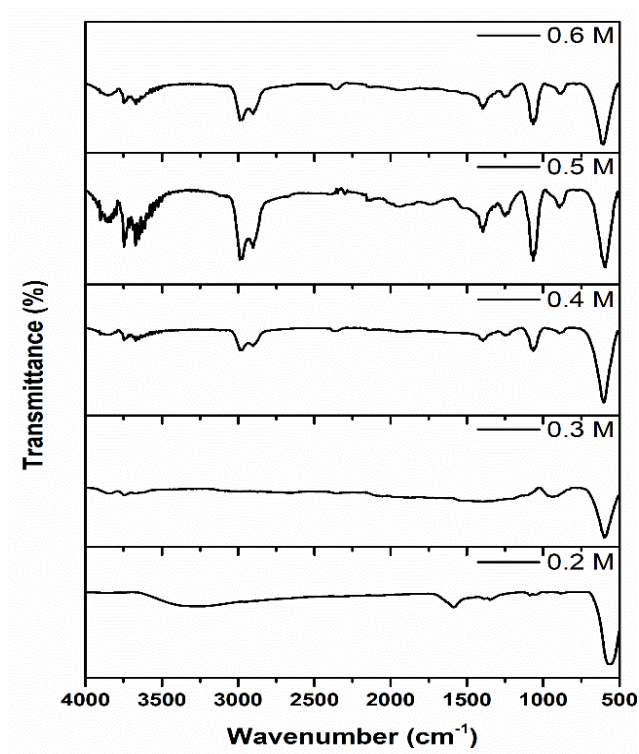


Fig. 4.29 FTIR analysis of varied L-Leucine molar ratio onto NFO

The presence of NH_3 and COO^- in the range $500 - 650 \text{ cm}^{-1}$ was observed in a waveform. Additionally, the broad H_3N^+ and aliphatic C-H stretching were overlaid on N-H stretch vibrations in the range $2000 - 3100 \text{ cm}^{-1}$. An asymmetric (H_3N^+) and carboxylate (CO)₂, symmetric (H_3N^+) N-H bend was noted between $1500 - 1700 \text{ cm}^{-1}$. The symmetric carboxylate (CO)₂ was detected around 1400 cm^{-1} and the torsional H_3N^+ , N-H oscillation was observed (Singh et al. 2008) confirming the functionalization of L-Leucine onto nickel ferrite (NFO@L).

All these functional groups were observed at an increased molar ratio of L-Leucine from 0.4 M to 0.6 M with an increase in the percentage transmittance. In Fig. 4.29, the more dominant peak of NFO nanoparticles was visible in 0.2 M and 0.3 M. Furthermore, there was a noticeable difference in the presence of functional groups at an increased L-Leucine concentration on NFO.

4.6.2 Effect of varied L-Leucine molar ratio onto NFO, reaction time and temperature on the crystallographic structure of NFO@L nanocomposite using XRD analysis

XRD analysis was used in determining the crystallite size and the nature of the so-formed nanocomposite. Fig.4.30 (a) depicts the XRD of L-Leucine and varied molar ratios of L-Leucine (0.2 M, 0.3 M, 0.4 M, 0.5 M and 0.6 M) onto NFO@L and the graph also revealed the sharp peaks of L-Leucine reflecting its highly monoclinic crystal system with the strong *hkl* orientation (004, 005). The XRD pattern of 0.2 to 0.4 M L-Leucine on NFO revealed the gradual development of amino acid attachment with dominating NFO peaks. The major peaks of the amino acid were evident in the 0.5 M L-Leucine, with the combination of both NFO orientations (311, 440, 622, 511, 222) similar to the reference ICDD 54-0964 (Liu et al., 2018) and L-Leucine orientation (003, 004, 005, 113, 014, 015, 114, 007) confirming the synthesis of NFO@L nanocomposite. Further increase of L-Leucine molar ratio to 0.6 M, a decrease in the sharp NFO peaks and L-Leucine peak of (005) could be seen indicating that an inadequate NaOH concentration to higher amino acid molar ratio may have hampered L-Leucine functionalization onto NFO. At this molar ratio, some of the precursors may have been reduced while others may have remained unreacted and so the nature of the nanocomposite exhibited an amorphous phase (N. et al., 2018). The optimized 0.5 M L-Leucine at 12 hrs reaction time at $150 \text{ }^\circ\text{C}$ was varied for lower hydrothermal synthesis reaction temperature of $100 \text{ }^\circ\text{C}$ which revealed the nanocomposite's more amorphous nature.

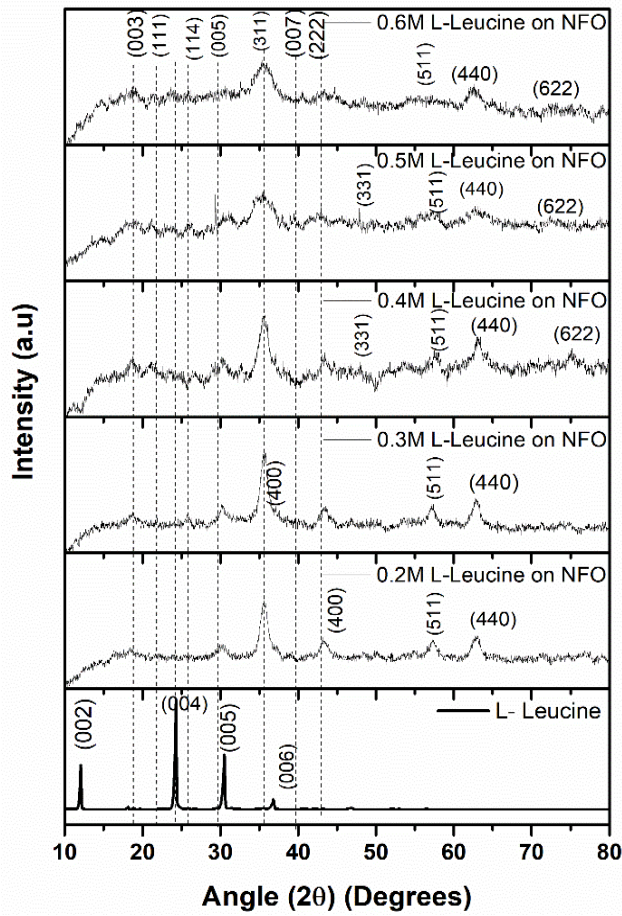


Fig. 4.30 (a) X-ray Diffraction analysis of NFO@L nanocomposite at (a) different molar ratios of L-Leucine onto NFO

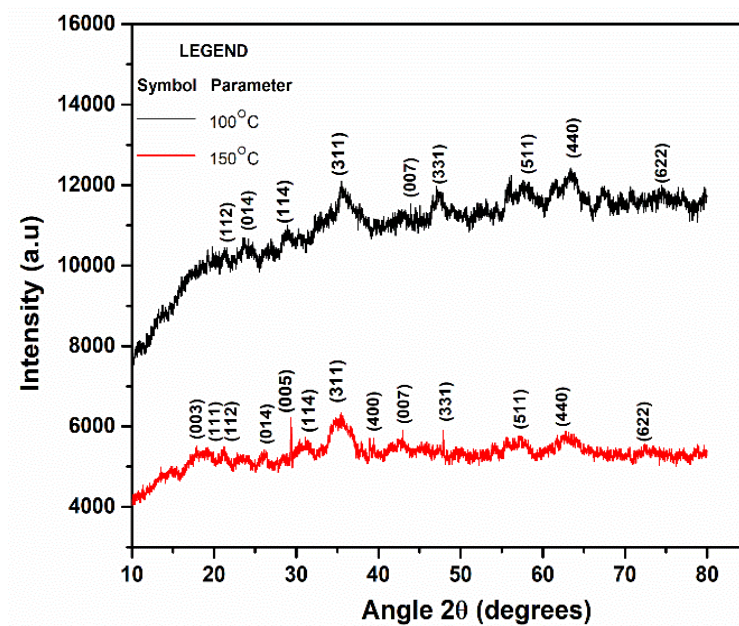


Fig. 4.30(b) XRD of NFO@L nanocomposite at two temperatures

Above 200 °C of hydrothermal synthesis reaction temperature, a sudden reduction in the weight loss of the nanocomposite from the TGA analysis was observed indicating the initiation of L-Leucine breakdown as shown in the XRD plot of Fig. 4.30 (b). Therefore, the temperature-varied hydrothermal synthesis of NFO@L was limited to 150 °C. Thus functionalization of L-Leucine onto NFO, which is polycrystalline, with amino acids providing surface passivating groups NH₂, COOH and OH, resulting in the NFO core, and L-Leucine shell was accomplished (Yang et al., 2017) by hydrothermal synthesis at optimum conditions of 150 °C and 12 hrs. The so-formed NFO@L, crystalline size was calculated using the De-bye Scherrer using equation (4.1) and the lattice parameter using equation (4.2). The lattice parameter (a) and miller indices *hkl* were presented in table 4.6. The average crystalline size of NFO@L is calculated to be 0.056 nm.

Table 4.6 XRD parameters of optimized NFO@L nanocomposite

2θ (degrees)	Lattice parameter (nm)	<i>hkl</i> miller indices
17.89	1.48	003
26.89	1.09	113
29.40	1.51	005
29.62	1.24	014
31.56	1.20	114
34.92	1.30	015
35.51	0.83	311
37.15	0.83	S222
43.21	1.46	007
57.08	0.83	511
62.69	0.83	440
75.17	0.83	622

4.6.3 FE-SEM/EDX of NFO@L nanocomposite

The surface morphology and the stoichiometric proportion of elements that constitute the NFO particles were analysed via the Field Emission - Scanning Electron Microscope imaging and Energy Dispersive X-ray Diffraction analysis.

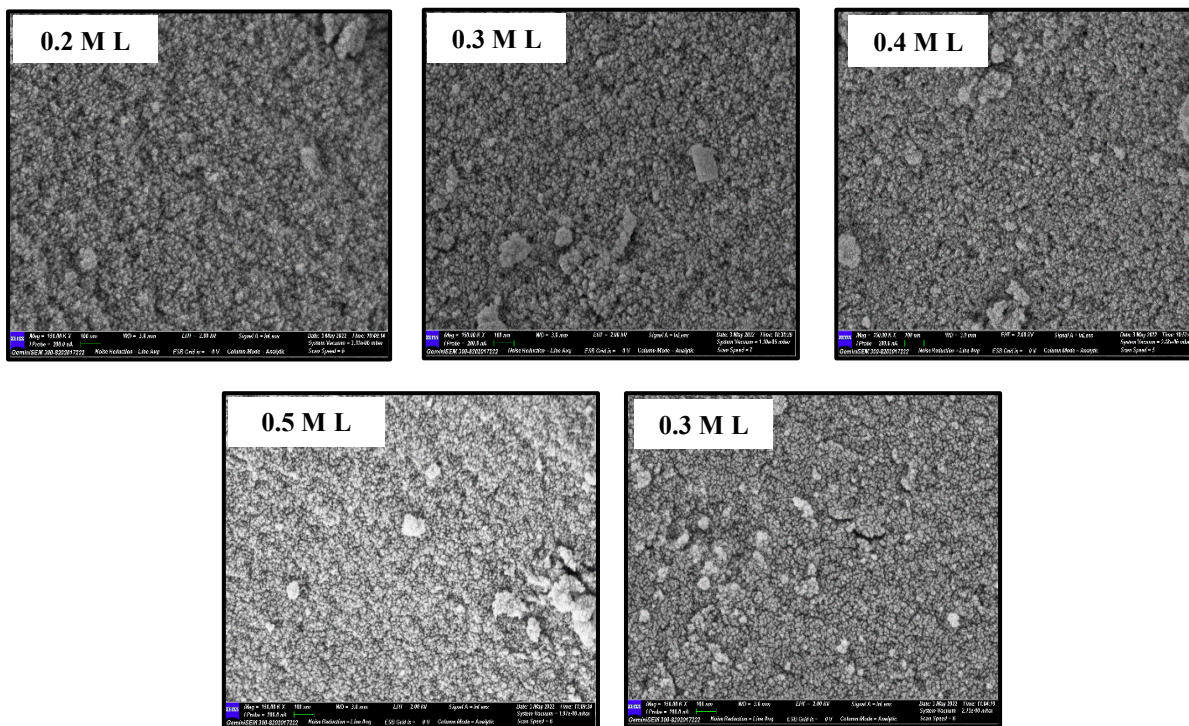


Fig. 4.31 FE-SEM image of varied L-Leucine molar ratio onto NFO@L

Fig. 4.31 depicts the tiny spherical image of the NFO@L nanocomposite at a magnification of 100 nm in conjunction with all of the FESEM images. The colour could be seen changing at the increased L-Leucine molar ratio, and some of the agglomerated particles could be seen in the FESEM image. Except for Nitrogen (N) and Hydrogen (H) in L-Leucine, all other elements were analysed and their atomic and weight percentages were listed in their optimized EDX image. The colour variation in FESEM images were observed with respect to increase in the L-Leucine molar ratio, and some agglomerated particles were also evident in the FESEM image as shown in Fig.4.31. All elements, except for Nitrogen (N) and Hydrogen (H) in L-Leucine were analyzed, and their atomic and weight percentages were documented in the optimized EDX image. Since hydrogen is the lightest element and the concentration of nitrogen is much lower than carbon in the L-leucine-attached nanocomposite, only a small peak for nitrogen (N) is visible, as shown in Fig. 4.32. It was noticed that increasing the molar ratio, increased the elemental composition (Carbon) in the NFO@L nanocomposite.

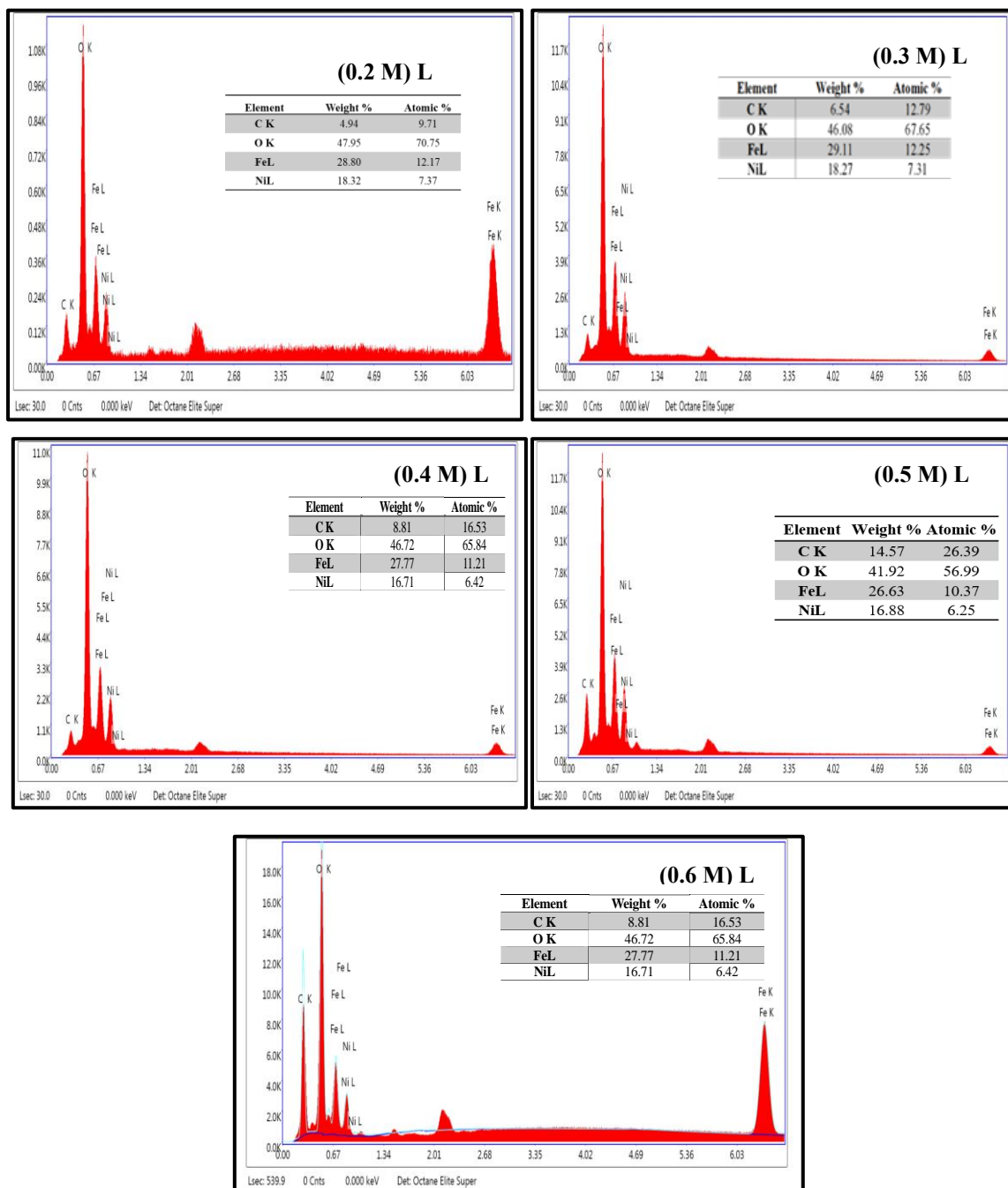


Fig. 4.32 EDX of varied L-Leucine molar ratio onto NFO@L nanocomposite

4.6.4 Atomic Force Microscope (AFM) and Particle Size Distribution from AFM and FE-SEM

A 3D view of the nanocomposite morphology with a spherical particle is shown in Fig. 4.33. The obtained graph estimated the grain size to be 7.41 nm with a mean surface roughness of 5.88 nm, and the average diameter of the particle to be 11.79 nm. The particle size distribution

from FESEM calculated using ImageJ software is shown in Fig. 4.34 (a) and (b). The average diameter of the nanocomposite was found to be 13.69 nm. Both the FESEM and the AFM average diameter of the particle is found in the range between 11 to 15 nm.

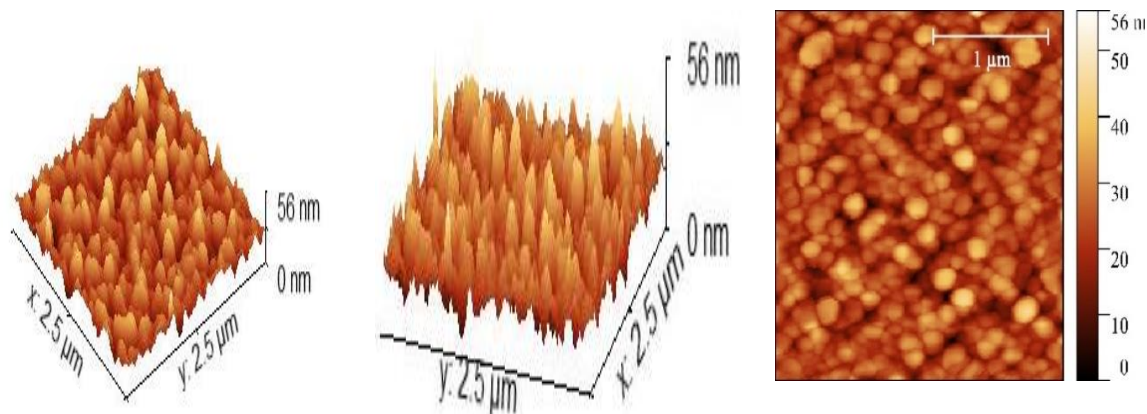


Fig. 4.33 Atomic Force Microscope (AFM) 3 and 2 Dimensions of the NFO@L Nanocomposite

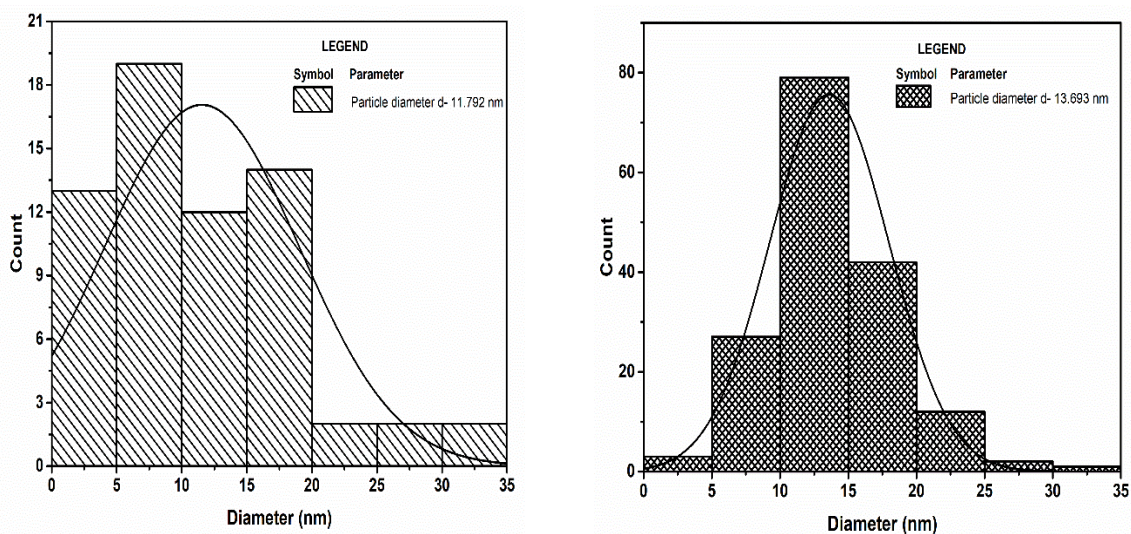


Fig. 4.34 Particle size distribution obtained from (a) AFM and (b) FESEM

4.6.5 TGA/DTG analysis of NFO@L nanocomposite (TGA/DTG)

The thermogravimetric and derivative thermogravimetric analysis (TGA/DTG) of NFO@L are shown in Fig. 4.35 reveals that a 4.2 % weight loss was observed upto 197.52°C which might be due to the evaporation of water molecules and combustion of organic components to CO₂. Above this temperature, a sudden steep downward line indicates 17.93 % weight loss till 415.76

°C which indicates the breakage and decomposition of L-Leucine present on the NFO@L. Further a 0.05 % weight loss is observed until 703.57 °C which may be due to recrystallization.

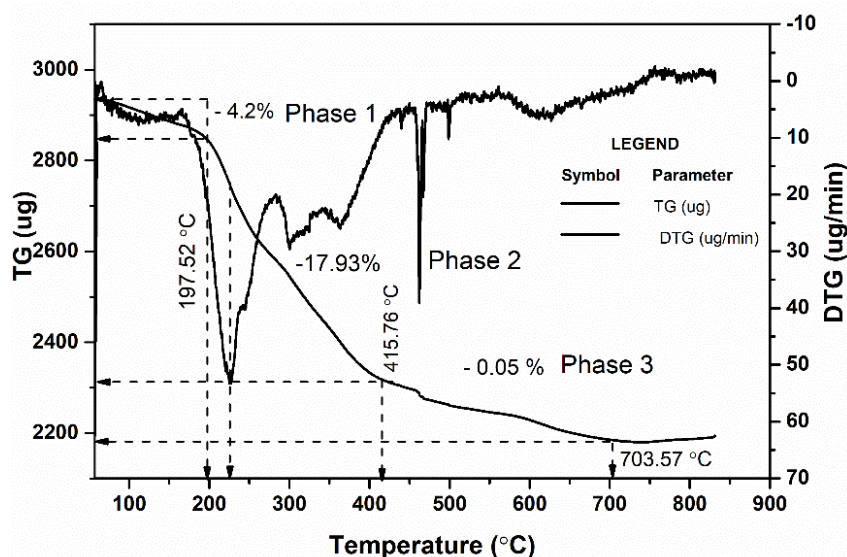


Fig. 4.35 TGA/ DTG of the NFO@L nanocomposite

On the whole, a 26.28 % weight loss is determined from 57.46 °C to 831.13 °C and from the TGA curve, it is inferred that the NFO@L nanocomposite might have exhibited multistage decomposition with no intermediates. At 226.77 °C in the DTG curve, a large exothermic peak indicating the initiation of L-Leucine breakdown in the NFO@L (Raula et al., 2007) and has completely decomposed within 342 °C in addition to that, the decomposition of inorganic salts (Rodante and Marrosu, 1990) and loss of oxygen-containing groups would have occurred within 415.76 °C; above this temperature no significant weight loss is observed (Mapossa et al., 2020; Sun et al., 2022). The multiple exothermic peaks in phase 2 between 197 to 400 °C might be due to the decomposition of two different materials in the nanocomposite. An exothermic peak at a high temperature of 503°C indicates the recrystallization of the nanocomposite.

4.6.6 VSM of NFO@L nanocomposite

In this section, the effect on the magnetic properties of NFO@L nanocomposite was analyzed using the vibrating sample magnetometer (VSM). Fig. 4.36 reveals a S-shaped curve reflecting the superparamagnetic nature of the nanocomposite which helps in the separation of the nanocomposite using an external magnetic force. The magnetic properties of the NFO@L

nanocomposite were estimated to be saturation magnetization (M_s) of the synthesized NFO@L is 0.66 emu/g with the retentivity (M_r) = 73.29 E-3 emu.

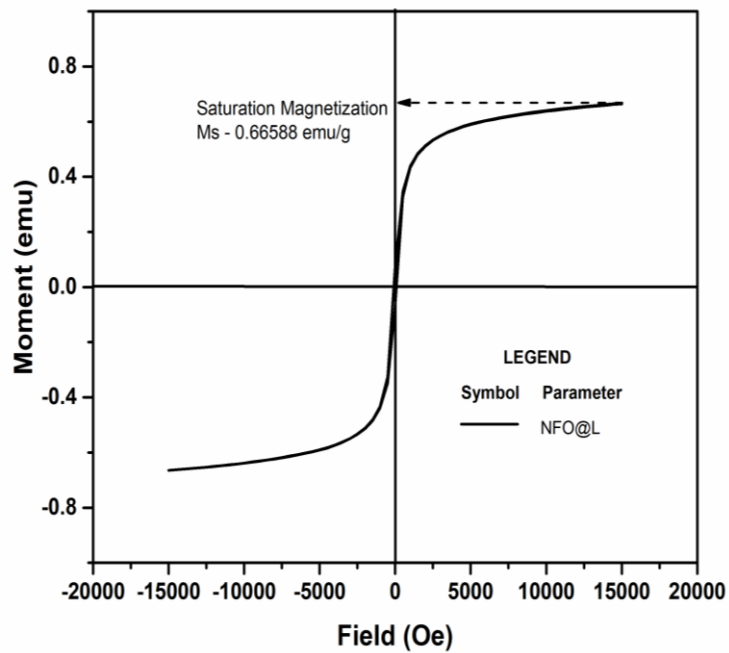


Fig. 4.36 VSM analysis of NFO@L nanocomposite

4.6.7 Electrokinetic Potential Analysis of NFO@L nanocomposite

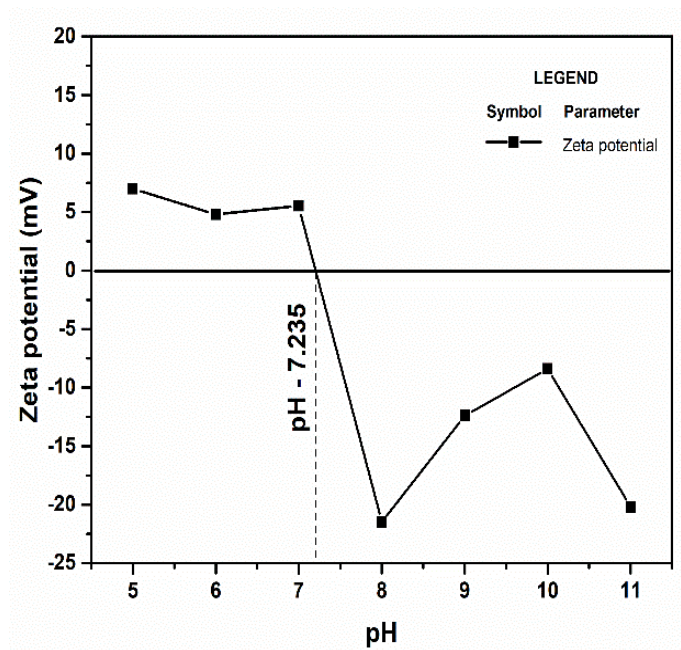


Fig. 4.37 Zeta potential of NFO@L nanocomposite

The electrokinetic analysis of the NFO@L nanocomposite was analyzed from acidic to basic pHs as shown in Fig. 4.37. The salt addition method with 50 mg of NFO@L nanocomposites in 50 mL of 0.1 M NaOH and HNO₃ for 24 hr at varied pH levels and at room temperature was used in analyzing the nanocomposite's isoelectric point. The isoelectric point (pH_{IEP}) of NFO@L is observed at pH = 7.20 and the maximum zeta potential value of -21.5 mV was attained at pH 8. Above this isoelectric point, NFO@L exhibited a negatively charged surface and below this point, the nanocomposite exhibited a positive surface charge. (Rodante et al. 1992).

4.6.8 Brunauer Emmett Teller (BET) specific surface area analysis and Barrett-Joyner Halenda (BJH) model of NFO@L nanocomposite

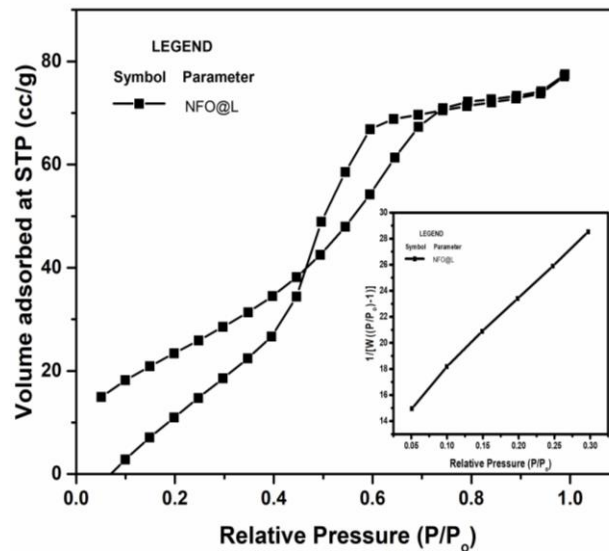


Fig. 4.38 N₂ Adsorption-desorption Hysteresis loop of NFO@L nanocomposite and a BET plot of NFO@L between $1/[W((W(Po/P)-1))]$ and relative pressure (P/P₀)

BET multi-point test was used in analyzing the specific surface area, pore volume, and pore radius of the NFO@L nanocomposite and the analysis was conducted under nitrogen gas at 77.35 K. The surface area, pore volume, and pore radius of the NFO@L are found to be 92.91 m²/g, 0.14 cc/g, and 18.95 Å. Fig. 4.38 hysteresis loop depicts the type IV adsorption isotherm (Thommes et al. 2015) that can behave as a super nano-porous adsorbent (NFO@L). Initially, in the condensed state, homogenous adsorption was observed followed by heterogeneous adsorption on the walls of the super nano-porous (NFO@L) adsorbent. The linear graph in Fig. 4.38 reveals the highly porous nature of the NFO@L nanocomposite (Zaidi et al. 2021).

4.6.9 Ninhydrin test for NFO@L nanocomposite

The reaction between ninhydrin and L-Leucine amino acid attached to the nanocomposite was confirmed by the visible colour change from colourless solution to Ruhemann's purple chromophore which indicated the positive results for the ninhydrin test (Kollarahithlu and Balakrishnan 2019).

4.6.10 Effect of varied molar ratio of L-Leucine on the NFO upon the removal of LFH and CIP

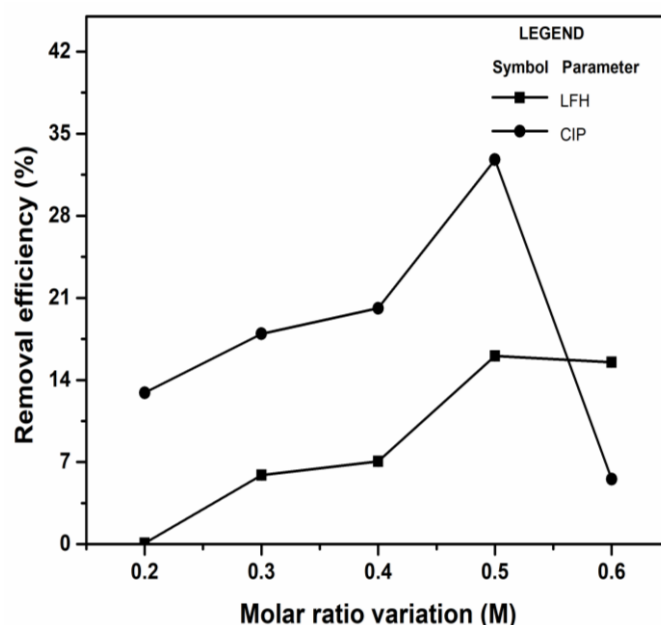


Fig. 4.39 Effect of varied L-Leucine molar ratio on the NFO for the removal of LFH and CIP

The L-Leucine molar ratio was varied in the range of 0.2 M, 0.3 M, 0.4 M, 0.5 M and 0.6 M onto NFO and the effect of varied molar ratio of L-Leucine onto NFO in the removal of CIP and LFH was studied. The removal efficiency of both pollutants was found to increase upto 16.05 % LFH and 32.79 % CIP with an increase in the L-Leucine molar ratio onto NFO till 0.5 M. Thereupon further increases to 0.6 M L-Leucine in the NFO, CIP showed a reduction in the removal efficiency and a saturated efficiency was seen in the LFH trend from the Fig. 4.39. This could be owing to the occurrence of smaller pores or pore blockages inside the NFO@L at higher molar ratios, which can limit the diffusion of pollutants into the interior of the

adsorbent, lowering adsorption capacity efficacy. It can also limit the accessibility of active spots, further limiting removal efficiency (Chew et al. 2010).

4.6.11 Effect of pH on the removal of LFH and CIP using NFO@L

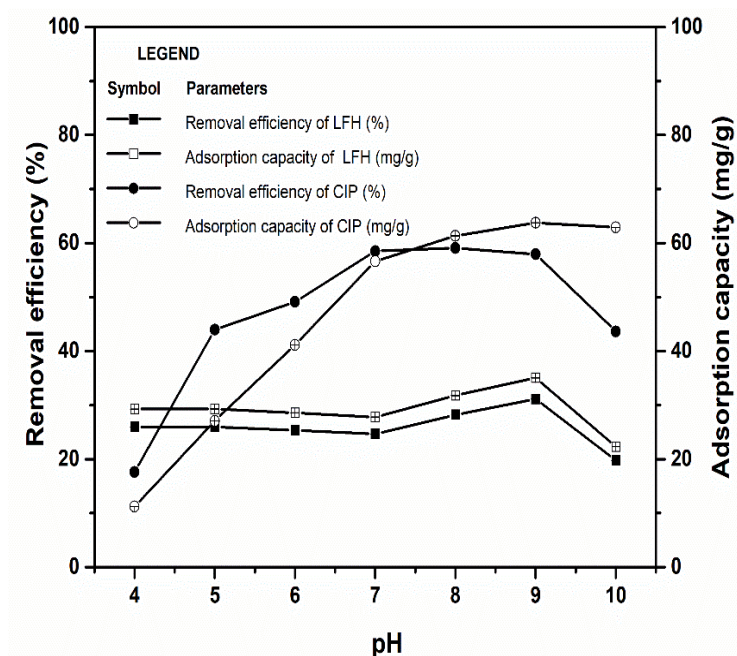


Fig. 4.40 The adsorption capacity of NFO@L and its removal efficiency in the removal of LFH and CIP at different pH

Fig. 4.40 depicts the graphical trend followed upon varying the pH from 4 to 10 and the effect on the adsorption capacity of NFO@L and removal efficiency of LFH and CIP in 100 mL solutions containing 10 mg NFO@L mass equilibrated for about 12 hrs. The maximum removal efficiency of 59.08 % CIP and 31.13 % LFH were obtained at pH 8 and 9 respectively and their respective adsorption capacity was calculated to be 63.82 mg/g and 35.09 mg/g. The surface charge, the isoelectric point of the NFO@L nanocomposite, and the amphoteric character of both pollutant molecules all play a significant role in the pH effect. According to the zeta potential analysis, the NFO@L surface is negatively charged and it is closer to the maximum pH of both CIP and LFH aqueous solutions.

CIP as an amphoteric molecule exists in mono-positive charge at $\text{pH} < 6$, mono-negative charge at $\text{pH} > 9$ as well as in zwitterionic form at neutral pH (Veclani and Melchior 2020). Furthermore, the pKa value of CIP for the carboxylic acid group is 6.1 and 8.7 for the amino

group at piperazine moiety, indicating that CIP exists in zwitterionic form between pH 6.1 to 8.7 implying that the CIP molecule has an equal number of positive and negative charges at pH 8. At the same time, if the $\text{pH} > \text{pH}_{\text{IEP}}$ the negative surface charge of NFO@L dominates whereas it is vice versa for $\text{pH} < \text{pH}_{\text{IEP}}$ (Li et al. 2015; Wu et al. 2013). The removal efficiency of CIP increased as the pH values increased from 4 to 8; above this pH, the efficiency decreased drastically owing to the deprotonation of the carboxylic group from the CIP molecule.

The optimal pH of the CIP solution is greater than the pK_a of the carboxylic group in CIP and less than the pK_a of the amino group in CIP, so the CIP molecule remains protonated at pH 8 (El-Shafey et al. 2012) and hence there might be a hydrogen bonding interaction between $-\text{NH}_2$ of the nanocomposite and $-\text{OH}$ group of the CIP (You et al. 2021a). In the case of LFH, it exists in the deprotonated form at alkaline conditions, as the optimal pH 9 is greater than both the pK_a value of the carboxylic group (5.38 or 5.49) and the amino group (7.85 or 8.78) (Guo et al. 2020b). The pK_a value of the amino group is nearer to the optimal pH 9 of the LFH solution and also the pH of the LFH solution $> \text{pH}_{\text{IEP}}$ 7.23 of the NFO@L. Increasing the pH from 4 to 7, both the removal efficiency of LFH and adsorption capacity of NFO@L remained nearly constant; beyond this, an increase in the efficiency and adsorption capacity was observed from pH 7 to 9, above this pH a reduction was observed. The increased efficiency from pH 7 to 9 might be owing to the transfer of free electron pairs on the amine nitrogen to the aromatic rings of the LFH in its molecular state and also since L- Leucine is hydrophobic, the LFH could have located itself in the cavity-water interface, a similar behaviour of pollutant is observed in the work of (Rajoriya et al. 2017). The dominating negative surface charge on the NFO@L has resulted in more electrostatic repulsion of the anionically charged LFH, and that might have led to the decreased efficiency at pH 9 when compared to the removal efficiencies of CIP. In the case of CIP, the removal mechanism would have occurred via electrostatic attraction with the dipole-dipole forces that existed between the polar molecules, along with the formation of a hydrogen bond with an electronegative halogen atom (El-Sheikh et al. 2019; Guo et al. 2020b; Peñafiel et al. 2021). In general, the benzene ring in the CIP structure undergoes π - π interactions with the nanocomposite, a similar mechanism has been cited in (Al-Buriahi et al. 2022).

4.6.12 Effect of NFO@L dosage on the removal of LFH and CIP

Along with the aforementioned mechanism in the pH, the surface properties of the nanocomposite were studied by varying the nanocomposite dosage and the resultant effect on

the removal percent of LFH and CIP and adsorption capacity of NFO@L is presented in Fig. 4.41. The maximum adsorption capacity for CIP is 8.72 mg/g and 5.96 mg/g for LFH. Almost 95 % of CIP was removed with a maximum NFO@L dosage of 100 mg in 100 mL at pH 8. In the case of LFH, 74.42 % was removed with a maximum adsorbent dosage of 70 mg in 100 mL at pH 9, both pollutants were equilibrated for about 12 hrs. The increase in NFO@L dosage increased the efficiency till the optimal value upon further raise of NFO@L dosage, both the removal efficiency and adsorption capacity almost became stable with a very slight decrease. The increased efficiency of both pollutants till the optimal value is due to the increase in surface area and availability of more active binding sites of NFO@L.

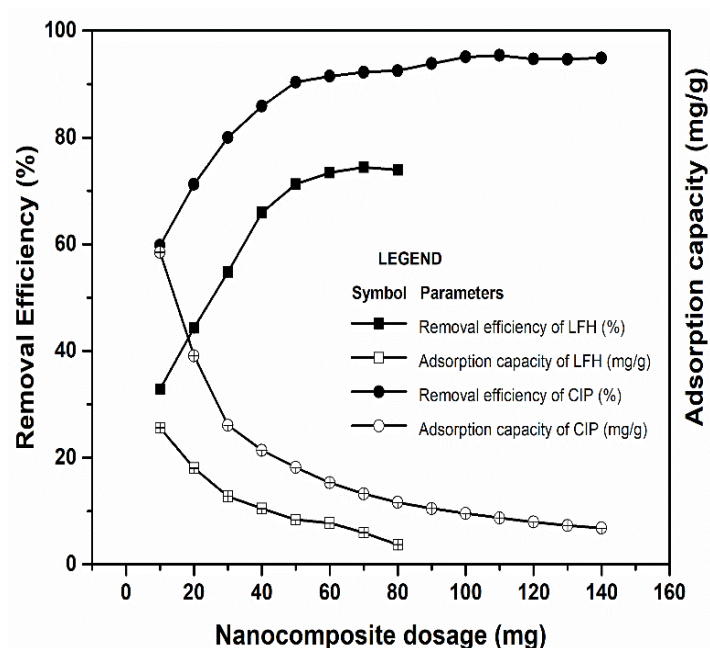


Fig. 4.41 The adsorption capacity of NFO@L and its efficiency in the removal of LFH and CIP upon varying the catalyst dosage

In contrast, the adsorption capacity decreased upon increasing the NFO@L dosage, which might be due to the increased cohesive interactions of nanocomposite-like aggregation/agglomeration and that could have resulted in a reduction in the effective surface area per unit mass of adsorbent and an increase in diffusion path length similar results have been reported in (Mashkoo et al. 2018; Zhang et al. 2019a). Apart from the surface area of the NFO@L, L-Leucine constitutes functional groups such as -COOH, NH₂, CH₃ and -OH in which NH₂ and -OH are exceptional chelation sites.

The optimal pH removal of both pollutants is at basic conditions and hence the increase of NFO@L dosage simultaneously increased the hydrogen bonding interaction between NH₂ of the NFO@L and -OH of the CIP. Meanwhile, in the case of LFH, the removal might have occurred through the transfer of free electrons and hydrophobicity as mentioned in section 4.6.11. The repulsive nature of like charges of LFH and NFO@L at the optimal pH and nanocomposite dosage resulted in decreased removal efficiencies compared to CIP (El-Sheikh et al. 2019; Guo et al. 2020b; Peñafiel et al. 2021).

4.6.13 Effect of initial concentration on the removal of LFH and CIP using NFO@L

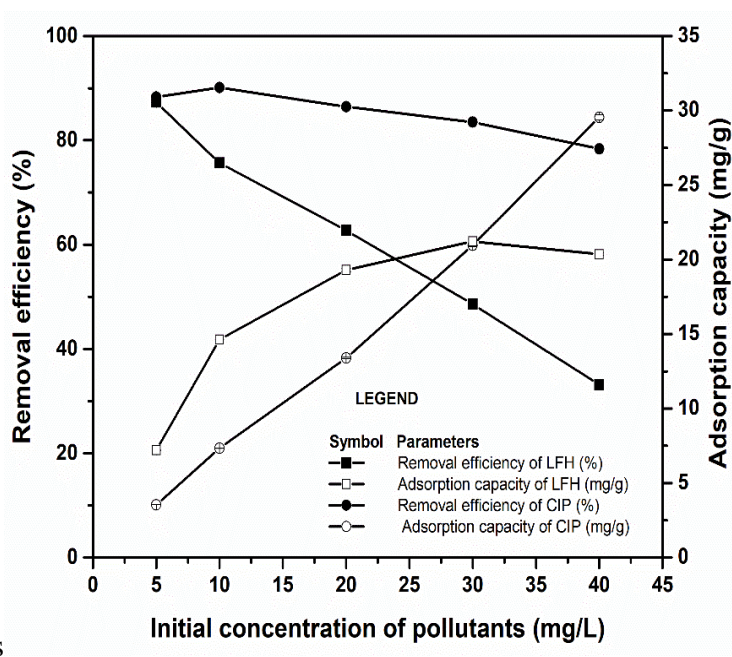


Fig. 4.42 The adsorption capacity of NFO@L and its efficiency in the removal of LFH and CIP at different initial concentrations

The effect of initial concentrations of LFH and CIP between 5 to 40 mg/L in 100 mL of working solution adsorbed over the optimum loading of NFO@L and pH for an equilibration time of 12 hrs has been studied. The removal efficiencies reduced from 88.22 % to 30.81 % and 88.31 % to 78.37 % for LFH and CIP respectively. The adsorption capacity increased and then slightly lowered at 40 mg/L of LFH aqueous solution from 8.11 to 19.37 mg/g as shown in Fig. 4.42, this might be because of the saturation of occupied sites. Upon further increase in the initial concentration, the overload of the pollutants onto the NFO@L surface resulted in the approachability to the saturation point. This implied that the optimized pH and NFO@L dosage

were most favourable to remove the LFH at a low concentration of the pollutant similarly in the case of CIP, 0.1 g of NFO@L in 100 mL of different initial concentrations resulted in an increased trend of adsorption capacity from 3.53 to 29.54 mg/g, which could be attributed to the increased mass molecular collision as driving force that pushed the CIP from the aqueous solution to the NFO@L surface (Nasiri et al. 2022).

4.6.14 Effect of time on the removal of CIP and LFH using NFO@L

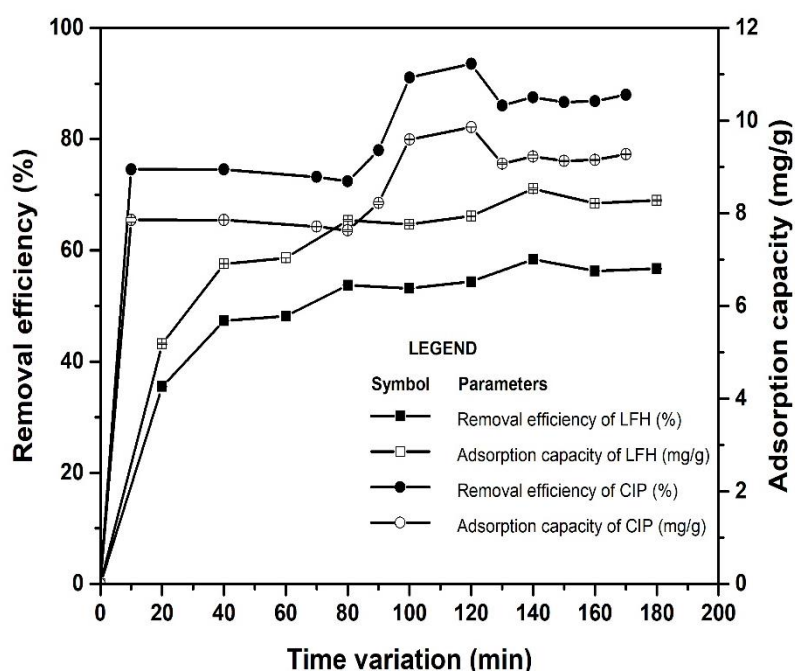


Fig. 4.43 The adsorption capacity of NFO@L and its efficiency in the removal of LFH and CIP upon varying the time

The optimized conditions from the above section were applied to study the reaction time in a 100 mL volume containing a 10 mg/L concentration of each pollutant. The effect of time on the removal percent of LFH and CIP and the adsorption capacity of NFO@L is displayed in Fig. 4.43. Almost 60 % of LFH was removed with the highest adsorption capacity of 8.52 mg/g within 140 min whereas 93.54 % of CIP was removed in 120 min with the highest adsorption capacity of 9.85 mg/g. Beyond this, the removal percent of both the fluoroquinolones decreased slightly. There observed a initial saturation after the first 15 min, this might be owing to the availability of vacant sites or there might have occurred adsorption-desorption equilibrium allowing for more efficient removal of the pollutant; after which the interaction of adsorbent-

adsorbate tends to slowly saturate by filling the available sites onto the nanocomposite with no significant shift in removal efficiency.

4.6.14 Effect of temperature on the removal of CIP and LFH using NFO@L

Fig. 4.44 illustrates the removal efficiency of LFH and CIP and the adsorption capacity of NFO@L trend at different temperatures (303 K, 313 K, 323 K, 333 K and 343 K). The maximal removal efficiency of 93.54 % and 7.77 mg/g of adsorption capacity of NFO@L towards CIP was favoured at 303 K.

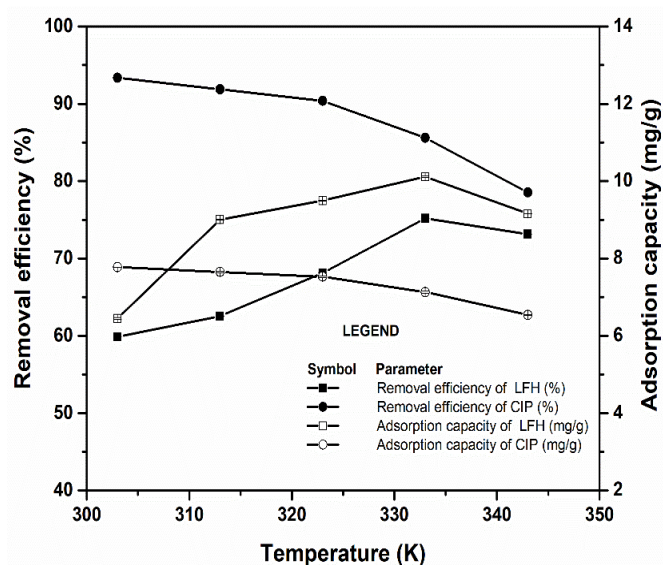


Fig. 4.44 The adsorption capacity of NFO@L and its efficiency in the removal of LFH and CIP upon varying the temperature

The increased temperature resulted in a reduction in removal efficiency, emphasising that adsorption does not require any external energy or high temperature to be maintained for the removal of CIP onto the NFO@L nanocomposite surface. The randomness of the CIP molecule increased as the temperature increased, potentially disrupting the bond between the NFO@L surface and the adsorbed CIP molecule onto it. As a result, CIP removal reduced as the temperature increased indicating an exothermic nature of the sorption process. In the case of LFH, a significant increase in efficiency of 75.19 % and an adsorption capacity of 10.11 mg/g at 333 K. The rate of LFH removal increased as temperature increased up to 333 K, indicating the absorption of heat energy favoured the LFH removal. The repulsion between LFH and NFO@L interactions was overcome by heat energy, resulting in increased efficiency at 333 K, after which there was a slight reduction in removal efficiency due to the reduction of the driving

force between LFH and NFO@L nanocomposite, which caused the adsorbed LFH molecule to escape from the nanocomposite (Al-Ghouti and Al-Absi 2020; Horsfall Jnr and Spiff 2005). Thus, the removal of LFH was favoured at 333 K, indicating an endothermic nature, and it was further validated by thermodynamic studies in section 4.6.18.

4.6.15 Adsorption Kinetics

The kinetics of adsorption helps in determining the rate law in designing a proper adsorption system moreover it also outlines the adsorption rate of CIP and LFH at the respective time at the NFO@L nanocomposite - pollutant interface.

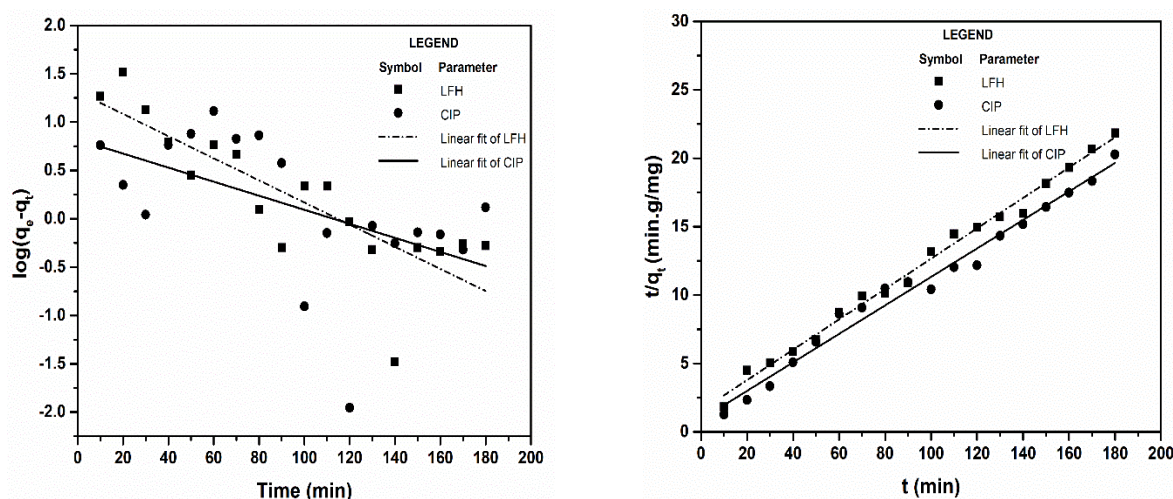


Fig. 4.45 A plot of (a) Pseudo first order kinetic model and (b) Pseudo second order kinetic model of CIP and LFH on NFO@L

A linear plot of t versus t/q_t i.e. pseudo-second order model showed a proper fit towards both the pollutant, indicating the chemisorption over the experimented time and the regression coefficient R^2 , k_1 , k_2 , $q_{e, cal}$ are listed in table 4.8. q_t is the adsorption capacity at time (mg/g), k_1 , k_2 is the equilibrium rate constant at the time, $q_{e, cal}$ equilibrium adsorption capacity. k_2 and $q_{e, cal}$ were calculated using slope and intercept (Ho and McKay 1999; Revellame et al. 2020) from the plot in Fig. 4.45 (a) and 4.45 (b).

Table 4.7 Estimated kinetic model parameters in the removal of CIP and LFH

Kinetic models	Pseudo first order kinetics			Pseudo second order kinetics		
Compounds	$q_{e,cal}$ (mg/g)	k_1 $(\frac{1}{min})$	R^2	$q_{e,cal}$ (mg/g)	k_2 (g/mg.min)	R^2
LFH	2.52	8.7×10^{-3}	0.36	8.67	0.18	0.99
CIP	1.94	6.8×10^{-3}	0.15	9.55	0.14	0.98

4.6.16 Adsorption Isotherm model for the removal of LFH and CIP

From the reaction time experimental datum, the kinetics and isotherm modelling were performed and studied in sections 4.6.16.1 to 4.6.16.3.

4.6.16.1 Langmuir and Freundlich Isotherm for the removal of LFH and CIP

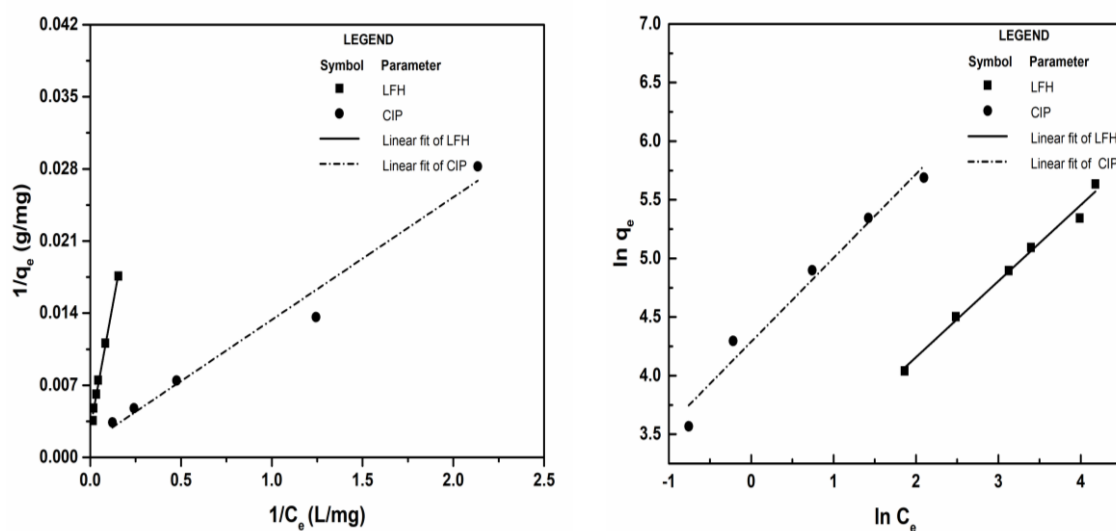


Fig. 4.46 (a) Langmuir Linear isotherm of CIP and LFH on NFO@L and (b) Freundlich isotherm of CIP and LFH on NFO@L

The removal mechanism involved in removing these pollutants has been verified for homogeneity and heterogeneity adsorption with similar or varied binding energies on the NFO@L surface active sites using Langmuir and Freundlich isotherm models (Appel 1973). The Langmuir constant, K_L and maximum monolayer adsorption capacity, q_{max} is calculated from the Langmuir linear plot between $(1/C_e)$ L/mg versus $(1/q_e)$ (g/mg) as shown in Fig. 4.46

(a). The Freundlich isotherm constant, K_F and $1/n$ is the constant both obtained from the straight- line graphical plot of $\ln C_e$ versus $\ln q_e$ as shown in Fig. 4.46 (b). The achievability of the adsorption process was witnessed from the $1/n$ value, which was in the mid of 0 to 1 for CIP which implies the chemisorption and the favourability of the adsorption process; whereas the $1/n$ value for LFH is greater than the unity, implying that the co-operative adsorption might have occurred (Foo and Hameed 2010).

Table 4.8 Separation factor of NFO@L upon LFH and CIP from the Langmuir isotherm

Initial Concentration (mg/L)	R_L (LFH)	R_L (CIP)
5	0.803	0.023
10	0.671	0.012
20	0.505	0.006
30	0.404	0.004
40	0.337	0.003

R_L is a dimensionless separation factor that indicates the favourability of the system and the values are presented in table 4.8. For both the pollutant R_L lies between 0 and 1 such that it indicates, that the adsorption is favourable (Khamparia and Jaspal 2017; Sawalha et al. 2007).

The q_{max} calculated from Langmuir isotherm showed a highest value of 34.18 mg/g for LFH and 8.40 mg/g for CIP. In Fig. 4.46 (a) and (b), the isotherm models proclaimed that the Langmuir isotherm is well-fitted exceeding the Freundlich isotherm for LFH while both the isotherm showed better fitting for the removal of CIP respectively.

4.6.16.2 Temkin isotherm for CIP and LFH removal using NFO@L

The study of Temkin isotherm was used in analyzing the interactions between the NFO@L nanocomposite and the fluoroquinolones. The isotherm illustrates that the quantity of heat of adsorption of pollutant molecules decreases linearly rather than logarithmic with the surface coverage of NFO@L. The value of B was calculated using the slope and intercept of the plot in Fig. 4.47 is listed in table 4.9 which was found to be < 8 kJ and > 0 that there might be a release of heat during adsorption indicating the exothermic nature of the process for both fluoroquinolones at 303 K (Araújo et al. 2018). Similar results were observed in the work of

functionalized multi-walled carbon nanotubes for the removal of toxic dyes (Saxena et al. 2020).

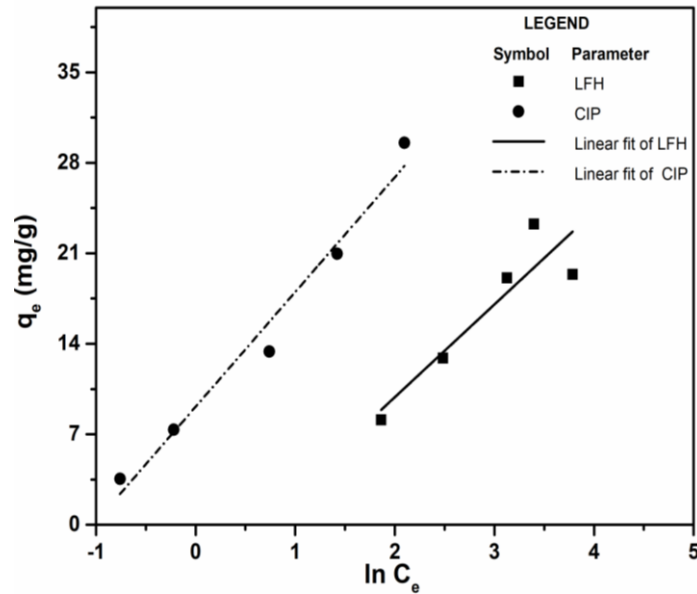


Fig. 4.47 Temkin isotherm plot of $\ln C_e$ versus q_e for CIP and LFH

4.6.16.3 Dubinin -Radushkevich isotherm for the removal of LFH and CIP

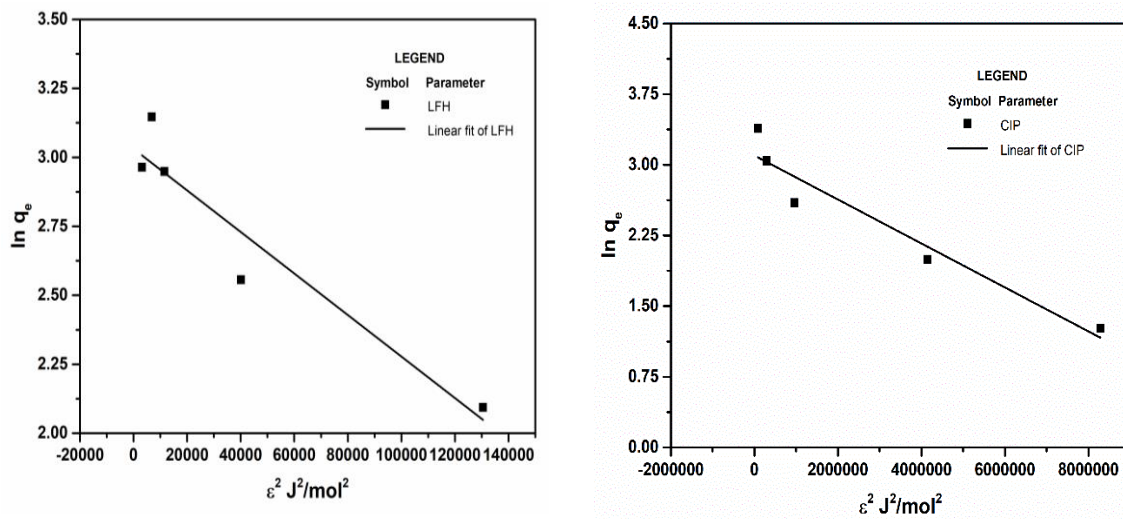


Fig. 4.48 Dubinin -Radushkevich isotherm plot of ϵ^2 versus $\ln q_e$ for the removal of (a) LFH and (b) CIP

Dubinin - Radushkevich accounts for the potential theory of adsorption and also includes assumptions such as adsorption occurs through micropore volume filling rather than multi-layer adsorption on the surface, which also includes the adsorption on the porous structure of

the nanocomposite (Araújo et al. 2018; Hu and Zhang 2019). The $q_{\max} = \exp(\text{intercept})$, $\beta = -$ slope, and E was calculated from the graphical plot between ε^2 versus $\ln q_e$ shown in Fig. 4.48 (a) and (b). The mean free energy in the D-R equation for CIP is high compared to the binding energy calculated from the Temkin isotherm conversely it is the reverse for LFH. It is evident from the listed values in table 4.9, that the mean free energy (DR isotherm) and binding energy (Temkin isotherm) are $< 8\text{kJ}$ indicating that less energy was required for the sorption of both pollutants at 303 K (Hu and Zhang 2019) indicating chemisorption of both the pollutants at 303 K.

All the isotherm variables are presented in table 4.9. On comparing all the isotherm models and from table 4.9 it is noted that the Langmuir isotherm is well-fitted exceeding all other isotherm models with a regression coefficient of 0.95 for LFH implying that the removal of LFH follows monolayer adsorption. On the contrary, Langmuir, Freundlich and Temkin isotherms fitted well for CIP with the regression coefficient of 0.96 which indicates that the removal at first could have followed homogenous subsequently heterogeneous adsorption might have occurred. The nanocomposite might have both the uniform and heterogeneous surface and hence it has fitted with the three models.

Table 4.9 List of parameters from the Langmuir, Freundlich, Dubinin–Radushkevich, Temkin isotherm

Isotherm and Parameters		LFH	CIP
Langmuir isotherm	q_{\max} (mg/g)	34.18	8.40
	K_L (L/mg)	0.04	8.17
	R^2	0.95	0.96
Freundlich isotherm	$1/n$	1.67	0.71
	K_F (mg/g)(L/mg)^{1/n}	0.18	1.53
	R^2	0.81	0.96
Temkin isotherm	E (J/mol)	349.02	281.81
	A_T (L/g)	0.98	1.032
	B	7.52E-6	2.33E-7
	R^2	0.77	0.96
Dubinin–Radushkevich isotherm	q_{\max} (mg/g)	8.23	8.39
	E (J/mol)	257.85	1464.89

4.6.17 Thermodynamics studies for the removal of CIP and LFH

The thermodynamic properties for the removal of LFH and CIP onto NFO@L nanocomposite surface at different temperatures (303, 313, 323 and 333 K) were estimated and analyzed for the feasibility and the spontaneity of the adsorption process. The thermodynamic parameters such as enthalpy (ΔH°) in kJ/mol and entropy (ΔS°) in kJ/mol.K were calculated from the slope and intercept of the plot $1/T$ versus $\ln K_{eq}$ is shown in Fig. 4.49. The experimental datum obtained from section 4.6.14 was used in plotting the van't Hoff plot and the Gibbs free energy change (ΔG°) in kJ/mol was calculated using the following equation

$$\Delta G^\circ = -RT \ln(K_{eq}) \quad (21)$$

$$\ln(K_{eq}) = \frac{\Delta S^\circ}{R} - \frac{\Delta H^\circ}{RT} \quad (22)$$

Where K_{eq} is the equilibrium constant (dimensionless), T is the temperature in Kelvin, and R is the gas constant (8.314 J/mol.K). The calculated thermodynamic parameters are listed in table 4.10. The negative value of ΔG° at all four different temperatures for both pollutants indicates the spontaneity of the adsorption process.

In the case of CIP, the $\Delta H^\circ < 0$ indicates the exothermic nature of the process with sorption involving chemical bonding interactions similar results were noted in (Elham Ahangaran et al. 2020) and the negative value of ΔS° indicated the increase in orderliness at the pollutant - nanocomposite interface. In the case of LFH, the positive value of ΔH° indicates the endothermic nature of adsorption. Though the ΔH° value lies within the physisorption range of -20 to 40 kJ/mol, an increase in temperature increased the kinetic energy of interacting molecule by absorbing the heat energy along with the surface properties and that might have increased the collision between NFO@L and LFH, suggesting that the LFH removal followed chemisorption. The positive range of ΔS° suggests the randomness at the pollutant-nanocomposite interface throughout the adsorption process (Khan et al. 2010).

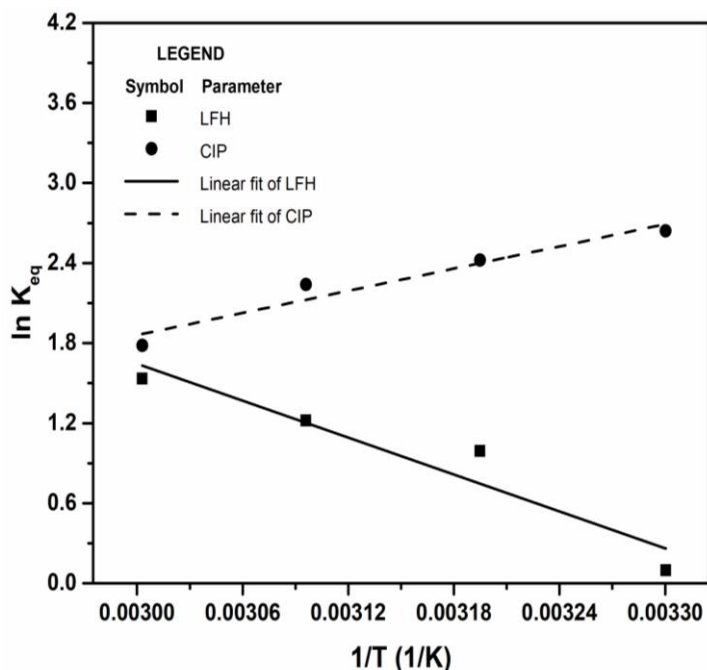


Fig. 4.49 van't Hoff plot for the removal of LFH and CIP

Table 4.10 Thermodynamic parameters for adsorption of LFH and CIP onto NFO@L

Pollutants	ΔH° (kJ/mol)	ΔS° (kJ/mol. K)	(-) ΔG° (kJ/mol)			
			303 K	313 K	323 K	333 K
LFH	38.33	0.12	19.92	20.57	21.23	21.89
			32.81	33.89	34.97	36.05
CIP	-23.03	- 0.05				

4.6.18 Regeneration and recycle studies of NFO@L nanocomposite

The recycling studies of the nanocomposite on the removal of two pollutants were presented in this section. The washed solvents revealed that the Methanol washing of NFO@L showed the highest removal efficiency of 92.98 % for CIP and 75.19 % for LFH. Further, the regenerated nanocomposite was used for up to four-cycle runs using methanol. Fig. 4.50 and 4.51, illustrate that there is a reduction in the removal efficiency of LFH to 57.20 % analogously CIP removal efficiency was also reduced to 79.69 % after four cycle runs. Table 4.11 depicts a comparative study of commercial adsorbents in the removal of LFH and CIP.

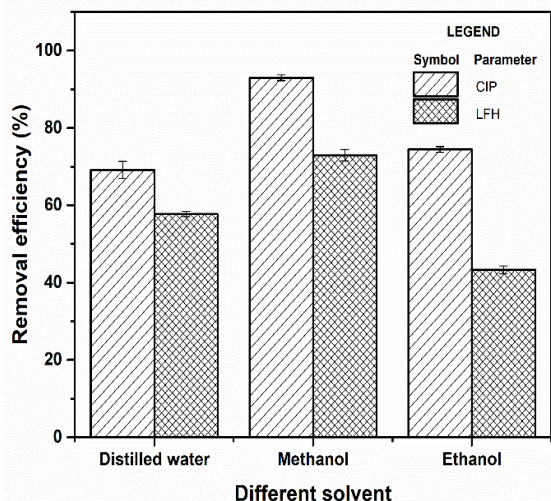


Fig. 4.50 Regeneration of the NFO@L using three different solvents

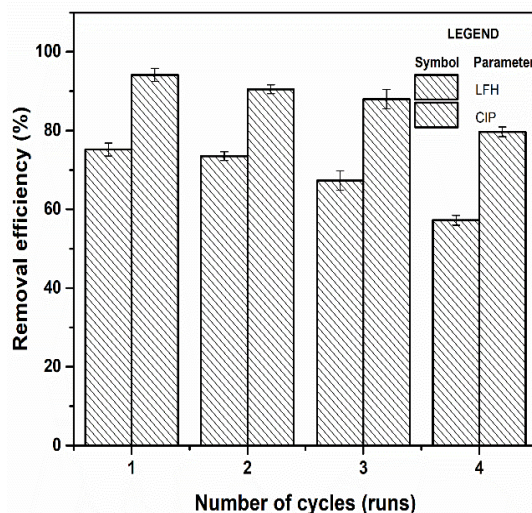


Fig. 4.51 Removal efficiency of LFH and CIP upon regenerated NFO@L after four runs

Table 4.11 A comparison of commercially used adsorbents in the removal of LFH and CIP

S. No	Pharmaceutical pollutants/ Adsorbent	Input Parameters	Results obtained	References
1	Ciprofloxacin / Sugarcane bagasse (SB) and powdered activated carbon (PAC)	Initial Concentration - 20 mg/L, dosage Sugarcane bagasse (SB) -3g/L at pH-6, Powdered activated carbon (PAC) -0.3g/L at pH-8	The adsorption capacity for sugarcane bagasse (SB) is 5.7 mg/g, saturation time is 60 min. Powdered activated carbon (PAC) - 50.1 mg/g, removal efficiency - 78 % for both the adsorbent, saturation time -100 min. (There are no regeneration and recycling experiments)	(Li et al. 2015)
2	Lomefloxacin Hydrochloride/ Activated carbon	Initial concentration -2 mg/L, powdered activated carbon dosage (PAC) -8 mg/L, equilibration time -48	Removal efficiency is 80-96 % at equilibration time between 30-40 hrs.	(Fu et al. 2016)

		hrs pH -7, temperature - 25°C.	Adsorption capacity (Langmuir isotherm) is 413 mg/g. (There are no regeneration and recycling experiments)	
3	Ciprofloxacin/ Bentonite	Initial Concentration - 500 mg/L, pH -2 to 8, adsorbent dosage -2.5 g/L, agitation speed - 100-300 rpm, ionic strength (KCl) -5-50 mM, time -0 -210 min	Optimum time -30 min, adsorption capacity -147 mg/g. (There are no regeneration and recycling experiments)	(Genç et al. 2013)
4	Ciprofloxacin/ Activated Carbon	Initial concentration -3-30 mg/L, pH - 5, equilibration time -72 hrs, adsorbent dosage - 2.5 mg.	Adsorption capacity (Activated Carbon) -230 mg/g (There are no regeneration and recycling experiments)	(Carabineiro et al. 2012)
5	Ciprofloxacin/ Montmorillonite	Initial concentration - 500 - 4000 mg/L, volume of solution -20 mL, Adsorbent dosage - 0.2 g, pH -2.5 - 11, equilibration time -24 hrs,	Equilibrium concentration -80 mg/L Adsorption capacity -330 mg/g, removal efficiency - 97 % (There are no regeneration and recycling experiments)	(Wang et al. 2010)
6	Ciprofloxacin and Lomefloxacin Hydrochloride/ Goethite	Initial concentration - 1.5µM, Adsorbent dosage -0.44 g/L, pH -5, time -4 to 6 hrs	Removal efficiency Ciprofloxacin -62 %, Lomefloxacin hydrochloride - 54 %	(Zhang and Huang 2007)
7	Ciprofloxacin hydrochloride/ NFO@L	Initial concentration -10 mg/L, adsorbent dosage -100 mg, equilibration time -12 hrs, pH -8, temperature -311, 313 and 323 K	Removal efficiency - 93.549 % at temperature - 303 K within 120 min, adsorption capacity – 8.40 mg/g	This work
8	Lomefloxacin hydrochloride/ NFO@L	Initial concentration -10 mg/L, adsorbent dosage -70 mg, pH -9, equilibration time -12 hrs, temperature -311, 313 and 323 K	Removal efficiency - 75.192 % at temperature - 333 K within 140 min, adsorption capacity – 34.18 mg/g	This work

4.6.19 FTIR image after adsorption of CIP and LFH

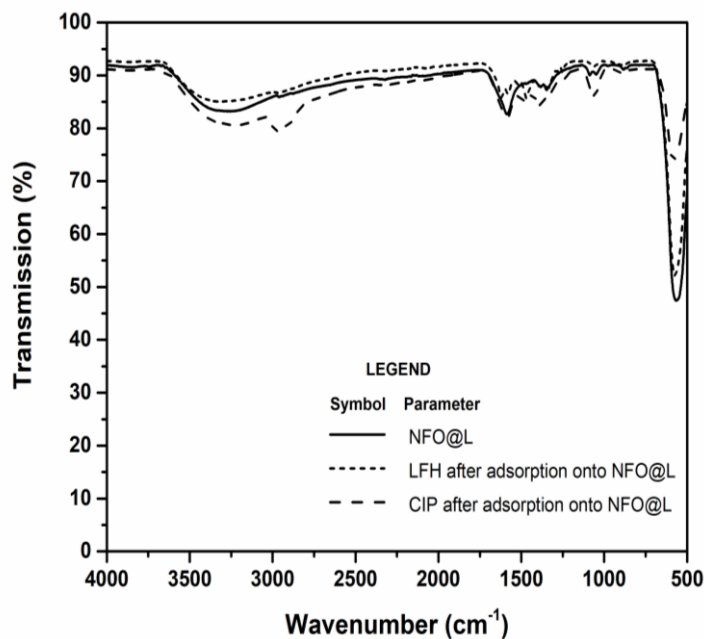


Fig. 4.52 A stacked FTIR of NFO@L nanocomposite and the composite after adsorption of CIP and LFH onto nanocomposite

Metal-oxide bonds, particularly in ferrite-based particles were identified in the range 1000 - 500 cm^{-1} with the highest stretching due to the tetrahedral metal-oxygen bond observed in the range 600 -550 cm^{-1} and the lowest stretching found in the range between 450 -385 cm^{-1} (Jacob et al. 2011a). The presence of NH_3 and COO^- in between 500 – 650 cm^{-1} is in waving form; in addition to this, N–H and C–H stretching vibrations that correspond to 2500 – 3200 cm^{-1} confirmed the functionalization of L-Leucine onto Nickel Ferrite (NFO@L). A peak near 2300-2500 cm^{-1} indicates the NH_2^+ overtones and combinations; a bending at 1713.48 cm^{-1} is due to the C=O carboxylic acid stretch and a downward stretch was visible between 2850-3000 cm^{-1} due to the presence of Nujol, as well as the attachment of Fluorine group could be seen in the after adsorption of LFH on NFO@L trend (Sanzgiri et al. 1994).

The existence of CH_2 on the benzene ring in ciprofloxacin could be seen in the after-adsorption of ciprofloxacin on the NFO@L trend in the wavenumber 1510 cm^{-1} . The carbonyl and hydroxyl stretching vibrations in the $-\text{COOH}$ could be seen in 1700 -1800 and 3400 -3500 cm^{-1} wavenumber, respectively, while the peaks between 2800 -3000 cm^{-1} correspond to $-\text{CH}_2$ and $-\text{CH}$, all these stretching and bending's could be seen in all three FTIR image (Zhang et al. 2020b). The functional group O–H contributes to the bending between 1400 and 950 cm^{-1}

whilst the peak near 750 cm^{-1} is attributed to CH_2NH , affirming the attachment of ciprofloxacin and lomefloxacin hydrochloride to NFO@L respectively (Brittain 1993; Tan et al. 2012) as shown in Fig. 4.52.

4.7 Nickel ferrite (NFO) as a nanocatalyst/PMS

NFO as a nano-catalyst with an oxidizing agent (PMS) experimented with varied affecting parameters for the degradation of CAF and LFH and the final analyte was analyzed with LC-MS analysis, and ICP-OES were featured and discussed in this section from 4.7.1 to 4.7.11.

4.7.1 Effect of bare NFO on the degradation of CAF and LFH

Initially, adsorption experiments were conducted with the NFO catalyst alone, before determining the activation of PMS using NFO for the degradation of CAF and LFH.

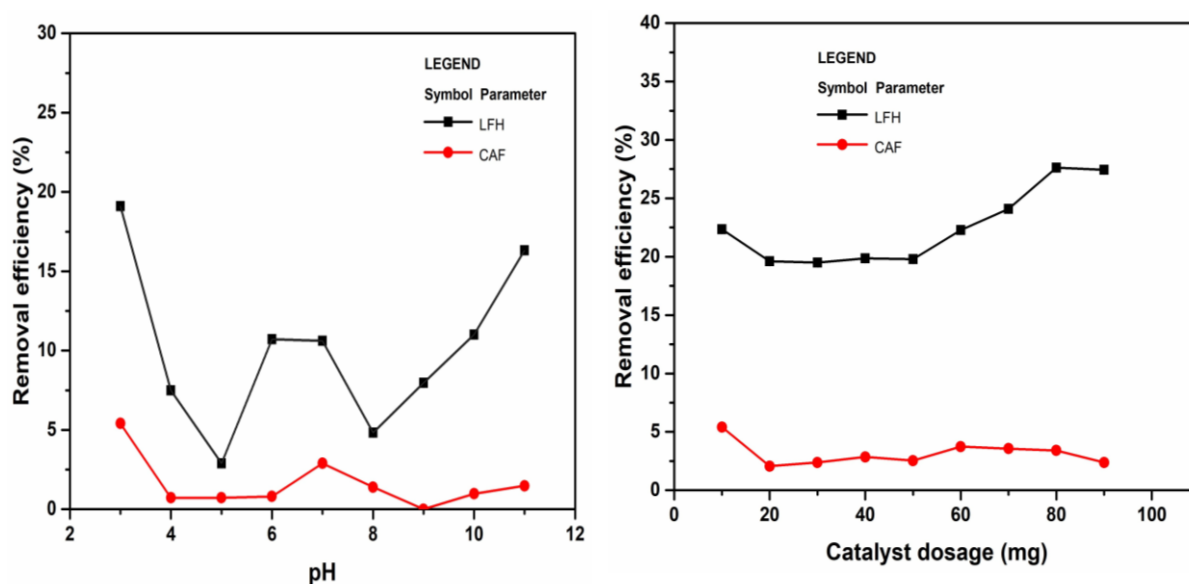


Fig. 4.53 (a) Effect of pH on the removal of LFH and CAF using Bare NFO

Fig. 4.53 (b) Effect of catalyst dosage on the removal of LFH and CAF using Bare NFO

From Fig. 4.53 (a) and (b) it could be depicted that the varied pH and catalyst dosage showed a lower removal efficiency of 5.4 % of CAF and 19.11 % of LFH at pH 3 whereupon varying the catalyst dosage from 10 to 90 mg at pH 3 showed negligible effect on the CAF and a 27.47 % increase in efficiency of LFH was observed at 80 mg. The result shows that NFO alone has very less affinity towards the removal of CAF and LFH.

4.7.2 Effect of PMS with no catalyst on the degradation of CAF and LFH

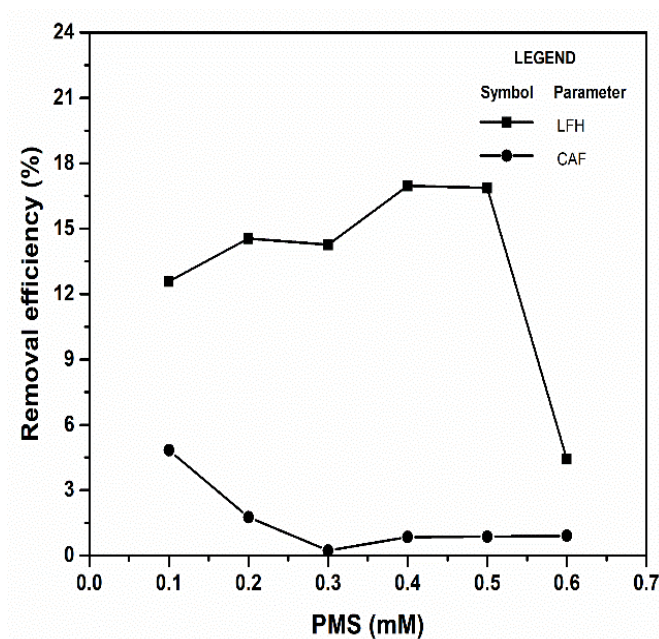


Fig. 4.54 Effect of PMS alone on the degradation of CAF and LFH

The experiments were conducted in a 100 mL volume of solution with PMS, without the catalyst, and no change in pH for each of the pollutants; from which 0.4 mM and 0.1 mM were found to be optimum with removal efficiencies of 16.87 % and 5.12 % for LFH and CAF respectively, as shown in Fig. 4.54. When the PMS concentration was increased from 0.1 mM to 0.6 mM, LFH degradation decreased beyond the optimum value, whereas CAF degradation efficiency decreased until 0.3 mM, after which a slight rise with a steady state maintained in the efficiency was observed. Two-electron oxidation would have occurred in LFH via PMS-produced hydroxylated N-oxide and dealkylated low antibacterial activity products that could attack the aliphatic N4 amines on the piperazine ring. As a result, the generation of amide and aldehyde moieties could have occurred via dealkylation and hydroxylation reactions. Thus, using PMS alone for the degradation of CAF and LFH is less reactive to pollutants containing electron-deficient moieties such as nitro and carboxy groups, which could also explain the low degradation efficiency (Ding et al., 2021) meanwhile it also indicates the slow self decomposition of PMS without activation (Andrew Lin and Chen 2016). Since the NFO catalyst and PMS alone were insufficient for the degradation of CAF and LFH separately. A combination of NFO catalyst and PMS was subjected to step-by-step varied parametric studies such as pH, NFO catalyst dosage, PMS dosage, pollutant concentration and reaction time.

4.7.3 Effect of pH on the degradation of CAF and LFH using NFO

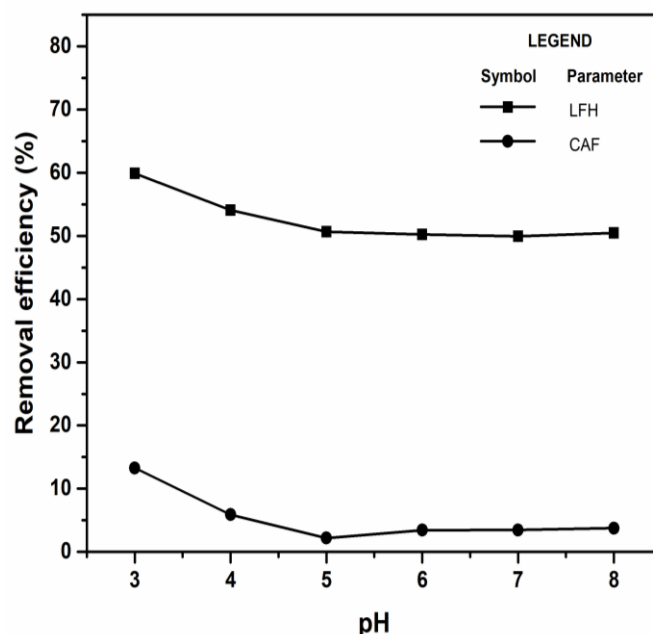


Fig. 4.55 Effect of pH on the degradation of CAF and LFH using NFO

The activation energy, oxidation potential, surface charge, and stability of nickel ferrite nanoparticles can all be greatly influenced by pH (Sun et al., 2022). From the aforementioned parametric studies, the optimized PMS, 0.4 mM (LFH) and 0.1 mM (CAF), was further subjected to varied pH (3-8) in the presence of 10 mg NFO catalyst in a 100 mL volume of solution containing 10 mg/L concentration. Fig. 4.55 shows that pH 3 has a peak removal efficiency of 13.78% CAF and 60 % LFH. At pH 5, H^+ ions scavenge sulfate and hydroxyl radicals, as shown in equations 24 – 33; additionally, PMS is unaffected by pH less than 6 and at extreme alkaline conditions of pH 12. In highly acidic pH 1 conditions, PMS hydrolyzes to form H_2O_2 (Ghanbari and Moradi 2017). When the pH of the reaction is raised to more alkaline conditions (pH >10), the oxidative capacity of $\bullet OH$ is not as good as that of $SO_4^{\bullet -}$, so the degradation efficiency remains stable. Metal ion precipitation at pH > 3 is also one of the reasons for maximum degradation in the homogeneous system at pH-3 (Ghanbari and Moradi 2017; Sun et al. 2022a). The negative surface of NFO observed from the zeta potential result and the contaminant solution pH 3 has a strong affinity in the removal of LFH whereas in the case of CAF, the efficiency has increased in the combined effect of NFO/PMS system in comparison with the effect of NFO and PMS separately. A similar observation of catalyst affinity to pollutants under acidic conditions was also found in the literature (Andrew Lin and Chen 2016). The increase of solution pH increased the production of OH^- ions concentration

that ended up in more negatively charged ions at the same time the negative surface charge of the NFO catalyst and solution pH inhibited the formation of $\text{SO}_4^{\cdot-}$ leading to the lesser removal efficiency of both the pollutant in the basic solution pH (Andrew Lin and Chen 2016).

4.7.4 Effect of NFO dosage on the degradation of CAF and LFH

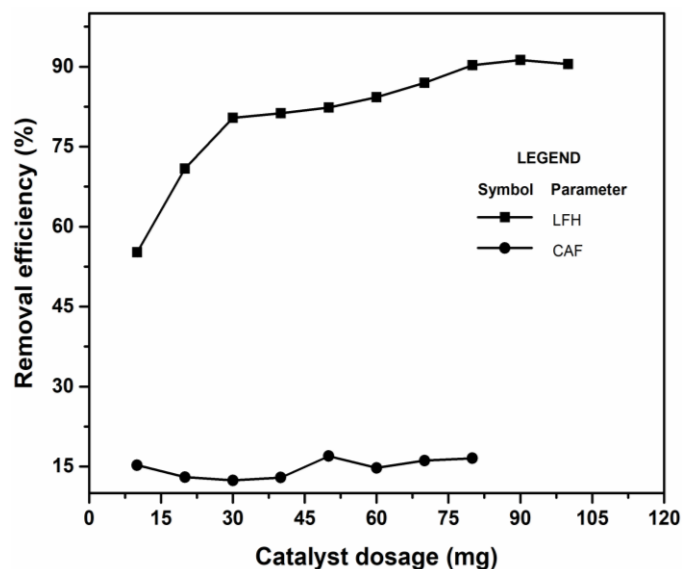


Fig. 4.56 Effect of varied NFO dosage on the degradation of CAF and LFH

Fig. 4.56 shows that when the optimised PMS and pH were fixed, and the amount of NFO was varied from 10 to 100 mg for LFH and 10 mg to 80 mg for CAF, nearly 92.80 % of LFH and 16.94 % of CAF were degraded. Increasing the dosage increased the degradation efficiency of LFH and CAF until it reached its optimal amount, indicating that increasing the NFO dosage increased the number of active sites for the PMS to interact with and produce free radicals on the catalyst surface above that no significant shift was observed while measuring; thus, 90 mg was chosen as the optimum value, whereas in the case of CAF above 50 mg, there is no significant increase; rather, the efficiency slightly varies, indicating that there is no further production of free radicals and saturation of active sites in the NiFe_2O_4 nanoparticles.

4.7.5 Effect of variation of PMS in the optimized dosage on the degradation of LFH and CAF

By varying the PMS with an optimized catalyst dosage and pH, the exact amount of PMS required for the degradation of LFH and CAF was estimated. In this case, LFH and CAF were

chemically degraded with an optimal PMS molar of 6 and 3 mM, respectively, with a peak removal percent of 99.42 % and 98.64 %, as shown in the graph in Fig. 4.57.

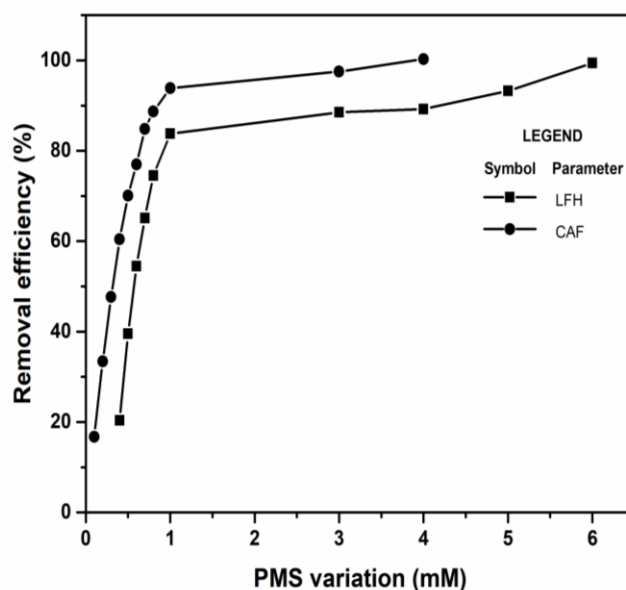


Fig. 4.57 Effect of varied PMS with the optimized dosage on the degradation of LFH and CAF

Excessive PMS dosage could harm the NFO/PMS AOP system. Increasing of PMS dosage above the optimum condition may react and eradicate sulfate radicals and generate low reactivity radicals (SO_5 and HO_2). As a result, additional experiments were carried out with 6 mM and 3 mM of PMS in the degradation of LFH and CAF, respectively, with the optimized NFO dosage and PMS, which induced sufficient radical production, provided enough surface area with the mesoporous structure, as well as the adsorption capacity, and resulted in the degradation of LFH and CAF using $\text{NiFe}_2\text{O}_4/\text{PMS}$. The varied PMS dosage at the optimized NFO mass implies that the degradation of CAF and LFH is the main deciding factor as the sulfate radicals were produced from PMS rather than NFO which acts as an activator only (Homem and Santos 2011).

4.7.6 Effect of initial concentration of CAF and LFH on the degradation efficiency

The pollutant's initial concentration is a substantial factor that can affect the optimum catalyst dosage, removal efficiency and kinetics (Mahalakshmi et al., 2007). The above parameters were held constant while each of the initial LFH and CAF concentrations in a conical flask was

varied. The pollutant's initial concentration is a substantial factor that can affect the optimum catalyst dosage, removal efficiency and kinetics (Mahalakshmi et al., 2007). The above parameters were held constant while each of the initial LFH and CAF concentrations in a conical flask was varied. Over 12 hrs, increasing the initial concentration from 10 to 40 mg/L, reduced the CAF and LFH degradation efficiency from 99.42 to 87.61 % and 98.64 % to 93.06 %, respectively as displayed in Fig. 4.58. As the pollutant's initial concentration increases eventually more of the reactant molecule adheres to the surface of the NFO catalyst which may result in a reduced radical generation. Mostly, the degradation rate increases with an increase in the catalyst dosage at a low pollutant initial concentration, this might be due to the sufficient amount of radical generation. Hence the generated radicals ($\text{OH}\cdot$ and $\text{SO}_4^{\bullet-}$) from the optimized conditions in the $\text{NiFe}_2\text{O}_4/\text{PMS}$ system at 10 mg/L concentration of LFH and CAF may be insufficient to degrade the increased initial pollutant concentration range greater than 10 mg/L of both pollutants (Mirzaei et al. 2016).

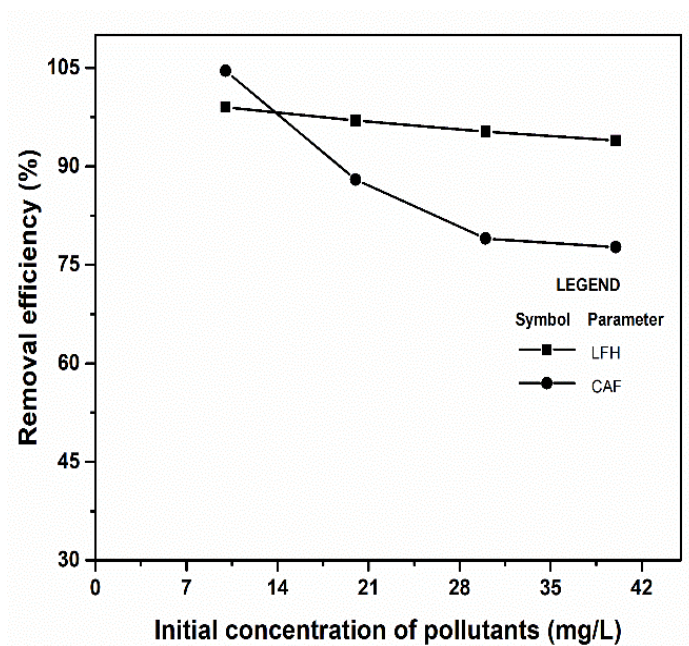


Fig. 4.58 Effect of initial concentration on the degradation of CAF and LFH

The higher the initial concentrations of CAF and LFH, the more of these pollutants and their intermediates existed in the solution, while the number of reactive species produced in the reaction system remained constant under the same conditions, resulting in stronger competition for reactive species, catalyst deactivation and a drop in degradation trend was observed in Fig. 4.58 with the varied initial concentration of both pollutants (Wang et al. 2017). As aforementioned specific surface of the NFO catalyst is comparatively less compared to other

commercial adsorbents and catalysts; hence lower the specific surface area with larger crystals at higher initial pollutant concentration might lead to catalyst deactivation. From this observation, the NFO catalyst behaviour implies that the pollutant concentration completely depends on the NFO catalyst-pollutant initial concentration mass ratios (Mirzaei et al. 2016).

4.7.7 Effect of reaction time on the degradation of CAF and LFH

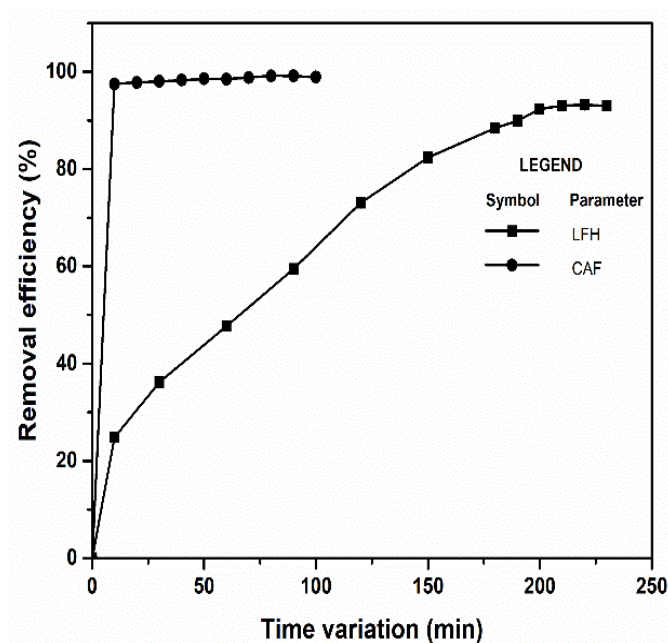


Fig. 4.59 Effect of reaction time on the degradation of CAF and LFH

The maximum time required to chemically degrade CAF and LFH using PMS was determined by varying the time from 0 to 230 min for LFH and 0 to 100 min for CAF. Fig. 4.59 shows the stability of both pollutants even after extending the reaction time above its optimal reaction time in which almost 100 % of CAF and 98.61 % of LFH were degraded. Different pollutant might follow different degradation pathway, CAF degrades in lesser time comparable to LFH. This might be due to its chemical structure, breaking down of intermediates and the presence of oxidizable function groups. The utilisation of the entire, free radicals produced by the NiFe₂O₄ nanocatalyst and PMS, as well as the simultaneous saturation of active sites on the nanocatalyst surface, resulted in steady state degradation of both pollutants above the optimal time (Mirzaei et al. 2016).

4.7.8 Effect of PMS, NFO dosage and reaction time on the LFH and CAF mixed solution (LC)

A reaction mixture containing two different pollutants have been experimented to study the behaviour of NFO catalyst. NFO was experimented with LFH and CAF mixed solution (LC) since each of the solutions (LFH and CAF) showed better efficiency at pH 3; the LC solution was experimented with varied PMS concentrations, NFO dosage and reaction time was experimented at pH 3. Fig. 4.60 (a) displays the calibration graph of the LFH and CAF mixed solution (LC). 7 mM of PMS concentration degraded 95.88 % of LC solution at an equilibration time of 12 hrs as shown in Fig. 4.60 (b). Further, NFO dosage was varied at an optimized PMS of 7 mM in which 20 mg of NFO degraded 96.03 % of the LC solution. All the above-equilibrated parameters are kept constant and the reaction mixture was analyzed with varied reaction time. The NFO catalyst showed good efficiency with 20 mg of catalyst dosage in a 100 mL volume of solution. Reduced removal efficiency was observed in Fig. 4.60 (c) upon increasing the catalyst dosage might be because the agglomeration of the catalyst at increased catalyst dosage interferes with the LC reaction mixture leading to an occupied active surface and hence decreases the generation of radicals by reducing the activity of the catalyst (Ahmadi et al. 2017).

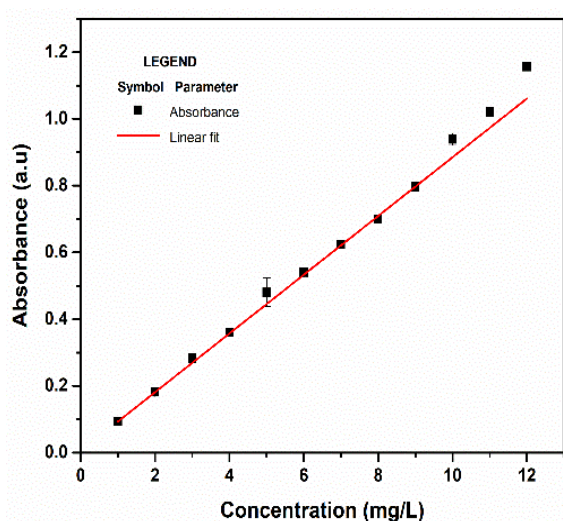


Fig. 4.60 (a) Calibration graph of LFH and CAF mixed solution (LC)

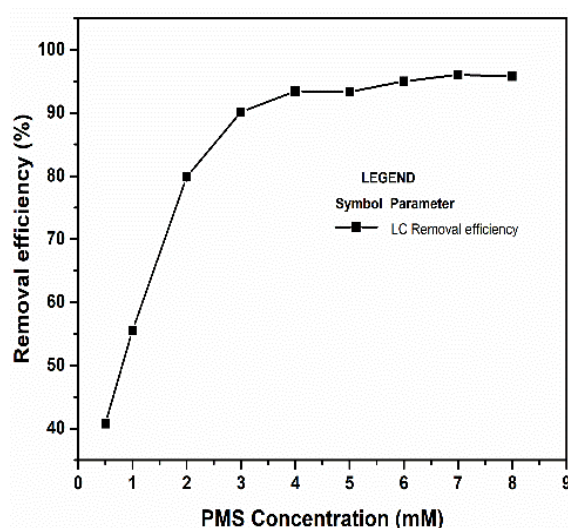


Fig. 4.60 (b) Variation of PMS Concentration in the LFH and CAF mixed solution (LC) at pH 3

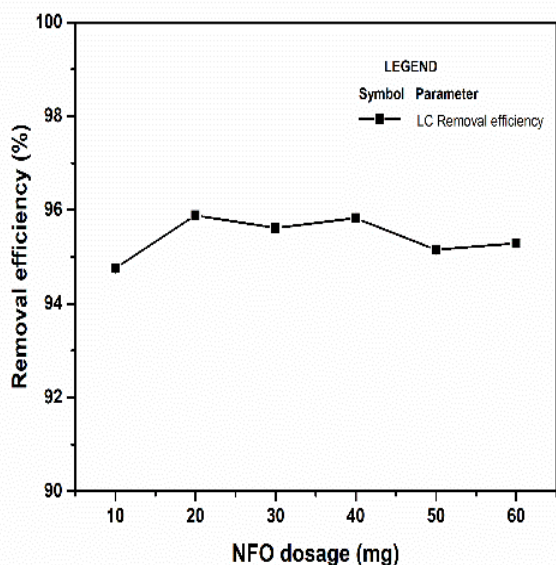


Fig. 4.60 (c) Variation of NFO dosage at optimized PMS in the LFH and CAF mixed solution (LC)

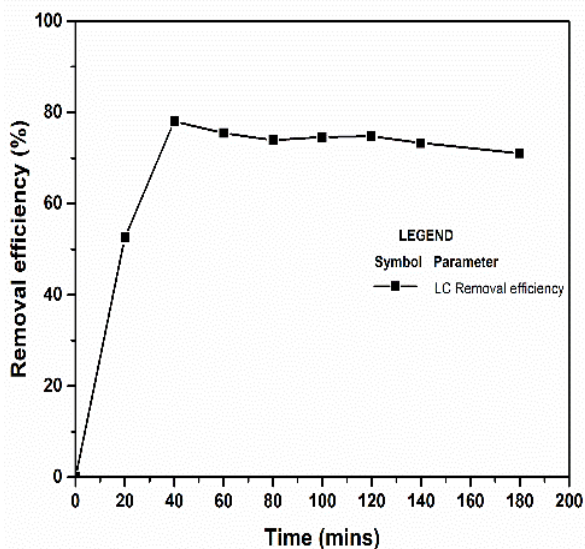


Fig. 4.60 (d) Variation of reaction time at optimized NFO dosage in the LFH and CAF mixed solution (LC)

Fig. 4.60 (d) displays a degradation of 78.07 % of LC solution at a reaction time of 40 mins upon varied reaction times. A decreased efficiency was observed in comparison with the LFH and CAF separately. The degraded intermediate metabolites can also affect the catalytic activity of the NFO (Ahmadi et al. 2017).

4.7.9 Mechanism involved in the generation of free radicals



As shown in equations (4.3) and (4.4), the rate-determining step is the formation of numerous NiOH^+ and FeOH^{2+} on the NFO surface upon PMS stimulation. The resulting FeOH^{2+} reacts with Ni^{2+} to form NiOH^+ , as shown in equations (4.5) and (4.6). NiOH^+ and Fe^{3+} combine with hydrogen bonds and HSO_5^- on the surface of the nanoparticles to form $\text{NiFe}_2\text{O}_4\text{-O-H-HSO}_5^-$, which is then split into NiO^+ , $\text{SO}_4^-\cdot\text{H}_2\text{O}$, and NiOH^+ as in equation (4.7). This reaction operates as a cycle, resulting in the repeated formation of NiOH^+ , NiO^+ also oxidises in the presence of H^+ to form Ni^{3+} , which then combines with HSO_5^- to form Ni^{2+} , as shown in equations (4.8) and (4.9). On the other hand, Fe^{3+} on the surface of NiFe_2O_4 stimulates HSO_5^- , which splits to $\text{SO}_4^-\cdot$ and $\text{SO}_5^-\cdot$ as described in equations (4.10) and (4.11), and this $\text{SO}_4^-\cdot$ combines with H_2O to form SO_4^{2-} , $\cdot\text{OH}$, H^+ as mentioned in equation (4.12). As an outcome of the combined effect of the $\text{NiFe}_2\text{O}_4/\text{PMS}$ system, the metal ions Ni and Fe could reform to Ni^{2+} - Ni^{3+} - Ni^{2+} and Fe^{3+} - Fe^{2+} - Fe^{3+} on the surface of NFO nanoparticles, and the valence states of Ni and Fe could re-transform to divalent and trivalent states, resulting in the generation of $\text{SO}_4^-\cdot$ and $\cdot\text{OH}$ (Zhang et al. 2022).

4.7.10 Degradation kinetic studies of CAF and LFH

The kinetic experiments aid in determining the rate constant in the degradation of CAF and LFH utilizing PMS-activated NFO nanoparticles. The pseudo zero order kinetics assumes that the rate is independent of reactant concentration, whereas the pseudo first and second order kinetics assume that the rate is directly proportional to reactant concentration, while the latter depends on the reacting species involved in the reaction. The experimental datum was used to plot the pseudo zero order, pseudo first order, and pseudo second order kinetics, and is shown below.

Pseudo zero order of reaction

$$\text{Rate} = -\frac{d[C_f]}{dt} = k[C_f]^0 = k = \text{constant} \quad (4.13)$$

Pseudo first order of reaction (Langmuir Hinshelwood model)

$$[C_f] = [C_o]\exp(-kt) \quad (4.14)$$

$$\ln \frac{C_f}{C_o} = kt \quad (4.15)$$

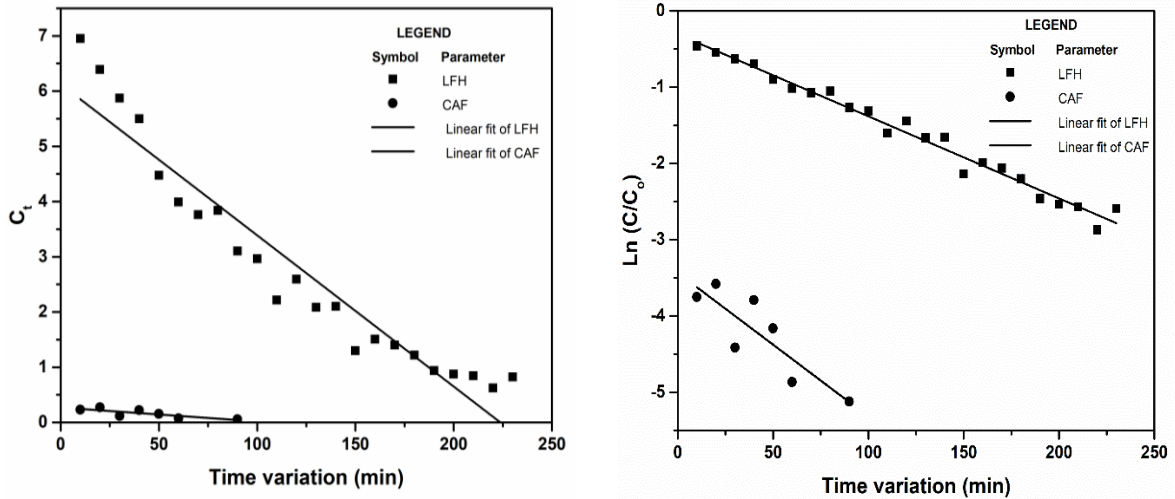


Fig. 4.61 (a) Zero order reaction **(b)** Pseudo first order kinetics for the removal of LFH and CAF

Pseudo second order of reaction (Ho model)

$$\frac{1}{C_f} = \frac{1}{C_0} + kt \tag{4.16}$$

$$\frac{1}{C_0} - \frac{1}{C_f} = kt \tag{4.17}$$

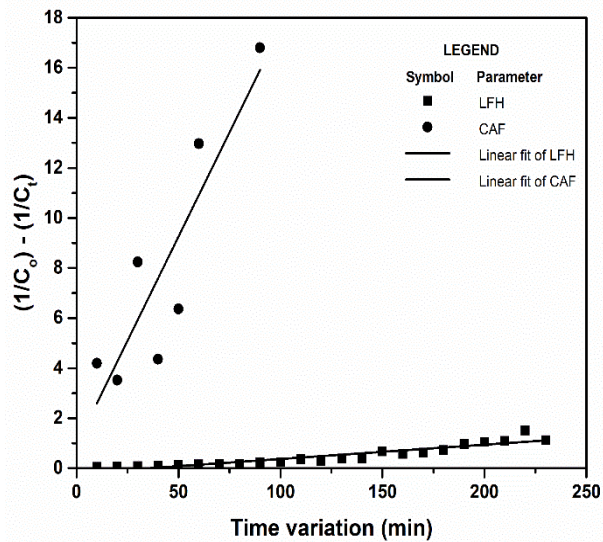


Fig. 4.61 (c) Pseudo second order kinetics for the removal of LFH and CAF

Fig.4.61 (a) and (b) show the pseudo zero order and first order kinetics revealing a negative rate constant from table 4.12. The first-order kinetic model is related to the low concentration of sulphate and hydroxyl radical species produced during the process. In this case, NFO/PMS radical-induced degradation, Ho's pseudo-second-order kinetic model fits better as shown in Fig. 4.61 (c) which is attributed to the fact that the degradation process requires numerous steps that imply the occurrence of different species, predominantly sulfate and hydroxyl radicals, which can be identified using liquid chromatography-mass spectroscopy.

The pseudo-second-order model showed better fitting for both pollutants suggesting that the degradation process is controlled by the reactions that occurred in the system owing to chemisorption in the NFO nanocatalyst as a result of radical-induced degradation of both pollutants. The negative value of k and its regression value reflects that the reaction is not proceeding in the positive manner and this might be either due to the accumulation of byproducts or the presence of competing reactions or otherwise equilibrium could have established.

Table 4.12 Kinetic parameters in the removal of LFH and CAF

Order of reaction	Zero order reaction		Pseudo first order kinetics		Pseudo second order kinetics	
	Pollutants	R ²	k ₀ (mg/L.min)	R ²	k ₁ (min ⁻¹)	R ²
LFH	0.91	-0.027	0.97	-0.01076	0.85	0.005
CAF	0.59	-0.002	0.69	-0.0188	0.74	0.1664

4.7.11 Regeneration and recycle studies of NFO nanoparticles

Distilled water, methanol, and ethanol were used to regenerate the nanocatalyst. All three regenerated nanocatalysts were tested in optimized conditions, and all of the regenerants showed removal efficiency of LFH within 90-94%, whereas in the case of CAF, the washing of used NFO nanoparticles in the degradation of CAF showed above 90% removal efficiency for the distilled water washing compared to other regenerants, as shown in Fig. 4.62 (a), and thus the distilled water was chosen as the most economical and eco-friendly regenerant.

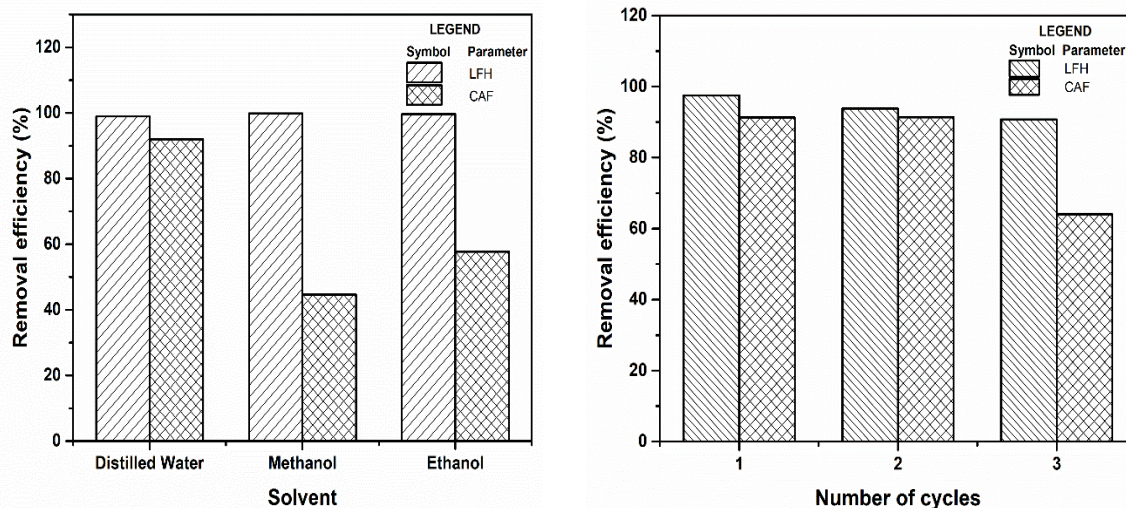


Fig. 4.62 (a) Regeneration of NFO nanoparticles on different solvents **(b)** Three recycle runs of NFO nanoparticles for the degradation of CAF and LFH

The experiments were conducted in three-cycle runs by washing the used nanocatalyst with distilled water, and the degradation of LFH and CAF in the three-cycle runs is shown in Fig. 4.62 (b), which was found to be (94.32%, 94.01%, 90.68%) for LFH and (97.89, 93.83, 64.1%) for CAF, implying a very slight reduction in the degradation efficiency for the three cycle runs. As a result of the recycle and regeneration experiments, it was noticed that distilled water could effectively regenerate the nanocatalyst and degrade the LFH upto 90% with three recycle runs and 90 % of CAF upto two cycle runs.

4.7.12 Degradation of LFH and CAF on the different water sources

The degradation of LFH and CAF in two different water sources, tap water and river water, was compared to the aqueous LFH and CAF solution prepared in distilled water. The 10 mg/L of LFH and CAF in both tap and river water was prepared, and degradation experiments were performed under optimized conditions, in which the distilled water and tap showed a similar trend to the river water regardless of other water parameters, as shown in Fig. 4.63.

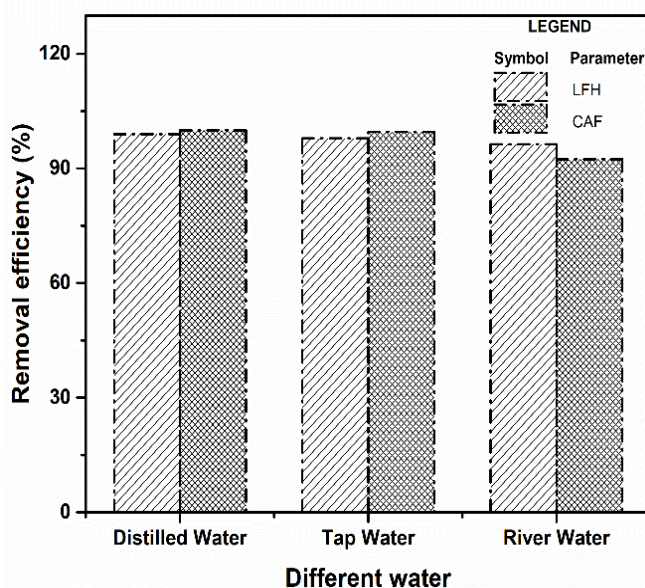


Fig. 4.63 Degradation of LFH on different water sources

4.7.13 Inductively coupled plasma -Optical emission spectroscopy (ICP-OES)

The leaching of iron and nickel ions in the LFH degradation was analysed using ICP-OES analysis and was estimated to be 0.15 mg/L and 0.05 mg/L from the catalyst in the final analyte; whereas no traces of iron ions were observed in the CAF degradation, 0.73 mg/L of nickel ions was leached from the catalyst in the final analyte. The iron content in the case of LFH degradation was within the acceptable limits of 0.3 mg/L in drinking water according to (BIS 2012) and natural freshwater (0.5 to 50 mg/L) according to WHO guidelines, and the permissible limit of nickel ions content in effluent discharged in public sewer and inland surface water is 3 mg/L according to Indian environmental protection rules 1986 (SCHEDULE VI) (IS 3025-43 (1992)). As a result, the leaching of nickel and iron ions was found to be within acceptable and permissible limits in both cases.

4.7.14 Identification of degraded products using Liquid chromatography-mass spectrometry (LC-MS)

LC-MS was used to analyze the degradation products of Lomefloxacin Hydrochloride (LFH) and Caffeine (CAF). Fig. 4.64 a and b and Fig. 4.65 a and b show the spectrum of the LFH and CAF aqueous solution in the initial and final analyte solution. Fig. 4.66 depicts the identified degraded fragments and pathways based on the m/z value of the spectrum. The dihydroxy

derivative piperazine ring was formed as a result of the addition of an oxygen atom to the direct product of Lomefloxacin Hydrochloride m/z 365. The oxidation of the piperazine ring has led to the formation of a piperazine ring keto derivative m/z 343. The loss of $C=O$ contributed to a compound with m/z 315. Direct hydroxyl radical attack could result in desethylene Lomefloxacin Hydrochloride with a loss of propyne group or despropylene LFH with a loss of acetylene group with m/z 268. Decarboxylation, demethylation, and fluorine substituent loss resulted in the formation of an intermediate compound with m/z 218. The formation of methyl formate and n-butyraldehyde with m/z 146 and 75 indicates that the LFH has been broken down into smaller molecules (Liu et al. 2012; Ma et al. 2020; Zhang et al. 2022).

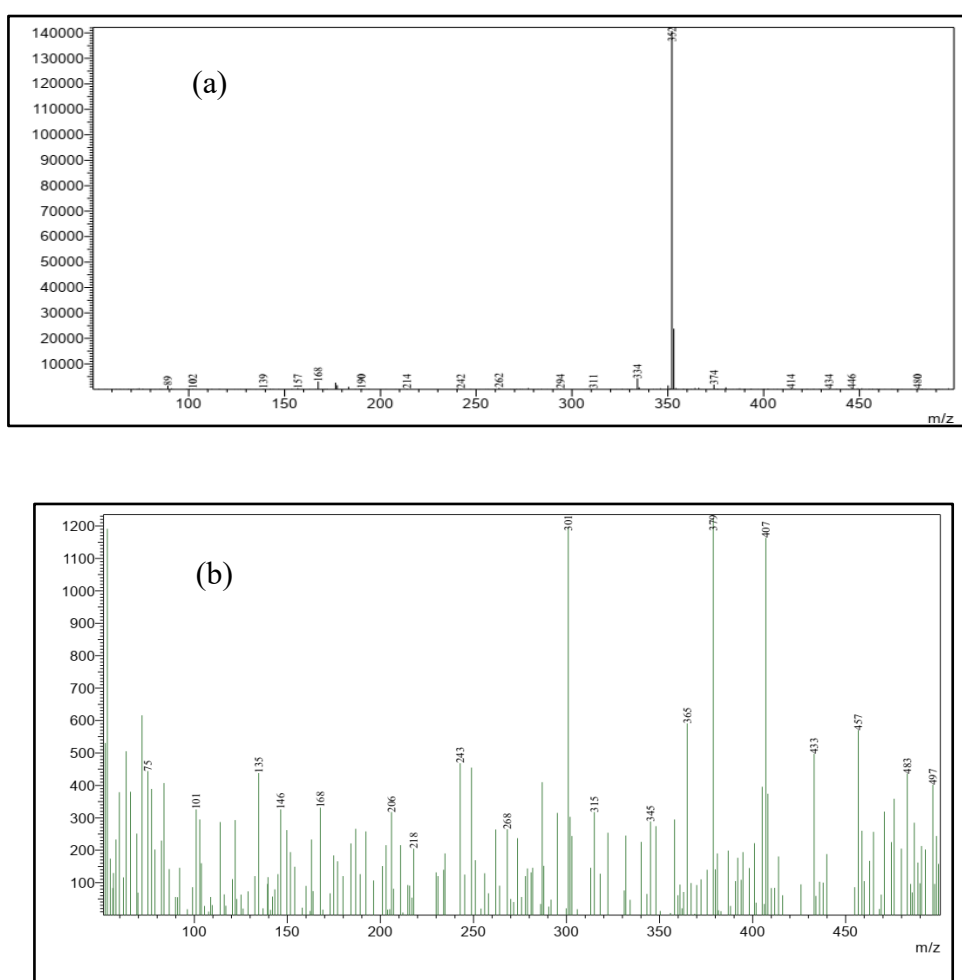


Fig. 4.64 Mass spectrum of Initial (a) and after (b) degradation of LFH

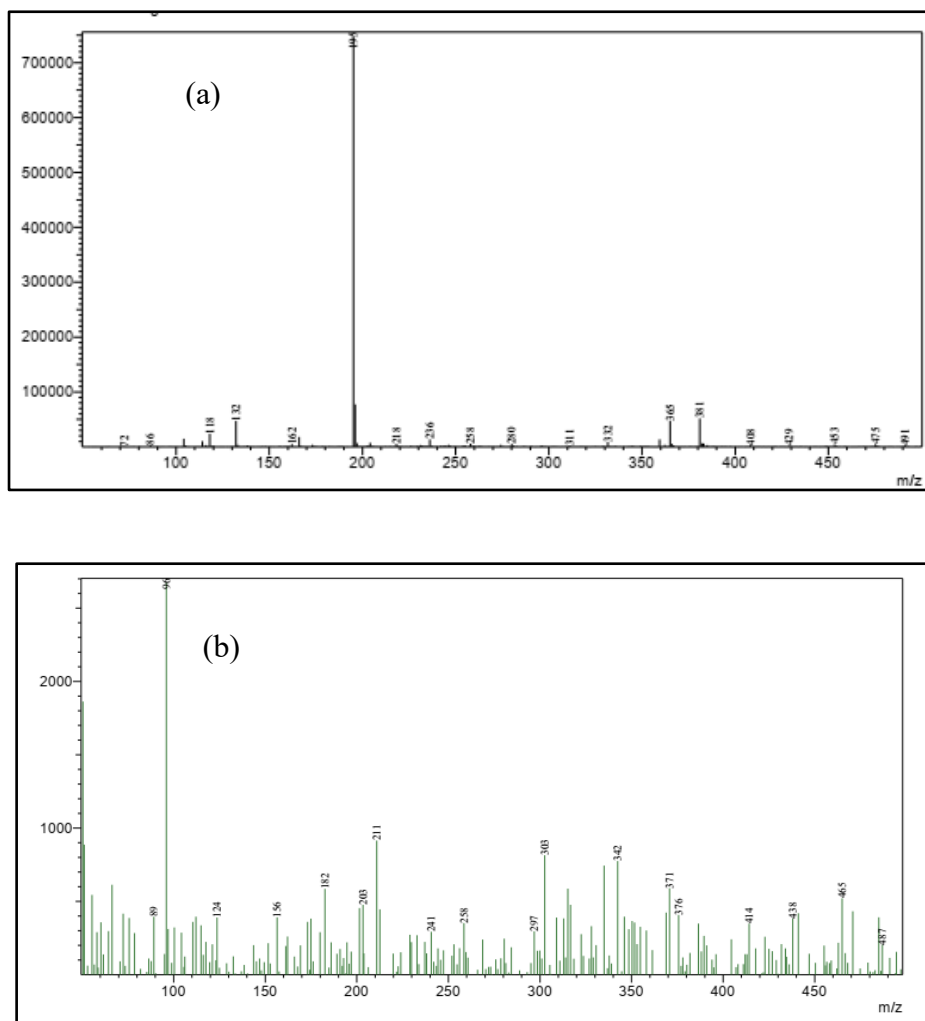


Fig. 4.65 Mass spectrum of (a) Initial and (b) after degradation of CAF

Caffeine with a m/z ratio of 195 first produces the compound with m/z 211, which then breaks down to form m/z 241, in which the ring structure opens and an addition of two keto groups $C=O$ results in m/z 258, which then splits into two intermediate products with the attachment of two acid groups to the nitrogen atom, m/z 297 and m/z 303. The two acid groups separate to form a xanthine fragment derivative with m/z 203 and 182. Furthermore, the compound with m/z 182 degrades into the imidazole structured compound m/z 156, which when oxidised yields compound such as CAF 8 with m/z 124, CAF 10 m/z 96, and CAF 11 m/z 89 (Lin et al. 2018; Ndabankulu et al. 2019; Wang et al. 2017). Fig. 4.67 depicts the CAF degradation pathway.

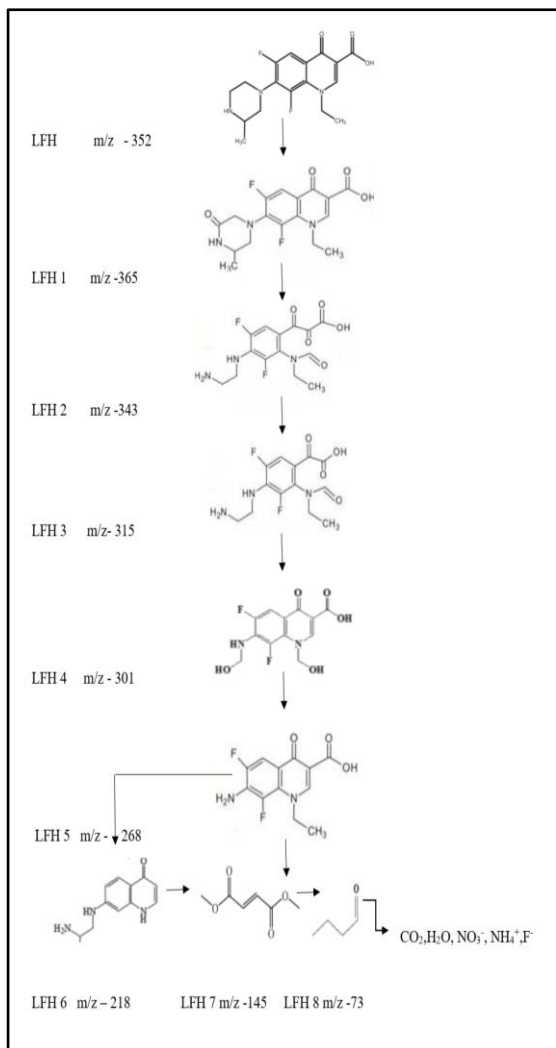


Fig. 4.66 Degradation pathway of LFH

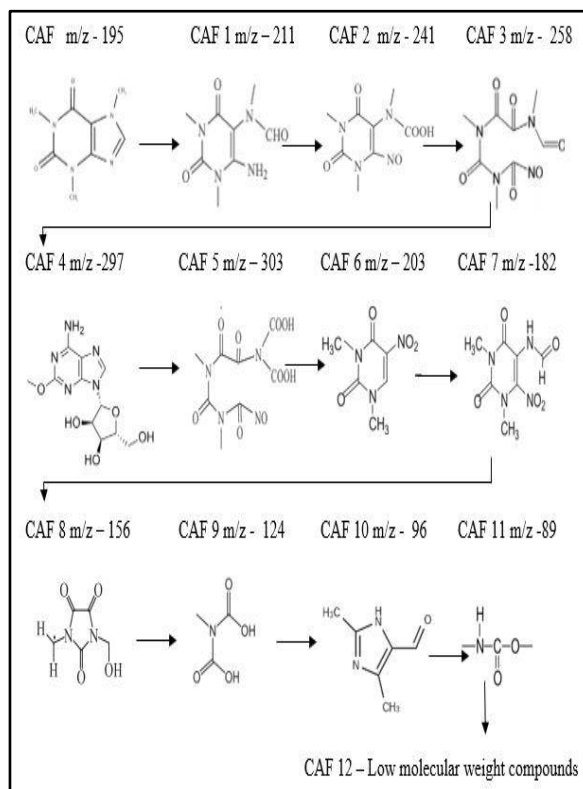


Fig. 4.67 Degradation pathway of CAF

4.8.15 LC-MS results of LC (Lomefloxacin Hydrochloride and Caffeine) mixed solution:

At a retention time of 10.79, the base peak and the molecular ion reflected a 100 % intensity at a m/z ratio of 352 and its molecular ion isotope peak reflected at m/z 353.2 in the initial mixed LC solution as shown in Fig. 4.69 (a). The [M+1] ion peak was observed at m/z 353.2 and [M+2] at m/z 354.2. At a degradation time of 40 mins, the LC solution was subjected to LC-MS analysis. At a retention time of 0.55, the most abundant peak as the base peak was observed at m/z 126 and the fragment ion was observed in Fig 4.68 (b) (after degradation of LC solution) m/z such as 85, 126,150,214,9,256,336.9.

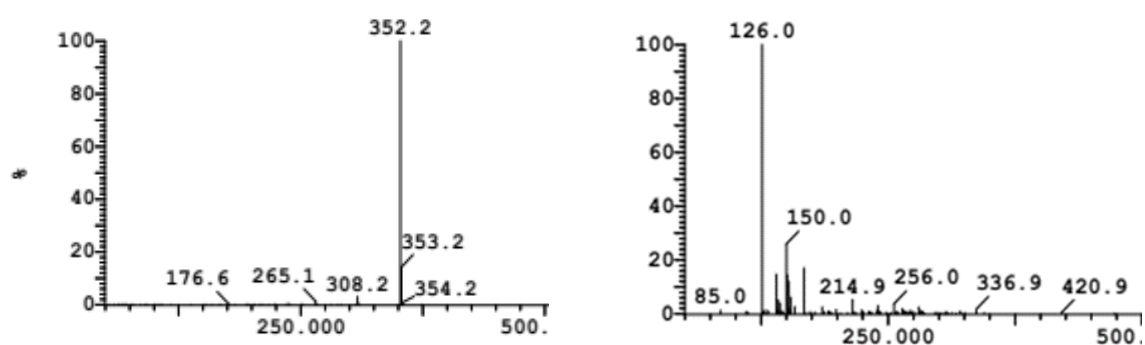


Fig. 4.68 (a) MS-MS spectrum of LFH and CAF mixed solution (Initial) **Fig. 4.68 (b)** MS-MS spectrum of LFH and CAF mixed solution (Final)

4.7.16 FTIR analysis of NFO/PMS system after degradation of CAF and LFH

NFO as a catalyst would function as an adsorbent due to their surface area, so the FTIR after chemical degradation was used to confirm the attachment of LFH and CAF functional groups. Fig. 4.69 illustrates the presence of CAF functional groups in the peaks between 1200 - 1700 cm^{-1} and 700-745 cm^{-1} , and similar results have been reported (Butt et al. 2019). The peaks around 1600-1700 cm^{-1} are caused by the stretching of the C=O and C=N rings in cyclic hydrocarbons. The aromatic C-H stretch is responsible for the N-H stretching vibrations observed around 3400 cm^{-1} and in the middle of the peaks 2900 - 3120 cm^{-1} (Rajam et al. 2013). Peaks near 3300 cm^{-1} indicate the presence of H-C-H in the methane group. All of these peaks can be seen in the FTIR spectrum after CAF degradation. Because of the NH_2^+ symmetrical and asymmetrical stretch, a compound Nujol would have appeared between 3000-2850 cm^{-1} and around 2700 cm^{-1} . Within 1700 cm^{-1} , the peaks correspond to C=O stretch, 1600 cm^{-1} to C=O pyridone carbonyl, and 1400 cm^{-1} to - CH_2 and - CH_3 . The C-H tri-substituted double bond can be seen near wavenumber 800 cm^{-1} in the FTIR spectrum after LFH degradation (Sanzgiri et al. 1994). The attachment of all these functional groups indicates that, in addition to the degradation of LFH and CAF, adsorption would have occurred due to the surface properties of the NFO nanoparticles.

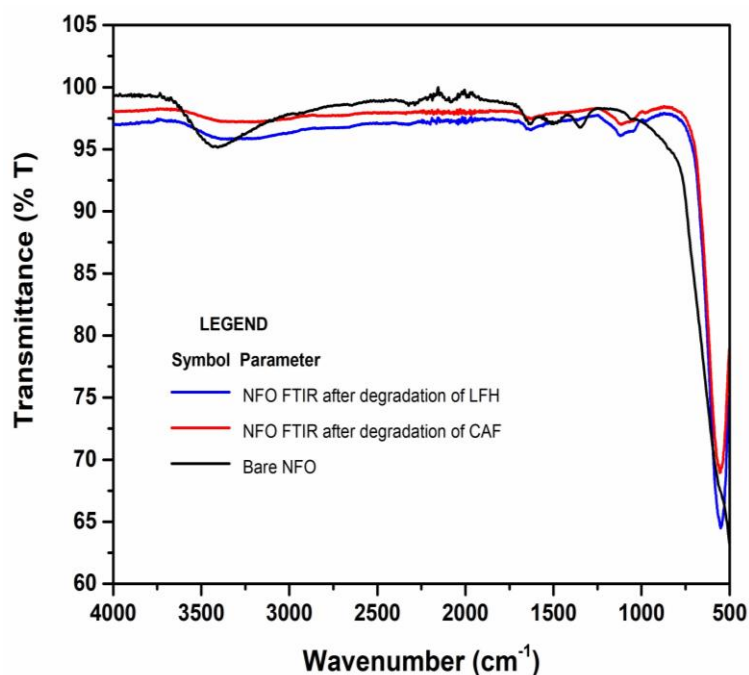


Fig. 4.69 FTIR of NFO/PMS system after degradation of CAF and LFH

FTIR of the NFO surface was analyzed after each batch experiment of LFH and CAF separately and have been observed for the modified NFO surface after the experiments. The FTIR trend of bare NFO surface tends to differ after each parametric study. A difference in H-O-H vibrations at 3416.68 and 1636.20 cm^{-1} in Fig.4.70 has been observed clearly in the pink dashed line and yellow line in both the Figures indicating that the NFO surface has been greatly adsorbed by the LFH and CAF separately. Similarly, bands such as between 2000 to 2350, 1300 to 1500, around 550 cm^{-1} in the LFH adsorbed surfaces. Around 3430, between 1900 to 2200, 1400 to 1650, a reduced spectral band around 550 cm^{-1} is observed in the CAF adsorbed surface. The remaining spectral bands showed a slight reduction compared to the NFO surface. All this modification implies that after each batch parametric study either the intermediate degraded compounds could have been adsorbed or the pollutant compound itself might have been adsorbed on the NFO catalyst surface. All the functional groups corresponding to wavenumbers have been mentioned in the aforementioned FTIR section.

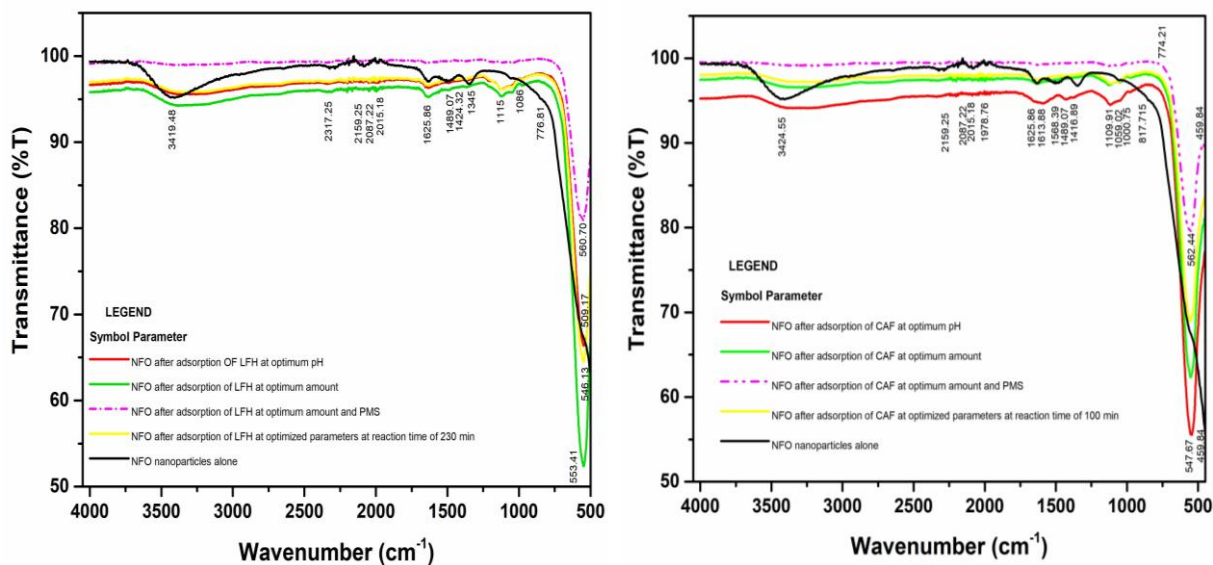


Fig. 4.70 FTIR of NFO/PMS/LFH and NFO/PMS/CAF after each parametric batch studies

4.7.18 Chemical oxygen demand analysis (COD)

The number of oxygen equivalents consumed by a strong oxidant during the chemical oxidation of organic materials was analyzed using chemical oxygen demand (COD). At the optimum conditions, the COD reduction in the final analyte of CAF and LFH after degradation experiments was estimated to be 20.8 % in CAF and 71 % in LFH. A 20.8 % reduction in COD reflects that the degradation process was less effective for CAF. This indicates that the CAF pollutant is more resistant to degradation, owing to their chemical structure or due to the presence of complex or stable compounds that are not easily broken down. Meanwhile, a 71 % reduction in COD indicates a significantly more effective degradation process for LFH indicating that the organic matter in LFH is more amenable to chemical degradation. The variation of COD reduction in both pollutants relies on various affecting parameters such as pH, nanoparticle dosage, PMS dosage and reaction time. Both pollutants were experimented with at pH 3, whereas less active sites and reaction time were provided for CAF in comparison with LFH which might have resulted in reduced COD removal similar results of affecting parameters were mentioned in the previous literature work (Subki et al. 2020).

CHAPTER 5

CONCLUSION

The detrimental effect of pharmaceutical pollutants in water resources at low concentrations has raised the need for a novel adsorbent. The nickel ferrite and its nanocomposite have been employed to target specific pharmaceutical pollutants such as KF, DCF, CIP, LFH and CAF in aqueous solutions. The NFO nanoparticles were synthesized using the co-precipitation method, upon which SiO₂ was functionalized using TEOS followed by attachment of β -CD molecule to form NFO@SiO₂@ β -CD nanocomposite which was used in the removal of KF and DCF. The hydrothermally synthesized L-Leucine functionalized nickel ferrite nanocomposite (NFO@L) was used in the removal of pharmaceutical pollutants, LFH and CIP. The potentiality of the synthesized NFO, NFO@SiO₂, NFO@SiO₂@ β -CD, and NFO@L nanocomposite was analysed for its physical, chemical, magnetic and thermal properties using various analytical techniques. The attachment of β -CD and SiO₂, onto NFO, β -CD onto NFO@SiO₂, and L-Leucine onto NFO was confirmed from the XRD, EDX, and FTIR analysis. The surface morphology and the specific surface area were determined from the FE-SEM image and BET test analysis. The thermal stability and the per cent weight loss of the NFO and functionalized NFO were estimated using TGA analysis. The particle size and zeta potential were determined using electrokinetic analysis and also from FE-SEM images using ImageJ software. The removal of KF, DCF, LFH, and CIP drugs and the degradation of CAF and LFH were confirmed with an experimental investigation of the synthesized NFO nanocomposite and NFO nanoparticles at different parameters. The adsorption isotherm and kinetics were studied in the experimental investigation. The regeneration and recyclability studies of the NFO@SiO₂@ β -CD, NFO@L and NFO nanoparticles were experimentally determined and the reusability of the nanocomposite and nanoparticles was investigated. Comparing the literature, the NFO@SiO₂@ β -CD nanocomposite showed a superior characteristic in the removal of DCF within 5 mins. The NFO@L nanocomposite showed similar results of CIP to other research work however a new economical and eco-friendly adsorbent has been developed compared to high temperature required activated carbon. Lomefloxacin hydrochloride and caffeine combination haven't been worked on so far each of the pollutants showed a very good degradation efficiency compared to the other literature works and this combination of the mixed solution has not been experimented till now and the nickel ferrite nanoparticles have

shown excellent results. The some of the significant findings were summarized in the following below.

5.1 Summary

To summarize the research findings, the functionalization of β -CD onto NFO@SiO₂ has been demonstrated to be an effective adsorbent for the removal of DCF comparable to KF. In comparison to LFH, the functionalization of L-Leucine onto NFO has proven to be an effective adsorbent for the removal of CIP. The CAF and LFH were efficiently degraded in the NFO/PMS combination, NFO could potentially serve as an effective nano catalyst in the presence of an oxidizing agent.

(a) NFO@SiO₂@ β -CD nanocomposite for the removal of KF and DCF

The following are the summary of the work that were derived upon synthesizing and experimenting with β -CD functionalized NFO@SiO₂ upon the removal of KF and DCF.

- The presence of Ni-O at 478 cm⁻¹ and Fe-O at 534 cm⁻¹ in the tetrahedral and octahedral modes confirmed the formation of NFO nanoparticles.
- The highly agglomerated pore-free NFO nanoparticles were seen to be in micron-size particles from FE-SEM imaging which revealed that the NFO nanoparticles have to be functionalized to get discrete uniform-sized particles however from the EDX the elemental composition seems to be in the stoichiometric ratio.
- NFO is crystalline with the maximal peak orientation (311) at 35.55° which was confirmed from the XRD analysis the maximum zeta potential of -26 mV was found at pH 11 and the negative surface of NFO was found to be dominant at all pH and the surface-to-volume ratio of the NFO nanoparticles was found to 112.02 m²/g from the BET analysis.
- The low saturation magnetization (M_s), retentivity value and coercivity (H_c) of the NFO nanoparticles revealed its soft magnetic nature with ease of magnetization and demagnetization.
- The specific surface area of the NFO@SiO₂ is 29.118 m²/g and the hysteresis loop from BET analysis indicates the type III isotherm and implies that NFO@SiO₂ might either be nonporous or mesoporous.
- The mesoporous nature of NFO@SiO₂@ β -CD nanocomposite was seen in the FE-SEM image with a specific surface area of 20.781 m²/g and an increase in average particle diameter of the nanocomposite of 109.1 nm was observed.

- As a result of functionalization, a decrease in the magnetic properties of NFO@SiO₂@β-CD nanocomposite was observed in comparison with the NFO nanoparticles.
- However, a reduction in thermal stability was reflected in 56.18 % of the weight loss of the NFO@SiO₂@β-CD at temperatures between 250 to 500 °C. A 10.23 % weight loss up to 250°C was found and the nanocomposite would be experimented within this temperature range and this slight reduction within the operating temperature is insignificant.
- 1.25 g β-CD functionalized NFO showed the maximal removal percent of 30.80 % of KF and 33.03 % of DCF.
- The maximal removal of 31.32 % of KF and 59.12 % of DCF at pH 5 and 3 with the adsorption capacity of 32.85 and 64.89 mg/g, respectively, DCF showed a better removal efficiency upon varying the pH compared to KF at an equilibration time of 12 hrs.
- The optimum dosage of 130 mg and 120 mg of NFO@SiO₂@β-CD removed almost 80.92 % and 80.83 % of KF and DCF respectively at an equilibration time of 12 hrs; upon varied time, 80 % of KF in 360 min and 94 % of DCF in 5 mins were removed using the NFO@SiO₂@β-CD nanocomposites. The functionalization of NFO worked well for DCF comparably with KF.
- The rate and mechanism of the removal process were evaluated from the kinetic and isotherm models in which the pseudo-second-order kinetic model and Freundlich adsorption isotherm fitted well indicating the chemisorption and layer-by-layer adsorption from the kinetic and isotherm model.
- The NFO@SiO₂@β-CD nanocomposites were regenerated and recycled for about four consecutive cycles; a greater shift in the removal efficiency of KF was observed compared to DCF which was noticeable as a result of the collapse of the pore structure, cavity and functionalization.
- Thus, the NFO@SiO₂@β-CD nanocomposite could serve as a potent adsorbent for the removal of DCF compared to KF, the regeneration capacity has to be improved to reduce the loss in functionalization in order to improve its number of recycle runs.

(b) L-Leucine functionalized nickel ferrite (NFO@L) nanocomposite for the removal of CIP and LFH

The following are the summary of the work that were derived upon synthesizing and experimenting with L-Leucine functionalized NFO for the removal of CIP and LFH.

- The synthesized NFO@L is a homogenous spherical particle having an average particle diameter between 11 to 15 nm implying its narrow size distribution plotted from the FE-SEM and AFM analysis using ImageJ software even after L-Leucine functionalization.
- The superparamagnetic nature of the nanocomposite was observed with a saturation magnetization of 0.66 emu/g, which affirms its restrained magnetic property after functionalization.
- The maximum zeta potential was observed to be -21.5 mV at pH 8 indicating its good dispersibility.
- The specific surface area of the nanocomposite was estimated to be 92.92 m²/g, considerably a better surface area among nanocomposites.
- The parametric experimental investigation revealed that almost 93.54 % CIP at (pH = 8, 100 mg, 10 mg/L, 303 K) and 75.19 % LFH at (pH = 9, 70 mg, 10 mg/L, 333 K) were removed.
- The after-adsorption FTIR image of LFH and CIP functional groups confirmed the adsorption of both pollutants onto NFO@L.
- The effect of temperature on the removal of both pollutants revealed the two different trends for two different pollutants belonging to the same class implying that the pK_a value, pH, functional groups, hydrogen bonding, electrostatic attraction with dipole-dipole forces and surface charge have played a vital role in targeting the specific pollutant.
- The kinetic and isotherm studies revealed that the pseudo second order kinetics and Langmuir isotherm model showed the best fit with the highest R² value such that the removal proved to be of monolayer surface sorption with chemical interactions on the NFO@L.
- Other isotherms such as Temkin and Dubinin–Radushkevich isotherms revealed that the removal of both pollutants required very less binding energy at 303 K. The thermodynamic parameters revealed that the removal process is exothermic for CIP and endothermic for LFH.
- The value of ΔG° also suggested that the adsorption of both pollutants is a favourable and spontaneous sorption process.

- The regeneration and recycling studies of used NFO@L with methanol for about four consecutive cycles revealed a small reduction in the removal efficiencies of CIP and LFH to 79.69 % and 57.20 % respectively.
- Hence, the NFO@L nanocomposite could serve as an effective adsorbent for the pharmaceutical drugs that are prevailing in the environment at low concentrations.

(c) Nickel ferrite (NFO) as a nano catalyst in the degradation of CAF and LFH

The following are the conclusions that were derived upon synthesizing and experimenting with the NFO/PMS AOP system for the degradation of CAF and LFH.

- The nickel ferrite nanoparticles were synthesised using the co-precipitation method, and their physical and chemical properties were investigated using various characterization techniques.
- The crystallinity of the nanocatalyst and the formation of NFO were confirmed by XRD and FTIR analysis. The crystallinity of the nanocatalyst was determined to be 1.712 nm.
- The particle size distribution and maximum zeta potential were calculated to be 43.87 nm and -54.07 mV at pH 11 reflecting its highly negative surface and good dispersibility at the most basic conditions.
- A magnification of 200 nm imaging from FESEM and AFM appears as agglomerated spherical particles, due to its high surface energy and the grain size from the AFM was estimated to be 0.2523 nm.
- The specific surface area of the NFO nanocatalyst is 112.02 m²/g which has a comparatively larger specific surface area than the above-mentioned nanocomposite.
- The batch experiment on the degradation of LFH, CAF and LC using NiFe₂O₄/PMS revealed that 98.61 % of LFH, 100 % of CAF and 78.07 % of LC were degraded within 220 min, 80 min and 40 min at pH 3, respectively.
- The kinetic study suggested that the pseudo second order kinetic fits better indicating its chemisorption in the radical-produced NFO/PMS system.
- From the LC-MS analysis, it was identified that the LFH, CAF and LC were broken down into smaller fragments.

- The after-degradation FTIR image of LFH and CAF activating PMS using NFO nanoparticles confirmed that the surface properties also played a role in the removal of both pollutants.
- The reduced COD of the final analyte of both pollutants indicated that the less active sites and reaction time were provided for CAF in comparison with LFH.
- The regeneration of the NFO nanocatalyst with distilled water yielded nearly 94.34 to 90.68 % LFH and 97.89 to 64.1 % CAF, indicating that the nanocatalyst is stable for two consecutive cycles.
- The leaching of nickel and iron ions from the catalyst was also found to be within limits. A comparison of various water sources revealed that activating PMS with NiFe_2O_4 could be a powerful nanocatalyst for use in contaminated water bodies.

5.2 Future scope of the study

The significance of magnetic spinel nickel ferrite nanocomposite is to be explored in a continuous flow process hence the real-time difficulties such as variability in the weather conditions, detection of contaminants, variation in sampling methods, calibration and maintenance in implementing the nanoparticle and nanocomposite, regulatory compliances, operating cost and its removal for further reusability studies could be identified and rectified so that the low concentrated micro and trace level of pollutants could be removed or degraded. The NFO functionalized nanocomposite has to experiment with other regenerants to improve its regeneration and recycling potential. A few more drugs have to experiment with NFO functionalized nanocomposite in their adsorption and desorption studies such that the laboratory-scale study can be extended to the pilot-scale level for the treatment of pharmaceutical pollutants contaminated water bodies, and municipal and hospital effluents with the NFO@L nanocomposite. The estimation of cost in implementing the nanosorbents and the commercial grade adsorbent is to be estimated in order to commercialize the nickel ferrite nanoparticles and nanocomposite.

LIST OF PUBLICATIONS AND CONFERENCES

Research article

1. **Ilango, I.**, Balakrishnan, R.M., Visvanathan, C. *et al.* Functionalization of β -cyclodextrin onto NiFe_2O_4 nanoparticles for the removal of ketoprofen and diclofenac from the aqueous solutions. *Int. J. Environ. Sci. Technol.* (2023). <https://doi.org/10.1007/s13762-023-05146-7>.
2. **Ilango, I.**, Balakrishnan R.M. Amino acid functionalized metal oxide nanocomposite for the removal of fluoroquinolones, *Journal of Cleaner Production* (2023), doi: <https://doi.org/10.1016/j.jclepro.2023.139071>
3. **Ilango, I.**, Balakrishnan, R. M, Visvanathan, C, Bui, X.-T. Stimulation of peroxymonosulfate by nickel ferrite nanoparticles for the degradation of lomefloxacin hydrochloride and caffeine. *Nanotechnology for Environmental Engineering*. Manuscript No. NTEE-D-24-00171 (Submitted).
4. **Ilango, I.**, Balakrishnan R.M. Removal and Degradation of Lomefloxacin Hydrochloride Using L-Leucine Functionalized Nickel Ferrite Nanocomposite (NFO@L). *CHEMOSPHERE CHEM141145* (Submitted).

Conferences

5. Kritiya Kaspanich, Chettiyappan Visvanathan, **Indumathi Ilango**, Balakrishnan, R. M, “Removal of Methylene Blue from Synthetic Textile Wastewater using PAC, Rice Husk, TiO_2 , Synthesized and Functionalized NiFe_2O_4 NPs, The 2nd International Conference on Green Technologies for Sustainable Water 2019, 1-5, December, 2019, Ho Chi Minh City, Vietnam
6. **Ilango, I.**, Balakrishnan, R. M, Visvanathan, C, Bui, X.-T. Stimulation of peroxymonosulfate using nickel ferrite nanoparticles for the degradation of lomefloxacin hydrochloride. *International Symposium on water sustainability & Green technologies - WSGT2022*, November 25 – 26, 2022, Ho Chi Minh City, Vietnam.

References

- Abdul Aziz, A. S., Manaf, L. A., Che Man, H., and Kumar, N. S. (2013). “Kinetic Modeling and Isotherm Studies for Copper(II) Adsorption onto Palm Oil Boiler Mill Fly Ash (POFA) as a Natural Low-Cost Adsorbent.” *BioResources*, 9(1), 336–356.
- Adeoye, J. B., Tan, Y. H., Lau, S. Y., Tan, Y. Y., Chiong, T., Mubarak, N. M., and Khalid, M. (2024). “Advanced oxidation and biological integrated processes for pharmaceutical wastewater treatment: A review.” *J. Environ. Manage.*, 353(October 2023), 120170.
- Adhikari, S., and Kar, T. (2012). “Experimental and theoretical studies on physicochemical properties of l-leucine nitrate—a probable nonlinear optical material.” *J. Cryst. Growth*, 356(1), 4–9.
- Ahammad, N. A., Ahmad, M. A., Hameed, B. H., and Mohd Din, A. T. (2022). “A mini review of recent progress in the removal of emerging contaminants from pharmaceutical waste using various adsorbents.” *Environ. Sci. Pollut. Res.*, (0123456789).
- Ahmadi, M., Ramezani, H., and Jaafarzadeh, N. (2017). “Enhanced photocatalytic degradation of tetracycline and real pharmaceutical wastewater using MWCNT / TiO₂ nano-composite.” 186, 55–63.
- Ahn, T., Kim, J. H., Yang, H., Lee, J. W., and Kim, J. (2012). “Formation Pathways of Magnetite Nanoparticles by Coprecipitation Method.”
- Al-Buriah, A. K., Al-shaibani, M. M., Mohamed, R. M. S. R., Al-Gheethi, A. A., Sharma, A., and Ismail, N. (2022). “Ciprofloxacin removal from non-clinical environment: A critical review of current methods and future trend prospects.” *J. Water Process Eng.*, 47(December 2021), 102725.
- Al-Ghouti, M. A., and Al-Absi, R. S. (2020). “Mechanistic understanding of the adsorption and thermodynamic aspects of cationic methylene blue dye onto cellulosic olive stones biomass from wastewater.” *Sci. Rep.*, 10(1), 15928.
- Aliahmad, M., Noori, M., Hatefi, K., N, Sargazi, and M. (2013). “Synthesis of nickel ferrite nanoparticles by co-precipitation chemical method.” *Int. J. Phys. Sci.*, 8(18), 854–858.
- Alijani, H. Q., Pourseyedi, S., Torkzadeh-Mahani, M., Seifalian, A., and Khatami, M. (2020). “Bimetallic nickel-ferrite nanorod particles: greener synthesis using rosemary and its biomedical efficiency.” *Artif. Cells, Nanomedicine Biotechnol.*, 48(1), 242–251.
- Allothman, Z. A., and Apblett, A. W. (2009). “Preparation of mesoporous silica with grafted chelating agents for uptake of metal ions.” *Chem. Eng. J.*, 155(3), 916–924.
- AlOthman, Z. A., Badjah, A. Y., Alduhaish, O. M., Rathinam, K., Panglish, S., and Ali, I. (2021). “Synthesis, characterization, kinetics and modeling studies of new generation pollutant

ketoprofen removal in water using copper nanoparticles.” *J. Mol. Liq.*, 323, 115075.

ALothman, Z. A., Badjah, A. Y., Alharbi, O. M. L., and Ali, I. (2020). “Synthesis of chitosan composite iron nanoparticles for removal of diclofenac sodium drug residue in water.” *Int. J. Biol. Macromol.*, 159, 870–876.

Amulya, M. A. S., Nagaswarupa, H. P., Kumar, M. R. A., Ravikumar, C. R., Prashantha, S. C., and Kusuma, K. B. (2020). “Sonochemical synthesis of NiFe₂O₄ nanoparticles: Characterization and their photocatalytic and electrochemical applications.” *Appl. Surf. Sci. Adv.*, 1(August), 100023.

Andrew Lin, K. Y., and Chen, B. C. (2016). “Efficient elimination of caffeine from water using Oxone activated by a magnetic and recyclable cobalt/carbon nanocomposite derived from ZIF-67.” *Dalt. Trans.*, 45(8), 3541–3551.

Ansari, A. (2017). “Synthesis of nickel ferrite nanoparticles via chemical co-precipitation method.” *Adv. Mater. Proc.*, 2(1), 32–34.

Appel, J. (1973). “Freundlich’s adsorption isotherm.” *Surf. Sci.*, 39(1), 237–244.

Araújo, C. S. T., Almeida, I. L. S., Rezende, H. C., Marcionilio, S. M. L. O., Léon, J. J. L., and Matos, T. N. de. (2018). “Elucidation of mechanism involved in adsorption of Pb(II) onto lobeira fruit (*Solanum lycocarpum*) using Langmuir, Freundlich and Temkin isotherms.” *Microchem. J.*, 137, 348–354.

Arévalo-Cid, P., Isasi, J., and Martín-Hernández, F. (2018). “Comparative study of core-shell nanostructures based on amino-functionalized Fe₃O₄@SiO₂ and CoFe₂O₄@SiO₂ nanocomposites.” *J. Alloys Compd.*, 766, 609–618.

Ayazi, Z., Khoshhesab, Z. M., and Amani-Ghadim, A. (2018). “Synthesis of nickel ferrite nanoparticles as an efficient magnetic sorbent for removal of an azo-dye : Response surface methodology and neural network modeling.” 3(1), 109–123.

Baccar, R., Sarrà, M., Bouzid, J., Feki, M., and Blánquez, P. (2012). “Removal of pharmaceutical compounds by activated carbon prepared from agricultural by-product.” *Chem. Eng. J.*, 211–212(2012), 310–317.

Baki, M. H., Shemirani, F., Khani, R., and Bayat, M. (2014). “Applicability of diclofenac-montmorillonite as a selective sorbent for adsorption of palladium(II); Kinetic and thermodynamic studies.” *Anal. Methods*, 6(6), 1875–1883.

Balakrishna, K., Rath, A., Praveenkumarreddy, Y., Guruge, K. S., and Subedi, B. (2017). “A review of the occurrence of pharmaceuticals and personal care products in Indian water bodies.” *Ecotoxicol. Environ. Saf.*, 137(October 2016), 113–120.

Balakrishnan, R. M., Ilango, I., Gamana, G., Bui, X. T., and Pugazhendhi, A. (2021). “Cobalt

ferrite nanoparticles and peroxymonosulfate system for the removal of ampicillin from aqueous solution.” *J. Water Process Eng.*, 40(August 2020), 101823.

Balakrishnan, R. M., Uddandarao, P., Manirethan, V., and Raval, K. (2020). *Insights on the advanced processes for treatment of inorganic water pollutants. Inorg. Pollut. Water*, INC.

Baratam, S. R., and Harsha, M. V. (2020). “Preparation and Characterisation of Sustained Released Dosage Form for Ketoprofen using Natural Gums.” *Int. J. Pharm. Investig.*, 10(1), 54–58.

Barczak, M. (2018). “Synthesis and structure of pyridine-functionalized mesoporous SBA-15 organosilicas and their application for sorption of diclofenac.” *J. Solid State Chem.*, 258(September 2017), 232–242.

Baruwati, B., and Manorama, S. V. (2008). “Monodispersed NiFe₂O₄ nanoparticles: Nonaqueous synthesis and characterization.” *Mater. Chem. Phys.*, 112(2), 631–636.

Basheer, A. A. (2018). “New generation nano-adsorbents for the removal of emerging contaminants in water.” *J. Mol. Liq.*, 261, 583–593.

Bayazit, Ş. S., Danalıoğlu, S. T., Abdel Salam, M., and Kerkez Kuyumcu, Ö. (2017). “Preparation of magnetic MIL-101 (Cr) for efficient removal of ciprofloxacin.” *Environ. Sci. Pollut. Res.*, 24(32), 25452–25461.

Bazgir, S., Farhadi, S., and Mansourpanah, Y. (2022). “Adsorptive removal of tetracycline and ciprofloxacin antibiotics from water using magnetic MIL101-Fe metal–organic framework/NiFe₂O₄ decorated with Preyssler-Pope-Jeannin [NaP₅W₃₀O₁₁₀]¹⁴⁻ polyanion.” *J. Solid State Chem.*, 315(June), 123513.

Bhagat, C., Kumar, M., Tyagi, V. K., and Mohapatra, P. K. (2020). “Proclivities for prevalence and treatment of antibiotics in the ambient water: a review.” *npj Clean Water*, 3(1), 42.

Bharati, V. A., Patade, S. R., Bajaj, S., Parlikar, R., Keche, A. P., and Sondur, V. V. (2020). “Structural and magnetic properties of nickel ferrite nanoparticles prepared by solution combustion method.” *J. Phys. Conf. Ser.*, 1644(1).

Bhuyan, A., and Ahmaruzzaman, M. (2023). *Recent advances in new generation nanocomposite materials for adsorption of pharmaceuticals from aqueous environment. Environ. Sci. Pollut. Res.*, Springer Berlin Heidelberg.

BIS. (2012). “Indian Standard Drinking Water Specification (Second Revision).” *Bur. Indian Stand.*, IS 10500(May), 1–11.

Blanco-Esqueda, I. G., Ortega-Zarzosa, G., Martínez, J. R., and Guerrero, A. L. (2015). “Preparation and characterization of nickel ferrite-sio₂/ag core/shell nanocomposites.” *Adv. Mater. Sci. Eng.*, 2015(November).

- Boleda, M. R., Galceran, M. T., and Ventura, F. (2009). "Monitoring of opiates, cannabinoids and their metabolites in wastewater, surface water and finished water in Catalonia, Spain." *Water Res.*, 43(4), 1126–1136.
- Bratu, I., Astilean, S., Ionesc, C., Indrea, E., Huvenne, J. P., and Legrand, P. (1998). "FT-IR and X-ray spectroscopic investigations of Na-diclofenac-cyclodextrins interactions." *Spectrochim. Acta - Part A Mol. Biomol. Spectrosc.*, 54(1), 191–196.
- Brittain, H. G. (1993). *Analytical Profiles of Drug Substances and Excipients 23*. Academic Press Inc. (London) Limited.
- Bruce, I. J., and Sen, T. (2005). "Surface modification of magnetic nanoparticles with alkoxysilanes and their application in magnetic bioseparations." *Langmuir*, 21(15), 7029–7035.
- Buchberger, W. (2011). "Current approaches to trace analysis of pharmaceuticals and personal care products in the environment." *J. Chromatogr. A*, 1218(4), 603–618.
- Bui, T. X., and Choi, H. (2009). "Adsorptive removal of selected pharmaceuticals by mesoporous silica SBA-15." *J. Hazard. Mater.*, 168(2–3), 602–608.
- Butt, S., Hasan, S. M. F., Hassan, M. M., Alkharfy, K. M., and Neau, S. H. (2019). "Directly compressed rosuvastatin calcium tablets that offer hydrotropic and micellar solubilization for improved dissolution rate and extent of drug release." *Saudi Pharm. J.*, 27(5), 619–628.
- Carabineiro, S. A. C., Thavorn-Amornsri, T., Pereira, M. F. R., Serp, P., and Figueiredo, J. L. (2012). "Comparison between activated carbon, carbon xerogel and carbon nanotubes for the adsorption of the antibiotic ciprofloxacin." *Catal. Today*, 186(1), 29–34.
- Carvalho, P. N., Basto, M. C. P., Almeida, C. M. R., and Brix, H. (2014). "A review of plant–pharmaceutical interactions: from uptake and effects in crop plants to phytoremediation in constructed wetlands." *Environ. Sci. Pollut. Res.*, 21(20), 11729–11763.
- Chandrashekar Kollarahithlu, S., and Balakrishnan, R. M. (2021). "Adsorption of pharmaceuticals pollutants, Ibuprofen, Acetaminophen, and Streptomycin from the aqueous phase using amine functionalized superparamagnetic silica nanocomposite." *J. Clean. Prod.*, 294, 126155.
- Chen, D., Shen, Y., Wang, S., Chen, X., Cao, X., Wang, Z., and Li, Y. (2021). "Efficient removal of various coexisting organic pollutants in water based on β -cyclodextrin polymer modified flower-like Fe₃O₄ particles." *J. Colloid Interface Sci.*, 589, 217–228.
- Chen, P., Song, H., Yao, S., Tu, X., Su, M., and Zhou, L. (2017). "Magnetic targeted nanoparticles based on β -cyclodextrin and chitosan for hydrophobic drug delivery and a study of their mechanism." *RSC Adv.*, 7(46), 29025–29034.

- Cherpin, C., Lister, D., Dacquait, F., and Liu, L. (2021). “Study of the solid-state synthesis of nickel ferrite (NiFe₂O₄) by X-ray diffraction (XRD), scanning electron microscopy (SEM) and raman spectroscopy.” *Materials (Basel)*, 14(10).
- Chew, T. L., Ahmad, A. L., and Bhatia, S. (2010). “Ordered mesoporous silica (OMS) as an adsorbent and membrane for separation of carbon dioxide (CO₂).” *Adv. Colloid Interface Sci.*, 153(1–2), 43–57.
- Cho, S. H., Kim, S. Y., Lee, S. I., and Lee, Y. M. (2006). “Hydroxypropyl- β-cyclodextrin inclusion complexes for transdermal delivery: Preparation, inclusion properties, stability, and release behavior.” *J. Ind. Eng. Chem.*
- Conde, J., Dias, J. T., Grazú, V., Moros, M., Baptista, P. V., and la Fuente, J. M. de. (2014). “Revisiting 30 years of biofunctionalization and surface chemistry of inorganic nanoparticles for nanomedicine.” *Front. Chem.*, 2(JUL), 1–27.
- Crini, G. (2005). “Recent developments in polysaccharide-based materials used as adsorbents in wastewater treatment.” *Prog. Polym. Sci.*, 30(1), 38–70.
- Cunha, R. da, Silva, C. F., Santos, A. C. dos, Teixeira, L. S., Dinali, L. A. F., Carmo Batista, W. V. F. do, Nascimento, C. S., and Borges, K. B. (2023). “Polyaniline-coated magnetic nanoparticles to enhance removal of diclofenac from aqueous media.” *Surfaces and Interfaces*, 43(October).
- Danalioğlu, S. T., Kerkez Kuyumcu, Ö., Abdel Salam, M., and Bayazit, Ş. S. (2018). “Chitosan grafted SiO₂–Fe₃O₄ nanoparticles for removal of antibiotics from water.” *Environ. Sci. Pollut. Res.*, 25(36), 36661–36670.
- Dao, T. H., Tran, T. T., Nguyen, V. R., Pham, T. N. M., Vu, C. M., and Pham, T. D. (2018). “Removal of antibiotic from aqueous solution using synthesized TiO₂ nanoparticles: characteristics and mechanisms.” *Environ. Earth Sci.*, 77(10), 0.
- Dehghan, A., Mohammadi, A. A., Yousefi, M., Najafpoor, A. A., Shams, M., and Rezania, S. (2019). “Enhanced kinetic removal of ciprofloxacin onto metal-organic frameworks by sonication, process optimization and metal leaching study.” *Nanomaterials*, 9(10).
- Dhaouadi, F., Sellaoui, L., Taamalli, S., Louis, F., Bakali, A. El, Badawi, M., Georgin, J., Franco, D. S. P., Silva, L. F. O., Bonilla-Petriciolet, A., and Rtimi, S. (2022). “Enhanced adsorption of ketoprofen and 2,4-dichlorophenoxyacetic acid on *Physalis peruviana* fruit residue functionalized with H₂SO₄: Adsorption properties and statistical physics modeling.” *Chem. Eng. J.*, 445(May).
- Diallo, B., Topka, K. C., Puyo, M., Lebesgue, C., Genevois, C., Laloo, R., Samelor, D., Lecoq, H., Allix, M., Vergnes, H., Senocq, F., Florian, P., Sarou-Kanian, V., Sauvage, T., Menu, M. J.,

Caussat, B., Turq, V., Vahlas, C., and Pellerin, N. (2021). "Network hydration, ordering and composition interplay of chemical vapor deposited amorphous silica films from tetraethyl orthosilicate." *J. Mater. Res. Technol.*, 13, 534–547.

Doorslaer, X. Van, Dewulf, J., Langenhove, H. Van, and Demeestere, K. (2014). "Fluoroquinolone antibiotics: An emerging class of environmental micropollutants." *Sci. Total Environ.*, 500–501, 250–269.

Duo, J., Li, W., Wang, Y., Wang, S., Wufuer, R., and Pan, X. (2022). "Photothermal Catalytic Degradation of Lomefloxacin with Nano Au/TiO₂." *Water*, 14(3), 339.

Dutra, E., Duarte, V., Gurgel, M., Gurgel, M., and Vieira, A. (2024). "Journal of Water Process Engineering Adsorption of diclofenac and losartan using multi-walled carbon nanotubes functionalized with iron nanoparticles via the green route : Equilibrium , thermodynamics , and machine learning studies." *J. Water Process Eng.*, 58(January), 104923.

Egizbek, K., Kozlovskiy, A. L., Ludzik, K., Zdorovets, M. V., Korolkov, I. V., Marciniak, B., M, J., Chudoba, D., Nazarova, A., and Kontek, R. (2020). "Stability and cytotoxicity study of NiFe₂O₄ nanocomposites synthesized by co-precipitation and subsequent thermal annealing." *Ceram. Int.*, 46(10), 16548–16555.

El-Nahhal, I. M., Salem, J. K., Kuhn, S., Hammad, T., Hempelmann, R., and Bhaisi, S. Al. (2016). "Synthesis and characterization of silica-, meso-silica- and their functionalized silica-coated copper oxide nanomaterials." *J. Sol-Gel Sci. Technol.*, 79(3), 573–583.

El-saied, H. A., and El-Fawal, E. M. (2021). "Green superabsorbent nanocomposite hydrogels for high-efficiency adsorption and photo-degradation/reduction of toxic pollutants from waste water." *Polym. Test.*, 97, 107134.

El-Shafey, E.-S. I., Al-Lawati, H., and Al-Sumri, A. S. (2012). "Ciprofloxacin adsorption from aqueous solution onto chemically prepared carbon from date palm leaflets." *J. Environ. Sci.*, 24(9), 1579–1586.

El-Sheikh, A. H., Qawariq, R. F., and Abdelghani, J. I. (2019). "Adsorption and magnetic solid-phase extraction of NSAIDs from pharmaceutical wastewater using magnetic carbon nanotubes: Effect of sorbent dimensions, magnetite loading and competitive adsorption study." *Environ. Technol. Innov.*, 16, 100496.

Elfassy, E., Basel, Y., and Mastai, Y. (2016). "Crystallization of amino acids at the chiral ionic liquid/water interface." *CrystEngComm*, 18(45), 8769–8775.

Elhalil, A., Elmoubarki, R., Farnane, M., Machrouhi, A., Sadiq, M., Mahjoubi, F. Z., Qourzal, S., and Barka, N. (2018). "Photocatalytic degradation of caffeine as a model pharmaceutical pollutant on Mg doped ZnO-Al₂O₃ heterostructure." *Environ. Nanotechnology, Monit.*

Manag., 10, 63–72.

Elhalil, A., Elmoubarki, R., Machrouhi, A., Sadiq, M., Abdennouri, M., Qourzal, S., and Barka, N. (2017). “Photocatalytic degradation of caffeine by ZnO-ZnAl₂O₄ nanoparticles derived from LDH structure.” *J. Environ. Chem. Eng.*, 5(4), 3719–3726.

Elham Ahangaran, Aghaie, H., and Fazaeli, R. (2020). “Study of Amoxicillin Adsorption on the Silanized Multiwalled Carbon Nanotubes: Isotherms, Kinetics, and Thermodynamics Study.” *Russ. J. Phys. Chem. A*, 94(13), 2818–2828.

Enache, D. F., Vasile, E., Simonescu, C. M., Răzvan, A., Nicolescu, A., Nechifor, A. C., Oprea, O., Pătescu, R. E., Onose, C., and Dumitru, F. (2017a). “Cysteine-functionalized silica-coated magnetite nanoparticles as potential nanoadsorbents.” *J. Solid State Chem.*, 253(June), 318–328.

Enache, D. F., Vasile, E., Simonescu, C. M., Răzvan, A., Nicolescu, A., Nechifor, A. C., Oprea, O., Pătescu, R. E., Onose, C., and Dumitru, F. (2017b). “Cysteine-functionalized silica-coated magnetite nanoparticles as potential nanoadsorbents.” *J. Solid State Chem.*, 253, 318–328.

Fàbrega, F., Kumar, V., Schuhmacher, M., Domingo, J. L., and Nadal, M. (2014). “PBPK modeling for PFOS and PFOA: Validation with human experimental data.” *Toxicol. Lett.*, 230(2), 244–251.

Falconer, I. R., Chapman, H. F., Moore, M. R., and Ranmuthugala, G. (2006). “Endocrine-disrupting compounds: A review of their challenge to sustainable and safe water supply and water reuse.” *Environ. Toxicol.*, 21(2), 181–191.

Falyouna, O., Faizul Idham, M., Maamoun, I., Bensaida, K., Ashik, U., Sugihara, Y., and Eljamal, O. (2022). “Promotion of ciprofloxacin adsorption from contaminated solutions by oxalate modified nanoscale zerovalent iron particles.” *J. Mol. Liq.*, 359, 119323.

Fent, K., Weston, A. A., and Caminada, D. (2006). “Ecotoxicology of human pharmaceuticals.” *Aquat. Toxicol.*, 76(2), 122–159.

Fernandes, T. A., Mendo, S. G., Ferreira, L. P., Neng, N. R., Oliveira, M. C., Gil, A., Carvalho, M. D., Monteiro, O. C., Nogueira, J. M. F., and Calhorda, M. J. (2021). “Photocatalytic degradation of acetaminophen and caffeine using magnetite–hematite combined nanoparticles: kinetics and mechanisms.” *Environ. Sci. Pollut. Res.*, 28(14), 17228–17243.

Floriano, J. F., Barros, N. R. de, Cinman, J. L. F., Silva, R. G. da, Loffredo, A. V., Borges, F. A., Norberto, A. M. Q., Chagas, A. L. D., Garms, B. C., Oliveira Graeff, C. F. de, and Herculano, R. D. (2018). “Ketoprofen Loaded in Natural Rubber Latex Transdermal Patch for Tendinitis Treatment.” *J. Polym. Environ.*, 26(6), 2281–2289.

Foo, K. Y., and Hameed, B. H. (2010). “Insights into the modeling of adsorption isotherm

systems.” *Chem. Eng. J.*, 156(1), 2–10.

Franco, M. A. E. de, Carvalho, C. B. de, Bonetto, M. M., Pelegrini Soares, R. de, and F ris, L. A. (2018). “Diclofenac removal from water by adsorption using activated carbon in batch mode and fixed-bed column: Isotherms, thermodynamic study and breakthrough curves modeling.” *J. Clean. Prod.*, 181, 145–154.

Fr hlich, A. C., Foletto, E. L., and Dotto, G. L. (2019). “Preparation and characterization of NiFe₂O₄/activated carbon composite as potential magnetic adsorbent for removal of ibuprofen and ketoprofen pharmaceuticals from aqueous solutions.” *J. Clean. Prod.*, 229, 828–837.

Fu, H., Ding, X., Ren, C., Li, W., Wu, H., and Yang, H. (2017). “Preparation of magnetic porous NiFe₂O₄/SiO₂ composite xerogels for potential application in adsorption of Ce(IV) ions from aqueous solution.” *RSC Adv.*, 7(27), 16513–16523.

Fu, H., Li, X., Wang, J., Lin, P., Chen, C., Zhang, X., and Suffet, I. H. M. (2016). “Activated carbon adsorption of quinolone antibiotics in water: Performance, mechanism, and modeling.” *JES*, 1–8.

Gan, Y. X., Jayatissa, A. H., Yu, Z., Chen, X., and Li, M. (2020). “Hydrothermal Synthesis of Nanomaterials.” *J. Nanomater.*, 2020, 1–3.

Gao, D., Zhang, Y., Yan, H., Li, B., He, Y., Song, P., and Wang, R. (2021). “Construction of UiO-66@MoS₂ flower-like hybrids through electrostatically induced self-assembly with enhanced photodegradation activity towards lomefloxacin.” *Sep. Purif. Technol.*, 265(February), 118486.

Gen , N., Dogan, E. C., and Yurtsever, M. (2013). “Bentonite for ciprofloxacin removal from aqueous solution.” *Water Sci. Technol.*, 68(4), 848–855.

Georgin, J., Franco, D. S. P., Boit Martinello, K. Da, Lima, E. C., and Silva, L. F. O. (2022). “A review of the toxicology presence and removal of ketoprofen through adsorption technology.” *J. Environ. Chem. Eng.*, 10(3), 107798.

Ghanbari, F., and Moradi, M. (2017). “Application of peroxymonosulfate and its activation methods for degradation of environmental organic pollutants: Review.” *Chem. Eng. J.*, 310, 41–62.

Ghazal, H., Koumaki, E., Hoslett, J., Malamis, S., Katsou, E., Barcelo, D., and Jouhara, H. (2022). “Insights into current physical, chemical and hybrid technologies used for the treatment of wastewater contaminated with pharmaceuticals.” *J. Clean. Prod.*, 361(November 2021), 132079.

Ghosh, S., Badruddoza, A. Z. M., Hidajat, K., and Uddin, M. S. (2013). “Adsorptive removal of emerging contaminants from water using superparamagnetic Fe₃O₄ nanoparticles bearing

aminated β -cyclodextrin.” *J. Environ. Chem. Eng.*, 1(3), 122–130.

Gor, A. H., and Dave, P. N. (2020). “Adsorptive abatement of ciprofloxacin using NiFe₂O₄ nanoparticles incorporated into G. ghatti-cl-P(AAm) nanocomposites hydrogel: isotherm, kinetic, and thermodynamic studies.” *Polym. Bull.*, 77(11), 5589–5613.

Groisman, L., Rav-Acha, C., Gerstl, Z., and Mingelgrin, U. (2004). “Sorption of organic compounds of varying hydrophobicities from water and industrial wastewater by long- and short-chain organoclays.” *Appl. Clay Sci.*, 24(3–4), 159–166.

Gu, J., Wei, G., Zhu, Y., Zhang, L., Mo, S., Yao, Z., Yang, R., and Li, B. (2024). “Red mud-based CoFe₂O₄ activated by ball milling as effective peroxymonosulfate activator for the degradation of lomefloxacin hydrochloride: Preparation & activation, application and degradation mechanism.” *Chem. Eng. J.*, 487(February), 150500.

Guo, L., He, Y., Chen, D., Du, B., Cao, W., Lv, Y., and Ding, Z. (2021). “Hydrothermal synthesis and microwave absorption properties of nickel ferrite/multiwalled carbon nanotubes composites.” *Coatings*, 11(5), 1–8.

Guo, R., Chen, Y., Liu, B., Han, Y., Gou, J., and Cheng, X. (2022). “Catalytic degradation of lomefloxacin by photo-assisted persulfate activation on natural hematite: Performance and mechanism.” *Chinese Chem. Lett.*, 33(8), 3809–3817.

Guo, R., Chen, Y., Nengzi, L., Meng, L., Song, Q., Gou, J., and Cheng, X. (2020a). “In situ preparation of carbon-based Cu-Fe oxide nanoparticles from CuFe Prussian blue analogues for the photo-assisted heterogeneous peroxymonosulfate activation process to remove lomefloxacin.” *Chem. Eng. J.*, 398(August 2019), 125556.

Guo, R., Zhu, Y., Cheng, X., Li, J., and Crittenden, J. C. (2020b). “Efficient degradation of lomefloxacin by Co-Cu-LDH activating peroxymonosulfate process: Optimization, dynamics, degradation pathway and mechanism.” *J. Hazard. Mater.*, 399(March), 122966.

Han, Y., Lu, Z., Teng, Z., Liang, J., Guo, Z., Wang, D., Han, M. Y., and Yang, W. (2017). “Unraveling the growth mechanism of silica particles in the stöber method: In situ seeded growth model.” *Langmuir*, 33(23), 5879–5890.

Hassanien, R., Husein, D. Z., and Al-Hakkani, M. F. (2018). “Biosynthesis of copper nanoparticles using aqueous Tilia extract: antimicrobial and anticancer activities.” *Heliyon*, 4(12), e01077.

Hayasi, M., and Saadatjoo, N. (2018). “Preparation of magnetic nanoparticles functionalized with poly (styrene-2-acrylamido-2-methyl propanesulfonic acid) as novel adsorbents for removal of pharmaceuticals from aqueous solutions.” *Adv. Polym. Technol.*, 37(6), 1941–1953.

He, B., Song, L., Zhao, Z., Liu, W., Zhou, Y., Shang, J., and Cheng, X. (2022a). “CuFe₂O₄/CuO

magnetic nano-composite activates PMS to remove ciprofloxacin: Ecotoxicity and DFT calculation.” *Chem. Eng. J.*, 446(May).

He, B., Song, L., Zhao, Z., Liu, W., Zhou, Y., Shang, J., and Cheng, X. (2022b). “CuFe₂O₄/CuO magnetic nano-composite activates PMS to remove ciprofloxacin: Ecotoxicity and DFT calculation.” *Chem. Eng. J.*, 446(May), 137183.

He, Y., Dai, C., and Zhou, X. (2017). “Magnetic cobalt ferrite composite as an efficient catalyst for photocatalytic oxidation of carbamazepine.” *Environ. Sci. Pollut. Res.*, 24(2), 2065–2074.

Hignite, C., and Azarnoff, D. L. (1977). “Drugs and drug metabolites as environmental contaminants: Chlorophenoxyisobutyrate and salicylic acid in sewage water effluent.” *Life Sci.*, 20(2), 337–341.

Ho, Y. ., and McKay, G. (1999). “Pseudo-second order model for sorption processes.” *Process Biochem.*, 34(5), 451–465.

Homem, V., and Santos, L. (2011). “Degradation and removal methods of antibiotics from aqueous matrices e A review.” *J. Environ. Manage.*, 92(10), 2304–2347.

Horsfall Jnr, M., and Spiff, A. I. (2005). “Effects of temperature on the sorption of Pb²⁺ and Cd²⁺ from aqueous solution by *Caladium bicolor* (Wild Cocoyam) biomass.” *Electron. J. Biotechnol.*, 8(2), 162–169.

Hu, Q., and Zhang, Z. (2019). “Application of Dubinin–Radushkevich isotherm model at the solid/solution interface: A theoretical analysis.” *J. Mol. Liq.*, 277, 646–648.

Hua, Y., Liu, G., Lin, Z., Jie, Z., Zhao, C., Han, J., Chen, G., Li, L., Huang, X., Liu, Z., Lv, J., and Xu, D. (2024). “Engineering of zeolitic imidazolate frameworks based on magnetic three-dimensional graphene as effective and reusable adsorbent to enhance the adsorption and removal of caffeine from tea samples.” *Food Chem.*, 431(August 2022), 137143.

Huang, H., Heng, Y., Yu, Z., Zhang, X., Zhu, X., Fang, Z., and Li, J. (2024). “Journal of Colloid And Interface Science Solvent-free synthesis of defective Zr-based metal – organic framework from waste plastic bottles for highly efficient lomefloxacin removal.” *J. Colloid Interface Sci.*, 670(May), 509–518.

Huerta-Fontela, M., Galceran, M. T., and Ventura, F. (2008). “Stimulatory drugs of abuse in surface waters and their removal in a conventional drinking water treatment plant.” *Environ. Sci. Technol.*, 42(18), 6809–6816.

Husain, A., Abdul, H., Palaniandy, P., and Zouli, N. (2024). “Journal of the Taiwan Institute of Chemical Engineers Ciprofloxacin adsorption onto Pumice-bentonite composites : Modeling , kinetics , equilibriums and reusability studies.” *J. Taiwan Inst. Chem. Eng.*, (June), 105618.

Husein, D. Z., Hassanien, R., and Al-Hakkani, M. F. (2019). “Green-synthesized copper nano-

adsorbent for the removal of pharmaceutical pollutants from real wastewater samples.” *Heliyon*, 5(8), e02339.

IS 3025-43 (1992): Methods of sampling and test (physical and chemical) for water and waste water, Part 43: Phenols. (1992). *CHD 32 Environ. Prot. Waste Manag. (Bureau Indian Stand.*

Isasi, J., Arévalo, P., Martín, E., and Martín-Hernández, F. (2019). “Preparation and study of silica and APTES–silica-modified NiFe₂O₄ nanocomposites for removal of Cu²⁺ and Zn²⁺ ions from aqueous solutions.” *J. Sol-Gel Sci. Technol.*, 91(3), 596–610.

Jacob, B. P., Kumar, A., Pant, R. P., Singh, S., and Mohammed, E. M. (2011a). “Influence of preparation method on structural and magnetic properties of nickel ferrite nanoparticles.” *Bull. Mater. Sci.*, 34(7), 1345–1350.

Jacob, B. P., Kumar, A., Pant, R. P., Singh, S., and Mohammed, E. M. (2011b). “Influence of preparation method on structural and magnetic properties of nickel ferrite nanoparticles.” *Bull. Mater. Sci.*, 34(7), 1345–1350.

Jacob, N. M., Kuruva, P., Madras, G., and Thomas, T. (2013). “Purifying water containing both anionic and cationic species using a (Zn, Cu)O, ZnO, and cobalt ferrite based multiphase adsorbent system.” *Ind. Eng. Chem. Res.*, 52(46), 16384–16395.

Jadhav, V. V., Shirsat, S. D., Tumberphale, U. B., and Mane, R. S. (2020). *Properties of ferrites. Spinel Ferrite Nanostructures for Energy Storage Devices*, Elsevier Inc.

Jia, D., Monfort, O., Hanna, K., Mailhot, G., and Brigante, M. (2021). “Caffeine degradation using peroxydisulfate and peroxymonosulfate in the presence of Mn₂O₃. Efficiency, reactive species formation and application in sewage treatment plant water.” *J. Clean. Prod.*, 328(October), 129652.

Jjemba, P. K. (2006). “Excretion and ecotoxicity of pharmaceutical and personal care products in the environment.” *Ecotoxicol. Environ. Saf.*, 63(1), 113–130.

Jogannatha, R. B., Ramu, S. R., Padaki, M., and Balakrishna, R. G. (2017). “1. An efficient method for the synthesis of photo catalytically active ZnO nanoparticles by a gel-combustion method for the photo- degradation of Caffeine.” *Nanochem Res*, 2(1), 1–10.

Joshi, S., Kumar, M., Chhoker, S., Srivastava, G., Jewariya, M., and Singh, V. N. (2014). “Structural, magnetic, dielectric and optical properties of nickel ferrite nanoparticles synthesized by co-precipitation method.” *J. Mol. Struct.*, 1076, 55–62.

Kadam, V. V., Shanmugam, S. D., Ettiyappan, J. P., and Balakrishnan, R. M. (2021). “Photocatalytic degradation of p-nitrophenol using biologically synthesized ZnO nanoparticles.” *Environ. Sci. Pollut. Res.*, 28(10), 12119–12130.

Kaur, M., Kaur, N., and Vibha. (2016). “Ferrites: Synthesis and Applications for

- Environmental Remediation." *ACS Symp. Ser.*, 1238, 113–136.
- Kebede, T. G., Dube, S., and Nindi, M. M. (2019). "Biopolymer electrospun nanofibres for the adsorption of pharmaceuticals from water systems." *J. Environ. Chem. Eng.*, 7(5), 103330.
- Kennedy, A. M., Reinert, A. M., Knappe, D. R. U., Ferrer, I., and Scott, R. (2014). "SC." *Water Res.*
- Khairy, M., Bayoumy, W. A., Selima, S. S., and Mousa, M. A. (2020). "Studies on characterization, magnetic and electrochemical properties of nano-size pure and mixed ternary transition metal ferrites prepared by the auto-combustion method." *J. Mater. Res.*, 35(20), 2652–2663.
- Khamparia, S., and Jaspal, D. (2017). "Study of decolorisation of binary dye mixture by response surface methodology." *J. Environ. Manage.*, 201, 316–326.
- Khan, M. A., Kim, S. wook, Rao, R. A. K., Abou-Shanab, R. A. I., Bhatnagar, A., Song, H., and Jeon, B. H. (2010). "Adsorption studies of Dichloromethane on some commercially available GACs: Effect of kinetics, thermodynamics and competitive ions." *J. Hazard. Mater.*, 178(1–3), 963–972.
- Khorshidi, P., Shirazi, R. H. S. M., Miralinaghi, M., Moniri, E., and Saadi, S. (2020). "Adsorptive removal of mercury (II), copper (II), and lead (II) ions from aqueous solutions using glutathione-functionalized NiFe₂O₄/graphene oxide composite." *Res. Chem. Intermed.*, 46(7), 3607–3627.
- Khoso, W. A., Haleem, N., Baig, M. A., and Jamal, Y. (2021). "Synthesis, characterization and heavy metal removal efficiency of nickel ferrite nanoparticles (NFN's)." *Sci. Rep.*, 11(1), 1–10.
- Klavarioti, M., Mantzavinos, D., and Kassinos, D. (2009). "Removal of residual pharmaceuticals from aqueous systems by advanced oxidation processes." *Environ. Int.*, 35(2), 402–417.
- Kollarahithlu, S. C., and Balakrishnan, R. M. (2019). "Adsorption of ibuprofen using cysteine-modified silane-coated magnetic nanomaterial." *Environ. Sci. Pollut. Res.*, 26(33), 34117–34126.
- Kolpin, D. W., Furlong, E. T., Meyer, M. T., Thurman, E. M., Zaugg, S. D., Barber, L. B., and Buxton, H. T. (2002). "Pharmaceuticals, hormones, and other organic wastewater contaminants in U.S. streams, 1999-2000: A national reconnaissance." *Environ. Sci. Technol.*, 36(6), 1202–1211.
- Korekar, G., Kumar, A., and Ugale, C. (2020). "Occurrence, fate, persistence and remediation of caffeine: a review." *Environ. Sci. Pollut. Res.*, 27(28), 34715–34733.

- Koutavarapu, R., Tamtam, M. R., Myla, C. R., Cho, M., and Shim, J. (2021). “Enhanced solar-light-driven photocatalytic properties of novel Z-scheme binary BiPO₄ nanorods anchored onto NiFe₂O₄ nanoplates: Efficient removal of toxic organic pollutants.” *J. Environ. Sci. (China)*, 102, 326–340.
- Kozłowska, M., Rodziewicz, P., and Kaczmarek-Kedziera, A. (2017). “Structural stability of diclofenac vs. inhibition activity from ab initio molecular dynamics simulations. Comparative study with ibuprofen and ketoprofen.” *Struct. Chem.*, 28(4), 999–1008.
- Kumar, M., Singh Dosanjh, H., Sonika, Singh, J., Monir, K., and Singh, H. (2020). “Review on magnetic nanoferrites and their composites as alternatives in waste water treatment: Synthesis, modifications and applications.” *Environ. Sci. Water Res. Technol.*, 6(3), 491–514.
- Langmuir, I. (1916). “THE CONSTITUTION AND FUNDAMENTAL PROPERTIES OF SOLIDS AND LIQUIDS. PART I. SOLIDS.” *J. Am. Chem. Soc.*, 38(11), 2221–2295.
- Larous, S., and Meniai, A. H. (2016). “Adsorption of Diclofenac from aqueous solution using activated carbon prepared from olive stones.” *Int. J. Hydrogen Energy*, 41(24), 10380–10390.
- Lawal, I. A., Lawal, M. M., Akpotu, S. O., Azeez, M. A., Ndungu, P., and Moodley, B. (2018). “Theoretical and experimental adsorption studies of sulfamethoxazole and ketoprofen on synthesized ionic liquids modified CNTs.” *Ecotoxicol. Environ. Saf.*, 161(April), 542–552.
- Lee, S., Lee, J., Song, M., Ryu, J., An, B., Lee, C., Park, C., Lee, S., and Choi, J. (2015). “Effective regeneration of an adsorbent for the removal of organic contaminants developed based on UV radiation and toxicity evaluation.” *REACT*, 95, 62–70.
- Li, A., Deng, H., Wu, Y., Ye, C., and Jiang, Y. (2021). “Strong Adsorption of Phosphorus by ZnAl-LDO-Activated Banana Biochar: An Analysis of Adsorption Efficiency, Thermodynamics, and Internal Mechanisms.” *ACS Omega*, 6(11), 7402–7412.
- Li, H., Liu, L., Cui, J., Cui, J., Wang, F., and Zhang, F. (2020). “High-efficiency adsorption and regeneration of methylene blue and aniline onto activated carbon from waste edible fungus residue and its possible mechanism.” *RSC Adv.*, 10(24), 14262–14273.
- Li, J., Xu, M., Yao, G., and Lai, B. (2018). “Enhancement of the degradation of atrazine through CoFe₂O₄ activated peroxymonosulfate (PMS) process: Kinetic, degradation intermediates, and toxicity evaluation.” *Chem. Eng. J.*, 348(May), 1012–1024.
- Li, N., Gao, B., Yang, R., and Yang, H. (2022). “Simple fabrication of carboxymethyl cellulose and κ-carrageenan composite aerogel with efficient performance in removal of fluoroquinolone antibiotics from water.” *Front. Environ. Sci. Eng.*, 16(10), 133.
- Li, S., Tang, Y., Zhang, X., Dou, Y., and Shen, X. (2019). “Preparation and characterization of diclofenac sodium β-cyclodextrin inclusion complex eye drops.” *J. Incl. Phenom. Macrocycl.*

Chem., 94(1–2), 85–94.

Li, S., Zhang, X., and Huang, Y. (2017). “Zeolitic imidazolate framework-8 derived nanoporous carbon as an effective and recyclable adsorbent for removal of ciprofloxacin antibiotics from water.” *J. Hazard. Mater.*, 321, 711–719.

Li, X., Chen, S., Fan, X., Quan, X., Tan, F., Zhang, Y., and Gao, J. (2015). “Adsorption of ciprofloxacin, bisphenol and 2-chlorophenol on electrospun carbon nanofibers: In comparison with powder activated carbon.” *J. Colloid Interface Sci.*, 447, 120–127.

Li, Z., and Yang, P. (2018). “Review on Physicochemical, Chemical, and Biological Processes for Pharmaceutical Wastewater.” *IOP Conf. Ser. Earth Environ. Sci.*, 113(1).

Liang, X. X., Omer, A. M., Hu, Z. hong, Wang, Y. guang, Yu, D., and Ouyang, X. kun. (2019). “Efficient adsorption of diclofenac sodium from aqueous solutions using magnetic amine-functionalized chitosan.” *Chemosphere*, 217, 270–278.

Lin, K. Y. A., and Chen, B. J. (2017). “Magnetic carbon-supported cobalt derived from a Prussian blue analogue as a heterogeneous catalyst to activate peroxymonosulfate for efficient degradation of caffeine in water.” *J. Colloid Interface Sci.*, 486, 255–264.

Lin, K. Y. A., Lai, H. K., and Tong, S. (2018). “One-step prepared cobalt-based nanosheet as an efficient heterogeneous catalyst for activating peroxymonosulfate to degrade caffeine in water.” *J. Colloid Interface Sci.*, 514, 272–280.

Lindqvist, N., Tuhkanen, T., and Kronberg, L. (2005). “Occurrence of acidic pharmaceuticals in raw and treated sewages and in receiving waters.” *Water Res.*, 39(11), 2219–2228.

Liu, C., Nanaboina, V., Korshin, G. V., and Jiang, W. (2012). “Spectroscopic study of degradation products of ciprofloxacin, norfloxacin and lomefloxacin formed in ozonated wastewater.” *Water Res.*, 46(16), 5235–5246.

Liu, J., Yang, H., and Xue, X. (2019a). “Structure, morphology, and magnetic properties of NiFe₂O₄ powder prepared by molten salt method.” *Powder Technol.*, 355, 708–715.

Liu, S., Zhao, Y., Wang, T., Liang, N., and Hou, X. (2019b). “Core-Shell Fe₃O₄@MIL-100(Fe) Magnetic Nanoparticle for Effective Removal of Meloxicam and Naproxen in Aqueous Solution.” *J. Chem. Eng. Data*, research-article, 64(7), 2997–3007.

Liu, X., Liu, M., and Zhang, L. (2018). “Co-adsorption and sequential adsorption of the co-existence four heavy metal ions and three fluoroquinolones on the functionalized ferromagnetic 3D NiFe₂O₄ porous hollow microsphere.” *J. Colloid Interface Sci.*, 511, 135–144.

Lotfi, R., Hayati, B., Rahimi, S., Shekarchi, A. A., Mahmoodi, N. M., and Bagheri, A. (2019). “Synthesis and characterization of PAMAM/SiO₂ nanohybrid as a new promising adsorbent for pharmaceuticals.” *Microchem. J.*, 146(October 2018), 1150–1159.

- Lv, S., Song, Y., Song, Y., Zhao, Z., and Cheng, C. (2014). "Beta-cyclodextrins conjugated magnetic Fe₃O₄ colloidal nanoclusters for the loading and release of hydrophobic molecule." *Appl. Surf. Sci.*, 305, 747–752.
- Ma, Q., Nengzi, L., Li, B., Wang, Z., Liu, L., and Cheng, X. (2020). "Heterogeneously catalyzed persulfate with activated carbon coated with CoFe layered double hydroxide (AC@CoFe-LDH) for the degradation of lomefloxacin." *Sep. Purif. Technol.*, 235(October 2019), 116204.
- Maaz, K., Karim, S., Mumtaz, A., Hasanain, S. K., Liu, J., and Duan, J. L. (2009). "Synthesis and magnetic characterization of nickel ferrite nanoparticles prepared by co-precipitation route." *J. Magn. Magn. Mater.*, 321(12), 1838–1842.
- Maciel, A. P., Gomide, G., Silva, F. G. da, Guerra, A. A. A. M., Depeyrot, J., Mezzi, A., and Campos, A. F. C. (2023). "L-Lysine-Coated Magnetic Core–Shell Nanoparticles for the Removal of Acetylsalicylic Acid from Aqueous Solutions." *Nanomaterials*, 13(3), 514.
- Mahjoore, M., Aryafar, A., and Honarmand, M. (2022). "Cadmium Oxide Nanoparticles as A Novel Photo-Catalyst for Degradation of Ciprofloxacin Antibiotic in Aqueous Media." *J. Min. Environ.*, 13(1), 155–164.
- Mahmoud, M. H., Elshahawy, A. M., Makhlof, S. A., and Hamdeh, H. H. (2013). "Mössbauer and magnetization studies of nickel ferrite nanoparticles synthesized by the microwave-combustion method." *J. Magn. Magn. Mater.*, 343, 21–26.
- Maia, G. S., Andrade, J. R. de, Silva, M. G. C. da, and Vieira, M. G. A. (2019). "Adsorption of diclofenac sodium onto commercial organoclay: Kinetic, equilibrium and thermodynamic study." *Powder Technol.*, 345, 140–150.
- Majid, F., Rauf, J., Ata, S., Bibi, I., Malik, A., Ibrahim, S. M., Ali, A., and Iqbal, M. (2021). "Synthesis and characterization of NiFe₂O₄ ferrite: Sol–gel and hydrothermal synthesis routes effect on magnetic, structural and dielectric characteristics." *Mater. Chem. Phys.*, 258, 123888.
- Malay, O., Yilgor, I., and Menciloglu, Y. Z. (2013). "Effects of solvent on TEOS hydrolysis kinetics and silica particle size under basic conditions." *J. Sol-Gel Sci. Technol.*, 67(2), 351–361.
- Malik, R., Goyal, A., Yadav, S., Gupta, N., Goel, N., Kaushik, A., Kumar, V., Tikoo, K. B., and Singhal, S. (2019). "Functionalized magnetic nanomaterials for rapid and effective adsorptive removal of fluoroquinolones: Comprehensive experimental cum computational investigations." *J. Hazard. Mater.*, 364, 621–634.
- Manirethan, V., Gupta, N., Balakrishnan, R. M., and Raval, K. (2020). "Batch and continuous studies on the removal of heavy metals from aqueous solution using biosynthesised melanin-

coated PVDF membranes.” *Environ. Sci. Pollut. Res.*, 27(20), 24723–24737.

Manirethan, V., Raval, K., Rajan, R., Thaira, H., and Balakrishnan, R. M. (2018). “Kinetic and thermodynamic studies on the adsorption of heavy metals from aqueous solution by melanin nanopigment obtained from marine source: *Pseudomonas stutzeri*.” *J. Environ. Manage.*, 214, 315–324.

Manna, M., and Sen, S. (2022). “Advanced oxidation process: a sustainable technology for treating refractory organic compounds present in industrial wastewater.” *Environ. Sci. Pollut. Res.*, 25477–25505.

Mapossa, A. B., Dantas, J., Silva, M. R., Kiminami, R. H. G. A., Costa, A. C. F. M., and Daramola, M. O. (2020). “Catalytic performance of NiFe₂O₄ and Ni_{0.3}Zn_{0.7}Fe₂O₄ magnetic nanoparticles during biodiesel production.” *Arab. J. Chem.*, 13(2), 4462–4476.

Maryam, B., Buscio, V., Odabasi, S. U., and Buyukgungor, H. (2020). “A study on behavior, interaction and rejection of Paracetamol, Diclofenac and Ibuprofen (PhACs) from wastewater by nanofiltration membranes.” *Environ. Technol. Innov.*, 18, 100641.

Mashkoo, F., Nasar, A., Inamuddin, and Asiri, A. M. (2018). “Exploring the reusability of synthetically contaminated wastewater containing crystal violet dye using tectona grandis sawdust as a very low-cost adsorbent.” *Sci. Rep.*, 8(1), 1–17.

Miklos, D. B., Remy, C., Jekel, M., Linden, K. G., Drewes, J. E., and Hübner, U. (2018). “Evaluation of advanced oxidation processes for water and wastewater treatment – A critical review.” *Water Res.*, 139, 118–131.

Mirzaei, A., Chen, Z., Haghghat, F., and Yerushalmi, L. (2016). “Removal of pharmaceuticals and endocrine disrupting compounds from water by zinc oxide-based photocatalytic degradation : A review.” *Sustain. Cities Soc.*, 27, 407–418.

Mohammed, N. A. H., Shamma, R. N., Elagroudy, S., and Adewuyi, A. (2024). “Chitosan incorporated nickel ferrite photocatalyst for complete photocatalytic degradation of ciprofloxacin, ampicillin and erythromycin in water.” *Results Chem.*, 7(January), 101307.

Moulahcene, L., Skiba, M., Milon, N., Fadila, H., Bounoure, F., and Lahiani-Skiba, M. (2023). “Removal Efficiency of Insoluble β -Cyclodextrin Polymer from Water–Soluble Carcinogenic Direct Azo Dyes.” *Polymers (Basel)*, 15(3).

Munoz, M., Nieto-Sandoval, J., Álvarez-Torrellas, S., Sanz-Santos, E., Calderón, B., Pedro, Z. M. de, Larriba, M., Fullana, A., García, J., and Casas, J. A. (2021). “Carbon-encapsulated iron nanoparticles as reusable adsorbents for micropollutants removal from water.” *Sep. Purif. Technol.*, 257(November 2020).

N., A., Ang, B. C., M.A., A., and Bong, C. W. (2018). “Influence of Precursor Concentration

and Temperature on the Formation of Nanosilver in Chemical Reduction Method.” *Sains Malaysiana*, 47(1), 157–168.

Nagao, D., Osuzu, H., Yamada, A., Mine, E., Kobayashi, Y., and Konno, M. (2004). “Particle formation in the hydrolysis of tetraethyl orthosilicate in pH buffer solution.” *J. Colloid Interface Sci.*, 279(1), 143–149.

Narang, S. B., and Pubby, K. (2021). “Nickel Spinel Ferrites: A review.” *J. Magn. Magn. Mater.*, 519(June 2019).

Nasiri, A., Rajabi, S., Hashemi, M., and Nasab, H. (2022). “CuCoFe₂O₄@MC/AC as a new hybrid magnetic nanocomposite for metronidazole removal from wastewater: Bioassay and toxicity of effluent.” *Sep. Purif. Technol.*, 296(May), 121366.

Ndabankulu, V. O., Maddila, S., and Jonnalagadda, S. B. (2019). “Ozone facilitated degradation of caffeine using Ce-TiO₂ catalyst.” *J. Environ. Sci. Heal. - Part B Pestic. Food Contam. Agric. Wastes*, 54(2), 138–146.

Negarestani, M., Reisi, S., Sohrabi, M., Shayesteh, H., Farimaniraad, H., Mollahosseini, A., Hosseinzadeh, M., and Tavassoli, S. (2024). “Journal of Water Process Engineering In-situ growth of Al / Ni layered double hydroxide onto polyaniline-wrapped sisal fibers for highly efficient removal of pharmaceutical Ketoprofen and Ibuprofen contaminants : Batch and fixed-bed column studies.” *J. Water Process Eng.*, 57(October 2023), 104657.

Nguyet, D. T. T., Duong, N. P., Hung, L. T., Hien, T. D., and Satoh, T. (2011). “Crystallization and magnetic behavior of nanosized nickel ferrite prepared by citrate precursor method.” *J. Alloys Compd.*, 509(23), 6621–6625.

Njoku, V. O., Islam, M. A., Asif, M., and Hameed, B. H. (2014). “Utilization of sky fruit husk agricultural waste to produce high quality activated carbon for the herbicide bentazon adsorption.” *Chem. Eng. J.*, 251, 183–191.

Ogden, S. G., Lewis, D., and Shapter, J. G. (2008). “Silane functionalisation of iron oxide nanoparticles.” *Smart Mater. V*, 7267(December), 72670A.

Ong, B. H., Chee, E. S. C., Abd Hamid, S. B. O. A., and Lim, K. P. (2012). “Synthesis and characterization of nickel ferrite magnetic nanoparticles by co-precipitation method.” *AIP Conf. Proc.*, 1502(1), 221–229.

P, A., GK, P., Bhowmick, M., Sonkar, S., Karthikeyan, D., and T, S. (2022). “REVIEW ARTICLE • The Scope of Web-based Clinical Research in Pharmacy.” (May 2017).

Pal, A., Gin, K. Y. H., Lin, A. Y. C., and Reinhard, M. (2010). “Impacts of emerging organic contaminants on freshwater resources: Review of recent occurrences, sources, fate and effects.” *Sci. Total Environ.*, 408(24), 6062–6069.

- Pandis, P. K., Kalogirou, C., Kanellou, E., Vaitis, C., Savvidou, M. G., Sourkouni, G., Zorpas, A. A., and Argiris, C. (2022). “Key Points of Advanced Oxidation Processes (AOPs) for Wastewater, Organic Pollutants and Pharmaceutical Waste Treatment: A Mini Review.” *ChemEngineering*, 6(1).
- Pape, P. G. (2017). *Adhesion Promoters: Silane Coupling Agents. Appl. Plast. Eng. Handb. Process. Mater. Appl. Second Ed.*, Elsevier Inc.
- Patel, M., Kumar, R., Kishor, K., Mlsna, T., Pittman, C. U., and Mohan, D. (2019). “Pharmaceuticals of emerging concern in aquatic systems: Chemistry, occurrence, effects, and removal methods.” *Chem. Rev.*, review-article, 119(6), 3510–3673.
- Pavan, F. A., Camacho, E. S., Lima, E. C., Dotto, G. L., Branco, V. T. A., and Dias, S. L. P. (2014). “Formosa papaya seed powder (FPSP): Preparation, characterization and application as an alternative adsorbent for the removal of crystal violet from aqueous phase.” *J. Environ. Chem. Eng.*, 2(1), 230–238.
- Pavithra, K. G., Senthil Kumar, P., Sundar Rajan, P., Saravanan, A., and Naushad, M. (2017). “Sources and impacts of pharmaceutical components in wastewater and its treatment process: A review.” *Korean J. Chem. Eng.*, 34(11), 2787–2805.
- Peñafiel, M. E., Matesanz, J. M., Vanegas, E., Bermejo, D., Mosteo, R., and Ormad, M. P. (2021). “Comparative adsorption of ciprofloxacin on sugarcane bagasse from Ecuador and on commercial powdered activated carbon.” *Sci. Total Environ.*, 750, 141498.
- Pereira, M. B. B., França, D. B., Araújo, R. C., Silva Filho, E. C., Rigaud, B., Fonseca, M. G., and Jaber, M. (2020). “Amino hydroxyapatite/chitosan hybrids reticulated with glutaraldehyde at different pH values and their use for diclofenac removal.” *Carbohydr. Polym.*, 236(February), 116036.
- Pham, T. D., Bui, T. T., Nguyen, V. T., Bui, T. K. Van, Tran, T. T., Phan, Q. C., Pham, T. D., and Hoang, T. H. (2018). “Adsorption of polyelectrolyte onto nanosilica synthesized from rice husk: Characteristics, mechanisms, and application for antibiotic removal.” *Polymers (Basel)*, 10(2).
- Philip, J. M., Aravind, U. K., and Aravindakumar, C. T. (2018). “Emerging contaminants in Indian environmental matrices – A review.” *Chemosphere*, 190, 307–326.
- Phonsiri, V., Choi, S., Nguyen, C., Tsai, Y.-L., Coss, R., and Kurwadkar, S. (2019). “Monitoring occurrence and removal of selected pharmaceuticals in two different wastewater treatment plants.” *SN Appl. Sci.*, 1(7), 798.
- Plakas, K. V., Mantza, A., Sklari, S. D., Zaspalis, V. T., and Karabelas, A. J. (2019). “Heterogeneous Fenton-like oxidation of pharmaceutical diclofenac by a catalytic iron-oxide

ceramic microfiltration membrane.” *Chem. Eng. J.*, 373(February), 700–708.

Ponchel, A., Abramson, S., Quartararo, J., Bormann, D., Barbaux, Y., and Monflier, E. (2004). “Cyclodextrin silica-based materials: Advanced characterizations and study of their complexing behavior by diffuse reflectance UV-Vis spectroscopy.” *Microporous Mesoporous Mater.*, 75(3), 261–272.

Pruss, A., Kay, D., Fewtrell, L., and Bartram, J. (2002). “Estimación de la carga de enfermedades derivada del agua, el saneamiento y la higiene a Nivel global.” *Perspect. salud Ambient.*, 110(6).

Qi, F., Chu, W., and Xu, B. (2014). “Modeling the heterogeneous peroxymonosulfate/Co-MCM41 process for the degradation of caffeine and the study of influence of cobalt sources.” *Chem. Eng. J.*, 235, 10–18.

Quesada, H. B., Baptista, A. T. A., Cusioli, L. F., Seibert, D., Oliveira Bezerra, C. de, and Bergamasco, R. (2019). “Surface water pollution by pharmaceuticals and an alternative of removal by low-cost adsorbents: A review.” *Chemosphere*, 222, 766–780.

Quintero-jaramillo, J. A., Carrero, J. I., and Sanabria-gonz, N. R. (2024). “Caffeine Adsorption on a Thermally Modified Bentonite : Adsorbent Characterization , Experimental Design , Equilibrium and Kinetics.”

Radjenović, J., Petrović, M., Ventura, F., and Barceló, D. (2008). “Rejection of pharmaceuticals in nanofiltration and reverse osmosis membrane drinking water treatment.” *Water Res.*, 42(14), 3601–3610.

Ragavan, K. V., and Rastogi, N. K. (2017). “ β -Cyclodextrin capped graphene-magnetite nanocomposite for selective adsorption of Bisphenol-A.” *Carbohydr. Polym.*, 168, 129–137.

Rajam, K., Rajendran, S., and Banu, N. N. (2013). “Effect of Caffeine-Zn 2+ System in Preventing Corrosion of Carbon Steel in Well Water.” *J. Chem.*, 2013, 1–11.

Rajoriya, S., Bargole, S., and Saharan, V. K. (2017). “Degradation of a cationic dye (Rhodamine 6G) using hydrodynamic cavitation coupled with other oxidative agents: Reaction mechanism and pathway.” *Ultrason. Sonochem.*, 34, 183–194.

Ramirez-Ubillus, M. A., Melo Costa-Serge, N. de, Hammer, P., and Nogueira, R. F. P. (2022). “Correction to: A new approach on synergistic effect and chemical stability of graphene oxide-magnetic nanocomposite in the heterogeneous Fenton degradation of caffeine.” *Environ. Sci. Pollut. Res.*, 29(18), 27611–27611.

Ramos-Payan, M., MasPOCH, S., and Llobera, A. (2016). “An effective microfluidic based liquid-phase microextraction device (μ LPME) for extraction of non-steroidal anti-inflammatory drugs from biological and environmental samples.” *Anal. Chim. Acta*, 946, 56–

63.

Raula, J., Kuivanen, A., Lähde, A., Jiang, H., Antopolsky, M., Kansikas, J., and Kauppinen, E. I. (2007). "Synthesis of -leucine nanoparticles via physical vapor deposition at varying saturation conditions." *J. Aerosol Sci.*, 38(12), 1172–1184.

Reddy, D. H. K., and Yun, Y. S. (2016). "Spinel ferrite magnetic adsorbents: Alternative future materials for water purification?" *Coord. Chem. Rev.*, 315, 90–111.

Revellame, E. D., Fortela, D. L., Sharp, W., Hernandez, R., and Zappi, M. E. (2020). "Adsorption kinetic modeling using pseudo-first order and pseudo-second order rate laws: A review." *Clean. Eng. Technol.*, 1(December), 100032.

Rizzi, V., Romanazzi, F., Gubitosa, J., Fini, P., Romita, R., Agostiano, A., Petrella, A., and Cosma, P. (2019). "Chitosan film as eco-friendly and recyclable bio-adsorbent to remove/recover diclofenac, ketoprofen, and their mixture from wastewater." *Biomolecules*, 9(10).

Rocha, L. S., Pereira, D., Sousa, É., Otero, M., Esteves, V. I., and Calisto, V. (2020). "Recent advances on the development and application of magnetic activated carbon and char for the removal of pharmaceutical compounds from waters: A review." *Sci. Total Environ.*, 718.

Rodante, F., and Marrosu, G. (1990). "Thermal analysis of some α -amino acids using simultaneous TG-DSC apparatus. The use of dynamic thermogravimetry to study the chemical kinetics of solid state decomposition." *Thermochim. Acta*, 171(C), 15–29.

Rodante, F., Marrosu, G., and Catalani, G. (1992). "Thermal analysis of some α -amino acids with similar structures." *Thermochim. Acta*, 194(C), 197–213.

Rodriguez-Narvaez, O. M., Peralta-Hernandez, J. M., Goonetilleke, A., and Bandala, E. R. (2017). "Treatment technologies for emerging contaminants in water: A review." *Chem. Eng. J.*, 323, 361–380.

Sacco, O., Vaiano, V., and Matarangolo, M. (2018). "ZnO supported on zeolite pellets as efficient catalytic system for the removal of caffeine by adsorption and photocatalysis." *Sep. Purif. Technol.*, 193(October 2017), 303–310.

Sagadevan, S., Chowdhury, Z. Z., and Rafique, R. F. (2018a). "Preparation and Characterization of Nickel ferrite Nanoparticles via Co-precipitation Method." *Mater. Res.*, 21(2), 21–25.

Sagadevan, S., Chowdhury, Z. Z., and Rafique, R. F. (2018b). "Preparation and Characterization of Nickel ferrite Nanoparticles via Co-precipitation Method." *Mater. Res.*, 21(2), 1–5.

Sanzgiri, Y. D., Knaub, S. R., and Riley, C. M. (1994). *ANALYTICAL PROFILES OF DRUG*

SUBSTANCES AND EXCIPIENTS. Academic Press, Inc.

Sawalha, M. F., Peralta-Videa, J. R., Romero-González, J., Duarte-Gardea, M., and Gardea-Torresdey, J. L. (2007). “Thermodynamic and isotherm studies of the biosorption of Cu(II), Pb(II), and Zn(II) by leaves of saltbush (*Atriplex canescens*).” *J. Chem. Thermodyn.*, 39(3), 488–492.

Saxena, M., Sharma, N., and Saxena, R. (2020). “Highly efficient and rapid removal of a toxic dye: Adsorption kinetics, isotherm, and mechanism studies on functionalized multiwalled carbon nanotubes.” *Surfaces and Interfaces*, 21(June), 100639.

Schwaiger, J., Ferling, H., Mallow, U., Wintermayr, H., and Negele, R. D. (2004). “Toxic effects of the non-steroidal anti-inflammatory drug diclofenac. Part I: Histopathological alterations and bioaccumulation in rainbow trout.” *Aquat. Toxicol.*, 68(2), 141–150.

Sellaoui, L., Silva, L. F. O., Badawi, M., Ali, J., Favarin, N., Dotto, G. L., Erto, A., and Chen, Z. (2021). “Adsorption of ketoprofen and 2- nitrophenol on activated carbon prepared from winery wastes: A combined experimental and theoretical study.” *J. Mol. Liq.*, 333.

Shanmugavel, T., Gokul Raj, S., Ramesh Kumar, G., Rajarajan, G., and Saravanan, D. (2015). “Cost effective preparation and characterization of nanocrystalline nickel ferrites (NiFe₂O₄) in low temperature regime.” *J. King Saud Univ. - Sci.*, 27(2), 176–181.

Shanmugavel, T., Raj, S. G., Rajarajan, G., and Kumar, G. R. (2014). “Tailoring the Structural and Magnetic Properties and of Nickel Ferrite by Auto Combustion Method.” *Procedia Mater. Sci.*, 6(Icmpe), 1725–1730.

Shayesteh, H., Nodehi, R., and Rahbar-Kelishami, A. (2020). “Trimethylamine functionalized clay for highly efficient removal of diclofenac from contaminated water: Experiments and theoretical calculations.” *Surfaces and Interfaces*, 20(August), 100615.

Shelat, R., Chandra, S., and Khanna, A. (2018). “Detailed toxicity evaluation of β -cyclodextrin coated iron oxide nanoparticles for biomedical applications.” *Int. J. Biol. Macromol.*, 110, 357–365.

Shi, M., Zhang, C., Xie, Y., and Xu, D. (2014). “Stereoselective inclusion mechanism of ketoprofen into β -cyclodextrin: insights from molecular dynamics simulations and free energy calculations.” *Theor. Chem. Acc.*, 133(10).

Sigonya, S., Mokhothu, T. H., Mokhena, T. C., and Makhanya, T. R. (2023). “Mitigation of Non-Steroidal Anti-Inflammatory and Antiretroviral Drugs as Environmental Pollutants by Adsorption Using Nanomaterials as Viable Solution—A Critical Review.” *Appl. Sci.*, 13(2).

Silveira, C., Shimabuku-Biadola, Q. L., Silva, M. F., Vieira, M. F., and Bergamasco, R. (2020). “Development of an activated carbon impregnation process with iron oxide nanoparticles by

green synthesis for diclofenac adsorption.” *Environ. Sci. Pollut. Res.*, 27(6), 6088–6102.

Singh, P., Bhrara, K., and Singh, G. (2008). “Adsorption and kinetic studies of L-leucine as an inhibitor on mild steel in acidic media.” *Appl. Surf. Sci.*, 254(18), 5927–5935.

Sivagurunathan, P., and Gibin, S. R. (2016). “Preparation and characterization of nickel ferrite nano particles by co-precipitation method with citrate as chelating agent.” *J. Mater. Sci. Mater. Electron.*, 27(3), 2601–2607.

Soares, S. F., Fernandes, T., Sacramento, M., Trindade, T., and Daniel-da-Silva, A. L. (2019). “Magnetic quaternary chitosan hybrid nanoparticles for the efficient uptake of diclofenac from water.” *Carbohydr. Polym.*, 203(September 2018), 35–44.

Song, X. J., Qin, Z. Q., Wang, X. B., Yang, F., Fang, Q. L., and She, C. G. (2016). “ β -Cyclodextrin Modified with Magnetic Nanoparticles Noncovalently for β -Naphthol Removal from Wastewater.” *Synth. React. Inorganic, Met. Nano-Metal Chem.*, 46(1), 143–146.

Song, X., Liu, H., Cheng, L., and Qu, Y. (2010). “Surface modification of coconut-based activated carbon by liquid-phase oxidation and its effects on lead ion adsorption.” *Desalination*, 255(1–3), 78–83.

Soto-Cantu, E., Cueto, R., Koch, J., and Russo, P. S. (2012). “Synthesis and rapid characterization of amine-functionalized silica.” *Langmuir*, 28(13), 5562–5569.

Springer, V., Barreiros, L., Avena, M., and Segundo, M. A. (2018). “Nickel ferrite nanoparticles for removal of polar pharmaceuticals from water samples with multi-purpose features.” *Adsorption*, 24(5), 431–441.

Springer, V., Pecini, E., and Avena, M. (2016). “Magnetic nickel ferrite nanoparticles for removal of dipyrone from aqueous solutions.” *J. Environ. Chem. Eng.*, 4(4), 3882–3890.

Streit, A. F. M., Collazzo, G. C., Druzian, S. P., Verdi, R. S., Foletto, E. L., Oliveira, L. F. S., and Dotto, G. L. (2021). “Adsorption of ibuprofen, ketoprofen, and paracetamol onto activated carbon prepared from effluent treatment plant sludge of the beverage industry.” *Chemosphere*, 262(xxxx).

Subedi, B., Balakrishna, K., Joshua, D. I., and Kannan, K. (2017). “Mass loading and removal of pharmaceuticals and personal care products including psychoactives, antihypertensives, and antibiotics in two sewage treatment plants in southern India.” *Chemosphere*, 167, 429–437.

Subki, N. S., Akhir, N. M., Abdul Halim, N. S., and Nik Yusoff, N. R. (2020). “COD Reduction in Industrial Wastewater Using Activated Carbon Derived from Wodyetia Bifurcata Fruit.” *IOP Conf. Ser. Earth Environ. Sci.*, 549(1).

Sun, C., Zhou, R., E, J., Sun, J., and Ren, H. (2015). “Magnetic CuO@Fe₃O₄ nanocomposite as a highly active heterogeneous catalyst of persulfate for 2,4-dichlorophenol degradation in

aqueous solution.” *RSC Adv.*, 5(70), 57058–57066.

Sun, J., Wu, T., Liu, Z., Shao, B., Liang, Q., He, Q., Luo, S., Pan, Y., Zhao, C., and Huang, D. (2022a). “Peroxymonosulfate activation induced by spinel ferrite nanoparticles and their nanocomposites for organic pollutants removal: A review.” *J. Clean. Prod.*, 346(October 2021), 131143.

Sun, J., Wu, T., Liu, Z., Shao, B., Liang, Q., He, Q., Luo, S., Pan, Y., Zhao, C., and Huang, D. (2022b). “Peroxymonosulfate activation induced by spinel ferrite nanoparticles and their nanocomposites for organic pollutants removal: A review.” *J. Clean. Prod.*, 346(October 2021), 131143.

Sun, Y., Han, Z., Zhang, X., Qin, D., Chen, G., and He, X. (2022c). “Efficient removal of lomefloxacin by Z-scheme MrGO/Ag₂WO₄ heterojunction recyclable composite under visible light: Mechanism of adsorption and photodegradation.” *J. Environ. Chem. Eng.*, 10(1), 107120.

Suriyanon, N., Punyapalakul, P., and Ngamcharussrivichai, C. (2013). “Mechanistic study of diclofenac and carbamazepine adsorption on functionalized silica-based porous materials.” *Chem. Eng. J.*, 214, 208–218.

Taheran, M., Naghdi, M., Brar, S. K., Verma, M., and Surampalli, R. Y. (2018). “Emerging contaminants: Here today, there tomorrow!” *Environ. Nanotechnology, Monit. Manag.*, 10, 122–126.

Taj, M. B., Alkahtani, M. D. F., Raheel, A., Shabbir, S., Fatima, R., Aroob, S., yahya, R., Alelwani, W., Alahmadi, N., Abualnaja, M., Noor, S., Ahmad, R. H., and Alshater, H. (2021). “Bioconjugate synthesis, phytochemical analysis, and optical activity of NiFe₂O₄ nanoparticles for the removal of ciprofloxacin and Congo red from water.” *Sci. Rep.*, 11(1), 1–19.

Talib, A., and Randhir, T. O. (2016). “Managing Emerging Contaminants: Status, Impacts, and Watershed-Wide Strategies.” *Expo. Heal.*, 8(1), 143–158.

Tan, K. L., and Hameed, B. H. (2017). “Insight into the adsorption kinetics models for the removal of contaminants from aqueous solutions.” *J. Taiwan Inst. Chem. Eng.*, 74, 25–48.

Tan, Z., Tan, F., Zhao, L., and Li, J. (2012). “The Synthesis, Characterization and Application of Ciprofloxacin Complexes and Its Coordination with Copper, Manganese and Zirconium Ions.” *J. Cryst. Process Technol.*, 02(02), 55–63.

Tatarchuk, T., Mironyuk, I., Kotsyubynsky, V., Shyichuk, A., Myslin, M., and Boychuk, V. (2020). “Structure, morphology and adsorption properties of titania shell immobilized onto cobalt ferrite nanoparticle core.” *J. Mol. Liq.*, 297, 111757.

Tavassoli, S., Cheraghi, S., Etemadifar, P., and Mollahosseini, A. (2024). “Optimization and

characterization of silver nanoparticle - modified luffa for the adsorption of ketoprofen and reactive yellow 15 from aqueous solutions.” *Sci. Rep.*, 1–19.

Tejabhiram, Y., Pradeep, R., Helen, A. T., Gopalakrishnan, C., and Ramasamy, C. (2014). “Ferrous sulfate based low temperature synthesis and magnetic properties of nickel ferrite nanostructures.” *Mater. Res. Bull.*, 60(1), 778–782.

Thalla, A. K., and Vannarath, A. S. (2020). “Response to letter to the editor on the paper ‘occurrence and environmental risks of nonsteroidal anti-inflammatory drugs in urban wastewater in the southwest monsoon region of India.’” *Environ. Monit. Assess.*, 192(9), 1–13.

Thi Minh Tam, N., Liu, Y. G., and Thom, N. Van. (2022). “Magnetic gelatin-activated biochar synthesis from agricultural biomass for the removal of sodium diclofenac from aqueous solution: adsorption performance and external influence.” *Int. J. Environ. Anal. Chem.*, 102(19), 7569–7594.

Thomas Dippong, Levei, E. A., and Cadar, O. (2021). “Recent Advances in Synthesis and Applications of MFe₂O₄ (M = Co, Cu, Mn, Ni, Zn) Nanoparticles.” *Nanomaterials*, 4(11), 1560.

Thommes, M., Kaneko, K., Neimark, A. V., Olivier, J. P., Rodriguez-Reinoso, F., Rouquerol, J., and Sing, K. S. W. (2015). “Physisorption of gases, with special reference to the evaluation of surface area and pore size distribution (IUPAC Technical Report).” *Pure Appl. Chem.*, 87(9–10), 1051–1069.

Tiwari, D., Lalhriatpuia, C., and Lee, S. M. (2015). “Hybrid materials in the removal of diclofenac sodium from aqueous solutions: Batch and column studies.” *J. Ind. Eng. Chem.*, 30, 167–173.

Tomul, F., Arslan, Y., and Tran, H. N. (2019). “Metal-Loaded Carbonated Mesoporous Calcium Silicates: Synthesis, Characterization, and Application for Diclofenac Removal from Water.” *Ind. Eng. Chem. Res.*, 58(48), 22084–22093.

Tran, N. H., Reinhard, M., and Gin, K. Y. H. (2018). “Occurrence and fate of emerging contaminants in municipal wastewater treatment plants from different geographical regions-a review.” *Water Res.*, 133, 182–207.

Tran, T. Van, Nguyen, D. T. C., Nguyen, T. T., Le, H. T. N., Nguyen, C. Van, and Nguyen, T. D. (2020). “Metal-organic framework HKUST-1-based Cu/Cu₂O/CuO@C porous composite: Rapid synthesis and uptake application in antibiotics remediation.” *J. Water Process Eng.*, 36(February), 101319.

Tseng, H.-C., Lee, C.-Y., Weng, W.-L., and Shiah, I.-M. (2009). “Solubilities of amino acids in water at various pH values under 298.15K.” *Fluid Phase Equilib.*, 285(1–2), 90–95.

- Turk Sekulic, M., Boskovic, N., Slavkovic, A., Garunovic, J., Kolakovic, S., and Pap, S. (2019). "Surface functionalised adsorbent for emerging pharmaceutical removal: Adsorption performance and mechanisms." *Process Saf. Environ. Prot.*, 125, 50–63.
- Uddandarao, P., Hingnekar, T. A., Balakrishnan, R. M., and Rene, E. R. (2019). "Solar assisted photocatalytic degradation of organic pollutants in the presence of biogenic fluorescent ZnS nanocolloids." *Chemosphere*, 234, 287–296.
- Vara Prasad, B. B. V. S., Ramesh, K. V., and Srinivas, A. (2018). "Structural and magnetic properties of nanocrystalline nickel ferrite (NiFe₂O₄) synthesized in sol-gel and combustion routes." *Solid State Sci.*, 86, 86–97.
- Veclani, D., and Melchior, A. (2020). "Adsorption of ciprofloxacin on carbon nanotubes: Insights from molecular dynamics simulations." *J. Mol. Liq.*, 298, 111977.
- Wang, C. J., Li, Z., Jiang, W. T., Jean, J. S., and Liu, C. C. (2010). "Cation exchange interaction between antibiotic ciprofloxacin and montmorillonite." *J. Hazard. Mater.*, 183(1–3), 309–314.
- Wang, J., Ren, F., Yi, R., Yan, A., Qiu, G., and Liu, X. (2009). "Solvothermal synthesis and magnetic properties of size-controlled nickel ferrite nanoparticles." *J. Alloys Compd.*, 479(1–2), 791–796.
- Wang, J., Sun, Y., Jiang, H., and Feng, J. (2017). "Removal of caffeine from water by combining dielectric barrier discharge (DBD) plasma with goethite." *J. Saudi Chem. Soc.*, 21(5), 545–557.
- Wang, J., and Wang, S. (2016). "Removal of pharmaceuticals and personal care products (PPCPs) from wastewater: A review." *J. Environ. Manage.*, 182, 620–640.
- Wang, J., Wang, X., and Zhong, D. (2024). "Applied Surface Science Nanofibrous membranes modified by zwitterionic polyelectrolyte brushes for effective adsorption of ciprofloxacin hydrochloride." *Appl. Surf. Sci.*, 657(February), 159760.
- Wang, Y., He, L., Dang, G., Li, H., and Li, X. (2021). "Polypyrrole-functionalized magnetic Bi₂MoO₆ nanocomposites as a fast, efficient and reusable adsorbent for removal of ketoprofen and indomethacin from aqueous solution." *J. Colloid Interface Sci.*, 592, 51–65.
- Wang, Y., Zhang, W., Luo, C., Wu, X., Wang, Q., Chen, W., and Li, J. (2016). "Synthesis, characterization and enhanced electromagnetic properties of NiFe₂O₄@SiO₂-decorated reduced graphene oxide nanosheets." *Ceram. Int.*, 42(15), 17374–17381.
- Wei, Z., Li, H., Wu, J., Dong, Y., Zhang, H., Chen, H., and Ren, C. (2020). "3DRGO-NiFe₂O₄/NiO nanoparticles for fast and simple detection of organophosphorus pesticides." *Chinese Chem. Lett.*, 31(1), 177–180.
- Wiśniewska, M., Szewczuk-Karpisz, K., and Sternik, D. (2015). "Adsorption and thermal

properties of the bovine serum albumin–silicon dioxide system.” *J. Therm. Anal. Calorim.*, 120(2), 1355–1364.

Wong, Y. C., Szeto, Y. S., Cheung, W. H., and McKay, G. (2004). “Adsorption of acid dyes on chitosan—equilibrium isotherm analyses.” *Process Biochem.*, 39(6), 695–704.

Wu, G., Ma, J., Li, S., Guan, J., Jiang, B., Wang, L., Li, J., Wang, X., and Chen, L. (2018). “Magnetic copper-based metal organic framework as an effective and recyclable adsorbent for removal of two fluoroquinolone antibiotics from aqueous solutions.” *J. Colloid Interface Sci.*, 528, 360–371.

Wu, S., Zhao, X., Li, Y., Zhao, C., Du, Q., Sun, J., Wang, Y., Peng, X., Xia, Y., Wang, Z., and Xia, L. (2013). “Adsorption of ciprofloxacin onto biocomposite fibers of graphene oxide/calcium alginate.” *Chem. Eng. J.*, 230, 389–395.

Xiangfeng, C., Dongli, J., and Chenmou, Z. (2007). “The preparation and gas-sensing properties of NiFe₂O₄ nanocubes and nanorods.” *Sensors Actuators, B Chem.*, 123(2), 793–797.

Xiao, Y., Azaiez, J., and Hill, J. M. (2018). “Erroneous Application of Pseudo-Second-Order Adsorption Kinetics Model: Ignored Assumptions and Spurious Correlations.” 6–10.

Xu, J., Tian, Y., Li, Z., Tan, B. H., Tang, K. Y., and Tam, K. C. (2022). “β-Cyclodextrin functionalized magnetic nanoparticles for the removal of pharmaceutical residues in drinking water.” *J. Ind. Eng. Chem.*, 109, 461–474.

Xu, Q., Xu, Y., Xue, J., Zhu, F., Zhong, Z., and Liu, R. (2021). “An innovative alcohol-solution combustion-calcination process for the fabrication of NiFe₂O₄ nanorods and their adsorption characteristics of methyl blue in aqueous solution.” *Mater. Res. Express*, 8(9), 095003.

Yang, J., Chen, W., Liu, X., Zhang, Y., and Bai, Y. (2017). “Hydrothermal synthesis and photoluminescent mechanistic investigation of highly fluorescent nitrogen doped carbon dots from amino acids.” *Mater. Res. Bull.*, 89, 26–32.

You, J., Wang, L., Zhao, Y., and Bao, W. (2021a). “A review of amino-functionalized magnetic nanoparticles for water treatment: Features and prospects.” *J. Clean. Prod.*, 281, 124668.

You, Y., Shi, Z., Li, Y., Zhao, Z., He, B., and Cheng, X. (2021b). “Magnetic cobalt ferrite biochar composite as peroxymonosulfate activator for removal of lomefloxacin hydrochloride.” *Sep. Purif. Technol.*, 272(May), 118889.

Yuan, Y., Yang, D., Mei, G., Hong, X., Wu, J., Zheng, J., Pang, J., and Yan, Z. (2018). “Preparation of konjac glucomannan-based zeolitic imidazolate framework-8 composite aerogels with high adsorptive capacity of ciprofloxacin from water.” *Colloids Surfaces A Physicochem. Eng. Asp.*, 544(November 2017), 187–195.

- Zaidi, R., Khan, S. U., Farooqi, I. H., and Azam, A. (2021). "Investigation of kinetics and adsorption isotherm for fluoride removal from aqueous solutions using mesoporous cerium–aluminum binary oxide nanomaterials." *RSC Adv.*, 11(46), 28744–28760.
- Zhang, B., Wu, Y., and Fan, Y. (2019a). "Synthesis of Novel Magnetic NiFe₂O₄ Nanocomposite Grafted Chitosan and the Adsorption Mechanism of Cr(VI)." *J. Inorg. Organomet. Polym. Mater.*, 29(1), 290–301.
- Zhang, H., and Huang, C. H. (2007). "Adsorption and oxidation of fluoroquinolone antibacterial agents and structurally related amines with goethite." *Chemosphere*, 66(8), 1502–1512.
- Zhang, H., Nengzi, L., Wang, Z., Zhang, X., Li, B., and Cheng, X. (2020a). "Construction of Bi₂O₃/CuNiFe LDHs composite and its enhanced photocatalytic degradation of lomefloxacin with persulfate under simulated sunlight." *J. Hazard. Mater.*, 383(September 2019), 121236.
- Zhang, H., Wang, J., Zeng, Y., Wang, G., Han, S., Yang, Z., Li, B., Wang, X., Gao, J., Zheng, L., Liu, X., Huo, Z., and Yu, R. (2020b). "Leucine-coated cobalt ferrite nanoparticles: Synthesis, characterization and potential biomedical applications for drug delivery." *Phys. Lett. A*, 384(24), 126600.
- Zhang, H., Wang, J., Zhang, X., Li, B., and Cheng, X. (2019b). "Enhanced removal of lomefloxacin based on peroxymonosulfate activation by Co₃O₄/δ-FeOOH composite." *Chem. Eng. J.*, 369(March), 834–844.
- Zhang, L., Zhang, R., Wang, W., Han, S., and Xiao, P. (2021). "UV-enhanced nano-nickel ferrite-activated peroxymonosulfate for the degradation of chlortetracycline hydrochloride in aqueous solution." *RSC Adv.*, 11(33), 20580–20590.
- Zhang, X., Gao, Y., Li, Y., Zhou, Y., Ma, H., Shang, J., and Cheng, X. (2022). "Synthesis of magnetic NiFe₂O₄/CuS activator for degradation of lomefloxacin via the activation of peroxymonosulfate under simulated sunlight illumination." *Sep. Purif. Technol.*, 288(December 2021), 120664.
- Zhang, Y., Wang, W., Li, Q., Yang, Q., Li, Y., and Du, J. (2015). "Colorimetric magnetic microspheres as chemosensor for Cu²⁺ prepared from adamantane-modified rhodamine and β-cyclodextrin-modified Fe₃O₄@SiO₂ via host-guest interaction." *Talanta*, 141, 33–40.
- Zhou, Y., Sun, L., Wang, H., Liang, W., Yang, J., Wang, L., and Shuang, S. (2016). "Investigation on the uptake and release ability of β-cyclodextrin functionalized Fe₃O₄ magnetic nanoparticles by methylene blue." *Mater. Chem. Phys.*, 170, 83–89.
- Zong, Y., Ma, S., Gao, J., Xu, M., Xue, J., and Wang, M. (2021). "Synthesis of Porphyrin Zr-MOFs for the Adsorption and Photodegradation of Antibiotics under Visible Light." *ACS*

Omega, 6(27), 17228–17238.

Zunngu, S. S., Madikizela, L. M., Chimuka, L., and Mdluli, P. S. (2017). “Synthesis and application of a molecularly imprinted polymer in the solid-phase extraction of ketoprofen from wastewater.” *Comptes Rendus Chim.*, 20(5), 585–591.

BIO-DATA

Mrs. I INDUMATHI

Email address : indumathiveluilango22@gmail.com

Contact Number : +91 82200 82087

Permanent address : No.25 Mariyam Colony,

Seniar kulam street,

Karaikal – 609602

Puducherry – India.

EDUCATION

Program	Institution	CGPA/%	Year of Completion
M.Tech Environmental Engineering	Pondicherry Engineering College (PEC) (Autonomous)	8.48 / 10	2015-2017
B.Tech Chemical Engineering	Pondicherry Engineering College (PEC) (Pondicherry University)	8.22 / 10	2011-2015
Higher Secondary	Seventh Day Adventist Higher Secondary School (State Board)	89.5	2011
High School	Seventh Day Adventist Higher Secondary School (State Board)	92	2009

TECHNICAL SKILLS

Software proficiency : Microsoft Office Word, Microsoft Office Excel, Microsoft Office Power Point, Origin85, PYTHON.

Laboratory skills and other: Water quality Testing, Air quality Testing, Soil Testing, EIA report preparation.

Instrument Operation : UV-Visible Spectrophotometer, Atomic Absorption Spectrophotometer, Total Organic Carbon Analyzer, Thermogravimetric Analyzer, Inductive couple Plasma Analyzer, High Performance Liquid Chromatography, FE-SEM, XRD, Zeta size and Potential Analyzer, Fourier Transform Infrared Spectroscopy, Bomb Calorimeter, Atomic Force Microscope.

POSITIONS OF RESPONSIBILITY

- Teaching Assistant for Environmental air quality analysis lab I & II (*Course instructor: Prof. Raj Mohan B and Dr. Jithendra Paul, Department of Chemical Engineering*), NIT, Karnataka.
- Teaching Assistant for Mass transfer lab (*Course instructor: Dr. Hari Mahalingam and Dr. B. Ashraf Ali, Department of Chemical Engineering*), NIT, Karnataka.

PRESENTATION AND PUBLICATIONS

1. Kritiya Kaspanich, Chettiyappan Visvanathan, **Indumathi Ilango**, Balakrishnan, R. M., "Removal of Methylene Blue from Synthetic Textile Wastewater using PAC, Rice Husk, TiO₂, Synthesized and Functionalized NiFe₂O₄ NPs, The 2nd International Conference on Green Technologies for Sustainable Water 2019, 1-5, December, 2019, Ho Chi Minh City, Vietnam
2. Balakrishnan, R. M., **Ilango, I.**, Gamana, G., Bui, X.-T., & Pugazhendhi, A. (2020). Cobalt ferrite nanoparticles and peroxymonosulfate system for the removal of ampicillin from aqueous solution. *Journal of Water Process Engineering*, 101823. [doi:10.1016/j.jwpe.2020.101823](https://doi.org/10.1016/j.jwpe.2020.101823)
3. **Ilango, I.**, Balakrishnan, R. M, Visvanathan, C, Bui, X.-T. Stimulation of peroxymonosulfate using nickel ferrite nanoparticles for the degradation of lomefloxacin hydrochloride. International Symposium on water sustainability & Green technologies - WSGT2022, November 25 – 26, 2022, Ho Chi Minh City, Vietnam.
4. **Ilango, I.**, Susanna, D., Gabriella, R. et al. Zinc-decorated barium oxide nanorods for the effective sunlight-induced catalytic degradation of Irgalite violet

dye. *Nanotechnol. Environ. Eng.* **8**, 655–673 (2023).
<https://doi.org/10.1007/s41204-023-00329-6>.

5. **Ilango, I.**, Balakrishnan, R.M., Visvanathan, C. *et al.* Functionalization of β -cyclodextrin onto NiFe₂O₄ nanoparticles for the removal of ketoprofen and diclofenac from the aqueous solutions. *Int. J. Environ. Sci. Technol.* (2023).
<https://doi.org/10.1007/s13762-023-05146-7>.
6. **Ilango, I.**, Balakrishnan R.M. Amino acid functionalized metal oxide nanocomposite for the removal of fluoroquinolones, *Journal of Cleaner Production* (2023), doi: <https://doi.org/10.1016/j.jclepro.2023.139071>
7. **Ilango, I.**, Balakrishnan, R. M, Visvanathan, C, Bui, X.-T. Stimulation of peroxymonosulfate using nickel ferrite nanoparticles for the degradation of lomefloxacin hydrochloride and caffeine. *Nanotechnology for Environmental Engineering*. Manuscript No. NTEE-D-24-00171 (Submitted).

TEACHING AND RESEARCH EXPERIENCE

- 11 Months of teaching experience in the Department of Petrochemical Technology and Petroleum Engineering at Excel College of Engineering and Technology, Namakkal, Tamil Nadu. (Courses handled: Mass Transfer, Process Calculations, Petroleum Refinery Engineering)
- Guided one B. Tech project in the Department of Petrochemical Technology, Excel College of Engineering and Technology
- 2 years and 10 months of research experience in ASEAN-INDIA, DST Project under the Principal Investigator Prof. Raj Mohan. B in the Department of Chemical Engineering and Prof. Viswanathan Chettiyappan in the Department of Energy Environment and climate from Asian Institute of Technology, Thailand and Bui Xuan Thanh (Xuan-Thanh BUI) in the Key Lab of Advanced Waste Treatment Technology (VNU-HCM) - Dept. Water Science & Technology, Vietnam as Co-investigators. at National Institute of Technology Karnataka, (NITK) Surathkal, Mangalore.

- Research experience of 10-15 days at the Asian Institute of Technology AIT, BANGKOK Thailand under DST, SERB ASEAN -INDIAN Project.

AREA OF INTEREST

- Conversion of waste to useful adsorbent or catalyst and energy
- Instrumental analysis of water, air and soil
- Adsorption, advanced oxidation process and remediation techniques of water and soil

DECLARATION

I hereby declare that the above written particulars are true to the best of my knowledge.

Place: Surathkal, India

Date: 29-10-2024

I INDUMATHI